Cardiff School of engineering

Magnetics and Materials Research Group

Novel water-based processing route for producing structured graphene/alumina composites

Author:
Guillermo Menéndez Rodríguez

Supervisors:
Dr. Victoria García Rocha
Prof. Sam Evans
Prof. Gao Min

Submitted for the degree of Doctor of Philosophy (PhD)

January, 2022

Summary

Graphene/ceramic composites have settled as a promising vehicle for exploiting graphene's outstanding combination of mechanical, electrical and thermal properties. However, graphene is still not fully established in the industry after many years of thorough research, owing to its processing cost and scalability. Recent works have integrated innovative processing techniques (such as freeze-casting and nanoparticle deposition) to produce highly-structured ceramic-based composites inspired from hierarchical natural materials (e.g. nacre) to achieve mechanical performance beyond current synthetic materials.

This thesis explored a novel processing strategy for graphene/ceramic composites, using water-based graphene oxide (GO) suspensions and alumina powder as precursors. Reduced graphene oxide (rGO) aerogels of 1.5 – 4 mg cm^{-3} were obtained by freeze-casting water-based GO slurries after optimisation of GO concentration, additives content and freezing rate and later carbonisation at 900°C. After thermal annealing, the directional alignment of the aerogels was preserved with channel widths of 15 – 30 µm, verifying the significant elimination of oxidised groups in the GO sheets through chemical and structural characterisation and moderately restoring the electrical conductivity up to 20 S m^{-1}. Using this water-based processing approach, rGO aerogels were successfully decorated with alumina nanoparticles below 20 nm after exploring a scarcely researched gel synthesis route based on aluminium lactate.

An amphiphilic triblock copolymer (PF127) was included in the water-based alumina suspensions to enable the infiltration into rGO structures, otherwise prevented by their hydrophobicity. PF127/Al_2O_3 wt./wt. ratios were adjusted from extensive wettability and infiltration tests. After consolidation via Spark Plasma Sintering (SPS), the structure of embedded rGO scaffolds was preserved within the sintered alumina matrix, exhibiting channel widths of 5 – 15 µm. This work aimed to set the basis for a cost-effective environmentally-friendly approach to produce ordered graphene/ceramic composites through a scaffold and infiltration process, with high potential for obtaining stronger and tougher materials with electrical functionalities.

Acknowledgements

I want to thank the Engineering and Physical Sciences Research Council (EPSRC) and Cardiff University for providing the funding to make this project a reality and Prof Eduardo Saiz from the CASC group at Imperial College for the graphene oxide supplies. I want to thank Victoria for trusting me for this position and mentoring me from the very beginning, giving me the guidance to grow as a researcher and always vouching for me. Thank you to Gao and Sam for their fantastic supervision and continuous and kind support throughout these years of working together.

I want to extend my gratitude to all these people who helped me in more than one way:

My previous supervisor Salva who taught me many valuable lessons during our short time together and encouraged me to get a PhD in the UK. My colleagues Martin, Suk, Mo, Mazin, Godwin and the rest. Most especially Joe, my partner in crime during the second half of the project, who brought light to long laboratory sessions and always supported me inside and outside the university.

The Newport and Cardiff Materials Society (NCMS), Cardiff Materials Research Network (CMRN), Gregynog conference, Speaking of Science and Three Minute Thesis events for all the awards given. Particularly thankful to the European Ceramic Society (ECerS) for their grant to attend the ICACC19 and Winter Workshop in Florida and let me have a wonderful experience.

Emmanuel, Julian, Nacho, John, Daniel, and other technicians and lecturers, who helped me with many techniques and equipment. All the people at INCAR: María, Dani, Adri, Laura and the rest, who welcomed me from the very beginning and made hour-long car trips worthy. The undergraduate and master students I had the pleasure to mentor and contribute to their respective projects: Tom, Céline, Mo, Danniman, Longyao, John, Ryan and both Mechatronics teams.

The Uni gang for all the experiences together: Nefeli, Filipa, Corentin, Ben, Giovanni, Lucy, Sam, Natalia, Ema and the rest of the Cardiff Post-Apocalypse group. My fellow Miskin boys (Siamac, Howie and Mukhit). The support and laughs had with the Spanish couples: Pablo and Yanina, Unai and Itsaso, Mikel and Sara. My beloved bandmates and friends from Where the Waves Are Born who cherished me in the distance and let me pursue my dreams.

My family for their unconditional love and support in everything I do, I could not feel any luckier to have them. Especially my father and sister, who always took care of me and gave me all the strength I needed when things went south.

Luri for being the best companion I could ever ask for. For all the help with schematics, proofreading and PhD-related bits. Most importantly, for being by my side helping me with everything. Without you, I would not have made it past these hard years; thank you for being there for me.

Finally, I would like to thank my mother Ana María, the backbone of my life, without whom I would not have made it this far. I know you would be the proudest, and I hope you can see me now, wherever you are. I will never forget. - *Into the Earth, I'll have your name engraved.*

Conference attendance and Grants

- Gregynog Conference, UK, 2018. Poster and speaker. - *Best poster award*
- Speaking of Science, UK, 2018. Poster. - *Best poster award*
- CASC Ninth Summer School, UK, 2018.
- ACerS Winter Workshop and International Conference and Exposition on Advanced Ceramics and Composites (ICACC), USA, 2019. Speaker. - *Travel grant by the European Ceramic Society.*
- Cardiff Materials Research Network conference, UK, 2019. Poster and speaker. - *Best poster award*
- Young Persons' Lecture Competition, UK, 2019. - *Cardiff heat winner*
- Young Persons' Lecture Competition Regional Final, UK, 2019.
- 1DRAC meeting, UK, 2019. Speaker.
- XVI ECerS Conference, Italy, 2019. Speaker.
- Cardiff Materials Research Network conference, UK, 2020. Poster.
- Three Minute Thesis, UK, 2020. - *Cardiff Heat third place winner*
- UK Chapter Ceramics Talent, 2020. Speaker. - *Invitational*

Publications

- **Optimum silver contact sputtering parameters for efficient perovskite solar cell fabrication.** Martin C. Eze, Godwin Ugwuanyi, Meng Li, Hyginus U. Eze, Guillermo Menendez, Alex Evans, Victoria G. Rocha, Zhe Li, Gao Min. *Solar Energy Materials and Solar Cells.* Volume 230, 111185 (2021).
- **Enabling water-based processing of graphene/alumina composites using an infiltration approach with amphiphilic triblock copolymers.** Guillermo Menendez, Thomas Kynaston, Ignacio J. Villar-Garcia, Gao Min, Sam L. Evans and Victoria G. Rocha. *(Submitted to Journal of the European Ceramic Society).*

Contents

List of Figures

List of Tables

General introduction

In the context of materials science and engineering, advanced ceramics comprise a wide range of high-performing materials essential for aerospace applications, turbine blades, cutting tools and medical prostheses as notable examples. Advanced ceramics are carefully engineered and exploited due to their high hardness and capability to work in demanding environments under high-temperature and oxidative conditions. However, ceramic materials also exhibit some critical weaknesses like thermal fatigue and their lack of toughness and the ability to withstand impacts without failure.

Achieving ceramics that are both strong and tough is a widely researched topic in materials science, as these two properties are generally mutually exclusive. One approach to pursue this goal consists of integrating secondary constituents in the ceramics formulation (e.g. polymers, metals or other ceramics) delivering ceramic-based composites with more balanced properties and extended durability. One of the most promising materials for this purpose is graphene, owing to its remarkable combination of mechanical, electrical and thermal properties, especially in the form of graphene nano-platelets (GNP) or reduced graphene oxide (rGO) for scalable and cost-effective processing.

The production of ceramic-based composites with extensive hierarchy has also emerged as a pathway to obtain strong and tough materials with superior properties compared to those produced through random mixing of their constituents. Inspired from biomaterials like nacre, bone or muscle, highly-structured composites can prevent the quick expansion of internal cracks leading to quick failure, while maintaining high strength and hardness.

Joining these two approaches outlined: the implementation of a powerful secondary constituent such as graphene, and a carefully tailored structure by applying non-conventional ceramic processing routes, consolidates an attractive strategy to produce materials with enhanced performance and added functionalities. This work aims to provide knowledge towards the development of highly-structured graphene/ceramic composites, maintaining a non-toxic water-based approach that may comply with the challenges in structural design and assembly in current and near-future engineering.

Chapter 1

Literature Review

1.1 Advanced structural ceramics

Ceramics are defined as inorganic and non-metallic materials of polycrystalline nature. [37]. Among the broad range of ceramics utilised throughout history (pottery, refractories, glasses, cement), the so-called advanced ceramics started to be manufactured in the early 1900s. These ceramics are carefully engineered in structure and composition, maximising their structural, electrical and environmental properties [38].

Several advanced ceramic materials (e.g., silicon carbide (SiC), boron nitride (B_4N), alumina (Al_2O_3) or yttria-stabilised zirconia (YSZ), to name a few) have become industry standards owing to their high melting points (above 2000 °C), chemical stability and resistance to oxidation, high strength, high wear resistance and non-toxicity [38, 39]. As for this remarkable set of properties, ceramic materials can be found in a plethora of high-performance applications such as turbine blades, bearings, inert medical prostheses, high-temperature furnaces or thermal and electrical insulators [38].

However, advanced ceramics also present major flaws limiting their use in challenging conditions. In general, advanced ceramics do not withstand thermal shock adequately and are prone to failure due to thermal fatigue [39]. As a result of their high strength, they also appear brittle in nature, exhibiting none or minimal plastic deformation, which leads to sudden failure upon the formation of internal cracks.

1.1.1 Ceramic-based composites

It is common to transform pure ceramic materials into composites (a material consisting of two or more constituents with distinct physical and chemical properties) by integrating a second material in their formulation to improve their most criti-

cal weaknesses like thermal shock resistance and low fracture toughness. Combining these constituents can produce a new bulk material of better-balanced characteristics outperforming each separate component.

In ceramic-based composites, secondary materials generally consist of a softer phase (such as a polymer or a metal) that can reduce the brittle behaviour of the ceramic by providing some degree of plasticity at the cost of lowering the strength and hardness of the material. Ceramics can also be integrated with other ceramics (in the form of ceramic-matrix composites) by selecting different source materials or morphologies (e.g. unidirectional fibres) that can moderately improve the mechanical performance maintaining resistance to oxidation and ultra-high temperatures. Examples of these are ultra-high-temperature ceramics (UHTC) based on nitrides, borides or carbides (e.g. TiC, ZrN or TiN) with their derived composites which can offer chemical stability above 2000 °C [40].

A simple relationship known as the rule of mixtures is conventionally followed to provide an approximate value of the properties from two distinct constituents in composite materials, which can be applied to density, Young's modulus, or electrical and thermal conductivities [11]. This rule estimates the overall value of a composite property (X_c) by employing the volume fractions from both constituents (V_1 and $V_2 = (1 - V_1)$) across one direction and their respective values X_1 and X_2, which is generally expressed as:

$$X_c = V_1 X_1 + (1 - V_1) X_2 \tag{1.1}$$

This example is a lineal model simplification assuming parallel/in-series stacking of each material. Other expressions such as the inverse rule of mixtures can provide better predictions on different scenarios depending on the materials stacking. Integrating complex structuring of the constituents in the composite can increase properties beyond the values predicted by the rule of mixtures, as explored in later sections of this review.

1.1.2 Traditional processing of ceramics

The processing of ceramic-based materials is inherently challenging due to their lack of ductility and malleability combined with their high melting points (commonly above 2500 °C) compared to metals. Instead of a process of classical melting and solidification route applied on the latter, ceramics are traditionally produced via powder processing, which requires diffusional mass transport to achieve consolidation [41]. This process is divided into several steps (Figure 1.1) comprising the preparation of the ceramic powder, shaping and compaction (achieving the intended shape of the component, referred to as green body), firing/sintering, and a final machining or

polishing step.

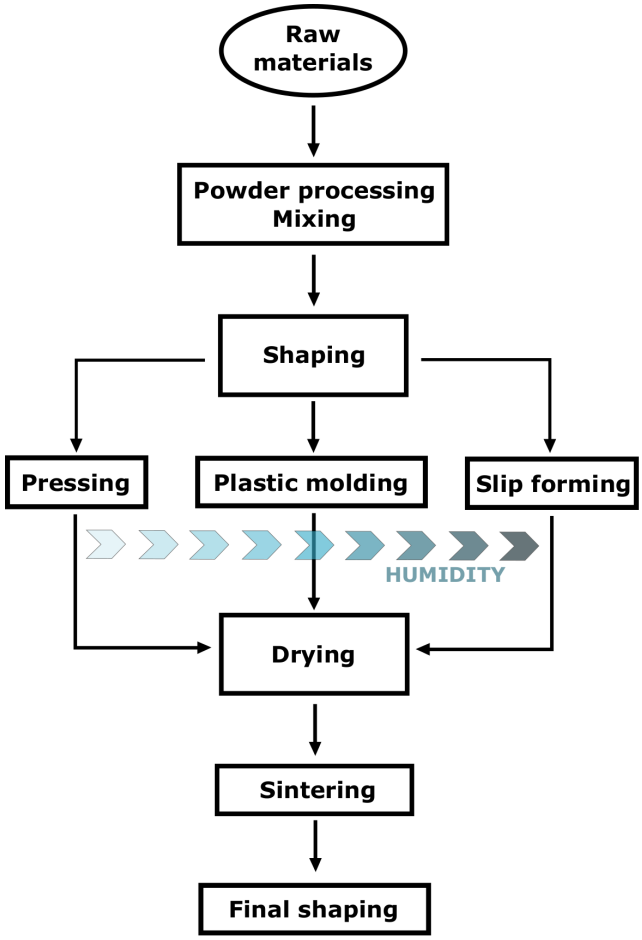

Figure 1.1: *Stages of traditional ceramic processing. Adapted from Moreno (2012) [1].*

The degree of humidity applied during the shaping stage can vary greatly, resulting in various conditions from complete dry processing (powder/pellet pressing) to slip forming. According to Moreno (2012), these can be divided into three main categories divided by humidity level [1]:

- Dry pressing methods with humidity typically below 7 vol.%
- Plastic forming in the humidity range of 15 – 50 vol.% depending on the technique from extrusion to injection moulding
- Colloidal shaping processing with humidity levels over 50 vol.%

Above 50 vol.% moisture, ceramics are primarily in suspension (or slurry) form. Solid particles in suspension are affected by various phenomena such as gravity, the particles' own Brownian motion and the attractive vs repulsive interactions between different particles, all of which play a role in controlling agglomeration and the system's stability [42]. Additives are commonly included in the suspension formulation

to improve its stability by enhancing the attractive forces between particles (by addition of binders and flocculants) or the repulsive forces (dispersants and deflocculants) to reduce agglomeration.

1.1.2.1 Sol-gel synthesis route

Among wet processing routes, sol-gel stands out as an alternative non-conventional technique for producing high-purity advanced ceramics such as alumina, silica or titania. The sol-gel process is highly flexible and can be applied to produce a variety of microstructure and shape forms, including porous foams, nanoparticles, fibres and coatings through an aqueous or non-aqueous approach [2, 43]. Typical sol-gel routes require the preliminary consolidation of a solution, consisting of a dispersion of colloids (solid particles with typical diameters below 1 μm) suspended in a liquid. The colloidal dispersion can be rendered stable by electrostatic and steric interactions, achieved through pH tuning or physical blocking of neighbouring particles, respectively [44]. The solution is then destabilised into a gel, a 3D network of material interconnected via polymeric chains of length greater than a micrometre [38, 45]. The produced gel can be greatly adjusted by shifting the precursor concentration, the pH and temperature of the suspension or the gelation time.

The complete transformation of a solution into a gel can be summarised in the following steps: hydrolysis, condensation/polymerisation, drying and thermal treatment as represented in Figure 1.2:

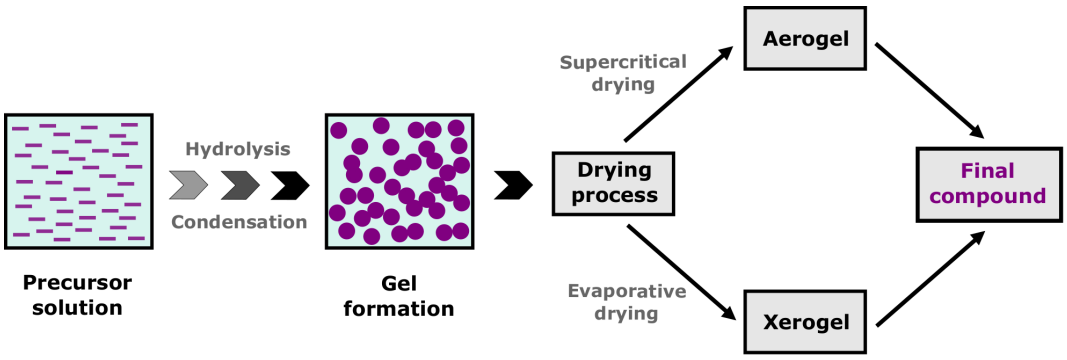

Figure 1.2: *General steps in a sol-gel processing method. Adapted from Rao et al. (2017) [2].*

The colloidal solution is destabilised during the first stage to initiate the reaction. This can be achieved by several means, either by including a catalyst in the mixture or by tuning the pH of the solution. Assuming a metal alkoxide precursor in the form of $M-(OR)$ in water, the following hydrolysis reaction takes place:

$$M-(OR)+H_2O \longrightarrow M-(OH)+R-(OH) \tag{1.2}$$

Upon the formation of $R-(OH)$ units, the phenomenon of polycondensation quickly ensues by crosslinking of the species present in the sol $M-(OR)$ and $M-(OH)$ by two concurrent processes:

$$\begin{aligned} M-(OR)+M-(OH) &\longrightarrow M-O-M+R-(OH) \\ M-(OH)+M-(OH) &\longrightarrow M-O-M+H_2O \end{aligned} \tag{1.3}$$

Hydrolysis and condensation reactions occur simultaneously at multiple sites in the solution during mixing [45]. The progressive linking of the colloids eventually results in a change of viscosity in the whole mixture, producing a three-dimensional network that shows characteristics more typical of a gel than a liquid. Natural ageing of the gel through several hours/days can extend polycondensation even further, which can be similarly achieved at shorter times by applying moderate temperatures above 50 °C [46].

Once the gel is fully developed, and the active species in the mixture have been exhausted, a drying stage is applied to remove the solvent and develop the former wet gel into a xerogel, only composed of the crosslinked polymeric chains. The rate and nature of the drying step can induce substantial changes in the resulting network, for which controlling the thermodynamics of this stage is critical. Heat-treatment is the final stage that ensures the conversion of the polymeric gel into an inorganic compound with the desired crystallography providing densification. This consolidation process is also necessary to remove the amounts of adsorbed water and residual chemical groups trapped in the produced gel that can persist up to 500 °C [47].

1.1.2.2 Sintering

Following the ceramics processing depicted in Figure 1.1, ceramic green bodies require a sintering stage: the transformation of powder compacts into solid pieces via firing [41]. Sintering is generally performed at temperatures above half the material's melting point, leading to a substantial reduction of porosity and an increase in density (approximately from 2 - 6 g cm^{-3} depending on the family of advanced ceramics). Sintering can also be accomplished with or without forming a liquid phase, either directly from one of the components or as the by-product of a sintering reaction between the precursor powders (also known as reaction sintering).

In the absence of a liquid phase, the process is called solid-state sintering, which follows a three-step process comprising neck formation, neck growth, and a final stage of grain coarsening and achievement of nearly theoretical density (Figure 1.3) [4].

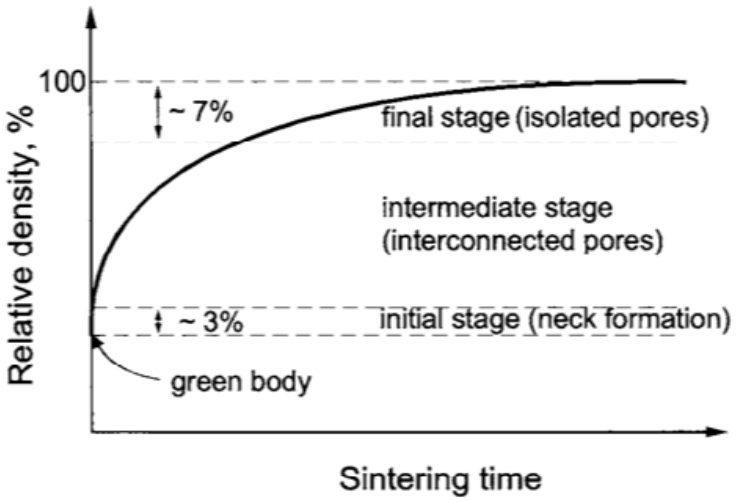

Figure 1.3: *Evolution of relative density throughout the three stages of solid-state sintering. From Kang (2005) [3].*

The formation of a neck between two solid particles is initially controlled by surface atomic diffusion, forming a bridge of material enlarged via mass transport. Increasing the temperature results in the activation of other mechanisms, such as lattice and grain boundary diffusion, which continue neck growth while reducing the interconnection of pores in the material. Different parameters such as the source powder size and shape distribution, temperature, time, pressure or atmosphere during sintering all affect the kinetics of the process, which is driven to favour the reduction of the total surface energy of the system. This reduction can be expressed by the following thermodynamic equation [4]:

$$\Delta(\gamma A) = A\Delta\gamma + \gamma\Delta A \tag{1.4}$$

Where γ refers to the specific surface energy at the particles interface and A to the total surface area of the solid particles. The change in specific surface energy $\Delta\gamma$ is due to densification, which in solid-state sintering relates to the evolution of solid/vapour interfaces in favour of solid/solid interfaces. The reduction in the surface area component ΔA is produced by aggregation of particles resulting in grain coarsening (Figure 1.4). After most pores have been removed during the final sintering stage, grain coarsening is also activated from a similar principle of interfacial area reduction, decreasing the system's overall energy. At this stage, grain coarsening and final densification are competing processes. Optimising the sintering parameters (most notably, time and temperature) is required to limit excessive grain growth, generally detrimental to the material's mechanical strength and performance.

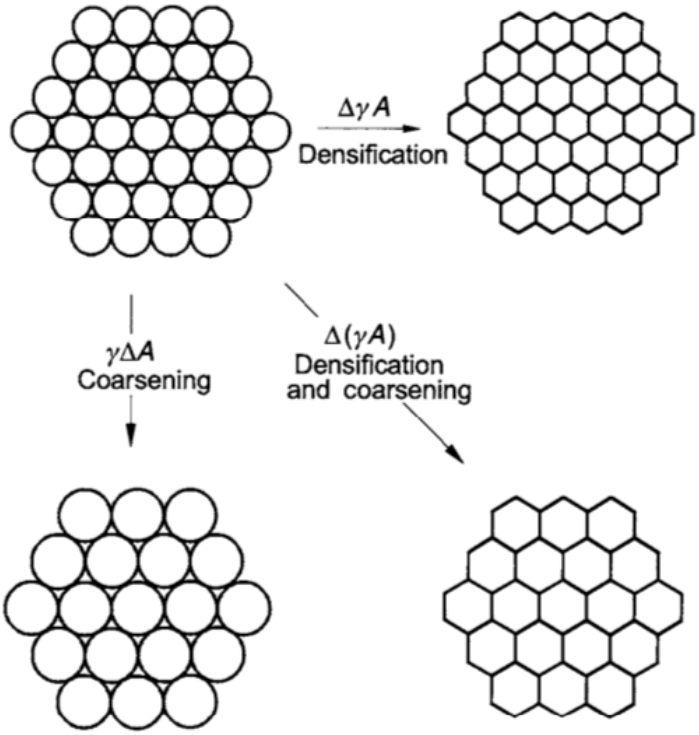

Figure 1.4: *Densification and grain coarsening processes competing during sintering. From Kang (2005) [4].*

The degree of densification obtained during sintering is generally enhanced by applying pressure (either unidirectionally or isostatically), limiting grain growth and modifying the obtained texturing. Novel sintering techniques developed during the 20th century also integrated the application of an electric field to enhance the consolidation process. The most common sintering techniques typically used for advanced ceramics consolidation can be divided into the following:

- **Pressureless sintering**: Most conventional sintering procedure where densification is only achieved through heating without any pressuring involved [48].
- **Hot Pressing**: Enhanced sintering achieved by the combination of temperature and unidirectional pressing, with generally low heating rates (below 100 °C min^{-1}).
- **Hot Isostatic Pressing (HIP)**: Upgrade from standard hot pressing in which the pressure is applied evenly from every direction using a controlled gas atmosphere obtaining higher shape control.
- **Microwave sintering**: Non-conventional technique in which the temperature increase is achieved by transforming microwave electromagnetic fields into thermal energy [49].

- **Spark Plasma Sintering (SPS)**: Non-conventional sintering technique that combines the application of direct electrical current and uniaxial pressure to enhance the sintering process. It is also referred to as Pulsed Electric Current Sintering (PECS) or Field Assisted Sintering Technology (FAST) in the literature [6].
- **Flash sintering**: Field-assisted non-conventional technique developed in recent years allowing very rapid densification with heating rates approaching thousands °C min^{-1}. Sintering is driven by a power surge (referred to as the 'flash event') occurring after a sudden drop of the electrical resistivity in the sample [5, 50].

Although both SPS and Flash sintering are similar current-assisted techniques, some notable differences exist among them. While in SPS, an electrically conductive graphite mould carries most of the current applied, that mould is absent in Flash sintering with the current forced to flow through the ceramic powders. The latter's 'flash event' also results in a substantial drop of around 1000 °C in the required sintering temperature. It is characterised by bright light emission absent in the SPS process (Figure 1.5).

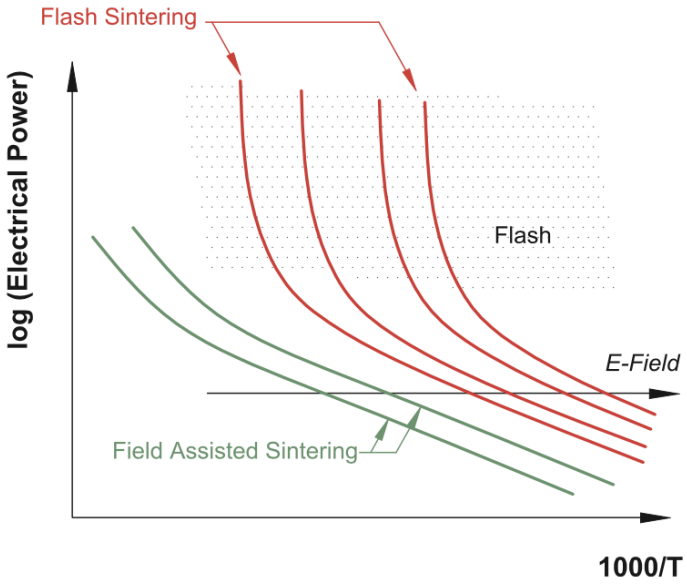

Figure 1.5: *'Flash event' characteristic of Flash sintering accompanying a sudden increase in electrical power. From Biesuz et al. (2019) [5].*

Among these techniques, SPS has rapidly advanced as a standard for sintering high-performing ceramic materials, producing both electrically conductive and non-conductive elements on-demand. Its ease of operation, high reliability and reduced sintering time (below 30 minutes) permit achieving fully dense materials while limiting undesired changes to their microstructure [6, 51]. The technology behind the technique was first conceptualised in the 1960s [52]. However, it gained traction from the start of the 21st century because of its significant advantages compared to

traditional sintering processes in the industry such as hot pressing or HIP (Figure 1.6).

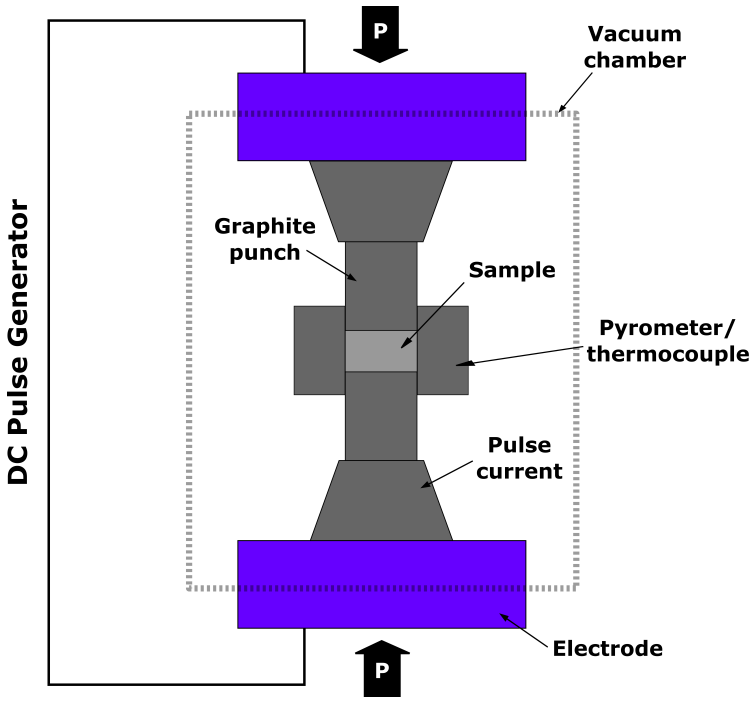

Figure 1.6: *Schematic of an SPS equipment. Adapted from Guillon et al. (2014) [6].*

The direct current applied by SPS flows through the conductive graphitic dies and conductive samples in the chamber, generating heat by the Joule effect (i.e. the transformation of electric energy into heat upon flowing through a resistor) [51] according to the formula:

$$Q = I^2Rt \tag{1.5}$$

Where Q is the heat produced, I is the intensity of the applied electric current, R is the resistance value, and t is the time.

Solid particles then experience a massive local rise in temperatures at contact points with other neighbouring particles, leading to fast necking and diffusion that reduces intergranular gaps while limiting grain growth [53]. This permits the application of ultrahigh heating rates (up to 600 °C min^{-1}) and reduces sintering temperatures a few hundred degrees compared to conventional processes [38].

Prospects of SPS usage have integrated new concepts of pressure-less sintering for mechanically weak materials [54], near-net-shape components, and massive scale-up industrialisation [53]. As modern materials increase in complexity, Finite Element Method calculations are required to account for actual in-situ behaviour with die/punch geometry modifications that optimise compaction and prevent structural

damage [6, 55]. All these advances reinforce the use of SPS as a promising tool for efficient sintering of ceramic-based materials and pave the way for achieving multi-materials with optimised microstructure and hierarchy.

1.2 Bioinspiration to design structural ceramic composites

The concept of bioinspiration refers to an intersection between biology and engineering, from which structural and functional solutions found in natural materials are taken as inspiration for improving current artificial materials. Biomaterials exhibit intricate and unique features, leading to an outstanding balance of properties, durability, or self-repair compared to their constituents [56]. Understanding the basic principles present in those natural composites can develop innovative concepts exceeding current advanced materials.

It is essential to clarify that these biomaterials would not perform better than artificial alternatives in equally challenging environments, as biomaterials' properties have been far exceeded by current metals, ceramics and composites employed throughout the industry. To avoid confusion, some recent authors distinguish between biomimesis and bioinspiration. While the former would aim to fully replicate materials found in nature through a synthetic approach, the latter only searches to learn the strategies employed by these materials, extrapolating them to novel designs of high-performing artificial materials [57, 58].

Although it is impossible to mimic nature in every aspect, a bioinspired approach can be valuable to provide innovative ideas and develop enhanced systems for synthetic materials and specifications [56]. One notable example is the lotus leaf (Figure 1.7a), which exhibits a signature superhydrophobic (or water-repelling) behaviour that enables a self-cleaning mechanism with the repelled water droplets, removing dirt particles from the leaf surface. This property results from the hierarchical assembly of micro-sized roughness in the leaf combined with nanometric crystalloids [7, 59]. Another remarkable example comprises the highly adhesive properties of gecko feet (Figure 1.7b) due to their toe pad structural features with hundreds of thousands of keratinous hairs or setae. This setae arrangement permits geckos to climb vertically through wet and rough walls, becoming the largest animal able to overcome its body weight by sheer adhesion [60].

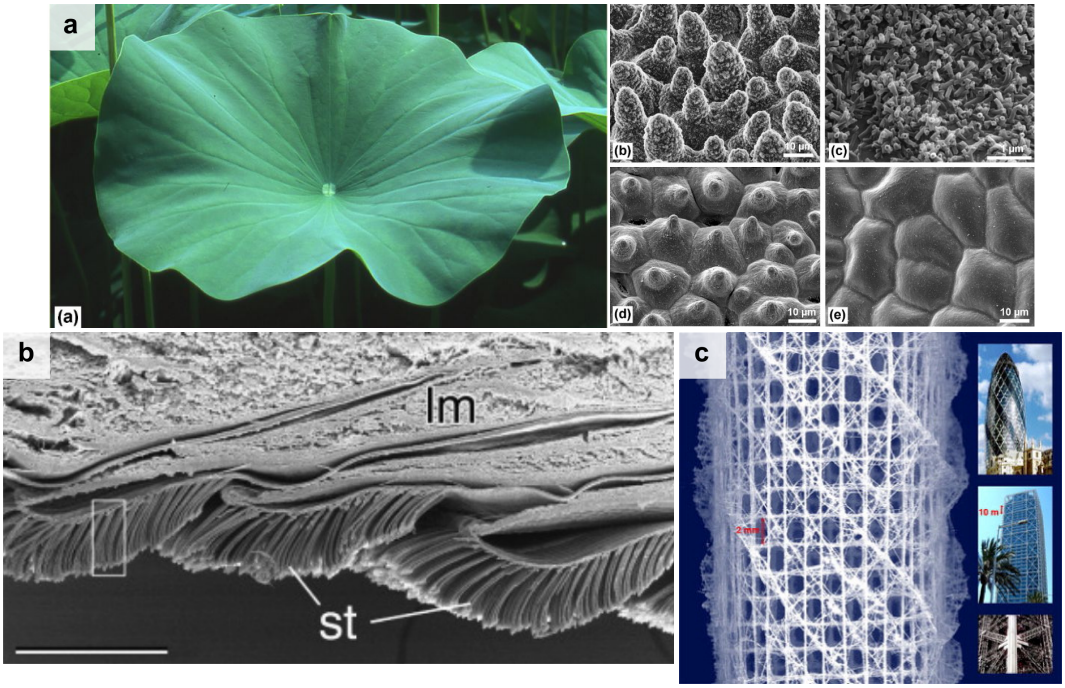

Figure 1.7: *Collection of remarkable biomaterials examples. a) Lotus leaves including SEM images of the upper and lower leaf side, adapted from Ensikat et al. (2011) [7], b) Setae arrangement characteristic of Gecko feet from Meyers et al. (2008), c) Euplectella sponge. Adapted from Aizenberg et al. (2005) [8] and Meyers et al. (2008) [9].*

In terms of mechanical properties, glass sponges like the Euplectella (Figure 1.7c) have been widely referenced as a prime example of nature's ability to improve inherently poor building materials like biosilica [8, 61]. Employing a tailored 7-level hierarchy, Euplectella sponges maintain mechanical stability and flexibility withstanding the bending forces from ocean currents that would otherwise result in fatal failure of its brittle constituents. Achieving flexibility and crack resistance in hard and strong materials is a general challenge to materials science, for the conflicting nature between strength and fracture toughness [62]. Biocomposites approach this challenge by applying complementary toughening mechanisms.

1.2.1 Fracture toughness mechanisms

The property of fracture toughness plays an essential role in the quest to find better-performing materials for cutting-edge engineering applications. Fracture toughness describes the ability of a material to resist fracture, measured in the amount of energy needed to cause total failure in the presence of a crack. Contrary to strength, which is measured in terms of applied stress to the material, fracture toughness can be evaluated through different methods. Typically, the toughness of brittle materials is compared through the K_{IC} parameter, indicating the material's resistance to crack initiation under linear-elastic conditions, simplifying the fracture conditions with independence of the crack extension length [63].

High-strength materials exhibit limited fracture toughness, as these two properties are mutually exclusive in most cases [62], limiting their use in high demand applications. The inhibition of crack growth inside a material depends on applying both intrinsic and extrinsic mechanisms shown in Figure 1.8. While intrinsic mechanisms are related to plasticity and the modification of the material's properties ahead of forming cracks, extrinsic mechanisms act behind the crack tips and only affect the growth of the crack itself, while being generally dependent on its length [10, 15, 62].

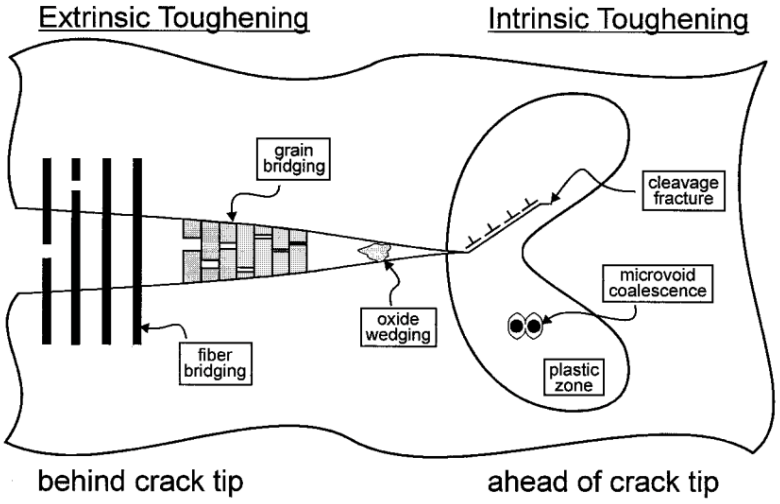

Figure 1.8: *Extrinsic and intrinsic toughening mechanisms acting behind and ahead of the crack tip, respectively. From Ritchie (1999) [10].*

Intrinsic mechanisms are usually found in metals and other ductile materials that can increase their strength by including dislocations or changes in their microstructure, also enabling their mechanical conformation. On the other hand, ceramics (and overall brittle materials) need to take advantage of extrinsic mechanisms to arrest crack growth that can otherwise propagate easily and result in quick fatal failure. Some examples of extrinsic mechanisms are listed as follows [11, 15, 64, 65]:

- **Fibre/grain bridging**: Ligament bridges arising from the structural features in the material that remain unbroken behind the crack tip and inhibit its growth.
- **Crack deflection**: Structural features such as weak interfaces/constituents that deflect and control the established crack path, requiring higher forces to extend the crack.
- **Pull-out**: Tearing of structural bridges (fibre, grain, etc.) from the opposite side of the crack interface, resulting in higher friction and energy required to continue the crack growth.
- **Void growth**: Formation of pores in the material structure that act as local crack arresters and relieve stress before re-opening of the crack tip.

- **Delamination**: Sliding of platelet-like structures that contributes to energy dissipation.

Such mechanisms can help release the accumulated stress around the crack tip, increasing the energy required to extend the crack and raising the overall fracture toughness of the material. Classical measurements like the K_{IC} parameter are not sufficient to evaluate the overall fracture toughness of materials activating extrinsic mechanisms dependent on the crack extension. More advanced non-linear testing methods are required (like the calculation of the J integral) applying a more accurate representation of the material's resistance to fracture that considers the contributions of inelastic deformation to arrest crack propagation [12, 63, 66].

1.2.2 Strength vs toughness in natural composites

Nature's ability to produce materials with highly-ordered structures integrating intrinsic and extrinsic mechanisms appears to overcome the mutually exclusive balance between strength and toughness [64]. By combining these toughening mechanisms, biocomposites experience an increase in the resistance to crack extension by employing a carefully engineered structure that prevents the spread of cracks generated during fracture. It has become one of the most promising pathways towards achieving both stronger and tougher advanced materials that have been conventionally obtained through random mixing approaches or without control of the material's internal structure.

There are numerous examples of biocomposites containing a mixture of soft and brittle constituents with extended hierarchy across many length scales, from the nano- to the macro-level (e.g., sea sponges, mollusc shells, bamboo, human bones, or muscles [8, 9, 11, 62, 67]). Many of the strategies employed by these materials can serve as bioinspiration and be extrapolated to artificial advanced composites sharing similar structural designs [56]:

- Wood and insect cuticles as fibre-reinforced organic matrix composites
- Bone and antler as fibre-reinforced ceramers
- Mollusc shells as lamellar/prismatic ceramic matrix composites

As shown in Figure 1.9a by Wegst (2015), the specific strength of some natural materials compared to their specific stiffness (normalised by density) competes with common engineering materials, even exceeding them at the low stiffness region. By integrating a range of hierarchical levels, the toughness of natural composites like bone and nacre has proven enhanced beyond the combination of their constituents (Figure 1.9b), overcoming the values predicted by the rule of mixtures [11, 68]. In the

case of the alumina/PMMA composite in the example, the application of extrinsic mechanisms permitted increasing the fracture toughness from 5 to 30 MPa $m^{1/2}$.

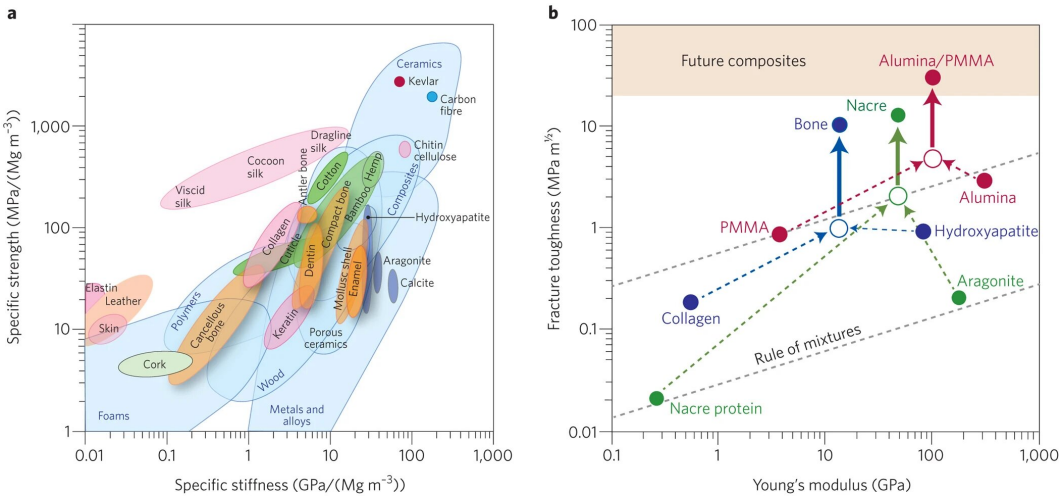

Figure 1.9: *a) Ashby plot of specific strength and stiffness of natural and synthetic materials. b) Exceptional toughness of natural composites (and nacre-inspired alumina/PMMA pairing) applying extensive extrinsic mechanisms. From Wegst (2015) [11].*

One of the most referenced examples for enhanced strength/toughness balances in nature is nacre, also known as mother of pearl. Nacre has become the archetype for hierarchical ceramic-based composites, aiming to replicate the material's brick-and-mortar structure that maximises strength and toughness [69]. This brick-and-mortar structure is composed of 95 vol%. layered aragonite ($CaCO_3$) in the form of 200 – 900 nm nanoplatelets and a 5 vol.% of interlaminar organic material mostly consisting of proteins and polysaccharides [12, 66, 70, 71].

While the hard inorganic aragonite provides the strength of nacre, the organic phase glues the nanoplatelets together, permitting the energy dissipation and the redistribution of stress around strain-concentration sites. The combination of extrinsic mechanisms (such as inelastic shearing bore by nanoasperities at the aragonite/organic interface or the breaking of aragonite micro-bridges) leads to fracture toughness in nacre about one order of magnitude higher than what was expected from its constituents (Figure 1.10) [12, 72].

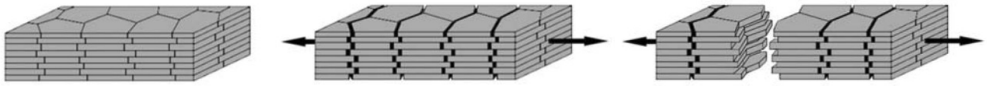

Figure 1.10: *Nacre failure mechanisms. Adapted from Barthelat (2007) [12].*

The measured fracture toughness (either by the traditional K_{IC} value or through the calculation of the J integral) can be presented as a function of the crack extension Δa. Larger cracks can increase the perceived value of toughness due to the extrinsic mechanisms activating behind the crack tip (crack deflection, pull-out, etc.). This

results in a signature rising curve known as an R-curve, verified for nacre and similar biomaterials (Figure 1.11), highlighting the potential benefits of integrating extrinsic toughening mechanisms in synthetic materials [63, 66].

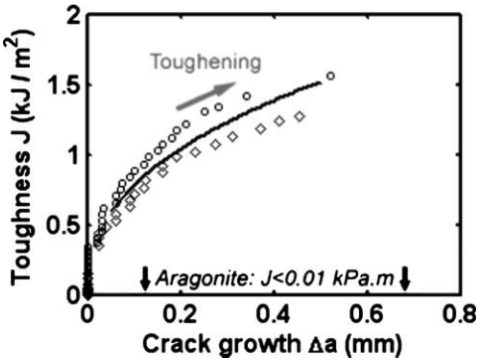

Figure 1.11: *Example of J-R-curve in nacre. From Barthelat (2007) [12].*

1.3 Novel approaches for bioinspired advanced ceramics

Innovative processing methods have been explored to translate bioinspired structures (such as nacre's) into the advanced ceramics field and overcome the main challenge of intensive self-assembly needed to build complex hierarchies. Several examples take advantage of wet chemistry processing and non-conventional sintering techniques [73], mimicking nacre's intricate structure with one soft, binding phase and a second more brittle material that provides the strength [15].

1.3.1 Hierarchical processing via freeze-casting

Freeze-casting (also known as ice-templating) is a versatile and straightforward technique to produce oriented, highly-porous materials by applying a controlled unidirectional solidification front [13, 74]. This processing method has its origins in the late 20th century as a near-net-shape forming technique for producing components with the dimensions of casting moulds of higher complexity [75, 76], later finding an additional market in the food-processing industry. Freeze-casting has resurfaced in the early 21st century [77–81] due to its potential in advanced materials processing for novel applications (e.g., bone substitutes, drug delivery, acoustic insulations, or piezoelectric materials [82]) applying extended particle assembly with long-range structural ordering.

In a standard freeze-casting process, a suspension containing solid particles of a target material is cast on a mould and frozen along one direction by controlling the temperature gradient. As the solvent starts solidifying, solid particles in the suspension get trapped in the gaps between the forming crystals. This freezing front progresses through the suspension until the whole sample is solidified, creating

an interconnected network of solid material embedded in the frozen solvent. After freezing is complete, the solvent is sublimated by a combination of low pressure and temperature without compromising the formed structure [13, 14, 74, 77, 83, 84].

After removal of the solvent, a final consolidation stage of the material green body is generally required to provide the aerogel with mechanical stability, which can be accomplished via infiltration with a second phase or by thermal annealing (sintering in the case of ceramics or carbonisation in the case of carbon-based structures). A schematic of the complete process, including this final post-treatment, is depicted in Figure 1.12:

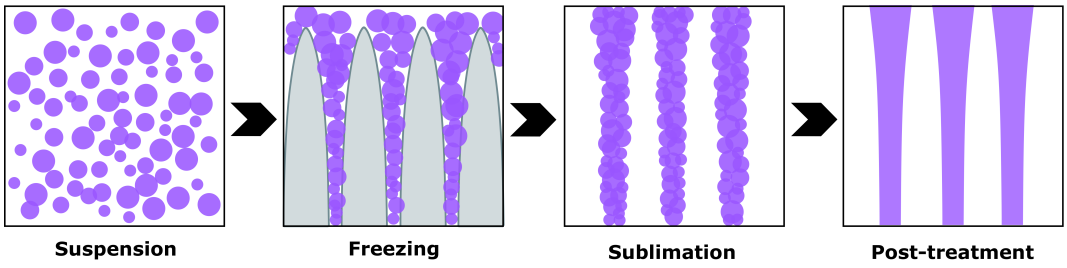

Figure 1.12: *Diagram of freeze-casting stages. Adapted from Deville (2013) and Shao et al. (2020) [13, 14].*

Some benefits of freeze-casting reside in its great versatility and simplicity, ease of implementation and compatibility with organic solutions [85]. Although the scalability of the technique can be compromised (as bigger structures may collapse upon sublimation of the solvent [68, 82]), freeze-casting is highly compatible with different materials and solvents, being water and camphene the most common selections [85, 86]. Water is a desirable solvent based on its low cost, great availability and environmentally friendly characteristics [1, 87]. Tuning the process parameters such as the solid volume content, freezing rates and the additives in suspension can significantly impact the structuring of the cast material [88]. The morphology of the solid particles and their size distribution can affect the homogeneity and surface smoothness of the produced structure [89].

An excessively fast freezing rate may impede the diffusion of particles out of the growing solvent crystals and lead to their entrapment. In contrast, slow cooling leads to broader lamellar structures with higher spacing [83]. Suspended particles in the solvent are subjected to opposite repulsive (F_r) and attractive (F_a) forces upon the solidification front, because of the balance between inter-particle van der Waals interaction and the viscous drag from the solvent. Many factors such as the solids particle size, solvent thickness layer at the solid/liquid interface, or the dynamic viscosity of the liquid can affect the balance of repulsive and attractive forces during casting. From this balance, a critical freezing front velocity is defined (v_{cr}), above which the solid particles would not be allocated by the solidification front, getting trapped within the growing crystals of the solvent instead (Figure 1.13) [14, 84, 86].

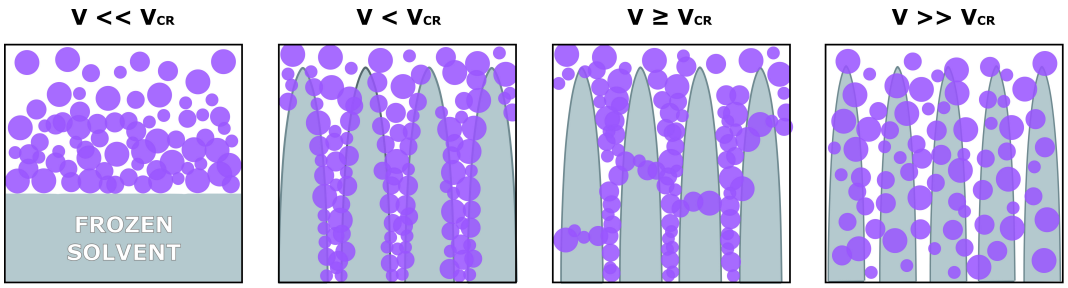

Figure 1.13: *Different examples of freezing front progression compared to the critical velocity v_{cr}. Adapted from Shao et al. (2020) [14].*

Including certain additives such as NaCl, sucrose or glycerol in the suspension formulation can result in extended hierarchy levels in the freeze-cast structure. These additives in suspension can increase the surface roughness of the formed crystals [83] or work as freezing inhibitors, affecting growth kinetics and the mesostructure of the rising ice [90]. Additionally, long-range ordering can be obtained by patterning the surface of the cold metal fingers providing the freezing front, which can help improve the material's mechanical properties [74, 90].

Alumina has been a reference material in the freeze-casting of advanced ceramic aerogels, with extensive works exploring the influence of solid loadings in suspension from (20 – 60 vol.%), various solvents and particle sizes [77, 83, 88, 90–94]. Recent notable examples in the advanced ceramics field also include the works from Zeng et al. (2015) [95], creating a boron nitride scaffold via freeze-casting with anisotropic superelasticity, Knoller et al. (2017) [96] validating the conformation of vanadium oxide structures by assembling as-synthesised nanofibers in water, and Si et al. (2018) [97], consolidating super-elastic lamellar structures made of SiO_2 nanofibers. Many materials have been readily verified as compatible with freeze-casting processing, with most works in the previous two decades already collected in many reviews, especially Scotti et al. (2018) [87] and its associated open data repository *FreezeCasting.net*. For such reason, this review will not extend on this topic.

The possibilities of freeze-casting can also be expanded to the field of ceramic-based composites. Interconnected lamellar structures produced by freeze-casting of advanced ceramics can act as the hard phase, infiltrated with a polymeric second phase to accommodate the loading stress, analogous to the respective aragonite and organic phases in the brick-and-mortar structure of nacre [14, 66, 71, 98, 99]. This processing route can be expanded beyond the integration with polymers (by direct analogy with nacre), integrating the ceramic aerogels with metals [100] or even other ceramics [15, 86] while maintaining the same processing approach.

Innovative changes to the standard freeze-casting procedure have been implemented during the last decade, aiming to expand the possibilities of the technique and increase the ordering range of produced materials. Two independent cold sources can be applied to reduce external temperature fluctuations and provide tempera-

ture gradients of higher accuracy [92, 101]. The introduction of external electric or magnetic fields can also increase the ordering levels obtained in the structure [102]. Electrostatic fields (10 kV m^{-1}) perpendicular to the freezing direction [103] have been applied to control the direction and consistency of aligned ceramics, obtaining lamellar structures with a tunable degree of inclination. Additionally, external magnetic fields can align magnetic-responsive nanoparticles (e.g. Fe_3O_4) in the solvent, creating multiple directions of long-range ordering by combining the directional ice-growing preference with the magnetic field orientation [104, 105]. Concentric rotation of the magnets controlling the secondary alignment level can modify the magnetic flux direction and tailor the microstructure of the cast material beyond the physical restrictions of the mould wall barriers.

1.3.2 Extended hierarchy through nanoparticle deposition

Recent works have integrated ceramic nanoparticle (NP) decoration of the composite building blocks, aiming to increase the internal hierarchical levels of structural ceramic-based materials. This approach can be combined with other processing routes, like freeze-casting, producing structures with complementary ordering ranges (micro- vs nano-level) similar to nacre and other structural biomaterials previously presented.

As concrete examples, Bouville et al. (2014) [15] produced a nacre-inspired material by selecting a multi-phase ceramic precursor (alumina platelets 7 μm diameter, alumina nanoparticles of 100 nm and a silica-calcia liquid phase of 20 nm) under the application of gradient-controlled freeze-casting (Figure 1.14). Upon consolidating the ceramic, integrating these hierarchy levels in the composite led to a remarkable combination of toughness (17.3 MPa $m^{1/2}$) and strength (470 MPa), overcoming previous limits of 10 MPa $m^{1/2}$ for alumina-based materials after exceeding 400 MPa strengths. The optimisation of the ceramic building blocks integrating the alumina nanoparticles helped form nano-asperities and inorganic bridges reminiscent of biomaterials, which could hinder crack growth and redistribute the load, otherwise resulting in fatal failure [15].

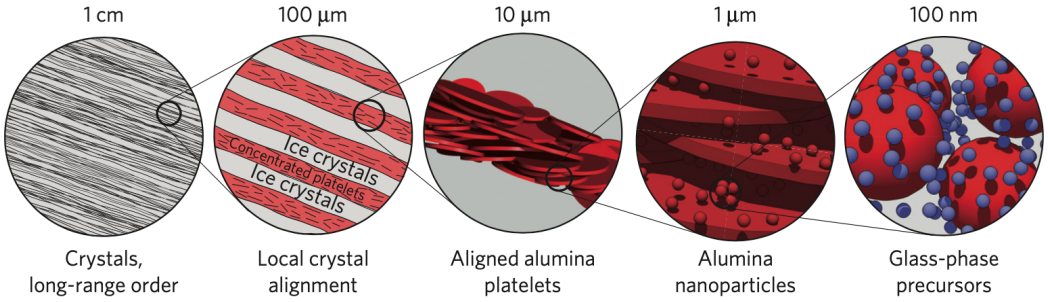

Figure 1.14: *Hierarchical levels in the nacre-inspired material processed by Bouville et al. (2014) [15].*

Pelissari et al. (2018) [106] prepared hierarchical ceramic refractories by similarly integrating magnetically-responsive alumina platelets with finer alumina nanoparticles, consolidated by hot press sintering. In this work, the micro-structuring of the material was achieved via Magnetically Assisted Slip-Casting after functionalisation of the platelets with Fe_3O_4 nanoparticles instead of through freeze-casting. This procedure produced analogous nacre-inspired structures, reaching a combination of strength and toughness at room temperature (nearly 700 MPa and 11 MPa $m^{1/2}$, respectively) superior to previous alternatives without structural optimisation.

The conformation of nano-asperities in the microstructure can be achieved by the inclusion of pre-made nanoparticles in the formulation of the composite and by the synthesis in-situ of ceramic nanoparticles from a chemical precursor added to the starting materials through thermal treatment. Henry et al. (2021) [107] recently expanded the work from Bouville et al. (2014) [15], producing similar nacre-inspired ceramic composites, enhancing the hierarchy of alumina platelets by integration with Al_2O_3 and ZrO_2 nanoparticles. The zirconia nanoparticles were obtained from an alkoxide solution precursor followed by ageing and thermal treatment at 850 °C.

As another example, Wang et al. (2016) [108] applied an NP-decoration approach to the production of graphene/TiC composites, based on the sol-gel synthesis of TiO_2 and TiC nanoparticles from a titanium isopropoxide precursor deposited on a graphene-based structure. The gel was treated at 550 °C first to produce a mesoporous Ti-O-C intermediate material, further reduced at 1450 °C to render TiC particles around 100 nm, allowing to tune the C/Ti ratio in the final composite by the application of successive NP deposition runs.

This last work can serve as an introduction to the role of graphene as an additive in ceramic-based materials, also highlighting its potential in the field of bioinspired composites for producing interconnected networks providing structural support and additional functionalities [39].

1.4 Graphene for developing graphene/ceramic composites

1.4.1 Graphene structure and prospects

Graphene consists of one single layer of carbon atoms arranged in a hexagonal lattice and constitutes the base for graphite and other carbon derivatives in the sp^2 hybridisation such as nanotubes or fullerenes (Figure 1.15) [16, 109, 110]. Since its theoretical prediction 75 years ago [111] and its experimental verification through a simple scotch tape method [109], it has gained attention from the media and become one of the most extensively researched topics in materials science during the 2010s. Graphene has also paved the way for the exploration of other $2D$ materials, such as metal-organic frameworks (MOFs), silicene or phosphorene whose third dimension is reduced to their theoretical minimum of one atomic layer [112, 113].

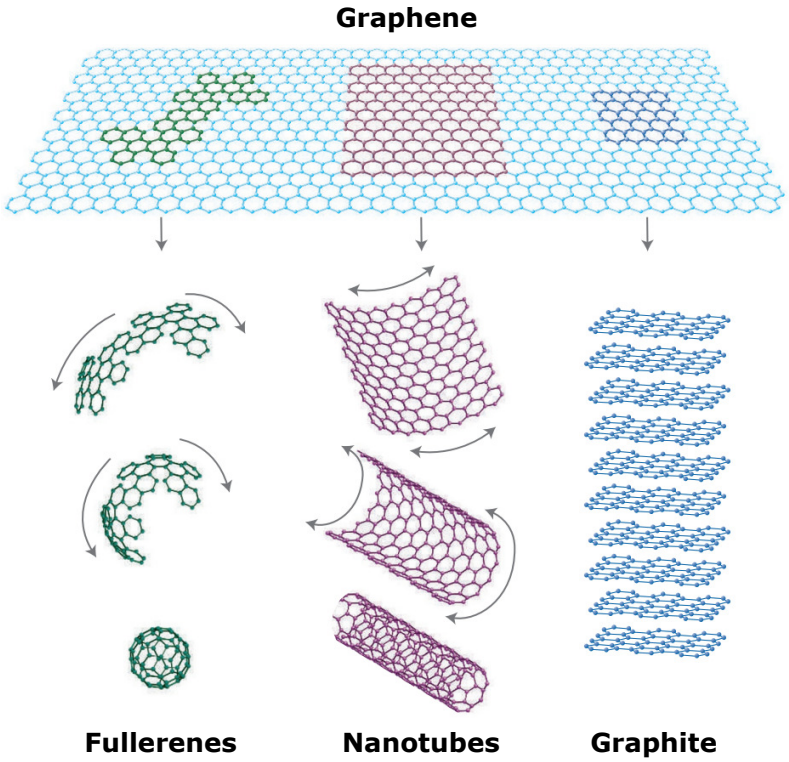

Figure 1.15: *Graphene as the building block for fullerenes, carbon nanotubes (CNTs) and bulk graphite. Adapted from Geim et al. (2007)[16].*

From this burst in popularity, one may ask what is unique about graphene compared to an already existing nanometric alternative such as single-walled carbon nanotubes (SWCNTs), visualised as single graphene sheets rolled into a hollow cylinder as in Figure 1.15 [114]. Graphene's unique structure provides the material with an outstanding combination of properties: Young's modulus of 1,100 GPa, fracture strengths of 125 GPa, thermal conductivity of 5,000 W $m^{-1}K^{-1}$, and charge carrier mobility of 200,000 cm^2 $V^{-1}s^{-1}$ in the case of single-layer graphene [115–118]. How-

ever, these numbers are highly dependent on the presence of structural defects [119]. Graphene's high specific surface area of 2630 m^2 g^{-1} [120] additionally sets it apart from other carbon counterparts. Instead of the point/linear linking occurring in the case of $1D$ CNTs stacking, the superposition of $2D$ graphene sheets manifests in an area-to-area fashion, which successfully exploits its surface area advantage [23, 110], leading to enhanced electrical conductivity.

The most significant prospects of graphene rely on its unconventional electronic properties that led to the Nobel Prize in Physics awarded to Andrew Geim and Konstantin Novoselov in 2007, worth mentioning in this review despite not being its primary focus. The remarkably high charge carrier mobility shown by pristine graphene relates to electrons behaving like relativistic particles governed by Dirac's equation (applied where the mass of the particle is deemed negligible) instead of the quadratic Schroedinger equation generally used in condensed-matter physics [16, 121, 122]. This seemingly ballistic transport below the micrometre scale occurs at the Dirac points, regions where the conduction band transitions to the valence band arising from graphene's honeycomb lattice structure and its associated Brillouin zones (Figure 1.16). Owing to this behaviour, graphene's carriers are also referred to as massless Dirac fermions in the literature.

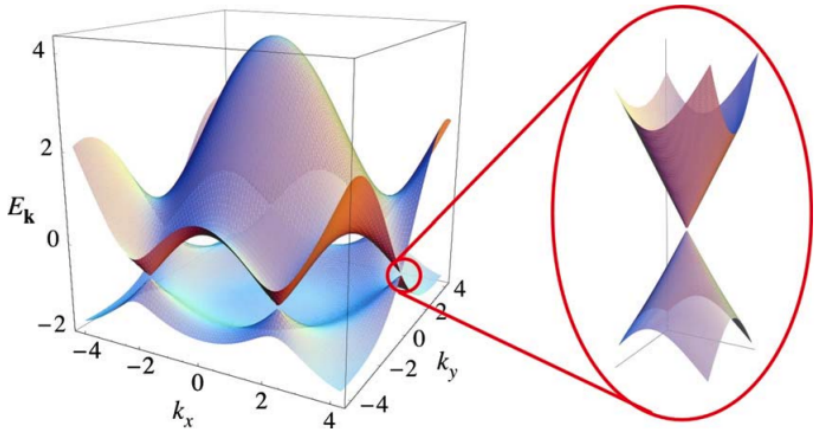

Figure 1.16: *Band structure of single-layer graphene showing the linear dispersion at the Dirac point. From Hill et al. (2011) [17].*

Other graphene's attributes such as its flexibility, extremely low weight and transparency have opened possibilities for innovative applications such as electric batteries, ultracapacitors, filtration devices, drug carriers or flexible and wearable electronics [123]. The combination of graphene's $2D$ structure and its susceptibility to change its electronic properties under doping can be exploited as electrochemical sensors [17].

In the structural engineering field, immediate graphene prospects comprise its use as reinforcement for composites, providing higher mechanical and electrical per-

formance in already existing materials envisioned for aerospace applications, medical prostheses, or advanced sports equipment, to highlight a few. Despite its great potential, the translation of graphene's quasi-theoretical properties from a $2D$ isolated monolayer to a more useful $3D$ environment is still not resolved. Several challenges prevent the full expansion of graphene in the industry, such as the impracticality of producing large quantities of defect-less material and its current costly production.

Alternatives to pristine graphene have been explored, aiming to balance its quality grade and the properties obtained in the final material while maintaining a cost-effective approach. A few examples of these include few-layer graphene (FLG) with 2 to 10 layers of graphene sheets stacked together and graphene nano-platelets (GNP), of further aggregation up to 100 nm [18]. This range of quasi-graphene materials have been widely approached through the last decade and are related to the different mechanical and chemical methods for obtaining graphene addressed in the next section.

1.4.2 Graphene precursors

Various synthesis routes have been developed to produce graphene using both bottom-up and top-down approaches [124]. A bottom-up perspective involves obtaining the material from the assembly of smaller building blocks, in this case, by arranging graphene's carbon atoms in self-sustained sp^2 layers. In contrast, a top-down approach requires scaling down any macroscopic material, such as the exfoliation of graphite sources into separate nanometric layers of graphene (Figure 1.17).

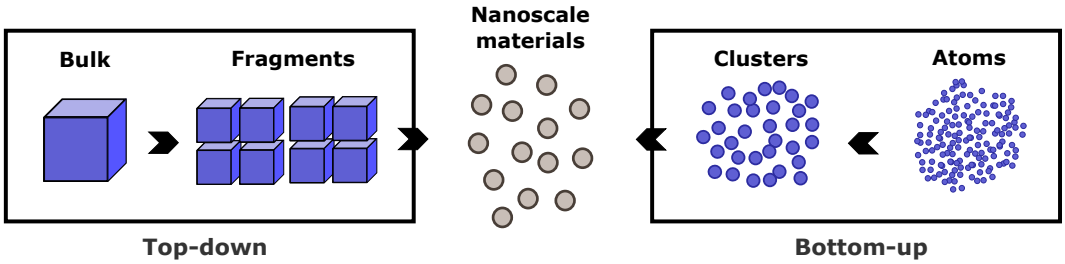

Figure 1.17: *Bottom-up vs top-down processing strategies.*

While bottom-up approaches generally lead to purer graphene because of the defect-less structural formation, the higher purity comes at the expense of higher production costs. The scalability of the material is also compromised due to the greater difficulty in obtaining large areas of pristine material. In contrast, top-down approaches starting from bulk graphite are more cost-effective but lead to aggregated or disrupted graphene of lesser quality that cannot meet the high-purity requirements needed for most optical and electronic applications.

According to the review from Miranzo et al. (2017) [18], the standard methods for producing graphene could be classified into six main groups listed below, including

some examples from the literature. Some of these approaches yield graphene-like materials of less purity than pristine graphene (e.g. few-layer graphene (FLG), graphene nano-platelets (GNP) or graphene oxide (GO)), aiming to achieve a compromise of properties and scale-up the graphene production.

- **Chemical Vapour Deposition (CVD)**: Bottom-up approach in which carbon atoms are deposited through CVD on a metal substrate, producing single and few-layer graphene domains later transferred to a secondary non-conductive substrate. In a typical example based on transition metals substrates such as Ni or Cu, a carbon feedstock (CH_4 or C_2H_2) is supplied at atmospheric pressure under temperatures of 900 – 1000 °C to trigger the formation of continuous 1 – 12 stacked graphene layers [125]. Although this process is not suitable for producing larger extensions of material (above 400 cm^2), the deposited graphene sheets retain high purity suitable for electronic applications.

- **Epitaxial growth on SiC**: Bottom-up approach focused on the growth of graphene seeds formed on SiC crystals at high vacuum and high temperature [126]. Under these conditions, the silicon atoms are desorbed, leaving behind the carbon atoms that self-arrange in a sp^2 structure forming the graphene layers.

- **Chemical route**: Top-down approach that uses potent oxidant agents to disrupt the stacked structure of graphite, applying extended functionalisation to the graphene sheets. Although this method yields a heavily oxidised material known as graphene oxide (GO), partial restoration of the properties from former graphene sheets can be achieved through thermal or chemical reduction methods to obtain what is known as rGO [127].

- **Suspension methods**: Top-down approach to exfoliate graphite into graphene sheets by using organic solvents in conjunction with physical separation methods such as filtration or gravity-sedimentation [128] and forces capable of inducing exfoliation (e.g. ultrasonication or shear forces in liquid medium).

- **Mechanical exfoliation**: Top-down approach in which several milling methods are applied to a graphite supply, producing single and multilayer graphene by sheer mechanical force. This method also includes the famous sticky tape technique (also known as micromechanical exfoliation) that first validated the experimental production of graphene [16, 109].

- **Unzipping of CNTs**: A scarcely explored method leaning on the longitudinal opening of multi-wall CNTs, exploiting their nature as wrapped graphene sheets. The work from Kosynkin et al. (2009) [129] mainly represents this technique, in which the CNT unzipping was performed through a solution-based oxidative process.

CVD and epitaxial growth on SiC are the most established bottom-up approaches for rendering pristine graphene films with minimal defect quantity and layer aggregation, mainly envisaged for electronic applications. However, graphene produced through these techniques remains expensive and harder to escalate from a technical standpoint [18]. For integration with other materials in composite form or applications requiring large quantities of graphene, top-down methods appear the most promising ones (Figure 1.18).

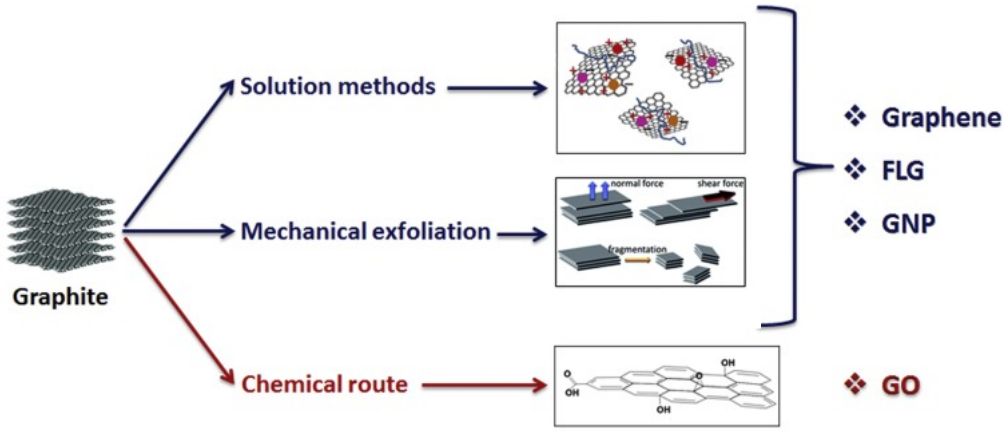

Figure 1.18: *Graphene processing methods most suitable for composite integration. From Miranzo et al. (2007) adapted from Yi and Shen (2015) [18, 19].*

Due to its hydrophobic behaviour shared by bulk graphite, graphene cannot be homogeneously suspended in water, limiting the application of wet chemistry processes. The chemical modification of graphite into graphene oxide (GO) has appeared as a promising alternative to produce higher amounts of graphene-like sheets compatible with wet-chemistry processing methods and integrated with other materials. However, the dispersibility of graphene (and its derivatives) is nearly inversely proportional to their obtained physical properties because of the increased defective regions in the material [130], for which the selection of an adequate precursor should be subjected to the envisioned applications.

1.4.2.1 Graphene oxide

Graphite oxide has been known and prepared for decades since its first synthesis route proposed by Brodie in 1859 [131], which requires the heavy oxidation of a graphite source. Graphite oxide can be readily exfoliated in water to graphene oxide (GO), a few-layer graphene sheet decorated with multiple functional groups comprising a top-down chemical approach. Despite its considerable reduction in mechanical properties compared to graphene (From Young's modulus of 1 TPa to roughly 200-250 GPa [132, 133]), GO has become a promising precursor for graphene, owing to its dispersibility in water and its ability to partially recover graphene properties upon reduction. It maintains a very high aspect ratio and surface area, consisting of a primarily

hydrophobic basal plane with hydrophilic edges (hence its amphiphilic label) with high potential for integration with other materials in the form of graphene-based composites.

A colloidal solution of GO can be prepared on organic (ethylene glycol, dimethylformamide, N-methylpyrrolidone) and aqueous media, enabling wet processing techniques [21, 134, 135]. Another attractive feature of using GO as a graphene precursor lies in its reported self-assembly behaviour with the formation of spontaneous liquid crystal (LC) phases [136]. The formation and stability of these phases arise from the high anisotropy of the planar GO sheets, being highly dependent on the properties of the suspension such as GO concentration and lateral flake size, pH and surface functionality that control the displayed LC morphology (isotropic, biphasic or nematic) [136, 137].

GO's functionalised sheets enable breaking the $\pi - \pi$ configuration of the original carbon network, creating an insulating but hydrophilic material instead of the original hydrophobic graphene sheets [138, 139]. The heavy oxidation also results in a significant transformation of carbon to the sp^3 hybridisation ($C - C$), contrasting with the predominant sp^2 hybridisation ($C = C$) characteristic of graphitic systems like pure graphene. GO's functionalisation is still discussed by different authors, owing to the competing processes occurring during its synthesis. It is established that hydroxyl ($C - OH$), epoxide ($C - O$), carbonyl ($C = O$) and carboxyl ($O = C - O$) groups are the most predominant species in the defective graphene structure after oxidation (Figure 1.19) [20, 140, 141], with epoxide and hydroxyl groups generally represented on the basal plane with carbonyl and carboxyl groups located at the sheet edges. The presence of these functional groups reduces the interplanar bonding of GO sheets in suspension, with layers easily exfoliated in contrast to non-functionalised graphene [142].

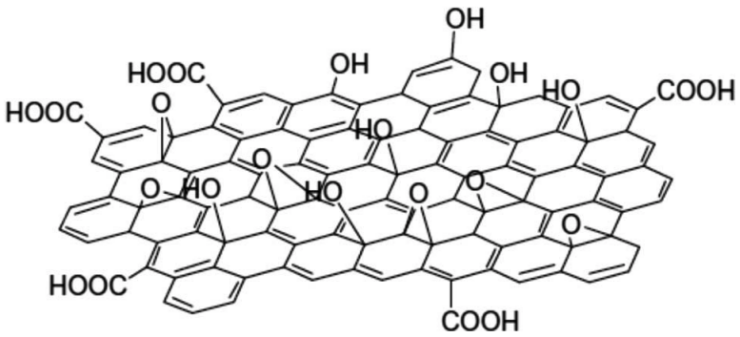

Figure 1.19: *Recreation of functional groups present in GO sheets. From Nasrollahzadeh et al. (2015) [20]*

Most of GO's potential as a graphene precursor relies on its easy processing and possibility of scaled-up production [116]. Larger quantities of suspended GO with tunable concentration can be synthesised at a reduced cost, envisioned for applications where the electrical properties are not essential. GO synthesis routes

are based on well-established oxidation procedures followed for graphite oxide, in which strong acids are applied to a graphite source while including additional steps of exfoliation and centrifugation. Graphite oxide has been typically obtained through three main procedures [116, 143, 144]:

- **Brodie route**: Oldest preparation method dating from 1859 using $KClO_3$ and fuming HNO_3 as oxidising agents. This process lasts for four days and encompasses a high explosion risk [131].
- **Staudenmaier route**: Improvement on Brodie's method in which the HNO_3 acid is replaced by a mixture of HNO_3 and H_2SO_4 at higher temperatures (first described in the original publication in German [145]).
- **Hummers route**: Higher yield method replaces previous oxidising agents with a mixture of concentrated H_2SO_4, $NaNO_3$ and $KMnO_4$, reducing the total synthesis time to a couple of hours [143].

According to today's standards, the Hummers method is arguably the most reported graphite oxide synthesis route based on its high efficiency and relative safety [146], easily expanded to GO production. In a standard Hummers procedure, bulk powdered graphite is put in contact with $NaNO_3$ and H_2SO_4 and cooled down to 0 °C in an ice bath. The mixture is stirred vigorously while $KMnO_4$ is added, which leads to the formation of Mn_2O_7 that heavily attacks the graphite layers. Enough water is supplied after returning to room temperature, causing an exothermic reaction that reaches 98 °C. The mixture is further diluted with extra water and H_2O_2 to reduce the residual $KMnO_4$ and MnO_2 to soluble $MnSO_4$ [143]. Extended cycles of exfoliation and centrifugation/washing can delaminate the oxidised graphite layers, obtaining single to few-layer GO in suspension.

Variations of the traditional Hummers method have been applied to increase the GO yield and limit the toxicity of the process. A typical modified Hummers method was first introduced by Hirata et al. (2004) [147], similarly oxidising the graphite layers with $NaNO_3$, H_2SO_4 and $KMnO_4$ but applying increased oxidation times and a purification process of higher purity.

Another remarkable modification of the Hummers method was presented by Marcano et al. (2010) [148] to limit the production of toxic gases during synthesis and achieve better temperature control. This route excluded $NaNO_3$ from the mixture, increasing the content of $KMnO_4$ and substituting the H_2SO_4 from the traditional method with a 9:1 concentrated mixture of H_2SO_4/H_3PO_4. The addition of phosphoric acid in the formulation increased the procedure's safety. It also resulted in higher yield retaining more significant intact portions of graphitic basal planes, for which it has been preferred in recent years over the traditional Hummers route [134].

Chen et al. (2013) [146] proposed another modification removing the use of

$NaNO_3$ to reduce the environmental cost of GO production, limiting the toxic gases generated and simplifying the water purification process. The reaction yield was not negatively affected through this improvement, and the as-produced GO maintained dispersibility with comparable lateral flake sizes to those from analogous synthesis routes.

1.4.2.2 Reduced graphene oxide

The highly oxidised carbon regions of GO can be partially restored to former graphene's hexagonal sp^2-bonded configuration through a reduction step, with the complete bulk graphite to rGO processing route represented in Figure 1.20.

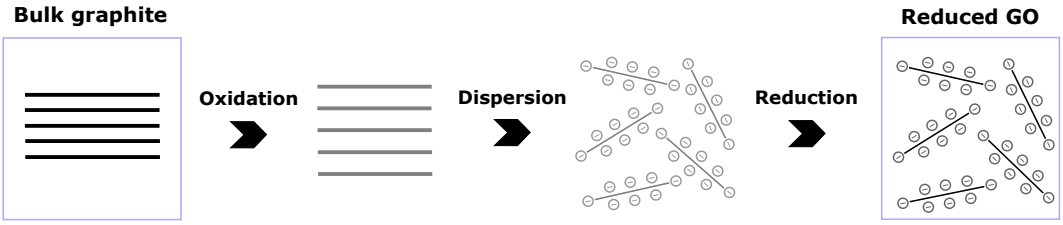

Figure 1.20: *Processing route for obtaining rGO from exfoliated graphite. Adapted from Li et al. (2008) [21].*

The reduction has been traditionally induced via chemical attack of hydrazine-based compounds such as hydrazine hydrate [120, 127, 149], dimethylhydrazine [110] and straight hydrazine vapour [150] Alternatively, lesser common agents like hydroquinone [151] have also been employed. In the most common chemical reduction procedure using hydrazine (N_2H_4), the proposed reduction mechanism consists of the ring-opening of the epoxide groups, producing alcohol and amino groups that are later dehydrated. The resulting diimide is removed at the working temperatures (moderate heating of 100 °C), favouring carbon double bonding and re-establishing the former graphitic ring domains [127]. Although the use of hydrazine can induce the reduction of GO at lower temperatures, the use of this material should be preferably limited based on its toxicity [21].

An alternative reduction route can be achieved through thermal annealing under an inert atmosphere [140, 152, 153]. The energy provided by the applied temperature can similarly eliminate the humidity molecules and the oxidised groups attached to the graphene sheet surface, favouring the restoration of graphitic domains (Figure 1.21). The reduction temperature directly affects the oxygen elimination, from a minimum of 500 °C to ensure the removal of functionalities to temperatures above 1000 °C, yielding C/O ratios above 40. Although this reduction method can lead to higher reduction efficiency compared to chemically-driven methods, it is essential to limit the heating rates to prevent the exploding of the structure as in the process of GO exfoliation [140].

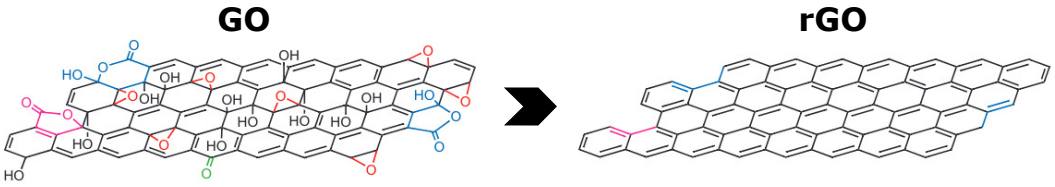

Figure 1.21: *Representation of the removal of functional groups in the GO sheet after reduction. Adapted from Gao et al. (2009) [22].*

Even after reduction, the material's highly defective structure carries a substantial decrease in performance compared to that of pristine graphene, retaining a non-negligible amount of oxygen and defects in the material. While the mechanical properties can be nearly restored, with Young's modulus of rGO resembling pure graphene (around 1 TPa), the electrical conductivity does not commonly exceed 200 S m^{-1} even after reduction at temperatures above 1500 °C. Reduced GO sheets undergo the restoration of former graphitic domains in the structure, which grants a blackened colour reminiscent of pure graphite [127, 153, 154] and display higher roughness when compared to mechanically exfoliated graphene. Localised regions in rGO sheets also show singular heptagon-pentagon pairs and defect clusters disturbing graphene's original six-membered ring structure [155].

For these reasons above, reduced GO is given a different name in the literature other than graphene, such as chemically modified graphene (CMG) or reduced graphene oxide (rGO) [140], the latter used throughout this work to avoid confusion. Even if its overall properties never reach pristine graphene, rGO provides a solid alternative to graphene obtained through mechanical cleavage or epitaxial growth due to its compromise between cost-effectiveness, ease of manufacture, and mechanical performance while retaining moderate electrical conductivity. The ability to tune the hydrophobicity of rGO by limiting or extending the degree of reduction permits high flexibility in the processing, improving the dispersibility of graphene in multi-material composites.

1.5 Recent progress on graphene/ceramic composites

1.5.1 Advantages and disadvantages of graphene as a ceramic additive

Graphene and graphene-like materials (FLG, GNP, rGO) are considered exceptional additive candidates for ceramic-based composites due to their combination of properties, leading to an increase in mechanical performance, wear resistance, electrical conductivity or electromagnetic interference (EMI) shielding of the ceramic matrix [18, 156].

Alumina-based composites containing graphene reinforcements (0 – 10 vol.%)

have been reported throughout the last decade, exhibiting strength and toughness increases of 35 – 80% compared to bulk alumina at a minor reduction of hardness ($<$ 15%) [23, 157–161]. Similar works were extended to other advanced ceramics like Si_3N_4 from Walker et al. (2011) [162], who validated increases of K_{IC} values above 200%, only experiencing a 25% hardness reduction after the inclusion of 1.5 vol.% of GNP in the formulation. Shin et al. (2014) [25] also applied this processing route for yttria stabilised zirconia (YSZ), achieving a 12% drop in hardness for rGO reinforcements of 4 vol.%, which resulted in toughness increases of 50% compared to the pure matrix material.

Graphene can soften the brittle behaviour characteristic of advanced ceramics, improving the material's toughness with moderate increases in bending strength, owing to graphene's flexible and strong nature. Graphene nanostructures embedded in the matrix can help provide extrinsic toughening mechanisms behind the crack tip (Section 1.2.1), in the form of graphene sheet pull-out and bridging the crack tip edges, with easier paths for crack extension and deflection provided by the graphene/ceramic interfaces preventing from traversing through the brittle ceramic matrices.

Another advantage of the inclusion of graphene additives resides in increased wear resistance. Once the graphene sheets embedded in the ceramic matrix are pulled out from the composite surface after wearing, these act as a self-lubricant layer that can reduce the friction coefficient of the material [163, 164]. Belmonte et al. (2013) verified an increase above 50% of the base wear resistance of Si_3N_4 ceramics when including 3 wt.% of GNP in the formulation, a work that established the potential of graphene inclusions to reduce friction under high contact pressure conditions [165]. As another example, Llorente et al. (2016) included GNP additions to SiC matrices, increasing the additive content up to 20 vol.% values attaining wear resistance improvements up to 70% [166]. Gutierrez-Gonzalez et al. (2015) applied a significantly reduced graphene content in graphene/alumina composites (0.22 wt.% in the consolidated material), noting an increase of 50% in the wear resistance when compared to plain alumina and validating the use of GO as the precursor for the graphene phase [163]. Graphene reinforcements can also trigger electrical functionalities in insulating ceramics upon their introduction in formulation. With the increase in graphene volume content, the electrical conductivity gradually augments until reaching a percolation limit. Above this critical volume, the conductivity of the composite is increased exponentially, arising from the creation of continuous graphene networks embedded in the composite that allow the electric current to flow through paths of lower resistance.

This percolation limit is highly dependent on the aspect ratio of graphene sheets and the quality of the precursor employed [18]. Achieving this internal network generally requires the addition of abundant reinforcement in the formulation at the cost of a higher deviation from the matrix properties. However, percolation can also be

achieved at very low concentrations, as shown by the works of Centeno et al. (2013) reporting percolation of graphene/alumina hybrids at 0.22 wt.% [23] and Hussainova et al. (2017) [167] producing electroconductive zirconia-based composites by adding hybrid graphene/alumina fibres with conductivities of 10 – 100 Sm^{-1} upon reaching network percolation at remarkably low carbon levels (0.6 vol.%). More examples are included in Figure 1.22 by Miranzo et al. (2017) [18], covering graphene/ceramic composites with enhanced conductivity up to 10000 S m^{-1} [23–31].

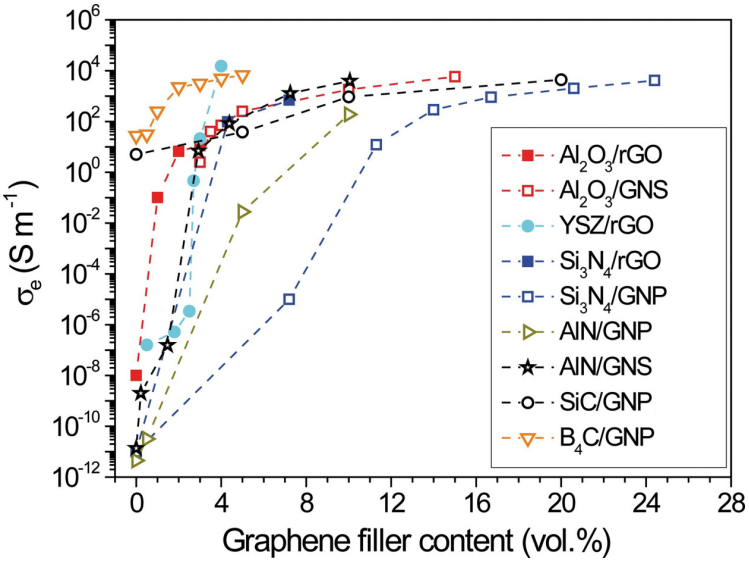

Figure 1.22: *Electrical conductivity increase of ceramic-based composites as a function of the graphene volume content (GO or GNP) in the ceramic matrix. Adapted from Miranzo et al. (2017) [18] with references in the legend from top to bottom corresponding to Centeno et al. (2013), Fan et al. (2012), Shin and Hong (2014), Ramirez et al. (2013), Ramirez et al. (2012), Simsek et al. (2017), Yun et al. (2015), Roman-Manso et al. (2016) and Tan et al. (2016) [23–31].*

Fluctuations in this range of electrical conductivity (for instance by disruption and cracking of the internal structure of the material) can be registered, opening the possibilities for ceramic-based components with sensing capabilities that retain high strength and toughness in demanding environments.

Additional advantages of including graphene in the ceramic formulation have been proposed, such as lightning protection or improved EMI shielding [168] with great potential for aerospace applications. Graphene inclusions can enhance the reflection and absorption mechanisms of neighbouring electromagnetic fields, reaching shielding effectiveness up to 40 dB [164] several orders of magnitude superior to plain advanced ceramics, generally transparent to electromagnetic radiation. Although EMI shielding is conventionally provided by metals, ceramic-based shields could exploit the advantageous properties of ceramics, working in high-temperature environments providing resistance to corrosion and high strength [164, 169].

Some major challenges remain in graphene/ceramic composites despite their huge

potential and the extended research performed throughout the last decade. Scalability and costliness issues still limit its spread into the industry, keeping it at the early stages of commercial development [130]. The difficulty in obtaining heterogeneous dispersions in a matrix material is a key disadvantage reported for graphene (common to CNTs) as a reinforcement in composites, leading to aggregation and an overall loss of mechanical properties compared to the expected behaviour [25, 39, 157, 170]. Even though graphene processing methods were significantly improved compared to CNT reinforcements, it remains a difficult task to achieve homogeneous dispersions of graphene due to the stacking tendency of its sp^2 planar graphitic domains and its hydrophobic (or water-repelling) behaviour.

Graphene's properties are also highly vulnerable to layer stacking and agglomeration, approaching the behaviour of bulk graphite upon increasing the stacking above 10 layers. Although there are suitable applications for non-pristine graphene, the electrical and mechanical properties are drastically reduced in the presence of stacked layers and defects in the structure [132]. As a result, the predominant use of graphene-like precursors (rGO, GNP) in composite processing permits a cost-effective approach, at the expense of electronic applications envisioned for graphene throughout the first decade of the 21st century based on the theoretical studies on graphene monolayers.

1.5.2 Spark Plasma Sintering of graphene/ceramic composites

All graphene/ceramic composites shown in the previous section required an optimised consolidation stage, performed either through hot pressing, Flash sintering or SPS as the most referenced techniques. Among these, SPS has taken a leading role, enabling a high degree of solid packing with densities over 99% by its combination of uniaxial pressure and direct electrical current (Section 1.1.2.2) [6, 51].

Graphene/alumina composites reported [86, 157, 158, 171] have been conventionally SPSed exploring several process parameters (maximum temperature reached, heating rates, isothermal dwelling times and exerted uniaxial pressure). Sintering temperatures of 1300 – 1500 °C, with pressures of 50 – 80 MPa have been predominant in the literature with heating rates over 100 °C min^{-1}, exploiting the capabilities of SPS that permit fast sample production. The duration of the isothermal stage has varied extensively in these reported works (1 – 10 min), constrained to the thermal and electrical conductivity of the sintered materials and the physical dimensions of the samples produced.

SPS-driven consolidation has been successfully extended to other graphene/ceramic pairings beyond alumina, examples being zirconia [25, 172], alumina-zirconia mixtures [167, 173], silicon carbide [174], silicon nitride [26, 175] or boron carbide [31], maintaining similar ranges of pressure and heating rates. The maximum sinter-

ing temperatures were adapted to the desired crystallographic phase for each ceramic matrix (e.g. from 1350 °C in zirconia mixtures to 1800 °C in the case of UHTCs like silicon or boron carbides), with increased temperatures also having an effect on the electrical capabilities of graphene, such as the graphitisation process occurring in rGO.

In these reviewed studies, the internal structure of the material during the fabrication of graphene/ceramic composites was not carefully tailored, with the constituents integrated in a random fashion during processing. Despite obtaining improvements of the properties compared to the bulk ceramic matrix, this processing approach could soon reach another upper limit that could not satisfy the complex demands of the near future engineering [40, 176]. Gaining more insight in tailoring the internal hierarchy of novel graphene/ceramic composites appears a promising solution, an example being the integration of bio-inspiration concepts in the materials processing strategies.

1.5.3 Towards hierarchical graphene/ceramic composites

The prospects of obtaining an interconnected $3D$ graphene network embedded in a ceramic-based composite have been recently explored as a pathway towards the current challenge of achieving programmable design and assembly in ceramic-based materials [40]. Maintaining the composite's internal hierarchy can lead to an increase of the mechanical properties based on graphene's natural strength and ability to deflect crack propagation while providing added functionalities such as increased electrical and thermal conductivity owing to the remarkable properties provided by graphene-like materials.

Hierarchical processing was primarily resolved for graphene/polymer hybrids via freeze-casting of graphene precursors in suspension. The colloidal stability of GO in suspension has permitted the conformation of graphene super-elastic structures exhibiting ultralow density after reduction (1 – 10 mg cm^{-3}) with oriented internal channels in the order of tens of micrometres [152, 154, 177, 178]. By infusing a polymeric phase, a range of electrically conductive polymer-based composites have been reported, useful for sensing purposes, EMI shielding or increased thermal conductivity [179–181].

Graphene/polymer hybrids have been taken a step further by providing more functionalities to the composite beyond the restoration of electrical conductivity and increase in mechanical properties. D'Elia et al. (2015) [182] proposed the selection of polyborosiloxane (PBS) as the polymeric phase based on its self-healing capabilities, permitting the conformation of a $3D$ interconnected graphene network produced via freeze-casting as a scaffold, providing structural integrity to the material during healing of the polymer matrix. Recently, freeze-cast graphene networks were simi-

larly integrated with memory-retaining epoxy resin to produce electrically conductive shape-memory composites [183], maintaining a very low carbon content (<1 wt.%).

Research on hierarchical graphene/ceramic hybrids has been significantly scarce in comparison. Some works implemented ceramic precursors as in the case of Wang et al. (2016) [108] (previously introduced in 1.3.2), the work from Wang et al. (2019) [184], in which the freeze-cast structure was made from combining GO and alumina in the precursor prior to hot-pressing, and the work by Sun et al. (2020) [164], which consolidated the ceramic phase by pyrolysis of a zirconium n-propoxide precursors, later expanded to other ceramics like alumina or silica.

Picot et al. (2017) developed a separate GO scaffold/infiltration approach in which the infiltrating ceramic phase consisted of polymer-derived ceramics (PDCs) [38, 185]. The integration of graphene and PDCs had already been explored by Ji et al. (2009) by integrating GO powder with a polysiloxane precursor later transformed to SiOC by a process of crosslinking and pyrolysis [186]. However, in Picot et al. work, the concept was expanded by applying a bioinspired approach, through which a polymethyl siloxane polymer was used to infiltrate a freeze-cast graphene-like network, later converted to a glass-ceramic (silicon oxycarbide glass) via pyrolysis at 900 °C and SPS at 1700 °C.

The substitution of PDC precursors with advanced ceramic slurries in the direct infiltration of graphene networks appears as a promising extension of this study, delivering a cost-effective processing route without chemically converting the matrix material and maintaining the attractive properties of advanced ceramics. Extending this strategy to water-based suspensions is also desirable, based on water's low cost, great availability and environmentally friendly characteristics [1, 87]. However, achieving this is not trivial due to the hydrophobic nature of graphene, repelling the water-based ceramic slurries and preventing the integration of both constituents. This challenge could be approached by the integration of amphiphilic additives in suspension that modify the surface behaviour of the ceramic particles, a strategy recently approached by Fan et al. (2021) [187].

Achieving a flexible, interconnected graphene network embedded within advanced ceramics could improve the material's toughness by providing extrinsic mechanisms to accommodate the stresses that lead to fatal failure upon loading, also paving the way for lightweight, electroconductive ceramics produced via a water-based cost-effective method. Such materials could be highly valuable for aircraft and shielding applications where ceramic-based materials have been increasingly used over the years, and yet non-insulating materials with a better combination of toughness and strength are required [40, 168].

Chapter 2

Aims and Objectives

The main objective of this thesis consisted of validating a water-based processing route for bioinspired graphene/ceramic composites through a scaffold and infiltration approach. It comes as an extension of previous approaches in producing highly-structured graphene/ceramic composites using polymer-derived ceramics (PDCs) [176]. In contrast, this work aims to apply the strategy to water-based alumina slurries, exploiting the amphiphilic capabilities of Pluronic F127 additions in the ceramic formulation and expand previous knowledge on the production of graphene-based aerogels via freeze-casting. A general processing strategy was defined (Figure 2.1) to overcome the main challenge of infiltrating a hydrophobic graphene scaffold, permitting ceramic and graphene phases to coexist in the bulk composite and maintaining coherence after consolidation.

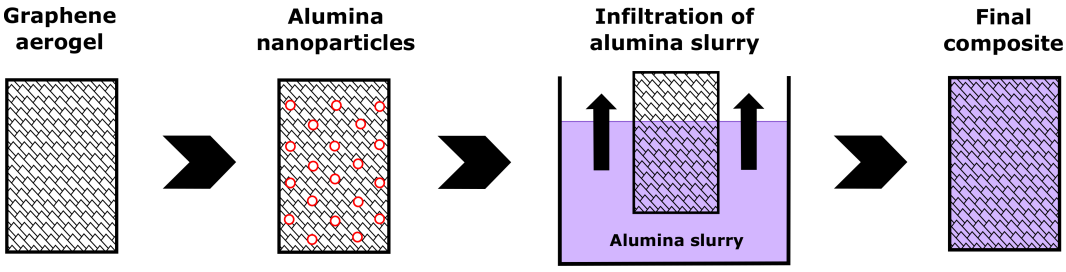

Figure 2.1: *General steps in the proposed processing strategy.*

Accomplishing this general objective required expertise in wet-chemistry, freeze-casting, sol-gel synthesis, carbonisation and advanced sintering techniques (Spark Plasma Sintering), along with a selection of chemical and structural characterisation techniques at every stage. The document has been divided in three self-contained results chapters that correlate to the three identified stages in the processing strategy proposed:

1. Production of self-supporting graphene aerogels and hierarchy enhancement via deposition of alumina nanoparticles.

2. Integration of alumina and graphene phases.

3. Consolidation of the novel graphene/alumina composite.

1. Achieving self-supporting graphene aerogels

The first stage objective comprised the conformation of interconnected graphene aerogels via freeze-casting and carbonisation, using colloidal graphene oxide (GO) suspensions in water as precursor. Settling a systematic procedure required defining freeze-casting parameters such as GO concentration in water, additives in formulation and freezing rates applied to the slurries. The scalability of the produced aerogels was additionally targeted, paving the way for later stages in the project and producing specimens large enough for future testing without damaging their consistency and self-standing behaviour. This has been approached by combined optimisation of the freeze-casting setup and the carbonisation cycle.

A secondary objective comprised evaluating the selected graphene precursors, with extensive characterisation applied to the two GO sources (*CU_GO* and *ICL_GO*) used throughout this work. This chapter also explored the decoration of graphene aerogels with alumina nanoparticles (NPs), designing an environmentally-friendly route of low toxicity based on aluminium lactate. This aerogel-decoration strategy aimed to implement an extended level of hierarchy in the material and explore a scarcely researched NP synthesis route previously applied for ceramic glasses and fibres.

2. Integration with water-based alumina slurries

The second stage objective consisted of solving the key challenge of infiltrating water-based alumina slurries into hydrophobic graphene aerogels, maximising wetting and delivering graphene/ceramic green bodies according to traditional ceramic processing routes. The aim was to study the effect of the amphiphilic copolymer (PF127) additions in the ceramic formulation, limiting its quantities while allowing the wettability of the graphene/alumina pairing.

A systematic approach was defined by adjusting the formulation of PF127/Al_2O_3 slurries in water and performing wettability and infiltration tests under lab-scale conditions, also applied to graphene aerogels with the extended hierarchy level. The scalability of this processing strategy was also approached, with the objective of producing scaled-up graphene/alumina green bodies ready for consolidation.

3. Consolidating a final composite

The third stage objective targeted the consolidation of graphene/alumina green bodies obtained in previous stages, preserving the graphene aerogels' structure provided by freeze-casting processing. The aim was to achieve unidirectionally aligned channels of graphene on the micrometre scale embedded in the ceramic matrix, mirroring previous works on bioinspired structures.

This stage required finding optimal parameters for SPS sintering, regarding the temperature and pressure cycles applied to deliver unbroken ceramic-based discs preserving integrity and a high degree of densification. The conditions were applied for both lab-sized and scaled-up scenarios, understanding the constraints of the processing strategy and outlining pathways for future optimisation of the processing route.

Chapter 3

Materials and Experimental Methods

3.1 Raw materials

Two types of water-based graphene oxide (GO) suspensions were used at different stages in the project acquired from various sources:

1. GOGraphene (William Blythe Ltd.) 1 wt.% GO suspension in water.
2. As-prepared 0.6 wt.% GO suspension from Imperial College London.

While GOGraphene (labelled *CU_GO* throughout the document) is a readily available commercial supply of GO suspensions, the suspension from Imperial College London (*ICL_GO*) was specifically synthesised for this research by Prof Saiz´s group at the Centre of Advanced Structural Ceramics (CASC) through a modified Hummers method [148]. Due to the limited availability of this custom suspension and the expected variability between different batches, *CU_GO* was selected for most of the early tests and characterisation before defining a general processing strategy. Silicon wafers (Graphenea) containing a 300 nm SiO_2 layer were used as substrates for GO films and suspensions.

Baikowski BA-15W alpha-alumina (specific surface area of 19.6 m^2 g^{-1}, particle size of 100 nm measured by SEM and density of 3.96 g cm^{-3}) was used as the main ceramic powder throughout the project. Additives added to water-based alumina and GO slurries consisted of sucrose powder ($C_{12}H_{22}O_{11}$, Sigma Aldrich) and polyvinyl alcohol beads (PVA, Sigma Aldrich). A triblock copolymer based on polyoxyethylene (PEO) and polyoxypropylene (PPO) in the form of $[PEO]_a$-$[PPO]_b$-$[PEO]_a$ ($a = 100$, $b = 65$, Mw = 12600 g mol^{-1}, Sigma Aldrich) commercially labelled as Pluronic F-127 (PF127) was also included in the formulation of water-based alumina suspensions.

Deionised (DI) H_2O was chosen as the aqueous suspension medium for water-based processing and cleaning purposes. Organic solvents used for the preparation of non-aqueous suspensions and cleaning purposes include ethanol (anhydrous - 99%, Sigma Aldrich), isopropanol (IPA, anhydrous - 95% purity, Sigma Aldrich) and acetone (95%, Fisher Scientific).

Infusion epoxy resin (IN2, Easy Composites Ltd.) was selected as the matrix for epoxy/graphene composites, cured for 24 hours using a slow hardener (AT30, Easy Composites Ltd.) by mixing in a 70:30 weight ratio.

Alumina nanoparticles were synthesised using aluminium-L-lactate in flake form (95%, Sigma Aldrich) as a precursor in DI H_2O. The pH of the lactate solutions was adjusted by dropwise addition of sodium hydroxide (NaOH, 1 M) and hydrochloric acid (HCl, 2 M). Commercial water-based 20 wt.% suspensions of alumina nanoparticles (α-phase, 30 nm, US Research Nanomaterials, Inc.) were also used for comparison purposes.

3.2 Materials and composites preparation

3.2.1 Slurry preparation

Throughout this work, GO and alumina solids were processed in slurry form (as suspensions of dense materials in water or other liquid media). Several steps were common in the preparation of each suspension. The required amount of solid material was initially weighted on an OHAUS Explorer EX 423 balance and added to a plastic container, or speed-mixing beaker described hereafter. For weighting even lighter materials, such as graphene oxide aerogels, a five-digit Precisa Balance 40SM-200A was used alternatively.

All granular powders (e.g. ceramics and sucrose) were weighted on disposable weighing boats with a stainless-steel spatula and added to the mixture. Liquids and low-viscosity slurries were weighted by drop-wise addition with a disposable Pasteur pipette or 1000 μl micropipette when higher precision was required.

A laboratory-sized instrument for rapid mixing SpeedMixer™ DAC 800.1 FVZ unit was included in most procedures requiring great mixture homogeneity to provide efficient contact between the formulated water-based slurries. Speed-mixing combines the spinning of a high-speed mixing arm in one direction with the opposite rotation of the basket. This combination (referred to as dual asymmetric centrifuge) provides degassing and efficient contact between the formulated water-based slurries, obtaining a homogeneous dispersion in under 10 minutes.

3.2.1.1 Wet ball-milling

In common with traditional ceramic processing routes, a wet ball-milling stage was included in the preparation of alumina suspensions (in the presence of PF127 additions) before their integration with graphene-based aerogels in the main processing. Ball-milling was applied to aid in breaking the alumina agglomerates from the supplied powder and reducing sedimentation.

Alumina balls of 3 mm in diameter were used as the milling media. The volume of alumina suspension, milling media and air to be introduced in a sample container was first based on a simple relationship with each part occupying 1/3 of the total volume (V_{total}):

$$\begin{aligned} V_{total} &= (V_{susp} + V_{mill} + V_{air}) \\ V_{susp} &= V_{mill} = V_{air} = \frac{1}{3} V_{total} \end{aligned} \tag{3.1}$$

With V_{susp}, V_{mill} and V_{air} representing the volume of alumina suspension, the milling balls and the remaining air, respectively. However, this relation was intended for 10 mm balls of equivalent weight, and it did not consider an extra 30 – 40% of volume loss due to the ball-packing [188]. Therefore, the volume for milling media was eventually lowered to 1/5 of V_{total} calculating the number of balls to put in the container based on weight instead.

$$\begin{aligned} m_{mill} &= V_{mill} \times \rho_{Al_2O_3} \\ m_{mill} &= N \times m_{ball} \end{aligned} \tag{3.2}$$

Where $\rho_{Al_2O_3}$ is the density of the alumina balls, and N is the number of alumina balls to add to the suspension. For example, on a container with a V_{total} of 200 mL, a target V_{mill} of 40 mL would be filled by the milling media (158 g). Alumina balls were added to the container on a precision scale until reaching this weight value. The quantities of water, alumina and PF127 in the ceramic slurry were obtained by relating the target volume of suspension in the container with the weight and density of each component:

$$\begin{aligned} V_{susp} &= V_{Al_2O_3} + V_{PF} + V_{H_2O} \\ V_{susp} &= \frac{m_{Al_2O_3}}{\rho_{Al_2O_3}} + \frac{m_{PF}}{\rho_{PF}} + \frac{m_{H_2O}}{\rho_{H_2O}} \end{aligned} \tag{3.3}$$

From the value of solid loading and PF127/Al_2O_3 wt./wt. ratio chosen for each suspension, a weight relation between the three components could be defined. As an example, for a 25 wt.% solid loading alumina slurry with a PF127/Al_2O_3 ratio of 0.15, the following relationship would apply:

$$m_{PF} = 0.15 \times m_{Al_2O_3}$$
$$m_{Al_2O_3} = 0.25 \times (m_{Al_2O_3} + m_{PF} + m_{H_2O}) \tag{3.4}$$

By integrating Equations 3.3 and 3.4, the wt.% of each component was obtained for each set of conditions and added to the milling container. After putting the suspension and milling media together, the container was tightly closed with Parafilm and rotated at 200 rpm for a minimum of 24 hours. The suspension was transferred to a different container and sieved to retrieve the maximum quantity of suspension while limiting water evaporation. The milled suspension was speed-mixed for an additional 10 minutes to reduce bubble formation arising from the addition of PF127 in the alumina slurry formulation, which is detailed further in Chapter 5.

3.2.2 Production of aluminium hydroxide gels

Aluminium hydroxide gels were produced by the sol-gel synthesis of aluminium-L-lactate in DI H_2O based on a synthesis procedure described by Zhang et al. (2003) [189, 190] and integrated with GO suspensions (Figure 3.1).

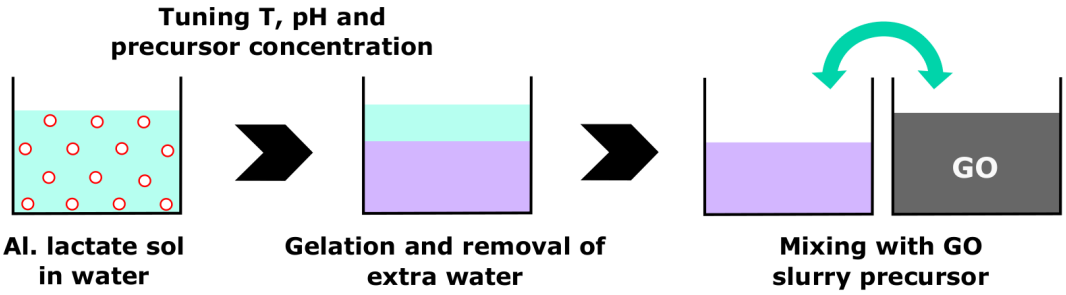

Figure 3.1: *Stages of aluminium hydroxide gel production, starting from the solution of aluminium-L-lactate precursor to the integration with GO suspensions.*

Various parameters such as temperature, pH, precursor concentration and ageing method were modified to identify the most suitable conditions to produce the gels with the assistance of Ms Céline Daurat during her 2018 CUROP summer placement. The starting conditions consisted of an aluminium lactate concentration of 0.1 - 0.5 M, a pH range from 2 to 10 (monitored with a pH meter and altered by dropwise additions of NaOH, 1 M and HCl, 1 M) and two different methods of ageing (Table 3.1). The first method consisted of ageing at room temperature for up to 1 week, whereas the second required controlled heating in a drying oven at 60 °C for 48 hours.

Table 3.1: *Experimental conditions tested for sol-gel of aluminium lactate precursor. RT = Room temperature.*

Al lactate concentration (mol/l)	**pH**	**Ageing temperature (°C)**
0.1	2	RT
0.1	3.4	RT
0.1	3.4	60
0.1	7	RT
0.1	7	60
0.1	10	RT
0.1	10	60
0.2	3.4	60
0.2	10	60
0.5	10	60

Magnetic stirring was maintained for 30 minutes to ensure the homogeneity of the measurements, using a Parafilm cover to prevent the evaporation of water in the process. 20 mL of DI H_2O was used to prepare 0.1 to 0.5 M solutions of aluminium lactate using 50 mL glass beakers and a precision scale. The mixture was homogenised using 30 min of magnetic stirring and a hot plate to control the temperature between 25 – 50 °C while covered with Parafilm-M to avoid solvent evaporation until a visible colour change occurred. The pH of ceramic precursors solutions was modified by adding sodium hydroxide (NaOH) 1 M or hydrochloric acid (HCl) 2 M, monitored with a Mettler Toledo SevenCompact pH meter. Once the pH was adjusted, the samples were stored in closed beakers at room temperature or heated in a fan-circulated oven (LTE Scientific Raven Oven 2) up to 50 °C for 48 h to accelerate the gelation process.

3.2.3 Processing aerogels via freeze-casting and freeze-drying

The fabrication of highly porous GO aerogels was achieved by freeze casting of graphene oxide suspensions in water and subsequent freeze-drying.

3.2.3.1 Freeze-casting setup

The custom-made freeze-casting setup consisted of two steel-based cylindrical containers (120 mm and 220 mm in diameter) containing a cylindrical copper finger (25 mm in diameter) to maximise thermal conductivity based on previous examples in the literature [152, 182, 191]. The outer cylinder was continuously filled with liquid nitrogen up to 50 – 60% capacity to ensure temperatures of –196 °C were achieved at a 2 – 10 °C min^{-1} rate. The inner cylinder holding the copper finger was filled with 2 - 3 cm of ethanol bath to level the temperature gradient provided by the liquid

nitrogen throughout the experiment.

A representation of the whole setup is included in Figure 3.2, highlighting the physical parts of the equipment and identifying the required consumables. Graphene oxide slurries were poured in a mould on top of the cold finger, ensuring the temperature gradient was unidirectionally applied from the bottom plane. To improve the fitting of the mould to the copper rod, a machined thin copper plate was placed on top of the finger as an intermediate layer.

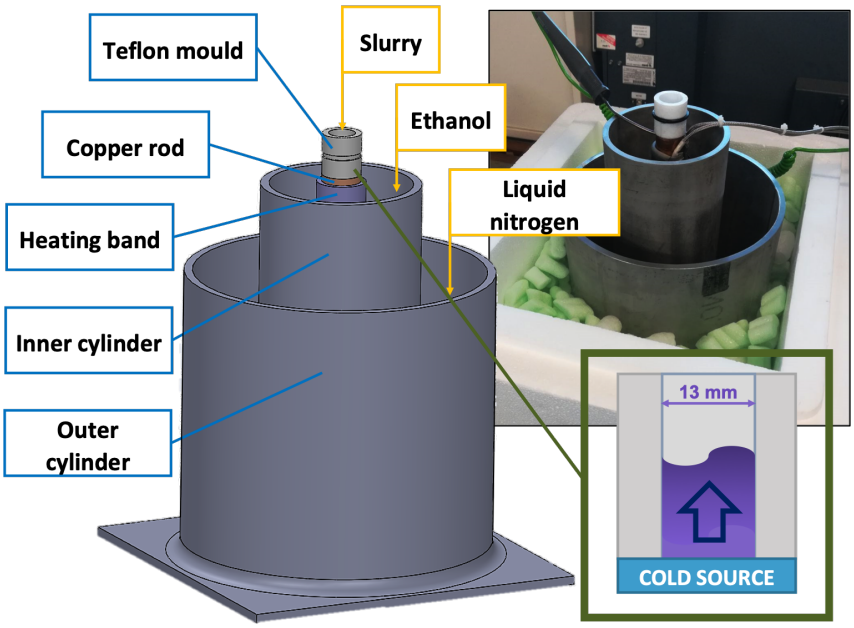

Figure 3.2: *Schematic of the custom freeze-casting setup with all key components. A picture of the real unit and a detailed perspective of the casting mould are also provided.*

The cooling gradient was applied by a heating band wrapped around the copper finger, connected to a Eurotherm controller-programmer with an attached type-K thermocouple monitoring the temperature reached. The heating band was positioned as close as possible to the thermocouple, as the loss of heat through conduction at low temperatures could lead to considerable thermal deviations above distances greater than 5 mm.

Moulds were machined from Teflon, which effectively prevented the sticking of the suspensions when casting complex shapes. 3D-printed polylactic acid (PLA) moulds were used for simpler shapes as an alternative due to their ease of manufacture and faster availability (Figure 3.3a). A 4-piece improved mould setup was designed with the help of CUROP student Mr Mohammad Arshad. This mould permitted a 90° rotation of the freezing direction during freeze-casting while maintaining the cylindrical outer shape of the produced aerogels (Figure 3.3b). Instead of previous 2-piece moulds, the improved mould was additionally sliced in four sections, easing the dismantling procedure without breaking the sample after freezing was complete.

Teflon was selected over PLA material despite its much higher operational cost to help preventing the sticking of GO suspension to the mould's sharper corners.

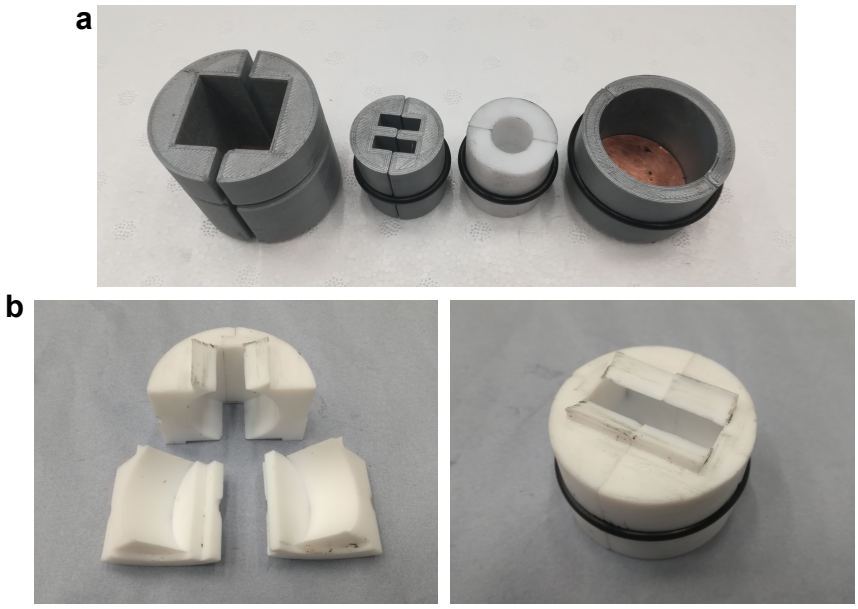

Figure 3.3: *a) Various Teflon and PLA mould concepts for freeze-casting. b) Improved 4-piece Teflon mould to produce cylindrical 30 mm aerogels with a perpendicular axis of revolution.*

A Eurotherm temperature controller/programmer 3216-CC-VH was used to program the cycle of freeze-casting in a flexible and controlled manner. The controller program covered the required heating/cooling steps needed to perform freeze-casting of the suspensions, with the following requirements identified for any given routine:

1. An initial temperature ($SP1$) maintained for an undetermined amount of time.
2. A consistent freezing rate of 1 to 10 °C min^{-1}.
3. Achieving a target temperature ($TSP1$) of at least –150 °C to guarantee complete freezing of the slurry.
4. The ability to stop the program at any given time before reaching ($TSP1$) to adapt to mould shapes and materials of different behaviour.

The controller was reset to the initial set point ($SP1$) defined at 20 °C once the program was terminated at any given time (generally when the sample appeared frozen entirely). After reaching the $SP1$ temperature again, the next cycle was initiated by casting a new slurry into the mould. A sketch of the program is included in Figure 3.4.

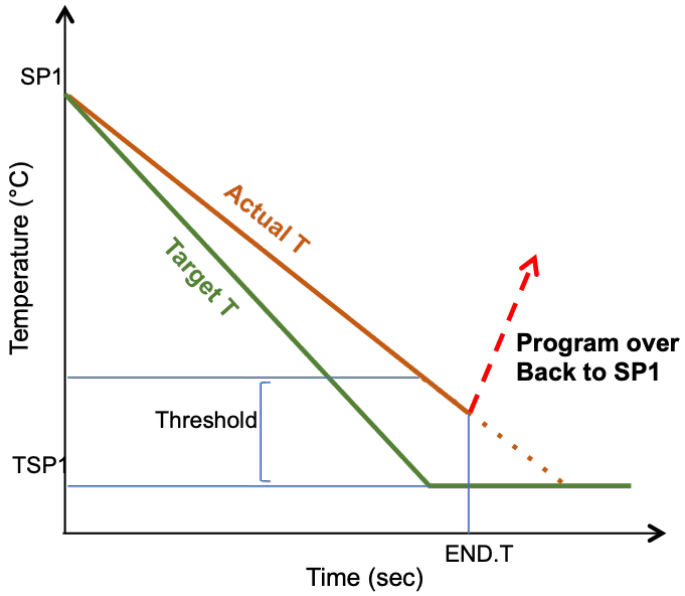

Figure 3.4: *Freeze-casting routine displaying the critical parameters involved, with the expected deviation between target and real temperatures achieved in the mould.*

The main advantage of this approach is its simplicity, which permitted a quick succession of freeze-casting cycles returning to the SP1 initial temperature at any given time. As a drawback, the temperature of the final heating step could not be controlled. However, it did not affect the results as the mould was always detached from the copper rod before this step. The PID internal controller of the Eurotherm was adjusted using an auto-tune function, after which the applied freezing rates were manually verified using a timer.

Various improvements were made on the freeze-casting setup to attain flexible freezing rates, aiming for more consistent aerogel production under all selected parameters. Despite minimising the distance between the heating band and the controller's measuring thermocouple and autotuning the controller's PID parameters, an upper limit of 5 °C min^{-1} freezing rate was verified in the setup (Figure 3.5). As higher freezing rates had been previously reported in the literature [152, 177], this limitation was attributed to poorer heat transmission in the custom-built freeze-casting setup.

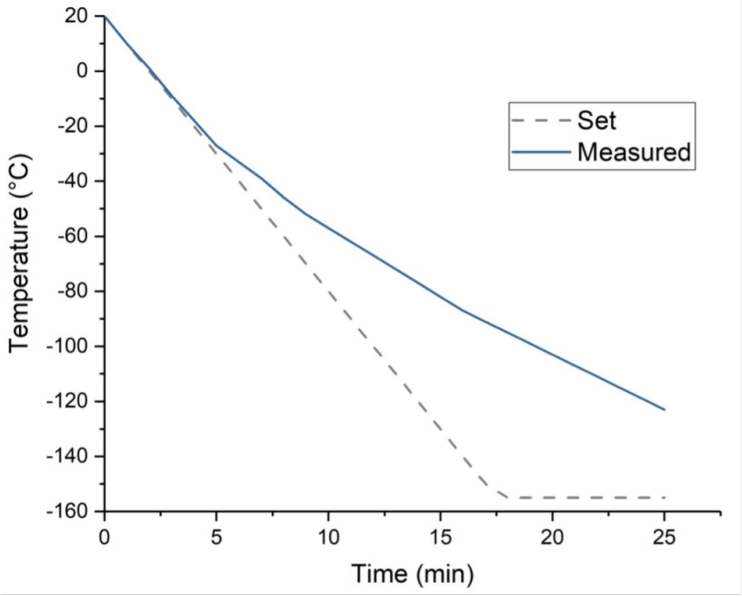

Figure 3.5: *Decay in temperature rate arising from poor thermal transmission in the freeze casting setup, manually verified using a timer.*

An improved version of the freeze-casting setup was alternatively used at the Institute of Science and Technology of Carbon (INCAR), with the base of the outer stainless steel cylindrical holder containing liquid nitrogen substituted with copper material of higher thermal conductivity. With this modification, liquid nitrogen became a more effective cold source, improving the heat transmission with the copper rod and enabling consistent temperature gradients of 10 °C min^{-1}, permitting faster casting times.

3.2.3.2 Freeze-drying

The ice present in the GO aerogels produced via freeze-casting was sublimated by freeze-drying on a Lablyo -85 (Frozen in Time Ltd., Figure 3.6), combining temperatures below –6 °C with pressures between 1 - 12 Pa. Samples were put in either B24/B29 round-bottom flasks or 150 mL neck filter bottles with rubber caps (SciQuip) depending on the physical state of the material and connected to any of the eight valves from the top manifold via B24 flask adapter tubes.

Optimal temperature and pressure conditions were set by enabling a dual compressor and a vacuum pump, activated once the temperature in the chamber decreased below -30 °C. High-vacuum silicone grease (Dow Corning) was also applied on every junction to maximise sealing. A minimum operation time of 48 h was needed to completely remove ice from the samples, increasing up to 4 – 5 days based on the specimen size and geometry. After completion, the obtained green bodies could be retrieved from the flasks/bottles with barely any humidity in the structure to perform weight and density measurements before carbonisation.

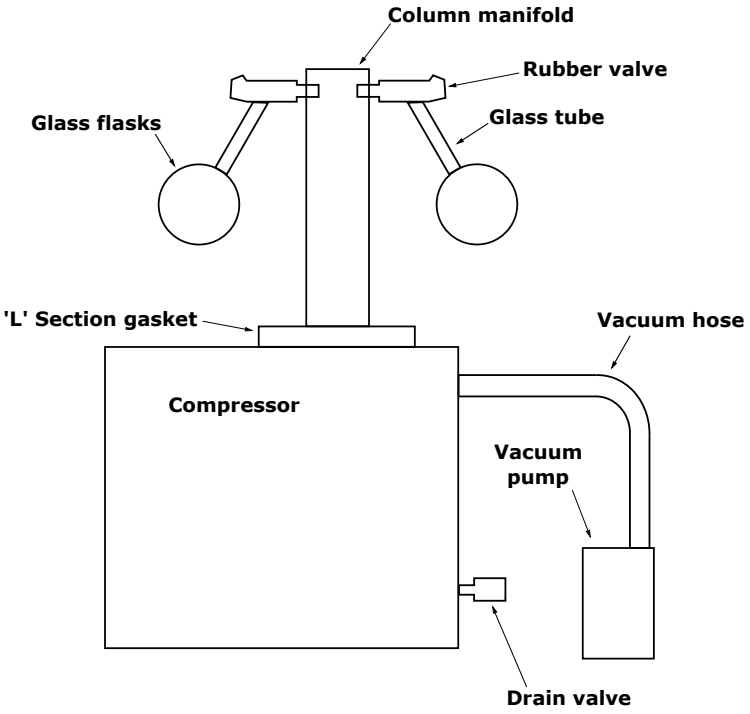

Figure 3.6: *Diagram of Lablyo -85 freeze-drying unit, provided by Frozen in Time Ltd.*

3.2.4 Aerogel post-processing - Carbonisation

Carbonisation of graphene-based samples was performed under an inert atmosphere on a Carbolite MTF 12/38/400 tubular furnace. A preliminary drying step was also included to ensure the total elimination of humidity in the samples after freeze-drying. This drying step was performed overnight under 100 °C inside a fan-circulated oven (LTE Scientific Raven Oven 2), covering the material with Pyrex glassware to mitigate the airflow generated by the fan.

In the tubular furnace, a 35 mm quartz straight tube (Multi-lab) was placed inside the chamber and connected to an argon gas line (Pureshield 11-W, 11.01 m^3) by combining KF-40 Swagelok adapters, cast clamps and Quick connect couplings. Samples were deposited on rectangular alumina crucibles (99.7% purity) placed in one end of the quartz tube and pushed to the chamber's centre with the help of a steel rod. An argon flow of 2 lpm (litres per minute) was regulated using a ball flowmeter (Brooks Instruments) attached to the inlet line and enabled 40 minutes before carbonisation to purge the air inside the chamber. The outlet tube was connected to a water-filled beaker with a rubber hose, verifying the argon flow by monitoring water bubbling (Figure 3.7).

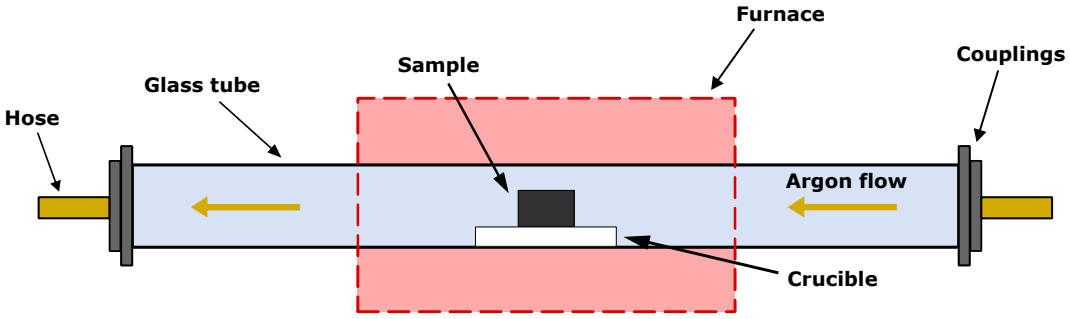

Figure 3.7: *Diagram of the tubular furnace setup for carbonisation of graphene-based samples.*

The annealing procedure applied to graphene-based samples was modified to compensate for the inability to control the applied heating rate in the tubular furnace. Freeze-dried GO aerogels were first put in the drying oven overnight to smoothen the initial weight loss caused by the remaining humidity. The aerogels were then transferred to the tubular furnace, reaching three intermediate temperatures of 100, 150 and 200 °C with 1 h dwelling times to ease the release of volatiles during this range of temperatures. Finally, the temperature was raised again to the original target of 900 °C and maintained for 1 h, leaving the sample to cool naturally under argon flow. The implications of applying an uncontrolled heating rate in the carbonisation of graphene-based samples are addressed in more detail in Chapter 4.

Achieving a specific carbonisation temperature within tight tolerances in graphene-based samples is critical regarding their final properties and restoration of the graphitic structure [130, 139, 153]. To verify the achieved temperatures, the tubular furnace was thoroughly calibrated up to 1000 °C using a type-K thermocouple placed at the central point of the chamber. The calibration was performed by registering three measurements:

1. Temperature marked by the inbuilt Eurotherm controller in the furnace.
2. Temperature registered by the external thermocouple in contact with the ceramic and under air atmosphere.
3. Temperature registered by the external thermocouple inside the quartz tube under low argon flow.

The testing cycle consisted of intermediate steps of 100 °C achieved with the inbuilt Eurotherm controller. Once the furnace reading stayed constant for more than one minute, the target temperature was deemed reached and maintained for a 10 min isothermal dwell. Afterwards, the next temperature target was selected, repeating until reaching a final temperature of 1000 °C, concluding with natural cooling under air (Figure 3.8).

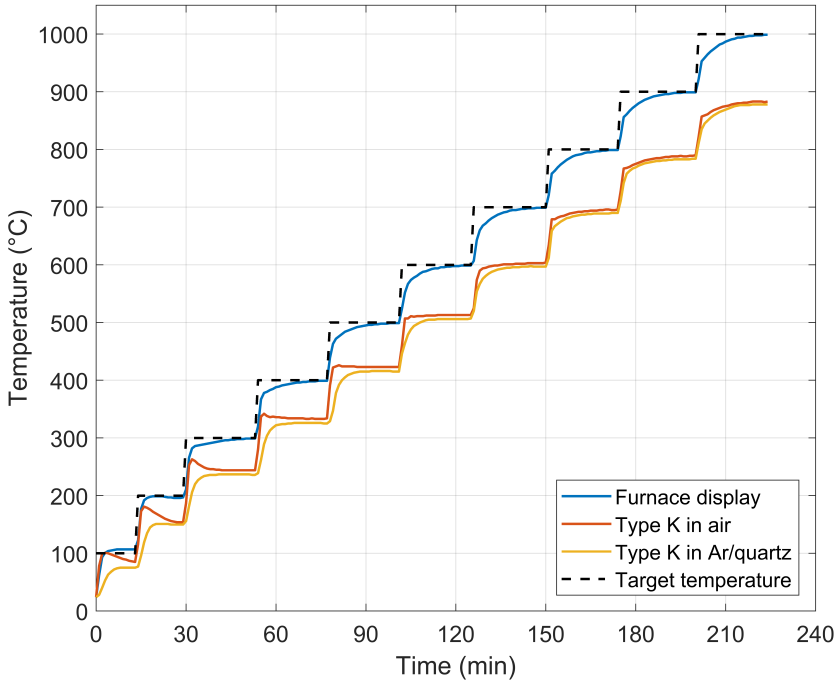

Figure 3.8: *Temperature calibration performed on the tubular furnace, both under air and argon atmosphere.*

The empirical formula $T_{act} = 0.9T_{sel} - 29.7$ was derived from this calibration procedure, with T_{act} being the desired temperature required by the process and T_{sel} the temperature to be selected in the in-built Eurotherm controller. Further tests were performed for temperatures under 300 °C due to the instability shown by the red thermocouple in Figure 3.8. In those tests, the behaviour inside and outside the tube (red vs yellow curves in the graph) was found equivalent, discarding any potential effects of the argon flow at lower temperatures.

3.2.5 Composite preparation via infiltration

Graphene-based aerogels were infused with epoxy resin through vacuum casting in a custom-made chamber by applying negative pressure. The technique ensured faster infiltration rates and the reduction of bubbles present in speed-mixed materials. The base resin and hardener were first put separately inside the vacuum chamber for at least 15 minutes. The pressure was maintained under 70 Pa using a vacuum pump, gently releasing the pressure by manipulating the chamber's closing valve to prevent sudden foaming and over-spilling of organic materials.

The resin and hardener were mixed on a 100:30 weight ratio and speed-mixed for 10 minutes. The graphene-based aerogels were placed in secondary containers, adding the epoxy/hardener mixture dropwise to the aerogels using a plastic pipette to prevent excessive damage to the structure. The containers were later placed under vacuum for an additional 20 minutes to enhance the infiltration and remove bubbles present in the epoxy mixture. A slow hardener was selected to prevent curing the

epoxy matrix before achieving complete infiltration of the scaffold due to the inherent slow processes of degassing and epoxy dropwise deposition.

Graphene aerogels were also infiltrated with water-based Al_2O_3/PF127 suspensions in the absence of a vacuum to prevent excessive foaming caused by the PF127 in suspension. The aerogels were first placed in an empty container, then Al_2O_3/PF127 droplets were added over the aerogels using a plastic pipette to wet them until complete infiltration. This process required extensive optimisation of the infiltration conditions and approach, detailed in Chapter 5.

3.2.6 Spark Plasma Sintering

3.2.6.1 Sample preparation and start-up

Spark Plasma Sintering (SPS) was selected as the sintering method for ceramic-based samples and composites in this work performed using a Type HP D 10-SD unit from FCT Systeme GmbH (with its background already presented in Section 1.1.2.2). All samples were sintered in detachable graphite dies of 20 mm and 30 mm diameter (Duragraph 120, Erodex Ltd. from Figure 3.9) previously wrapped with 0.2 - 0.35 mm graphite paper (Erodex Ltd.).

Figure 3.9: *Exploded view of the graphitic die assembly for 30 mm samples.*

The materials (powders or composite green bodies) were first weighed on a balance and transferred to the graphite die using a stainless-steel spatula. Once fixed the lower and upper graphite dies in the setup, cold pre-pressing was applied to fasten the assembly before its fitting inside the SPS chamber. A carbon felt was wrapped around the dies to provide better thermal insulation during sintering. An external chiller was filled with 100 L of type-3 DI H_2O (40 – 70 μS cm^{-1}), acting as the primary refrigeration system. After enabling the electrical switches and air extraction, compressed air and argon (3 bar) in-lines were supplied to the machine

for purging the chamber during operation.

3.2.6.2 Sintering cycles

To consolidate the composites designed in this work, different sintering programs were set based on the properties of the graphene/ceramic or ceramic materials. General standard parameters were shared by most sintering sequences and have been reviewed in this section, with specific cycles discussed in Chapter 6.

A pre-pressing of 2 kN was initially applied to fix the sample in position, manually exerted by controlling the movement of the bottom piston. After locking the chamber, the internal pressure was reduced to 100 mbar as an intermediate vacuum level, reaching a higher vacuum of 0.011 mbar by activating a secondary valve. A 10 kN cold-pressing segment was generally programmed at this stage before applying an electric current.

The current was activated according to selected parameters of power percentage, pulsating sequence and desired heating rate. The power percentage depends on the combination of current and voltage needed for the sequence, being 40 kW the maximum permitted by the machine. At lower temperatures, the heating rate is monitored by three Type-K thermocouples located inside the chamber, with a maximum measuring range of 1100 – 1200 °C. Above 250 °C, a pyrometer situated at the top part of the chamber monitored temperatures reached by the upper graphitic die.

Independent heating segments could be applied by varying heating rates, isothermal temperatures and dwelling times. The linear heating rate was automatically calculated and verified by the top pyrometer by selecting the target temperature and the duration of each segment. At the end of the sequence, a final cooling segment was needed, stopping the current and allowing the system to cool naturally. The electric current could be maintained during a controlled cooling segment to reduce the effect of thermal shock in the sample. Pressure values could be modified throughout the process, defining linear pressure rates for each segment in similarity with temperature rates. For instance, an extra segment was generally added after isothermal dwelling to remove the pressure before initiating controlled cooling. An overview of the applied segments during sintering is displayed in Figure 3.10.

Figure 3.10: *Overview of program segments applied in an SPS sintering cycle.*

The application of consecutive sintering cycles could eventually result in the fracture of graphite dies during the process, lowering the registered pressure between the hydraulic pistons and causing damage to the machine and the sample holders.

To avoid this issue, a limit threshold of 10 mm was defined for the relative piston movement permitted during the sintering cycle, considering the expected sample contraction in the chamber. Above this threshold, the machine stopped the program without experiencing further damage. Another working gas, such as argon, could additionally be selected as an alternative atmosphere in the process, requiring the addition of two extra pressing stages in the program. This was, however, not needed for the experiments performed.

3.2.7 Cutting and polishing of specimens

Prismatic ceramic and epoxy-based specimens were obtained using a Struers Accutom –100 cutting tool with Struers MOD10 diamond cut-off wheels. Each sample was attached to a graphite square sample holder with acrylonitrile adhesive and later retrieved by applying heat on a hot plate. The graphite holder was fixed to the mounting machine system by tightening two lateral screws that prevented movement during cutting. The cutting parameters were tuned for epoxy and ceramic-based materials considering the change in properties of each material (Table 3.2). The feed and force values for the diamond saw were carefully selected to prevent alignment deviations and bending of the blade from using excessive speeds.

Table 3.2: *Reference parameters used for cutting epoxy-based and ceramic materials.*

	Epoxy matrix	**Ceramic matrix**
Force level	MEDIUM	HIGH
Feed speed (mm/s)	0.08	0.02
Wheel speed (rpm)	1000	4000

A multi-cut feature was enabled to produce systematic cuts along one single direction with even spacing, which increased the reliability of the specimen dimensions when aiming for 3 - 4 mm widths.

Epoxy-based specimens were manually polished with a Buehler Metaserv Grinder and SiC abrasive paper. Rotational speed and the water flow were changed according to the variability between different samples and the difficulty in handling thin specimens obtained after cutting. The polishing protocol consisted of a 5-minute manual polishing under water using three progressively finer abrasive SiC papers (P1200, P2400 and P4000). The 'P' from the designation of SiC paper relates to the abrasive grit size according to the FEPA (Federation of European Producers of Abrasives) system, being inversely proportional to the particle size of the paper grains.

Ceramic-based materials were polished at the Nanomaterials and Nanotechnology Research Centre (CINN, Spain) [53] using a combination of Struers Rotopol-31 and RotoForce-4 equipment, following a more rigorous automatic procedure due to the increased hardness of the samples. The ceramic-based materials were first embedded

in epoxy resin under pressure at 150 °C and cured for 20 minutes. A four-stage polishing protocol was applied to three samples simultaneously, consisting of the following:

- 16 min clockwise rotation at 300 rpm applying 40 N force per sample on a Struers MD-Piano-120 resin-bonded diamond disc, using water as a lubricant.
- 4 min clockwise rotation at 300 rpm applying 40 N force per sample on a Struers MD-Piano-1200 resin-bonded diamond disc, also with water.
- 4 min clockwise rotation at 150 rpm on a Struers MD-Largo-9μm coated with DP-Spray polycrystalline diamond 9 μm. IPA was used as lubricant applied by continuous manual spraying.
- 4 min counterclockwise rotation at 150 rpm on a Struers MD-Largo-3μm coated with DP-Spray polycrystalline diamond 3 μm. IPA applied by manual spraying.

3.3 Background of materials and composites characterisation

3.3.1 Particle size distribution

An understanding of the size of particulate solids can be obtained through laser diffraction. In the case of wet laser diffraction, the solid particles are first dispersed in a liquid medium, subjected to mechanical stirring and ultrasonication to prevent the agglomeration of the material. By hitting the solid particles with a laser beam and measuring the produced light scattering, the volume occupied by the particles can be measured (Figure 3.11). The optical properties such as the refractive index of the studied material are required beforehand to relate the angle of scattering to the particle size. Assuming a perfect spherical volume, a distribution profile with the theoretical particle diameters can be obtained.

Dispersed fine colloidal particles can be prone to agglomeration once suspended in a water medium and travelling in a Brownian motion, increasing the perceived particle size evaluated by the light scattering [44]. The stability of colloids can be improved by enhancing the steric repulsion or electrostatic stabilisation in the system. While the former mechanism consists of the physical blockage of particles occupying the same space (e.g. by polymeric chains attached to the particle surface), the latter refers to the charge distribution and how particles of equal charge tend to repel each other in the liquid medium.

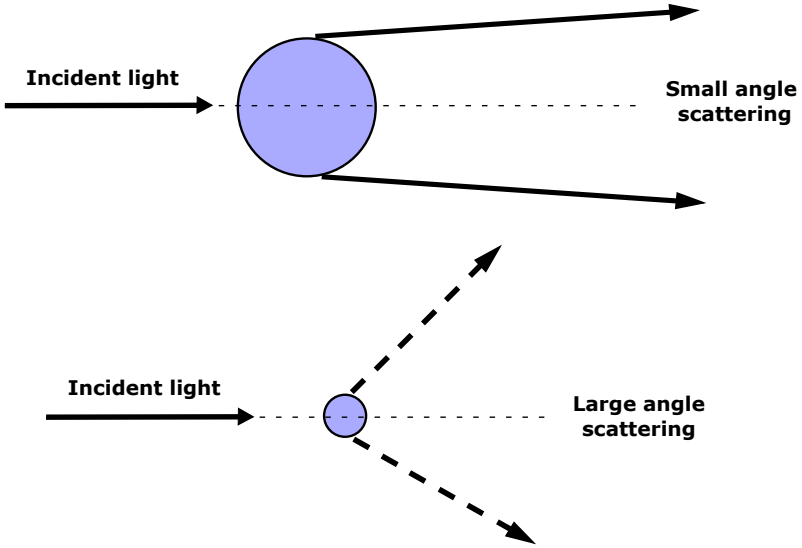

Figure 3.11: *Effect of light-scattering in the measurement of particle size via wet laser diffraction.*

The balance between repulsive and attractive forces in the dispersion determines the stability of the dispersion or tendency of aggregation, which would overcome the natural particle repulsion. The zeta potential can quantify the repulsion force experienced by approaching particles, with either −30 or +30 mV usually set as the stability limit and defined at the particle's double layer [192]. The double-layer comprises the particle's surrounding ions cloud of opposite charge linked by Coulomb interactions, which goes beyond the ions strictly bonded to the particle surface (known as Stern layer) [193, 194].

The particle size distribution can be compared through three standard diameters (D_{10}, D_{50} and D_{90}), representing the cumulative percentage of particles in the dispersion smaller than its value. For instance, 50 % of particles in a given distribution would have a diameter size smaller or equal to the obtained D_{50} value. Although D_{50} provides the strict median (average particle size in the distribution), complementary D_{10} and D_{90} diameters can give information regarding particle aggregation and the overall stability of the particles in suspension, identifying the need for surfactants or modified suspension conditions to obtain reliable size distributions.

3.3.2 Thermogravimetric analysis

Thermogravimetric analysis (TGA) is a characterisation technique that studies the mass loss of a given sample as a function of time/temperature in a controlled atmosphere. Under the effect of thermal gradients, materials experience different processes (adsorption, oxidation, sublimation [195]), which can be further understood by analysing their corresponding weight change. The simplicity of this technique allows a fully automated testing sequence of samples under various working gases (e.g. air, N_2 or CO_2).

The system consists mainly of two modules, a high precision balance and a furnace chamber. Samples are first positioned in a protected ring-shaped holder and transferred into a sample pan, weighted by the precision balance during the whole analysis. The machine automatically places the pan into the furnace, monitoring the change in weight as the temperature is raised or decreased according to the implemented annealing routine.

3.3.3 X-ray diffraction

X-ray diffraction (XRD) comprises a non-destructive characterisation technique used to identify the crystalline structure of materials. The fundamentals of XRD are based on the scattering of incident X-rays emitted from a source after reaching a sample (in single-crystal or powder form). The angle of diffracted rays will be dependent on the crystalline structure of the material, providing a series of resonance peaks depending on the constructive interference of crystallographic planes (h, k, l) in the material's lattice that satisfies a particular set of conditions.

The simplest scenario is obtained by satisfying Bragg's law equation, which comes as a simplification of Laue's general formulation [32]:

$$n\lambda = 2d \sin\theta \tag{3.5}$$

In which λ is the wavelength of the X-rays, d is the interplanar atomic spacing, θ is the angle of diffraction, and n is an integer number.

This phenomenon can be easily visualised by assuming the crystal planes in the atomic structure as optical mirrors, reflecting incident photons with an equal θ angle of reflection (Figure 3.12). In the case of X-ray diffraction, when the spacing d between crystallographic planes provides constructive interference of the incident X-rays of a particular wavelength, resonance peaks are obtained in the detector and assigned to the diffraction angle. This angle is registered as 2θ, accounting for the sum of equal angles between sample/emitter and sample/detector.

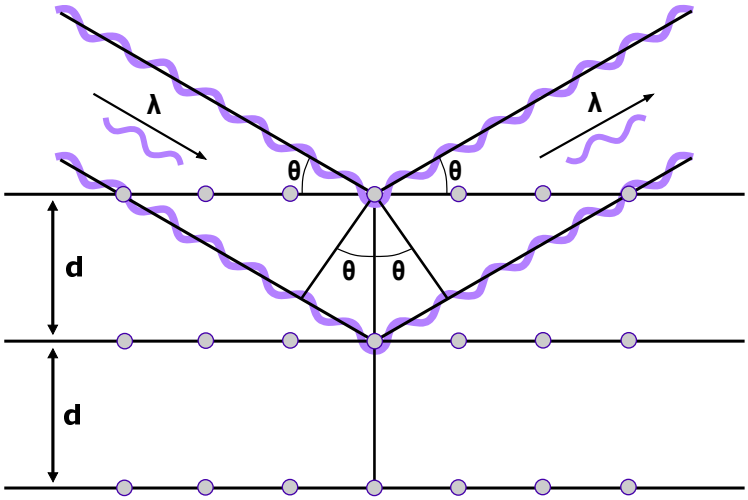

Figure 3.12: *Bragg's X-ray diffraction on a crystal lattice of interplanar spacing d, showing the constructive interference of an incident wavelength. Adapted from [32].*

By scanning a range of diffraction angles, a pattern of constructive peaks can be obtained and identified with the characteristic planes of known crystalline lattices. Comparing these patterns to reference spectra from the International Centre for Diffraction Data (ICDD) can be used to determine the composition of the material scanned and its degree of crystallinity.

3.3.4 Raman Spectroscopy

Raman Spectroscopy is a non-destructive, high-resolution characterisation technique that can provide structural and electronic information of a given material's surface. The fundamentals of Raman Spectroscopy reside in the inelastic scattering of an incident monochromatic laser beam against a sample material, with the ability to engage in vibrational modes as a function of their atom's orientation and bonding [196]. This interaction results in an energy exchange from the emitted photons to the sample, which is subjected to molecular vibrations because of the absorption of energy. These molecular vibrations highlight resonance peaks at selective wavelengths of the scattered laser. The profile obtained by these unique vibrations along the wavelength spectrum is characteristic of the material's molecular composition and can be used to identify its chemical structure.

In the case of graphene and graphitic materials, Raman Spectroscopy can provide plenty of information regarding perturbations, layers, quality and the presence of disorder and functional groups in the graphene flakes, based on the intrinsic dispersion of π electrons in the graphitic domains that induce Raman resonances [197–199]. The study of the Raman spectrum of graphite has been traditionally based on the works from Tuinstra and Koenig (1970) [200]. In their work, a single resonance was identified at 1575 cm^{-1} for single graphite crystals not affected by the degree of disorder in the sample and related to the motion of sp^2 carbon (Called G band). A

secondary band at approximately 1355 cm^{-1} (D band) is present in all other kinds of graphitic materials, requiring defects for its activation.

Studying the ratio of D and G band intensities obtained in graphene-based materials can give information regarding structural defects (by the activation of the D band) and the change in the size of the graphitic sp^2 domains. A second-order Raman scattering band ($2D$) is also present in the Raman spectra of graphene, appearing at around 2700 cm^{-1}, approximately double the frequency of the D band. Increasing the number of graphene layers leads to both a reduction in intensity and an increase in the frequency of the $2D$ shift. Studying the Raman spectrum can serve to identify the layers of graphene in the material, becoming hardly distinguishable from bulk graphite above the stacking of five graphene layers [198].

The evolution of D/G intensity ratio and G band positioning in graphene upon disordering has been based on a three-stage procedure (Figure 3.13) consisting of an initial change from graphite to nanocrystalline graphite (Stage 1), a secondary change to low amorphous sp^3 carbon (Stage 2) and a final transition from low to high amorphous sp^3 carbon (Stage 3) [33, 199]. Through this theory of amorphisation, an increase in the D band intensity of pristine graphene (thus, raising the D/G intensity ratio) would be directly associated with an increase in structural defects occurring during the first stage of annealing. During Stage 2, the disruption of sp^2 domains in the transformation to amorphous sp^3 carbon would dominate the process, lowering the D/G ratio instead.

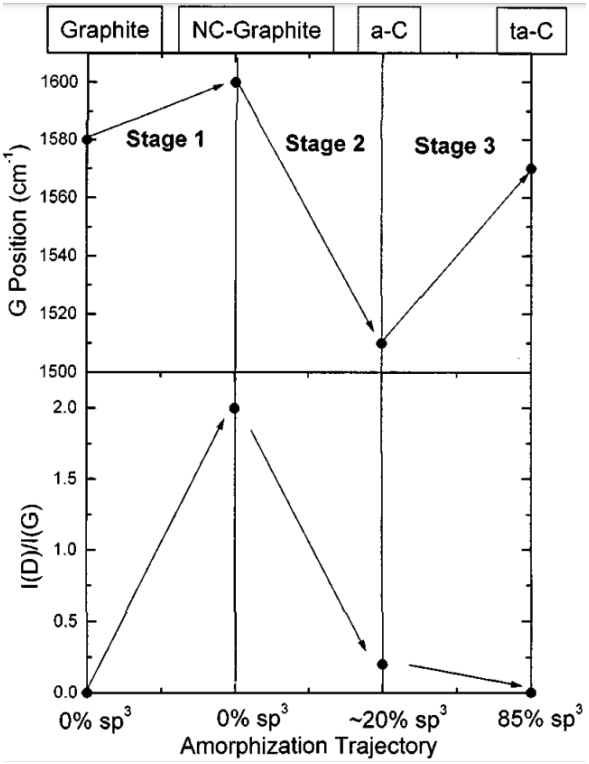

Figure 3.13: *Evolution of graphene's D/G ratio and G peak displacement upon amorphisation. From Ferrari (2000) [33].*

3.3.5 X-ray Photoelectron Spectroscopy

X-ray Photoelectron Spectroscopy (XPS) is a surface characterisation technique that can provide an extensive quantitative chemical analysis of a given material with a detailed elemental composition excluding hydrogen or helium. Through this technique, an X-ray beam is applied to the sample, inducing the excitation of electrons emitted from their corresponding orbitals and registered by a detector. The specific kinetic energy of the emitted photoelectrons can be related to the elements present in the examined material and obtaining information about the chemical bonding of these elements [201].

XPS is a powerful technique in the case of graphene-based materials obtained from graphene oxide (GO) precursors. The binding energy of the photoelectrons emitted from the carbon $1s$ (C1s) and oxygen $1s$ (O1s) orbitals can be related to the percentage of sp^2 and sp^3 carbon present in the material and identify the degree of graphitisation in the material, especially after chemical or thermal reduction processes. The deconvolution of carbon binding energies associated with the different oxidised groups present in GO sheets such as epoxide ($C-O$), carbonyl ($C=O$) and carboxyl ($O-C=O$) at approximately 286, 288 and 289 eV, respectively [141, 202] can serve to identify the degree and quality of the oxidation in the graphene-based material. XPS can also provide information about impurities in the graphene sheets arising from the synthesis method applied and its relative contribution to the general survey compared to carbon and oxygen elements.

3.3.6 Field-Emission Scanning Electron Microscopy

Scanning Electron Microscopy (SEM) is a technique for studying the microstructure and morphology of materials that substitute the illumination source and optical lens from optical microscopes with a focused electron beam [34]. The electron beam is first emitted from an electron source and accelerated at high energy. A series of apertures, magnetic lenses and electromagnetic coils focus the beam and target it onto the surface of a given specimen [203].

The interaction of beam and specimen produces multiple signals (such as secondary electrons (SE), backscattered electrons, Auger electrons, characteristic X-rays and others) collected by a specific detector, reacting to a determined energy band and converting the signal to photons. From studying these various signals, different information can be obtained from the material regarding its chemical composition or morphology at different depths. The SEM system operates under a high vacuum to avoid the interference of molecules from atmospheric gases with the electron beam, among other disturbances that can affect the scattering of electrons. A standard SEM system is comprised of the elements displayed in the schematic from Figure 3.14.

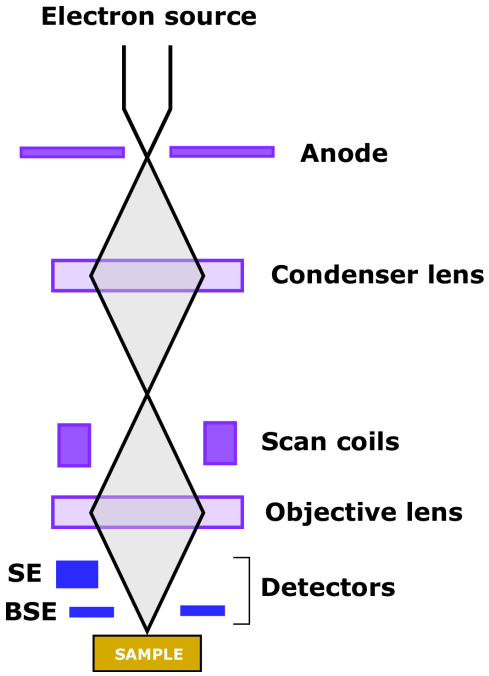

Figure 3.14: *Schematic with main components in a Scanning Electron Microscopy unit from electron emission to detection.*

Several parameters can affect both the resolution and focus of SEM images, of which the most relevant are the aperture, working distance and astigmatism. The aperture can exclude scattered electrons and control the spherical aberrations (defocus occurring at the image edges) by selecting an optimal aperture size [34]. Increasing the aperture size has a direct effect in widening the beam angle α, which reduces the depth of field (DF) or the cross-sectional width of the specimen that remains in focus. The selected working distance also affects the DF, with shorter distances widening the incident cone of electrons and reducing the DF as with bigger apertures (Figure 3.15). Tuning these two parameters is essential to identify a DF that leads to the highest resolution considering each specimen's topographical variation, with flatter topographies benefiting from shorter DF and vice versa.

Defects and contamination in column and aperture can also stretch the shape of the electron beam from the ideal circular cross-section into an elliptical one during the operation. To fix this issue, a series of coils are included in the column to work as a two-axis stigmator. The optimal beam cross-section can be attained by performing a correction cycle along the two axes, leading to the highest imaging resolution.

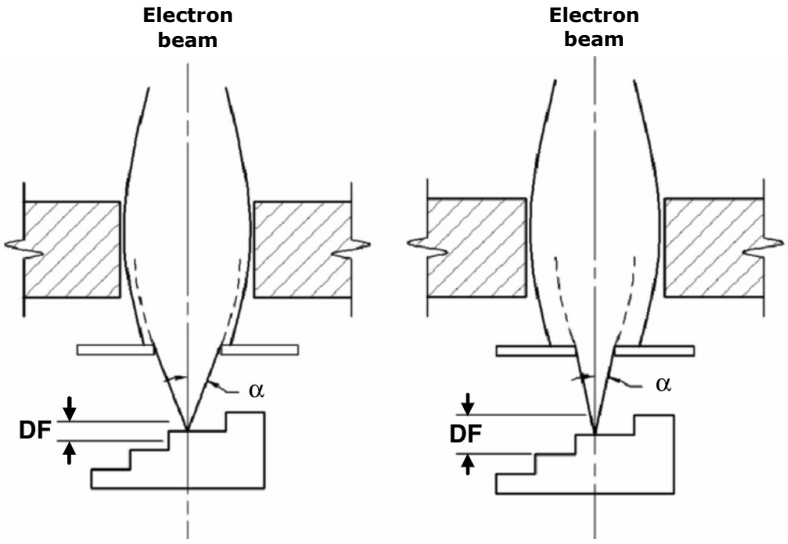

Figure 3.15: *Effect of aperture adjusting in the perceived depth of field (DF) of an SEM equipment. Adapted from Zhou et al. (2007) [34].*

3.3.7 Density measurements

Measuring the density of a material is one of the most straightforward characterisation techniques used to determine the material's properties and contrast different processing routes. However, the nomenclature behind density standards must be first understood. The basic definition of the density property consists of the mass of a material divided by the volume that it occupies. The so-called theoretical density refers to the density of the material in an absolute absence of defects and outside forces. It is generally obtained from extrapolating parameters at the atomic level. Although extremely hard to calculate for amorphous materials, it can be determined in crystalline materials by using the molecular weights and the unit cells dimensions that form the basic crystal structure, labeled (M_c) and (V_c) respectively.

$$\rho_{theo} = \frac{M_c}{V_c} \tag{3.6}$$

The actual density of any physical sample will never match the theoretical value of density due to the presence of defects and the aggregative behaviour of solid particles. A macroscopic evaluation of density can be done by measuring the apparent density or bulk density, which is obtained by dividing the mass of a given body of material (M) by the outer volume it occupies (V_{app}).

$$\rho_{app} = \frac{M}{V_{app}} \tag{3.7}$$

This measurement takes the external volume of the sample in the calculations, including all absence of material (internal voids and open pores) which was excluded from the theoretical assumption. Therefore, it can be used to determine the overall

percentage of porosity in the sample (ϵ), which is the amount of void material included in the measured volume when compared to the theoretical value of density [204].

$$\epsilon = \frac{\rho_{theo} - \rho_{app}}{\rho_{theo}} \times 100 \tag{3.8}$$

In the case of particulate solids, the particle density considers a solid particle as the minimum indivisible body of material independent of the degree of packing, representing a porosity of 0%. Knowing the particle density can be helpful in powder processing and technology to compare the experimental densities obtained through various techniques and determine the porosity of a particulate sample.

For a more precise bulk density calculation, an alternative method uses the Archimedes Principle, which relates the buoyancy, or upward force an object receives when immersed in a liquid, with the weight of the fluid displaced by the object. This principle can be used to obtain a value of density (ρ_{Arch}) based on the characteristics of the liquid, evaluating the volume of liquid displaced without measuring the volume of the immersed material as in the previous equation [205]. This shift eliminates the inaccuracies stemming from measuring the dimensions of irregular samples by using the measured dry weight of the sample (M) and comparing it to the sample's apparent weight when immersed in the fluid (M_{app}).

$$\frac{\rho_{Arch}}{\rho_{fluid}} = \frac{M}{M - M_{app}} \tag{3.9}$$

This technique, however, cannot be applied to hydrophobic materials, which comprises a significant limitation in its application. Other methods, such as helium pycnometry, can provide macroscopic density measurements close to the limit theoretical density stated above. This technique uses helium gas to fill all sample pores down to the angstrom level, later discharged to a separate chamber to determine the density of gas displaced. Combining this measurement with a precision weighing of the sample, accurate values of macroscopic density can be readily obtained.

3.3.8 Contact angle

The property of wettability can be defined by the ability of a liquid to maintain contact with a solid material in the presence of a third gaseous phase acting as the medium [206]. To evaluate the contact angle (CA) formed between two liquid and solid phases, it is first necessary to understand the general equilibrium state of any three material phases sharing a common interface (Figure 3.16). To preserve an equilibrium without one phase displacing another in this scenario, the net force along the boundary domain must be zero, which is related to the surface energy

between two phases γ_{ij} with i and j referring to any of the given (α, β, θ) angles in the schematic [207].

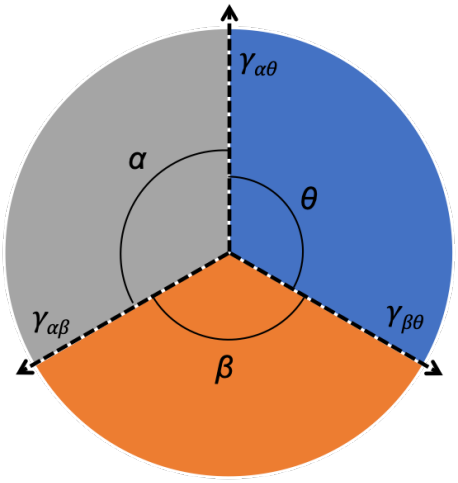

Figure 3.16: *Equilibrium of three fluids (blue, grey, orange) as a function of surface energy γ_{ij} and the angles between each biphase interface (α, β, θ).*

A set of equations can then be obtained by separating the net force into three components along the direction of each of the bi-phase interfaces [207]:

$$\begin{aligned} \gamma_{\alpha\theta} + \gamma_{\theta\beta}\cos\theta + \gamma_{\alpha\beta}\cos\alpha &= 0 \\ \gamma_{\alpha\theta}\cos\theta + \gamma_{\theta\beta} + \gamma_{\alpha\beta}\cos\beta &= 0 \\ \gamma_{\alpha\theta}\cos\alpha + \gamma_{\theta\beta}\cos\beta + \gamma_{\alpha\beta} &= 0 \end{aligned} \tag{3.10}$$

Assuming the grey, blue and orange fluids to represent a flat solid (S), a drop of liquid (L) and the gas medium (G) respectively, the β angle in both the schematic and the set of equations above equals 180°. This assumption permits simplifying the second equation as a function of the θ angle to what is known as Young's relation [208]:

$$\gamma_{LG}\cos\theta + \gamma_{SL} = \gamma_{SG} \tag{3.11}$$

The θ angle in such a case corresponds to the CA. It is defined at the intersection of the liquid/solid interface with the liquid/gas interface by drawing a tangent from the contact point along the liquid/gas interface [208]. The balance between the forces that spread the liquid droplet onto the solid surface and the cohesive forces that hold the droplet in shape determine the ability of the liquid to wet the surface.

A CA below 90° is a common indicator of favourable wetting with the surface, with the material labelled as hydrophilic if the liquid phase is assumed to be water (down to a total asymptotic wettability of 0°). Above 90°, the surface's wettabil-

ity is progressively hindered, applying the term hydrophobic instead (Figure 3.17). Surfaces exhibiting remarkably high contact angles (above 150°) are often classified as super-hydrophobic. A typical example of a super-hydrophobic material found in nature is the lotus flower [7, 59], which inspires the exploitation of self-cleaning paintings and other chemical surface treatments.

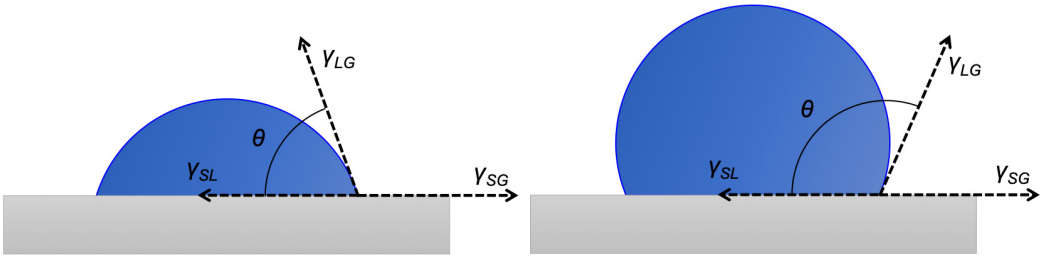

Figure 3.17: *Hydrophilic surface with a CA angle (θ) below 90° (left) vs a hydrophobic surface with θ above 90° (right).*

In practice, geometrical CAs will deviate from the theoretical angle extracted by the Young relation due to defects in the material and the effect of external forces, among other complexities. The most common method for measuring CAs is the examination of a sessile drop silhouette estimated via an optical goniometer or by image analysis [209].

Despite being widely used due to its simplicity, the sessile drop technique alone might not represent a fully stable CA. The inhomogeneities present in the material and the dependence on resting time and droplet size can acutely affect the CA extracted from static measurements alone. In this case, the obtained angles become an apparent value of CA instead of the actual CA in equilibrium. Complementary information could be obtained through dynamic CA evaluations, in which the contact line of droplet/surface is in constant motion. Studying the advancing (θ_a) and receding (θ_r) CAs by respectively injecting and extracting liquid from the droplet can produce a more accurate wettability profile [210]. A CA hysteresis (H) can be obtained from the difference of these values, a valuable parameter used to understand the effect of surface inhomogeneities and roughness under dynamic conditions.

$$H = \theta_a - \theta_r \tag{3.12}$$

3.4 Materials and composite characterisation

3.4.1 Chemical and structural characterisation

3.4.1.1 Particle size distribution

A Master-sizer 3000 from Malvern instruments was used in this work to evaluate the particle size of alumina powder by wet laser diffraction after suspension in DI H_2O. Two properties were needed beforehand to fulfil the system requirements: the material's density and refractive index. A materials database included in the software was used to obtain a preliminary refractive index of alumina.

The examined powder was first homogenised in its container to prevent heavier particles from being left at the bottom by the effect of gravity. As all measured powders were smaller than 300 μm, no additional sieving was performed. After a cleaning stage with three to five cycles of DI H_2O, including a final degassing stage, the background noise from clean DI H_2O was subtracted to compensate for errors generated from electrical noise and any dirt present in the lens.

Alumina powder was gently added to the measuring beaker to reach 20% obscuration in the water, stirring at 1200 rpm as a standard value. Ultrasonication was also applied to break the ceramic agglomerates. Two independent sets of measurements were performed for every sample, each containing at least six sequential measures performed automatically by the equipment. Various configurations of stirring and ultrasonication were tested to account for excessive aggregation or rupture of the particles, otherwise resulting in unstable sets of measurements.

3.4.1.2 Suspension viscosity

The viscosity (mPa s) of graphene oxide suspensions in water and different formulations of alumina slurries were evaluated at the Institute of Science and Technology of Carbon (INCAR) using a Fungilab rotational viscometer. A small sample adapter set was used to permit the analysis of $<$ 10 mL of suspensions with a set of three spindles (TL4, TL5 and TL6) from a low-viscosity spindle set. The temperature was kept at 20 - 22 °C throughout all tests.

After homogenisation via speed-mixing for 10 min, the suspensions were deposited in a cylindrical sample chamber and attached to the viscometer. The selected spindle was then connected to the rotor and initialised, applying a profile of rotational speeds from 0.1 to 250 rpm. The speed/spindle pairing was re-tuned until the equipment reached a torque level of 80%, registering the obtained viscosity value after stabilisation of the readings.

Due to the particulate nature of the suspensions analysed in this work, a complete profile of rotational speeds could not be obtained without compromising the stability of the suspensions. A more systematic evaluation of the rheological properties of the suspensions would require the use of a rheometer in the future.

3.4.1.3 Thermogravimetric analysis

The weight loss of ceramic and graphene-based materials was studied by thermogravimetric analysis on a Mettler Toledo TGA/DSC 3+. Alumina crucibles (Alox, 70 μl) were used to load the samples in the main chamber, aiming for a target sample mass of 11 mg in the crucible. However, due to some materials of extremely low density (e.g. reduced GO aerogels) not reaching this value, a minimum lower limit of 3 mg per sample was later established.

The experiment routines were built in the software editor, tailoring the target temperature, heating rate and working gas (either air or N_2) of the desired cycle. Unless otherwise stated, all tests were performed up to 1000 °C under a 5 °C min^{-1} heating rate [211] with an average of three measurements per sample. After completing the cycles and removing the alumina crucibles for cleaning, all data was extracted and re-plotted using *Origin* software.

3.4.1.4 X-ray Diffraction

Graphene-based materials and alumina powder were characterised by XRD using a Siemens Diffraktometer D5000. The sample powder was first ground on a mortar and compacted in a sample holder. The loaded holder was inserted in the chamber, fastened at the centre of rotation of the main moving platform that provides the diffraction angle. The crack-width of the system was adjusted using different gratings (0.6 - 2 mm) to tune the registered intensity at higher angles.

The scanning routine was performed on a 5 – 90° range for the 2θ angle reached through 0.02 step increments. The resulting XRD spectra were refined using Highscore Xpert software. Outlier resonances were initially removed, reducing the background noise by applying a bending factor of 5 in a standard correction and smoothing the signal. The most representative features of the plot were then highlighted through an embedded peak-search option. By comparing the corrected XRD spectra with the software data source (reference patterns from the ICDD database), the materials' crystallographic phases could be identified according to the percentage of affinity calculated by the software. The obtained XRD spectra were then re-plotted using *Origin* along with the reference patterns selected.

3.4.1.5 X-ray Photoelectron Spectroscopy

The chemical composition of graphene-based materials was characterised by X-ray Photoelectron Spectroscopy (XPS) on a Thermo Fisher Scientific K- alpha+ spectrometer at Cardiff University's School of Chemistry with the help of Dr David Morgan. Samples were analysed using a micro-focused monochromatic Al X-ray source (72 W) using the '400-micron spot' mode, providing an analysis defining elliptical X-ray spot of approximately 400 × 600 μm. The collected data was recorded at pass energies of 150 eV for survey scans and 40 eV for high-resolution scans with 1 eV and 0.1 eV step sizes, respectively. The charge neutralisation of the sample was achieved using a combination of both low energy electrons and argon ions.

Data analysis was performed in CasaXPS after calibrating the data to the lowest C1s component taken to a value of 284.5 eV for graphitic carbon. Quantification was made using a Shirley type background and Scofield cross-sections [212]. Supporting post-processing of the XPS spectra of graphene-based materials and the deconvolution of the signals was performed by Dr Ignacio Villar using CasaXPS software. All the spectra were later re-plotted using *Origin*.

3.4.1.6 Density measurements

The apparent density of produced aerogels and composite materials was evaluated by dividing each sample's weight by its measured external volume. The weight was obtained with either an OHAUS Explorer EX 423 or a 5-digit Precisa balance 40SM-200A. The volume was calculated by measuring the sample dimensions with an RS PRO 0.01 mm digital calliper, using 3-point averages for every dimension. In the case of irregular shapes, the closest simple geometrical shape was assumed (e.g. cylinders in the case of freeze-cast aerogels produced using cylindrical Teflon moulds).

Apparent densities were registered for produced graphene aerogels to study the effect of freeze-casting and thermal annealing. This density evaluation's simplicity and quick repeatability facilitated an easy comparison between different source materials and parameters to select the adequate conditions in the process.

Helium pycnometry was additionally performed at INCAR Institute to calculate the real density of commercial alumina powder on an AccuPyc 1330 pycnometer. 600 mg of sample were weighed on a precision plate and inserted on a cell of 3.06 cm^3 volume. The sample volume in the unit was measured by helium displacement, performing an average of 20 purge runs, after which the volume of the powder was accurately measured.

Sintered alumina samples were studied through Archimedes density measurements with the help of Mr Joseph Alemzadeh, using a Sartorius YDK 01 kit to determine porosity levels. A schematic of the setup is provided in Figure 3.18.

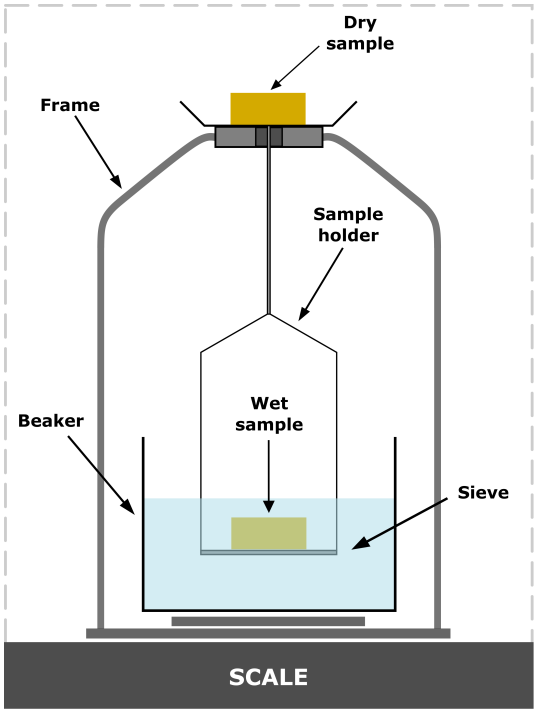

Figure 3.18: *Diagram of an Archimedes density measurement kit, used for determining the porosity (ϵ) of ceramic materials.*

The beaker in the balance (4-digit LA310S Sartorius) was preliminarily filled with DI H_2O, registering the dry weight of the measured samples (M) on the sample holder's plate on top of the balance. The specimens were then deposited on the immersed sieve to measure the apparent weight in the water (M_{app}), carefully avoiding the formation of bubbles arising from the air removal within the sample's pores. For every sample, the water temperature was registered with a temperature probe and used to obtain the precise density of DI H_2O (ρ_{fluid}) from reference tables provided by the manufacturer.

3.4.1.7 Contact angle measurements

Spin coating of graphene oxide films

GO-based films were first produced by spin coating on a Laurell Spin coater WS-650-23 unit. The films were produced by Mr Thomas Kynaston during his CUROP summer placement in 2019 (co-supervised by the author) via the spin coating technique, with drops of GO suspension spread on a thin homogeneous layer on top of a substrate. Substrates were cut from a silicon wafer using a straight diamond-tipped scribe (RS Pro), maintaining a minimum surface area of 10×10 mm^2 to prevent the material from entering the vacuum pump during spin coating. The substrates were attached to the spin-coater platform and held in place by the equipment's vacuum system.

40 mL of water-based GO slurry (0.37 wt.% GO) were prepared and speed-mixed for 12 minutes at 1950 rpm. The suspension was dropped on the silicon substrates using a 100 μl micropipette, initiating the spin-coating process with 1 minute of total duration, 3500 rpm of spinning velocity and acceleration of 3500 rpm s^{-1} to ensure good coverage of the substrate. The continuity of produced GO films was later verified using optical and scanning electron microscopy.

Partial thermal reduction of spin-coated GO films was applied using a secondary tubular furnace (Carbolite Gero 30-3000 °C series) with an alumina tube under vacuum. To preserve the integrity of the films, the cycle consisted of three isothermal stages (100, 250 and 400 °C), reached at 2.5 °C min^{-1} rates, and maintaining a 30 min dwelling time between each segment. The selection of this annealing cycle for spin-coating films is discussed in more detail in Chapter 4.

Optical tensiometer

Contact angles (CA) between drops of ceramic slurry and spin-coated GO films were evaluated at Cardiff University's School of Dentistry using an Attension Theta Lite optical tensiometer along with OneAttension software. A sessile drop technique was selected as the CA measurement mode due to its simplicity and ease of operation, understanding the constraints of this technique already defined in Section 3.3.8. In sessile drop mode, a single drop of liquid was poured on the substrate surface with the static CA value registered every 0.05 seconds.

200 and 300 μl plastic tips were used to deposit the suspension droplets with an automatic dispenser. The equipment was calibrated with a certified calibration ball, verifying the camera focusing on the edge of the ball. A stable drop was produced and held once the dual dispenser was filled with the suspension until the tensiometer camera validated its shape (Figure 3.19a). Additional focus could be performed on this step to ensure the correct measuring of the drop. The dispenser was then pressed down and released immediately, depositing the droplet and enabling the physical measurements of the angle between the substrate and the liquid (Figure 3.19b). A time range of 30 seconds was selected as a baseline for every test. After completion, the measured CA right and left angles with the corresponding deposition times were extracted and re-plotted using *Origin* software.

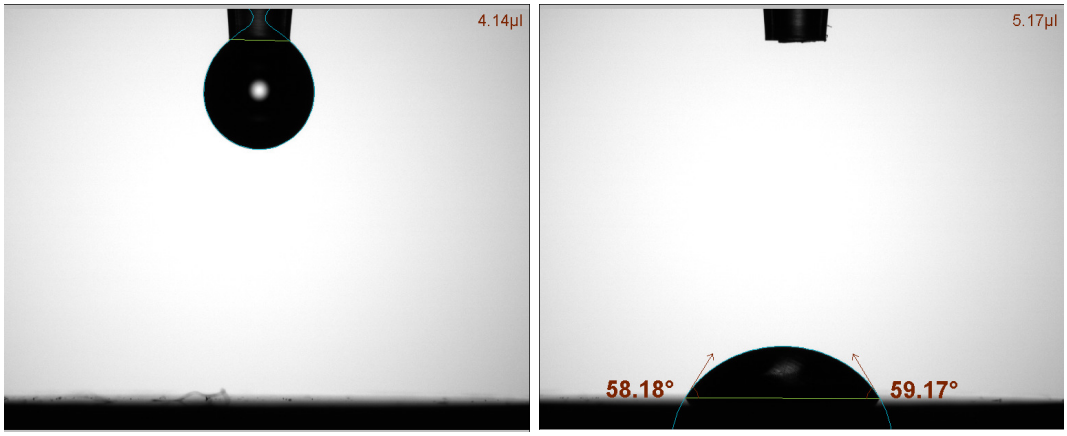

Figure 3.19: *Example of wettability test using a water droplet over a titanium substrate.*

3.4.1.8 Raman Spectroscopy

Spin-coated GO films from the previous section were characterised on a custom-made Raman setup providing flexibility and highly accurate results at the expense of more complex tuning and data post-processing (Figure 3.20). Raman measurements on this equipment were performed with the help of Dr John Haden, requiring extensive fine-tuning of several parameters, such as laser source, polarisation and noise reduction. The resulting signals were converted into the characteristic frequency vs intensity of Raman plots with *Origin* software.

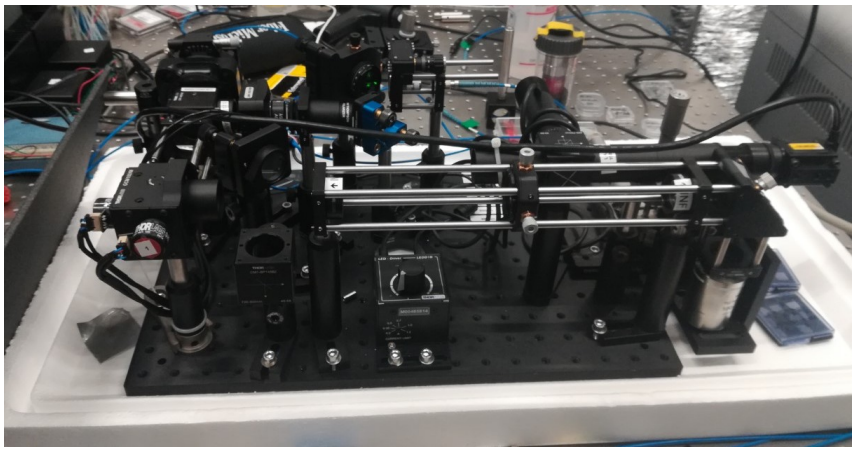

Figure 3.20: *Custom-built Raman equipment used for spin-coated graphene-based films.*

As a general guideline, the spectrometer settings consisted of laser power of 0.37 mW, a 100 μm input slit, a grating of 600 l mm^{-1} and 10 seconds exposure. Two acquisitions were stacked together for each measurement following a 'Step and glue' function on 530 – 660 nm. Laser polarisation was not deemed a crucial parameter after testing parallel and cross-polarization on the same sample, using the former

throughout all the experiments. Due to physical constraints in the sample holder, only films could be analysed with this equipment, which motivated the use of a second unit to characterise $3D$ graphene-based aerogels.

Raman Spectroscopy of graphene-based aerogels was additionally performed at Cardiff University's School of Chemistry using a commercial Renishaw inVia unit in conjunction with WIRE 3.4 software. A 514 nm laser with standard grating was selected. The samples were put in a holder and fixed in the inbuilt platform, focused by activating a green laser up to 0.05% power to prevent damage to the sample.

After focusing and positioning the sample, the spectral acquisition was performed by either dynamic or static analyses (referring to the whole spectrum or selected portions highlighting specific features, respectively). Due to the D, G and $2D$ shifts studied in carbon-based systems being relatively further apart in the spectrum, dynamic analyses were applied, adding selective static runs to provide quicker measurements of higher precision.

The fine-tuning of acquisition parameters was crucial to maximise the quality of results obtained, including the sample's exposure time to the laser, the number of run accumulations (which can enhance the signal to noise ratio) and the laser power percentage. The defined standard procedure included an exposure time of 10 sec, three accumulations per sample and a laser power of 5%. The effect of cosmic rays was also removed to obtain a cleaner spectrum. All obtained Raman spectra were extracted and replotted using *Origin* software.

3.4.2 Microstructural characterisation

3.4.2.1 Optical microscopy

Optical examination of GO flakes and graphene/epoxy composites was performed on a Leica DM LM microscope with an IDS UI-1460LE-C camera. Samples were placed on a glass slide and initially focused at 5× magnification, extended to 10×, 20× and 50× for imaging at higher precision. Although this microscope permitted modifying the polarisation of the light source, a 90° configuration was maintained for every use. All images were captured and pre-processed using OmniMet 10.0 software, applying a min-max contrast optimisation to highlight the sample features.

The pictures obtained through OmniMet were further analysed using *ImageJ* software. This free image processing tool was used to evaluate the size/area of different particles and samples and include scaling bars, performing additional brightness, contrast and colour corrections where necessary. Elliptical fitting (A tool embedded in the *ImageJ* package) was used for measuring the lateral size of graphene flakes from diluted GO suspensions.

3.4.2.2 Field-emission Scanning Electron Microscopy

The Field Emission Scanning Electron Microscopy (FESEM) pictures presented in this work have been obtained using a ZEISS 1540 XB microscope. Before insertion in the SEM transfer module, samples were tightened to a sample holder using stainless steel round stamps as support and sticky carbon tape when needed. After verifying a 10^{-6} mbar system vacuum and a 10^{-10} mbar gun vacuum, the sample holder was carefully transferred to the main chamber using an attachable steel rod, which was later unscrewed and retracted to isolate the main chamber again. A final 30 – 60 second purge ensured vacuum restoration, completing the sample loading process.

A target voltage of 5 – 10 kV was selected for the EHT (electron high tension) source. Sample positioning was needed to align the beam and the sample under two camera angles and determine a preliminary working distance, performed by rotating and displacing the holder using a joystick control. Once the sample was lined up with the EHT beam, a detector (SE2 or In-lens in this work) was selected according to the material characteristics and desired output. The beam wobbling was enabled to align the aperture and prevent shifts during focusing. Focus and astigmatism were gradually adjusted for each picture, correcting brightness and contrast for best results. As a general guideline, most images were obtained using a beam voltage of 5 kV, an In-lens detector and a 5 mm preliminary working distance.

3.4.3 Electrical Characterisation

The electrical conductivity of graphene/epoxy specimens was calculated at INCAR Institute in similarity with other reported works in the field [182, 213, 214]. The measured specimens were first polished and fixed to a custom-built holder between two electrical contacts wrapped on conductive copper wires. The conductivity equation was derived from the combination of Ohm's law and the material's resistivity ρ (Ω m) as a function of its cross-section (A) and the measured resistance (R) to electrical current flow through a given distance between two points (L).

$$\begin{aligned} V &= IR \\ \rho &= \frac{RA}{L} \end{aligned} \tag{3.13}$$

The conductivity per length unit σ (S m^{-1}) was calculated as the inverse of the obtained resistivity value, providing the general relationship:

$$\sigma = \frac{IL}{VA} \tag{3.14}$$

A current of 0.024 A was continuously circulated through the specimens. The

voltage between two points at L distance (generally fixed at 0.95 cm unless working on samples of smaller dimensions) was measured with a digital benchtop multimeter using two needle probes on both ends of the specimen. The cross-sectional area of the sample was measured with an RS PRO 0.01 mm digital calliper and calculated by 3-point averages of width and height dimensions. The obtained electrical conductivity values were averaged on three specimens from the same composition.

Chapter 4

Self-supporting graphene-based aerogels

4.1 Introduction

Hierarchical graphene-based aerogels exhibit great potential for many applications such as absorbents, Joule effect heaters or filtration devices [215] owing to graphene's flexible and ultra-light structure. Recently, graphene aerogels produced from various precursors (few-layer graphene (FLG) or graphene oxide (GO)) have been explored as a reinforcement/supporting phase in composites, providing electrical conductivity while increasing the mechanical strength and toughness of the material [18, 73].

The production of graphene-based aerogels below 10 mg cm^{-3} has been readily achieved through freeze-casting of colloidal GO suspensions, exhibiting interconnected channels of 10 – 100 μm widths as a function of the freezing rate applied [152, 177, 216]. However, adjusting the aerogels' dimensions, apparent density and microstructure obtained via freeze-casting is required before integrating a secondary ceramic phase and manufacturing a novel composite.

This chapter comprises the first step in the proposed strategy for graphene/ceramic composites, targeting the systematic production of self-supporting interconnected graphene aerogels via freeze-casting and carbonisation and their potential for scalability (Figure 4.1). The role of the GO precursor in flake lateral size, rheological behaviour and stability of the suspension has been evaluated, implementing several characterisation techniques to study water-based GO suspensions (CU_GO and ICL_GO) produced from natural graphite with two different particle sizes.

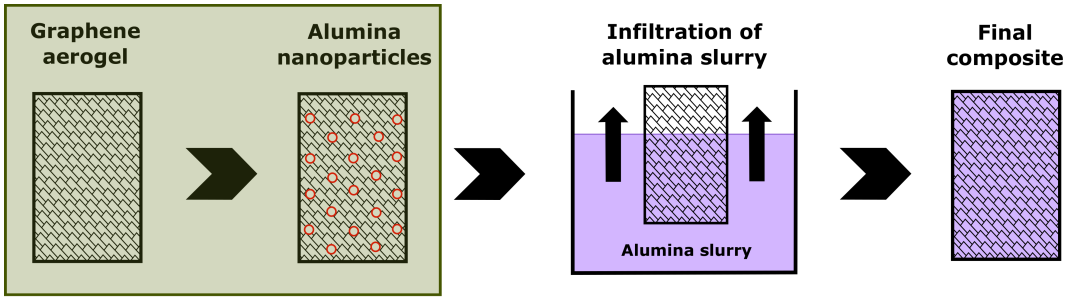

Figure 4.1: *First stage of the composite processing strategy: the production of graphene aerogels and the decoration with alumina nanoparticles.*

The design of an environmentally-friendly route to decorate graphene scaffolds with alumina nanoparticles (NPs) was also explored, extending the hierarchy of the material. High control of the alumina NPs morphology and crystallinity can be obtained by selecting a sol-gel synthesis approach, allowing for flexibility and high purity. In this work, the use of a relatively novel precursor, aluminium-L-lactate [190], has been explored based on its non-toxicity, compatibility with a pure water-based procedure and overall cost reduction.

4.2 Methodology

4.2.1 Preparation of water-based graphene-oxide suspensions

Average lateral sizes of GO flakes from CU_GO and ICL_GO suspensions were obtained through a combination of optical microscopy and *ImageJ* by the elliptical fitting of an average of 100 single flakes after discarding bigger agglomerates. 1 wt.% CU_GO and 0.6 wt.% ICL_GO suspensions were first diluted to 500 ppm in isopropanol to disaggregate the flakes and drop-cast on silicon substrates, previously cleaned by 10 min ultrasonication cycles in isopropanol and DI H_2O.

0.5 wt.% CU_GO suspensions were frozen and freeze-dried for 48 hours to produce a solid material (CU_GO_{fzd}), characterised before and after thermal reduction at 900 °C through X-ray Diffraction (XRD), Raman Spectroscopy, X-ray Photoelectron Spectroscopy (XPS) and Thermogravimetric Analysis (TGA). Equipment descriptions and characterisation procedures for these techniques have been presented in Chapter 3.

1 wt.% CU_GO and 0.6 wt.% ICL_GO slurries were diluted in batches of 20 to 80 mL of DI H_2O to 0.25 and 0.5 wt.% GO concentration. 10 wt.% solution of polyvinyl alcohol (PVA) in DI H_2O and pure sucrose powder were added as a binder and enhancer of surface properties respectively based on the total solid content of GO in a 0.5:0.5 ratio [94, 177, 183]. The resulting suspensions were speed-mixed at 1950 rpm for 10 minutes to provide homogeneous mixing and air bubble removal.

The viscosity of diluted *CU_GO* and *ICL_GO* suspensions was measured at 5 - 250 rpm with an average spindle torque of 50 – 80% at 20 °C.

4.2.2 Production and characterisation of graphene aerogels

2 - 5 g of *CU_GO* and *ICL_GO* suspensions were freeze-cast in Teflon moulds, tuning three primary parameters: GO concentration in suspension (0.25 and 0.5 wt.% in water), applied freezing rate (2 – 10 °C min^{-1}) and the ratio of PVA/sucrose additives to GO content in suspension (0 and 50 wt.%). Once frozen, each sample was carefully detached from the moulds and freeze-dried for 48 - 96 hours, depending on sample volume. The obtained freeze-dried aerogels (labelled CU_GO_{ag} and ICL_GO_{ag}) were measured in size and apparent density, assuming a cylindrical shape and averaging four samples produced from the same batch.

CU_GO_{ag} and ICL_GO_{ag} were reduced by thermal annealing on a tubular furnace up to 900 °C under argon atmosphere, evaluating their apparent density and volumetric shrinkage. The alignment and internal structure of reduced aerogels (CU_rGO_{ag} and ICL_rGO_{ag}) were studied under Field-emission Scanning Electron Microscopy (FESEM).

Epoxy/rGO composites were produced by epoxy infusion of CU_rGO_{ag} and ICL_rGO_{ag} samples left to dry for a minimum of 48 hours to cure the epoxy. Prismatic specimens (approximately 15 × 10 × 4 mm^3) were cut using a diamond saw to measure the electrical conductivity of the composites, with an average of three measurements taken for each condition.

4.2.3 Synthesis of alumina nanoparticles for decoration of graphene-based aerogels

Aluminium hydroxide gels were first produced by adding 1.238 g of aluminium lactate (95% purity) in powder form to a 50 mL glass beaker containing 20 mL of DI H_2O to achieve a 0.2 M solution. The mixture was then magnetically stirred at 300 rpm for 30 min, raising the pH to 10 by dropwise NaOH (1 M) additions. After ageing at 50 °C for a minimum of 24 h, the obtained $Al(OH)_3$ gels were frozen and freeze-dried for a minimum of 48 h to eliminate water present in the sample, later characterised through TGA and XRD after thermal annealing at 900 °C for 1 h.

As-prepared aluminium hydroxide gels were added to 0.5 wt.% *CU_GO* suspensions by dropwise addition, speed-mixed for 10 minutes to enhance homogenisation. A range of $CU\_GO/Al(OH)_3$ aerogels were produced by freeze-casting, labelled as $CU\_GO_{ag}(nN)$ based on the alumina/carbon (Al_2O_3/C) ratio n in the aerogel found by XPS analyses and N symbolising the nanoparticle decoration. The same procedure disclosed for standard CU_GO_{ag} and ICL_GO_{ag} aerogels was followed, in-

cluding freeze-drying and thermal annealing at 900 °C. The nanoparticle decoration and structural integrity of the $CU\_rGO_{ag}(nN)$ aerogels were examined via XPS and FESEM characterisation.

For comparison purposes, rGO/alumina aerogels ($CU\_rGO_{ag}(US\text{-}N)$) were produced by diluting 20 wt.% commercial alumina nanoparticle suspensions to 2 wt.% in DI H_2O to reduce agglomeration and added dropwise to 0.5 wt.% CU_GO suspensions mirroring the previous procedure. The mixtures were speed-mixed for 10 minutes, following a similar freeze-drying and thermal annealing process to obtain an equal distribution of particles in the graphene flakes. $CU\_rGO_{ag}(US\text{-}N)$ were examined via FESEM and compared with previous $CU\_rGO_{ag}(nN)$ aerogels with the as-synthesised nanoparticles.

4.3 Graphene oxide as graphene precursor for composites

4.3.1 Characterisation of graphene oxide

The selected GO precursors (CU_GO and ICL_GO) were first studied through elemental analysis to highlight the intrinsic differences between the two, additionally comparing their GO lateral flake size in suspension. The elemental analysis performed on each GO precursor after freeze-drying (CU_GO_{fzd} and ICL_GO_{fzd}) is displayed in Table 4.1, disclosing potential differences in the synthesis method for each suspension.

Table 4.1: *Elemental analysis of CU_GO_{fzd} and ICL_GO_{fzd} precursors (at.%).*

Sample Id	**C**	**O**	**N**	**S**	**H**
ICL_GO_{fzd}	46.34	39.76	1.60	1.78	2.57
CU_GO_{fzd}	41.71	46.33	0.93	1.34	2.99

The extent of oxidation in ICL_GO_{fzd} appeared slightly higher than in CU_GO_{fzd}, because of the change in the atomic C/O ratio from 1.16 to 0.90, respectively, indicating a lower presence of oxygenated groups in GO. This ratio is commonly found around 1 to 4 in the literature for GO materials [140, 216, 217], expecting some degree of variability arising from the inhomogeneous structure of GO that is dependent on selective oxidation during its synthesis. Being in the lower end of C/O ratio ranges from the literature, this analysis confirmed that both CU_GO and ICL_GO suspensions had been oxidised to a greater extent than GO precursors previously reported. The nitrogen and sulphur impurities found in the analysis were expected from the same oxidation process during GO synthesis [143]. However, the impurities content appeared slightly reduced in the commercial CU_GO suspension compared to the ICL_GO obtained by the custom improved Hummers method.

The GO flake size comparison between CU_GO and ICL_GO precursor suspen-

sions is presented in Figure 4.2. The optical microscope polarisation was adjusted to ensure the highest contrast between single flakes and the silicon background (Figure 4.2c,d). This background threshold was amplified using *ImageJ* to detect each single GO flake and perform an elliptical fit, relating the ellipses major axes to the lateral size of the flakes. Understanding the flakes' expected morphology was essential to correctly tune the size and circularity parameters during the elliptical fit (Figure 4.2e,f). The contrast grading of the flakes in the original pictures also served as a tool to identify single flakes, including holes and discarding agglomerates [141, 218, 219].

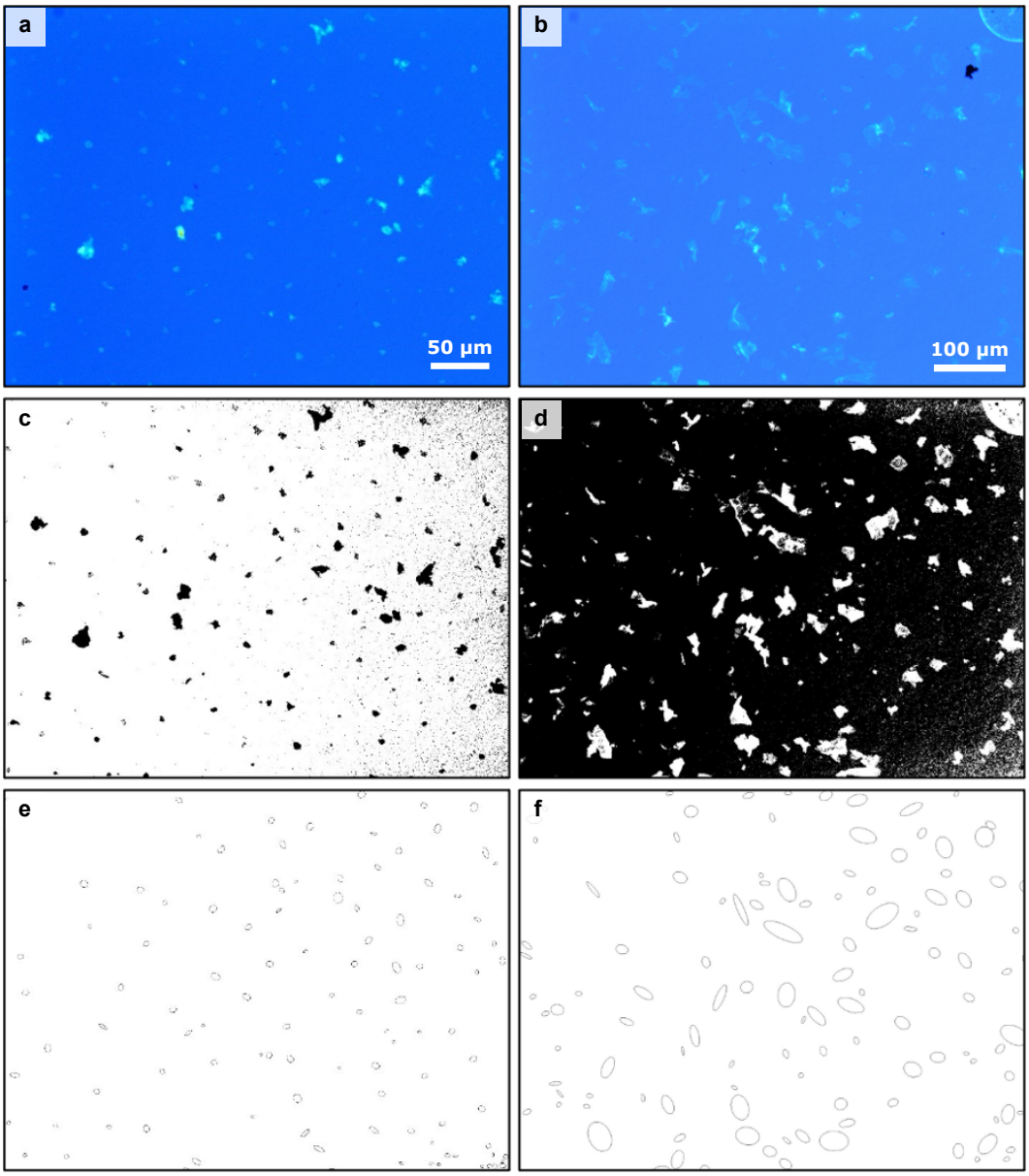

Figure 4.2: *a,b) Images of GO flakes dispersed on IPA and deposited on a silicon substrate by optical microscopy. c,d) ImageJ processing maximising image contrast. e,f) Elliptical fit of single-layer flakes detected (left column: CU_ GO percursor, right column: ICL_ GO precursor).*

ICL_ GO lateral flake size was found four times higher than *CU_ GO*, obtaining

31.6 and 7.2 μm, respectively on each precursor. Larger GO flake sizes are known to trigger the nematic liquid crystal behaviour at reduced concentrations in the suspension, while smaller flakes may require higher concentration levels [136]. Larger GO flakes are also linked to positive effects in graphene-based materials' expected mechanical, electrical, and optical properties once integrated with a secondary phase [130]. ICL_GO appeared a clear better candidate as a GO precursor for such reasons. However, due to the limited availability of custom-made ICL_GO suspension, commercial CU_GO was used throughout the project for early testing and optimisation, upgrading to ICL_GO after settling the processing conditions.

Various characterisation techniques were employed to study the structure and composition of freeze-dried GO sheets, which compose the building blocks of the water-based precursor suspensions. The changes occurring in the graphene oxide structure after thermal annealing at 900 °C were also analysed. For these characterisation tests, freeze-dried CU_GO suspension (CU_GO_{fzd}) was used as the reference material.

The analysis of the XRD spectra of freeze-dried GO before and after annealing at 900 °C (CU_GO_{fzd} and CU_rGO_{fzd}) verified a shift from a sharper 2θ peak at the 11 ° mark into a broader peak at 23 - 25 °, respectively, indicating a reduction in the interplanar spacing of the layers arising from the partial elimination of functional groups from the graphene oxide sheets. (Figure 4.3). This increase in diffraction angle verified the beginning of planar sp^2 carbon restoration in the material, with the 2θ values found in agreement with the literature [153, 216, 220].

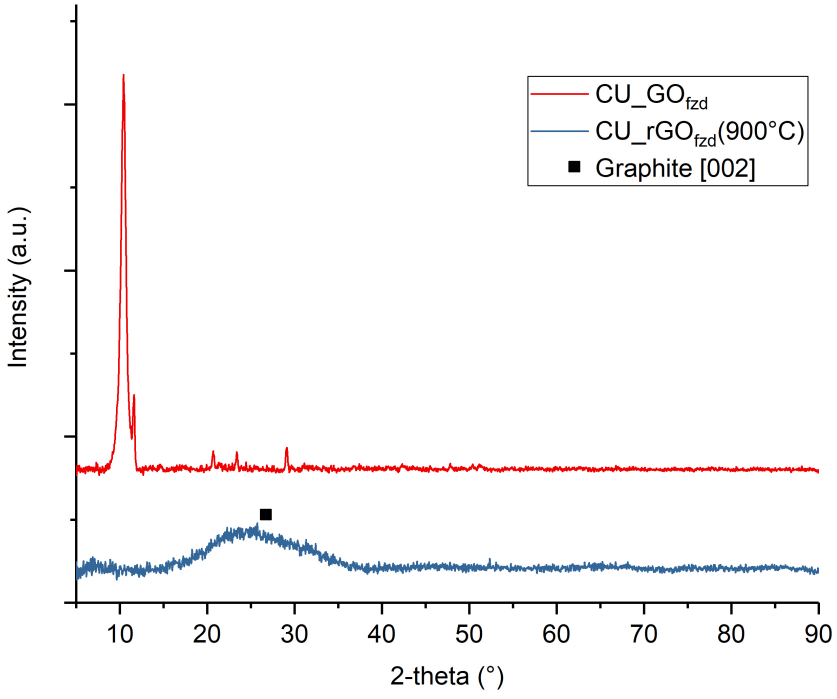

Figure 4.3: *XRD spectrum of CU_GO_{fzd} vs CU_rGO_{fzd} annealed at 900 °C, compared with the characteristic [002] peak of graphite.*

The lower intensity and broadening of the peak's FWHM (full width at half maximum) from CU_rGO_{fzd} confirmed a lower degree of crystallinity, although closer to the characteristic graphite peak at 26.5 ° corresponding to the [002] plane of the aromatic rings, confirming the $\pi-\pi$ stacking of the sheets [153]. Extending the annealing conditions up to 2000 °C can induce the graphitisation of the material, decreasing the obtained FWHM until obtaining a pattern resembling crystalline graphite. However, the low temperature of annealing selected (900 °C) only corresponds to the start of the carbonisation process.

CU_GO_{fzd} and CU_rGO_{fzd} were further analysed under Raman Spectroscopy (Figure 4.4). G and D shifts (corresponding to the sp^2 graphitic peak and the defect-activated band, respectively) were compared to study the effect of carbonisation and presence of defects and the characteristic second order $2D$ band appearing between 2500 and 3000 cm^{-1} [197]. D and G bands were obtained at 1354 and 1588 cm^{-1}, obtaining a ratio of intensity peaks between D and G shifts (from now on D/G ratio) of 0.85, with the $2D$ band around 2800 cm^{-1}. An upward trend was found in CU_GO_{fzd} intensity when increasing frequency along the X-axis. This trend was attributed to fluorescence properties of GO, which have been previously reported in the visible and infrared range [221] and can increase the perceived Raman intensity. The fluorescence effect was corrected for displaying purposes by subtracting a spectrum baseline created using ORIGIN software.

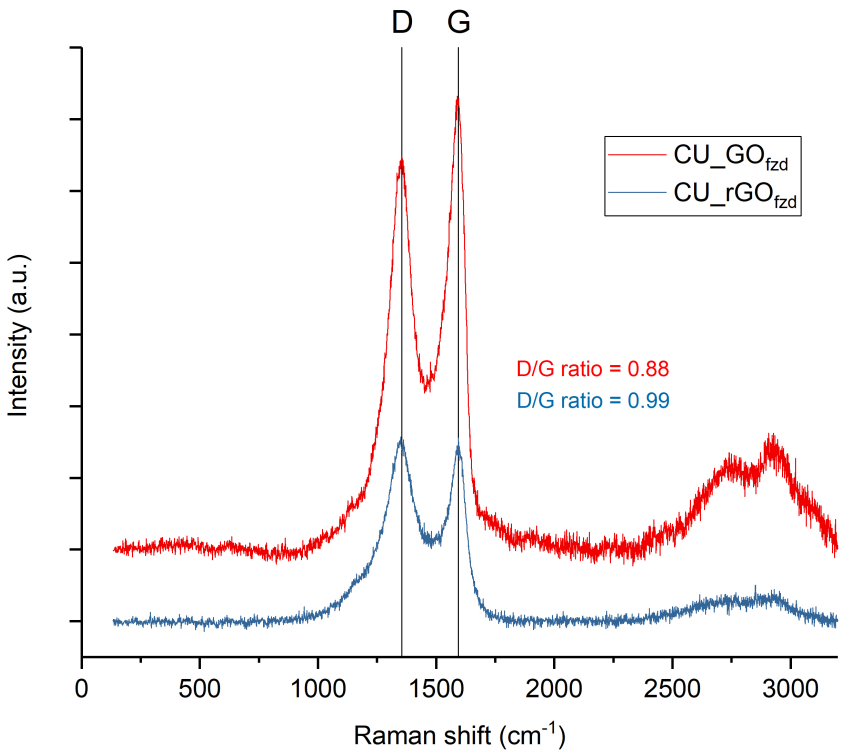

Figure 4.4: *Raman measurements for CU_GO_{fzd} and CU_rGO_{fzd} (annealed at 900 °C) displaying the D and G peaks with the measured D/G intensity ratio.*

D and G peaks in CU_rGO_{fzd} appeared at 1358 and 1597 cm^{-1}, with the dis-

placement of 9 cm^{-1} in the G band relating to the transition from amorphous carbon to the partial restoration of the graphitic domains. A slight increase in the D/G ratio from 0.88 to 0.99 was obtained for CU_rGO_{fzd}, along with an increase in the $2D$ second-order band associated with the D shift. This is in accordance with the expected behaviour after thermal annealing [140, 152, 153], although not sufficient to understand the structural changes undergone by the GO precursor. Some degree of D and G peak sharpening associated with GO reduction could be expected, as reported in the literature [152], but it was not confirmed through these measurements.

As CU_GO_{fzd} carbon structure is already disordered and predominantly in sp^3 hybridisation, the thermal reduction was expected to partially restore sp^2 graphitic domains competing with the formation of structural defects in the GO sheets (increasing the D/G ratio backwards to the graphene amorphisation theory from Ferrari and Robertson (2010) shown in Figure 3.13 [33]).

The composition of CU_GO_{fzd} and CU_rGO_{fzd} was additionally studied by XPS to expand upon the information obtained from previous Raman measurements and understand the nature of functional groups in the GO surface (Table 4.2). The high oxygen content of CU_GO_{fzd} relates to the functional groups present in the oxidised graphene sheets, predominantly in the form of epoxide ($C-O$), carbonyl ($C=O$) and carboxyl ($O-C=O$) groups [20, 22]. As these functional groups were removed from the main GO sheet via thermal annealing in CU_rGO_{fzd}, the C:O ratio evolved from 2.35 to 48.8. The remarkably high C:O ratio obtained after annealing shows one advantage of using temperature-driven reductions, as chemical reductions performed via hydrazine agents do not generally exceed a C:O ratio of 10 [127].

Table 4.2: *GO composition before and after thermal annealing at 900 °C obtained from a general XPS survey (at.%).*

Sample Id	**C**	**O**	**S**	**Si**	**Na**
CU_GOfzd	69.1	29.4	0.4	1.1	0.1
CU_rGOfzd	97.5	2.0	0.3	0.1	0.1

From the mix of sulphuric acid and sodium nitrate employed to oxidise graphite in a Hummers based GO synthesis, traces of sulphur and sodium impurities were expected to appear in the exfoliated GO flakes despite the applied cycles of centrifugation and washing [143]. In the CU_GO_{fzd} sample, a slight increase of silicon material was detected, which may be attributed to original impurities from the natural graphite used as a carbon source [222]. Selecting a bulk graphite precursor of higher quality grade could also increase the quality of the GO obtained. However, this would incur excessive costs, while the impurities found only represented a marginal contribution in the composition.

The different chemical states of C1s spectra were analysed to determine the oxidised carbon species present in the graphene sheets and the carbon hybridisation

state (Figure 4.5). Examination of the C1s spectra of CU_GO_{fzd} confirmed an increase in the sp^2:sp^3 hybridisation ratio from 0.48 to 6.68 after reduction at 900 °C. Significant depletion of epoxide, carbonyl and carboxyl groups attached to the graphene sheets (obtained at 286.0, 287.0 and 288.6 eV, respectively) was also confirmed as derived from the oxygen reduction in Table 4.2. It also established the partial restoration of the graphitic structure in CU_rGO_{fzd} from the original graphite precursor previously indicated by XRD and Raman measurements.

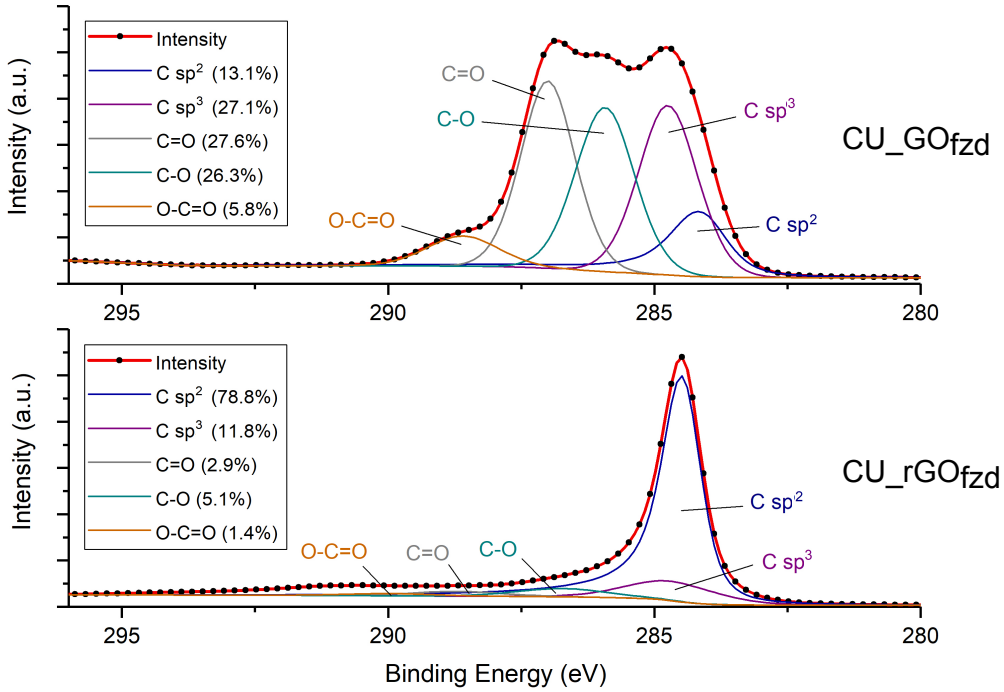

Figure 4.5: *Comparison of XPS C1s spectra of CU_GO_{fzd} (top) and CU_rGO_{fzd} (bottom) after thermal annealing at 900 °C including relative intensities for each deconvolution.*

The contributions of epoxide, carbonyl and carboxyl groups in the CU_GO_{fzd} spectrum matched those from the literature [141, 202] and appeared as significant as sp^3 carbon, shifting slightly towards higher energies after reduction. Although these oxidised groups are commonly reported in GO sheets, their relative contributions can vary extensively depending on the selected precursor [139, 176, 202]. As a surface analysis technique, XPS also shows GO's heterogeneous nature, with localised areas subjected to selective degrees of oxidation during the early synthesis of the precursor, resulting in different composition measurements depending on the region studied.

Binding energies from the O1s spectra of CU_GO_{fzd} and CU_rGO_{fzd} were also examined to obtain additional information about the oxidation in the graphene sheets (Figure 4.6).

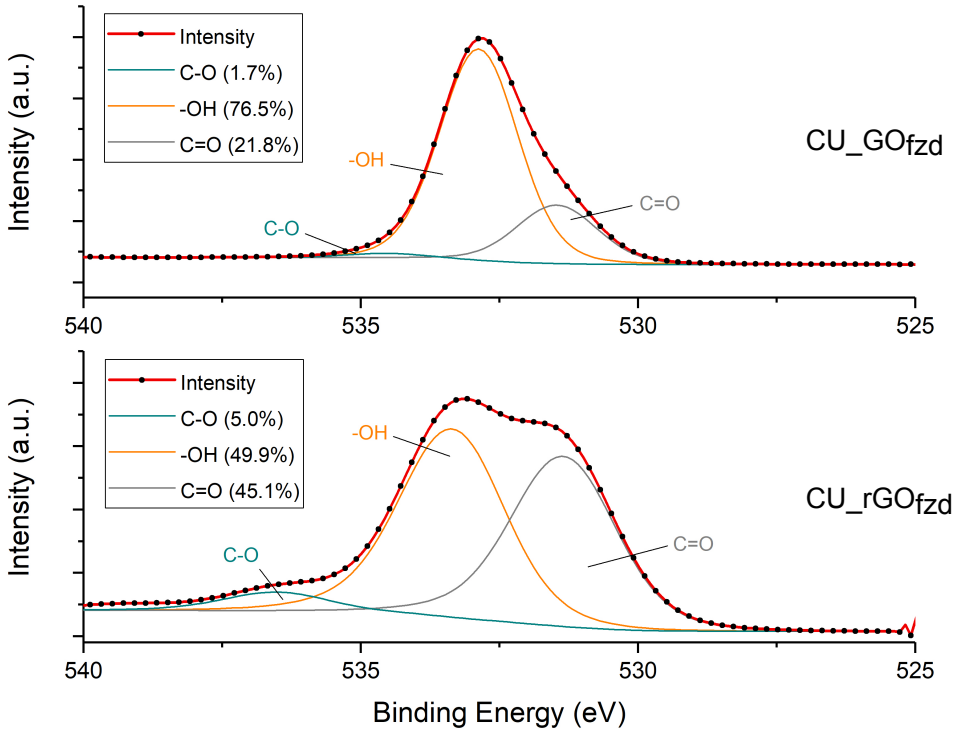

Figure 4.6: *Deconvolution of XPS O1s spectra for CU_GO_{fzd} (top) and CU_rGO_{fzd} (bottom).*

The analysis of O1s binding energies presented in this work was based on previous spectra deconvolutions by other authors [202, 223]. The O1s signals attributed to the hydroxyl ($-OH$) and epoxide groups ($C-O$) in the GO sheets have been identified separately at 533 and 534.5 eV, showing a third signal attributed to the carbonyl group at 531.5 eV. The relative contribution of the carbonyl group increased from 22 to 45% after reduction (taking into account the significant elimination of oxygen from 29 at.% to 2 at.% in the general XPS survey from Table 4.2). The hydroxyl and epoxide groups also displayed a slight shift towards higher binding energies that could be associated with a charging effect. An additional deconvolution has been presented in some works around 532 eV [223] corresponding to the carboxyl group. However, it was not identified in this evaluation, possibly due to its proximity with the carbonyl signal.

The elimination of functional groups from the GO sheets through thermal reduction accompanies a reduction in weight, which was evaluated through TGA measurements under N_2 atmosphere (Figure 4.7). An initial 10% weight loss was registered up to 120 °C in pre-treated CU_GO_{fzd}, which could be attributed to the remaining humidity in the samples. A secondary sharp weight loss occurs below 250 °C, matching the significant removal of oxidised groups detailed in the previous XPS analysis (Figure 4.5). At 900 °C temperature, a 55 - 60% weight loss was registered after a steady decline. In the literature, weight reductions of 60 - 75% of the initial GO material have been reported at similar temperatures [148, 179, 224], which is highly dependent on the composition and quality grade of the initial GO precursor.

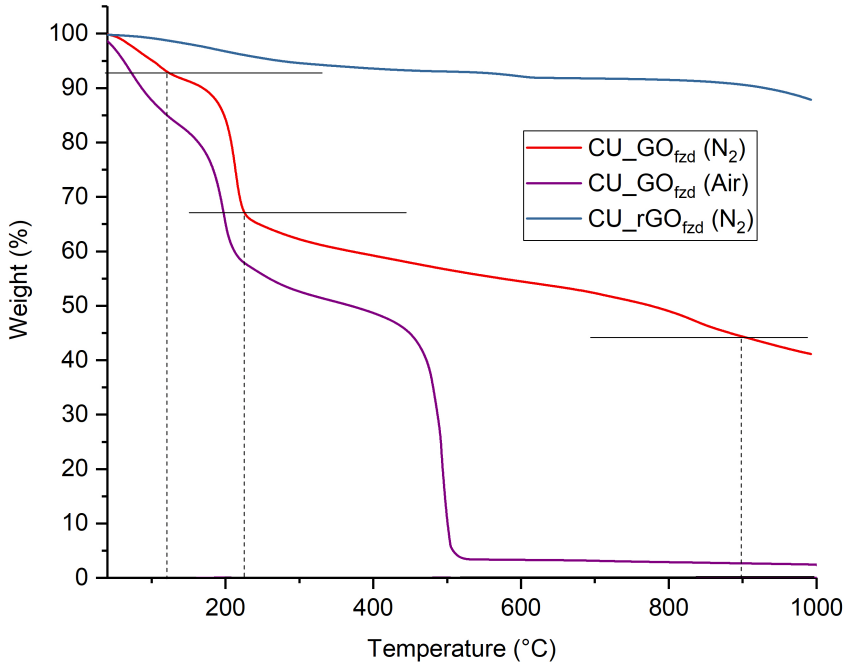

Figure 4.7: *TGA comparison between CU_GO_{fzd} (red) and CU_rGO_{fzd} (blue) under N_2 atmosphere, including CU_GO_{fzd} under air (purple). Performed at 5 °C min^{-1} up to 1000 °C.*

After thermal treatment at 900 °C, CU_rGO_{fzd} remained much more stable under similar temperature increases. An overall 10% weight loss was obtained, which could be attributed to atmospheric humidity and a residual elimination of functional groups from the GO flakes, validating the stability of reduced GO at inert atmospheres because of the partially restored graphitic domains.

The TGA measurements of CU_GO_{fzd} under nitrogen were contrasted with similar runs under air. In these conditions, the weight losses attributed to humidity and the elimination of attached functional groups in GO were maintained, although accentuated a marginal 10% up to 500 °C. Beyond this point, the carbon from the graphene sheets was completely burned in the presence of the atmospheric oxygen, which highlighted the importance of maintaining a non-oxidising atmosphere during the thermal reduction of GO [225].

4.3.2 Formulation of water-based graphene oxide suspensions

A remarkable advantage of selecting water-based GO suspensions as a precursor for the graphene-based phase in the composite resides on its ideal colloidal behaviour, permitting the flexible tuning of solid concentration in the slurry. This can be achieved without compromising the stability of the suspension, owing to the remarkable electrostatic repulsion of the GO flakes exhibiting low zeta potential (-40 mV) across a wide pH range of 5 - 12 [180, 192].

Colloidal water-based graphene oxide (GO) suspensions of 0.25 and 0.5 wt.% GO

in water were successfully prepared by dilution of the supplied 0.6 - 1 wt.% GO suspensions (*ICL_GO* and *CU_GO*, respectively), aiming to induce the deagglomeration of graphene flakes and achieve a higher quantity of dispersed GO monolayers. The slurries maintained homogeneity after applying a speed-mixing step (Figure 4.8). PVA and sucrose powder were included in the formulation as a binder and enhancer of surface properties respectively before freeze-casting as inspired by the literature [90, 152, 177].

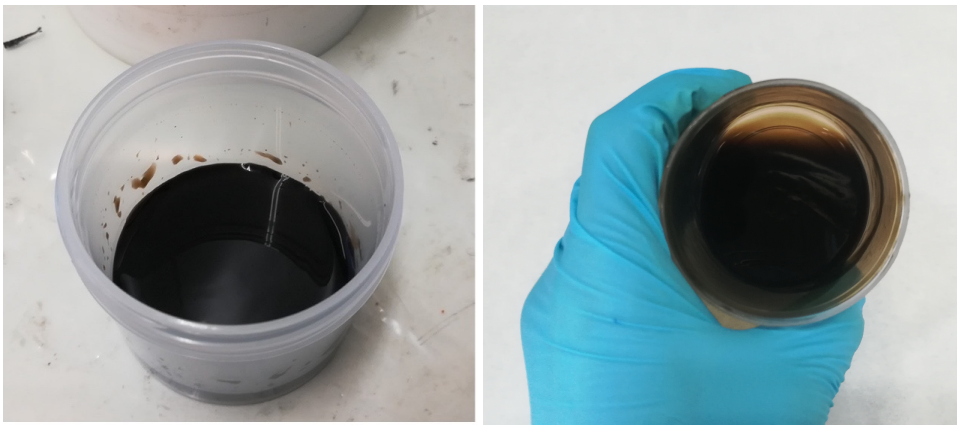

Figure 4.8: *Water-based 0.5 wt.% CU_GO and ICL_GO suspensions after speed-mixing at 1950 rpm for 10 minutes.*

The viscosity of 0.25 and 0.5 wt.% slurries with and without introducing freeze-casting additives in formulation (up to 50 wt.% of PVA and sucrose with respect to GO content in water) was studied via rotational viscometry. In *CU_GO* slurries, a substantial increase in viscosity from a 5 – 15 mPa s range to a 150 – 400 mPa s range (for 50 to 150 rpm spindle speeds) was found when increasing the GO content in suspension from 0.25 wt.% to 0.5 wt.%. The inclusion of additives in suspension did not increase viscosity in *CU_GO*, obtaining similar ranges for suspensions with and without the 50% additive content.

In *ICL_GO* suspensions, the behaviour obtained was significantly different. A spindle for higher viscosity measurements was required reaching a 500 – 2000 mPa s range for 0.25 and 0.5 wt.% GO suspensions. In this case, doubling the GO concentration in suspension did not result in an apparent increase in viscosity. However, the overall profile was substantially superior to the one obtained for *CU_GO* suspensions. This could be expected from the 4-time increase in GO lateral size (average of 31 vs 7 μm), resulting in higher flake interlocking in water. *ICL_GO* suspensions also manifest the effect of introducing PVA additions in the suspension, reaching 5000 – 12000 mPa s viscosity ranges due to the polymeric additions. Tailoring the viscosity of the GO slurries plays a vital role in later freeze-casting stages as the totality of the casting mould should be filled with the GO suspension before the initiation of a freezing front. High viscosity can lead to heterogeneous aerogel formation arising from defective mould filling. At the same time, highly liquid flows are

similarly undesirable due to excessive removal of solid material and potential leaking through the mould junctions.

Another attractive feature of using GO as a graphene precursor lies in its reported self-assembly behaviour arising from the formation of liquid crystal phases [136, 137, 217]. The degree of self-ordering and the liquid crystal phase displayed by the slurry are closely related to the GO concentration in suspension and the polar solvent selected (e.g. water, DMF or DMSO) and the GO flake lateral size (Section 4.3.1). The acute anisotropy of planar GO flakes of distinct aspect ratio (as in *CU_GO* and *ICL_GO*) can induce orientational ordering above a critical value of concentration and flake size, triggering the change from isotropic ordering to biphasic and nematic phases [136, 137]. From the measured GO flake sizes above 7 μm combined with the selection of 0.25 and 0.5 wt.% GO concentration in suspension, a nematic self-ordered phase for both *CU_GO* and *ICL_GO* precursors was expected, that can be preserved and accentuated by the controlled directional freezing from a freeze-casting processing method.

4.4 Production of graphene oxide aerogels by freeze-casting

4.4.1 Lab-sized graphene oxide aerogels

Lab-sized freeze-cast aerogels (*CU_GO$_{ag}$*) were produced by testing three processing parameters as presented in Table 4.3. Adjusting these parameters affected the internal consistency of the obtained aerogels and their self-standing behaviour, needed for better integration with the ceramic phase before composite consolidation. An extended labelling system *x:GO$_{ag}$(y:z)* has been used throughout the section and included in the table, with x being the GO concentration in the suspension (0.25 and 0.5 wt.%), y the freezing rate (2 – 10 °C min^{-1}) and z the additives (sucrose:PVA) wt.% referred to the GO solid content in suspension (0 – 50 wt.%).

Table 4.3: *Summary of conditions tested for freeze-casting of GO aerogels with the defined labelling system.*

Sample Id	**GO concentration (wt.%)**	**Freezing rate (°C min^{-1})**	**Sucrose:PVA (wt.% of GO)**
0.25:CU_GO$_{ag}$(5:0)	0.25	5	0:0
0.25:CU_GO$_{ag}$(5:50)	0.25	5	50:50
0.5:CU_GO$_{ag}$(5:0)	0.5	5	0:0
0.5:CU_GO$_{ag}$(5:50)	0.5	5	50:50
0.5:CU_GO$_{ag}$(2:50)	0.5	2	50:50
0.5:CU_GO$_{ag}$(10:50)	0.5	10	50:50

At least four specimens of each composition were freeze-cast on a Teflon mould of 19 mm in diameter and 15 - 25 mm height to reduce variability intrinsic to the

freeze-casting process. The produced CU_GO_{ag} were compared after freeze-drying for 48 hours and before any thermal treatment (Figure 4.9).

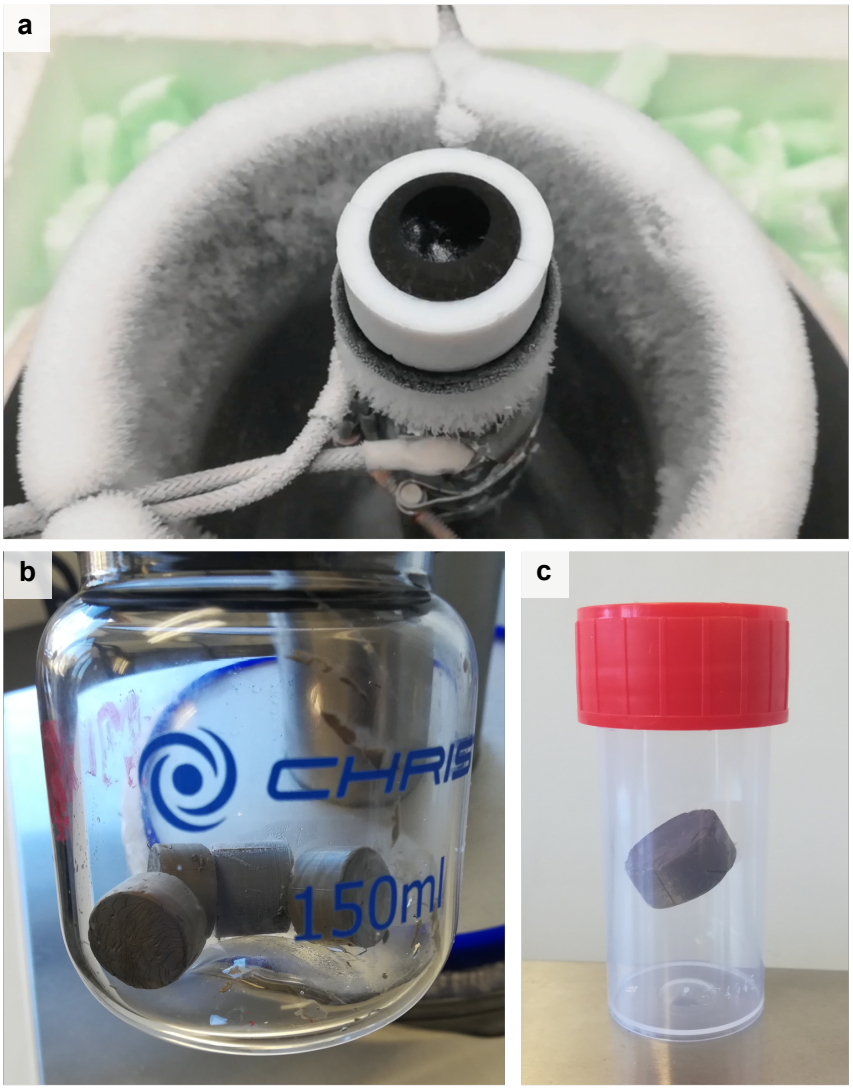

Figure 4.9: *a) Advancing solidification front during freeze-casting of 19 mm diameter aerogels. b) Simultaneous freeze-drying of GO aerogels at –80 °C under 12 Pa. c) As-produced 0.25:CU_ GO_{ag}(5:0) sample (measured apparent density of 3 mg cm^{-3}).*

The apparent density of the freeze-cast GO aerogels was measured for each condition and plotted against the content of additives in Figure 4.10. Without additives in formulation, the apparent density was lowered significantly. Aerogels prepared out of 0.25 wt.% GO slurry (*0.25:CU_ GO_{ag}(5:0)*) displayed an average apparent density of 3.1 ± 0.1 mg cm^{-3}, while aerogels prepared with 0.5 wt.% GO (*0.5:CU_ GO_{ag}(5:0)*) experienced a 87% increase to 5.8 ± 0.2 mg cm^{-3}. A 100% increase was not achieved due to slight deviations in the GO concentration of the commercial *CU_ GO* suspension, arising from water evaporation and slurry thickening after successive freeze-casting batches.

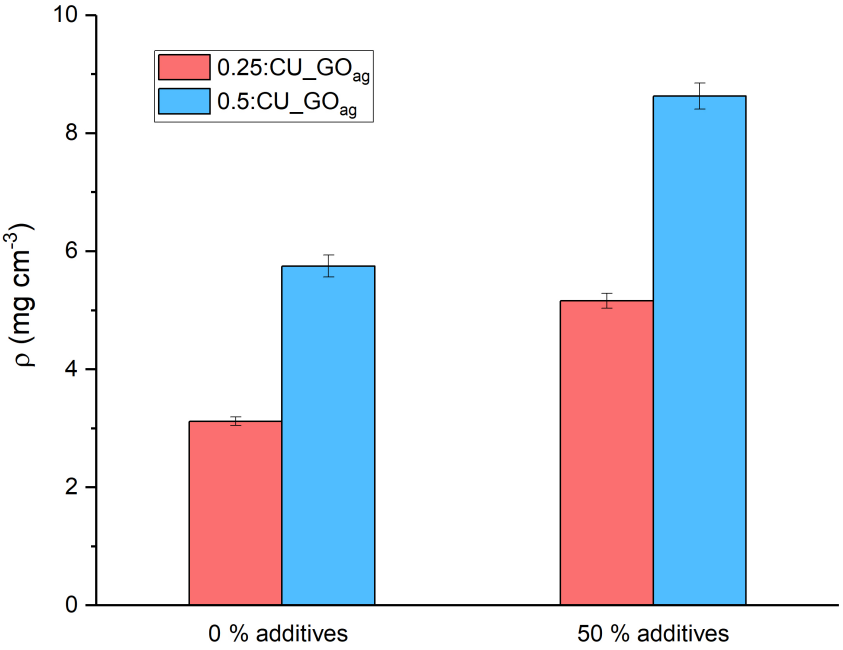

Figure 4.10: *Apparent densities for lab-scale GO aerogels freeze-cast from 0.25 and 0.5 wt.% GO suspensions with and without additives in formulation. Frozen at 5 °C* min^{-1}.

The inclusion of additives in the formulation led to an apparent density raise from 5.2 ± 0.2 to 8.6 ± 0.2 mg cm^{-3} (a 65% increase) after doubling the concentration of GO in the suspension formulation from 0.25 to 0.5 wt.% (*0.25:CU_* GO_{ag}*(5:50)* vs *0.5:CU_* GO_{ag}*(5:50)*). As the PVA additive content incorporated in suspension (10 wt.% in H_2O) was related to the solid GO content, modifying the GO concentration also introduced varying contents of extra water with the PVA additions, not taken into account in the formulation and reflected in a non-linear increase of the aerogel densities obtained. A range of GO aerogels of 3 – 9 mg cm^{-3} could be produced through these changes, agreeing with values reported in the literature for equal GO concentration in suspension [152, 154, 182]. All aerogels proved equally self-standing, with those produced from thicker 0.5 wt.% suspensions expected to deliver network channels of higher GO agglomeration.

Modifying the freezing rates had an expected negligible effect on the apparent density of the produced aerogels (Figure 4.11), obtaining a relative reduction of 5% from 11.7 ± 0.1 to 11.2 ± 0.1 mg cm^{-3} when testing 2 and 10 °C min^{-1} (*0.5:CU_* GO_{ag}*(2:50)* and *0.5:CU_* GO_{ag}*(10:50)*) attributed to weighing inaccuracies. The aerogels displayed in this figure were produced using different supplies of GO, PVA and sucrose only for test purposes, resulting in a marginal increase in weight compared to the aerogels from Figure 4.10.

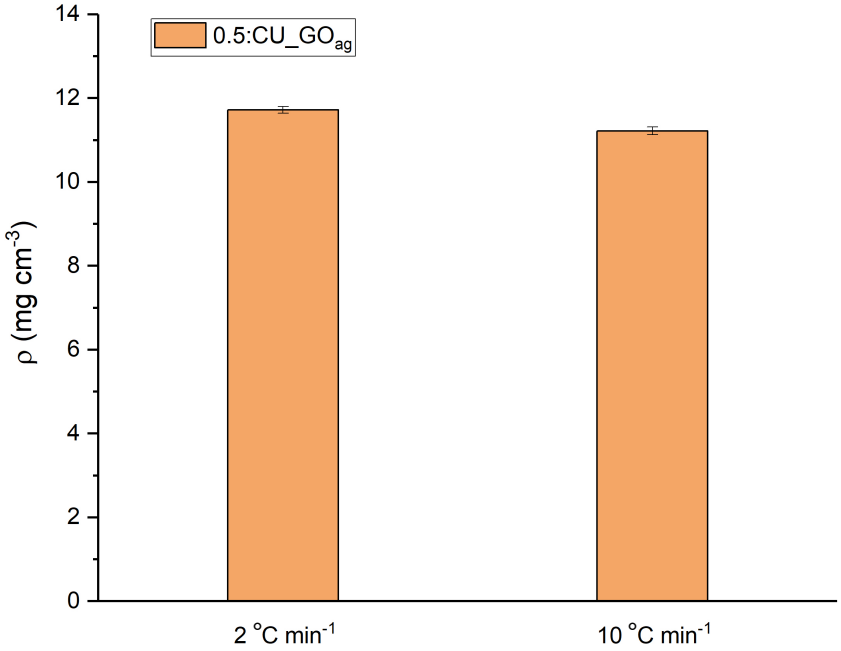

Figure 4.11: *Apparent densities for lab-scale 0.5:CU_ GO_{ag} aerogels with additives in suspension, freeze-cast at 2 and 10 °C min^{-1} freezing rates.*

The cooling distribution profile applied during freeze-casting is a crucial defining factor in the sample morphology [13, 14, 83]. An important consequence of modifying freezing rates resides in the impact on the internal structure of the aerogels, especially the channel widths. As introduced in Section 1.3, slower cooling rates during freeze-casting allow the solid particles to relocate around the growing ice crystals and provide widened channels. In contrast, faster rates entrap the solids at shorter distances delivering thinner channels [14].

The insulating nature of pre-annealed GO aerogels hinders the evaluation of their internal structure through electron microscopy unless sputtered with a metallic coating that prevents electron charging. For such reason, FESEM of the green aerogels studying their internal structure was not included in this section until the partial restoration of graphitic domains in the GO sheets performed via thermal annealing.

4.4.2 Scaled-up graphene oxide aerogels

One key theme of this chapter relates to optimising the graphene phase morphology, obtaining a fine interconnected structure with self-standing properties while limiting flake agglomeration. After validating the production of lab-sized self-standing GO aerogels, achieving sample scalability comprised an essential milestone aiming to produce a tough and electrically conductive ceramic-based composite for industrial applications, be it in aerospace, transportation or military fields (e.g. ceramic bearings, shield protection and ultra-lightweight components to name a few [73]). Laboratory-sized samples did not meet the physical dimensions required for these

applications or machining specimens for mechanical testing.

The flexibility of the freeze-casting technique permitted exploring a range of aerogel sizes and shapes (as shown in Figure 3.3a). The volumetric space available for sintering in the SPS graphitic dies during later stages (cylindrical dies of 20 - 30 mm in diameter) has been used as a reference to produce scaled-up aerogels. Cylindrical scaled-up CU_GO_{ag} (30 mm diameter, 33 mm height) were successfully freeze-cast using PLA moulds selected for their ease of manufacture and quick availability compared to Teflon (Figure 4.12a). The self-standing behaviour of the scaled-up aerogels was preserved under similar conditions as smaller aerogels shown previously, using *0.25:*CU_GO_{ag}*(5:50)* and *0.5:*CU_GO_{ag}*(5:50)* formulations, verifying the direct scalability of the envisioned freeze-casting processing. However, this setup was not compatible with later consolidation stages via SPS sintering due to the alignment direction of freeze-cast GO aerogels coinciding with the pressure direction applied during SPS, which would crush the aerogel's tailored structure in the process.

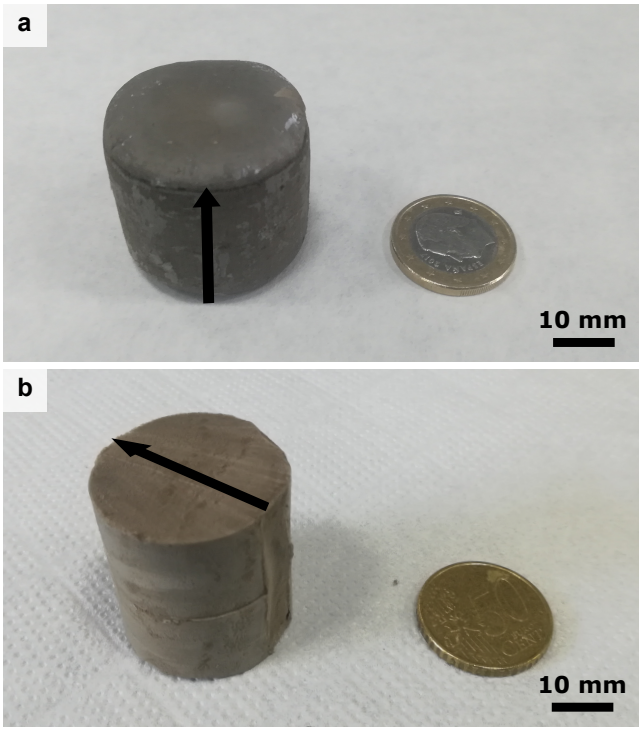

Figure 4.12: *a) Scaled-up 30 mm 0.5:*CU_GO_{ag} *aerogel. b) Scaled-up 30 mm 0.5:*$ICL\_GO_{ag}\perp$ *sample using the improved 4-piece mould with the perpendicular axis of revolution. The arrow indicates the freezing direction.*

30 mm scaled-up aerogels were alternatively obtained using the improved 4-piece freeze-casting mould with a cylindrical axis of revolution perpendicular to the freezing direction. *0.25:*ICL_GO_{ag}*(5:50)* and *0.5:*ICL_GO_{ag}*(5:50)* were produced from ICL_GO suspensions to validate the upgrade in GO precursor for future steps (Figure 4.12b). Extended freeze-casting times were required based on the reduced area of contact of the GO suspension with the copper plate, which affected the heat transmission inside the mould. However, the self-standing behaviour of the produced

aerogels was not compromised, as seen in the provided figures.

To differentiate scaled-up aerogels produced with the perpendicular alignment from standard aerogels, the symbol (⊥) has been included in their labelling. The apparent density of scaled-up *0.25:ICL_ GO_{ag}(5:50)*⊥ and *0.5:ICL_ GO_{ag}(5:50)*⊥ aerogels was found of 5.5 ± 0.4 and 9.1 ± 0.6 mg cm^{-3}, respectively. These values appeared on similar ranges to lab-sized equivalent aerogels from Figure 4.10 (5.2 ± 0.2 and 8.6 ± 0.2 mg cm^{-3}), with slight deviations attributed to the selection of another GO precursor of different starting GO concentration.

4.5 Self-standing highly-structured graphene aerogels

As-produced freeze-cast GO aerogels were partially reduced via thermal annealing. Thermally-driven GO reduction methods have been known to increase the risk of structure disruption by sudden material expansion compared to other chemical reduction methods (e.g. through hydrazine-based agents) [127]. A thermal reduction approach was still beneficial in this work to maximise the atomic C/O ratio in GO sheets obtained and withdraw from hydrazine's corrosive and highly flammable behaviour in favour of a safer method.

TGA of freeze-cast *0.5:CU_ GO_{ag}(5:50)* was performed and compared with *CU_ - GO_{fzd}* characterised in the previous section to determine the weight loss evolution across temperature and evaluate the effect of additives in the aerogels (Figure 4.13).

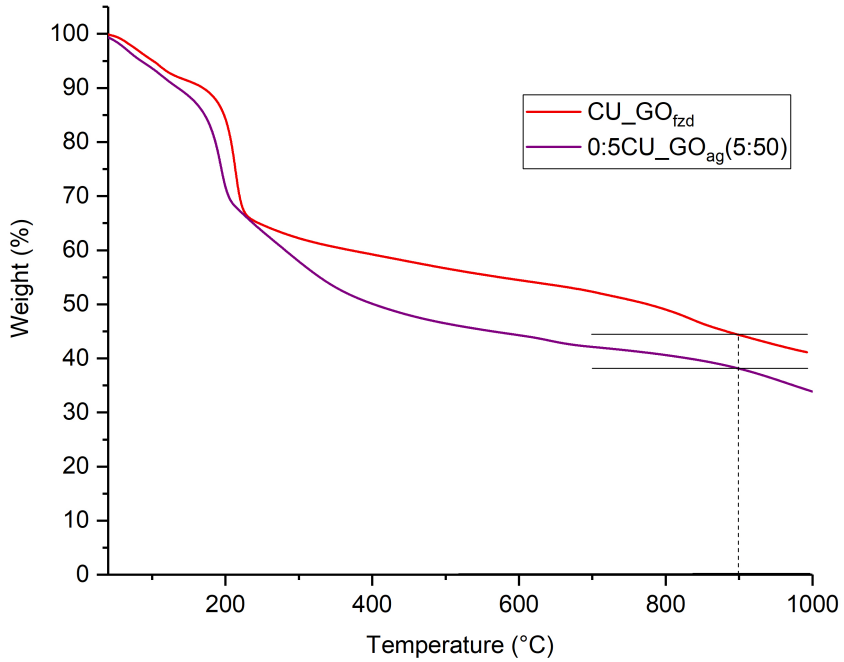

Figure 4.13: *Comparison of TGAs performed on CU_ GO_{fzd} and freeze-cast 0.5:CU_ GO_{ag}(5:50) aerogels at 5 °C min^{-1} under N_2 atmosphere.*

Both curves exhibited similar behaviour, with analogous initial dips in weight assigned to humidity removal in the samples and the functional groups attached to GO expected below the 250 °C mark. Beyond this temperature range, a more extended weight reduction was found in the aerogels, reaching the 900 °C annealing mark with an 8% extra reduction attributed to the additives included in the formulation. Overall, the addition of sucrose and PVA additives had a marginal effect in the thermogravimetric profile, assuming a 65% reduction in weight for the aerogels at 900 °C used in future calculations.

A reduction temperature of 900 °C was selected in the general processing, ensuring a sufficient degree of reduction and limiting the temperature-induced defects in the GO sheets triggered by the release of carbon dioxide [139, 153]. Previous reports have stated that from the 800 °C temperature mark onwards, restoration of electrical conductivity is achieved to a great degree while still not undergoing substantial disruption of the graphene-based sheets [153, 226].

As seen from the TGA results, a sudden release of oxidised groups attached to the GO sheets can be expected throughout the initial 250 °C of GO aerogel annealing. Undergoing an uncontrolled heating rate during this temperature range can also lead to structural damage by sudden expansion given the aerogel's fragile consistency and ultralow densities (3 – 10 mg cm^{-3}). After implementing an extended annealing cycle to compensate for the fixed heating rate of the tubular furnace (described in Section 3.2.4), reduced GO aerogels could be produced without visible disruption of the structure previously caused by a sudden release of volatiles (Figure 4.14a). This modification permitted the batch production of lab-scale GO aerogels of 10 - 20 mm in diameter, successfully extended to the production of 30 mm scaled-up samples (Figure 4.14b,d,e) without compromising the integrity of the aerogels.

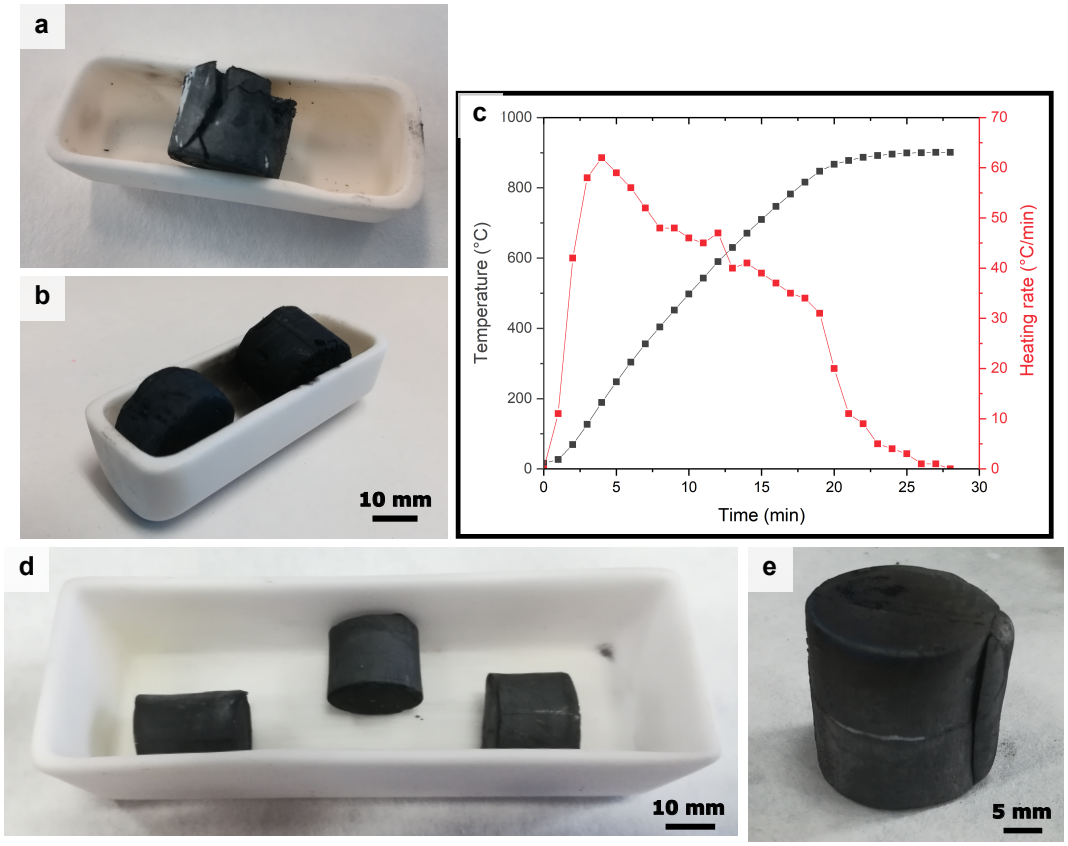

Figure 4.14: *a,b) Exploded CU_rGO_{ag} aerogel vs undamaged CU_rGO_{ag} scaffolds (19 mm diameter) after adjusting the carbonisation step at 900 °C. c) Registered heating rate of the Carbolite tubular furnace during GO annealing. d) Batch reduction of CU_rGO_{ag} aerogels. e) 30 mm $CU\_rGO_{ag}\perp$ aerogel.*

4.5.1 Effect of formulation parameters on structural properties

Modifying the freeze-casting parameters (concentration of the slurry, freezing rate and additives ratio) influenced the self-standing behaviour and the structural alignment of graphene-based aerogels obtained after thermal annealing. Before settling on a formulation, the effect of applying these conditions was studied by density measurements and FESEM.

Apparent density measurements were performed on lab-scale CU_rGO_{ag} scaffolds to evaluate the change in density and loss of material after thermal annealing at 900 °C (Figure 4.15), compared to previous values presented in Figure 4.10 for green aerogels. These results include aerogels prepared with 0.25 - 0.5 wt.% GO slurry with and without additives in suspension ($0.25{:}CU\_rGO_{ag}(5{:}0)$ vs $0.25{:}CU\_rGO_{ag}(5{:}50)$ and $0.5{:}CU\_rGO_{ag}(5{:}0)$ vs $0.5{:}CU\_rGO_{ag}(5{:}50)$). Although the self-supporting behaviour of the reduced aerogels was not affected, the samples were also found more fragile and susceptible to static electricity due to the extremely lightweightness of the material after reduction, with apparent densities of 1.5 - 4 mg cm^{-3}.

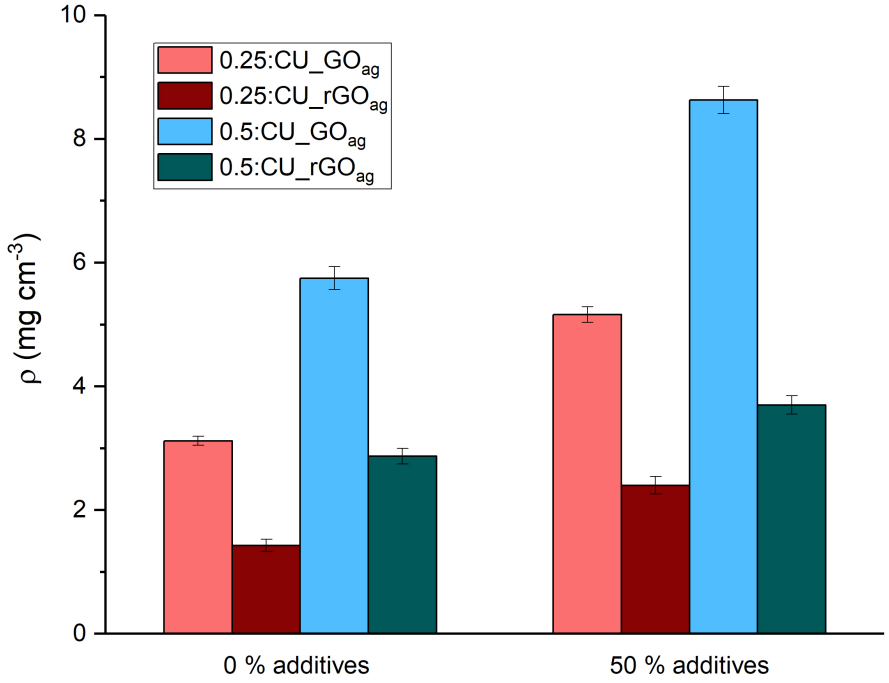

Figure 4.15: *Comparison of apparent densities of lab-scale CU_GO_{ag} aerogels before and after thermal annealing, as a function of the additive content (0 and 50%) and the GO concentration in the precursor slurry (0.25 - 0.5 wt.%).*

Densities were similarly reduced by an approximate of 50 – 60% in all CU_rGO_{ag} samples, reaching 1.4 - 2.4 (± 0.1) mg cm^{-3} values for both *0.25:*CU_rGO_{ag}*(5:0)* and *0.25:*CU_rGO_{ag}*(5:50)* and 2.8 - 3.7 (± 0.1) mg cm^{-3} for *0.5:*CU_rGO_{ag}*(5:0)* and *0.5:*CU_rGO_{ag}*(5:50)*. The substantial weight reduction anticipated by the TGA measurements was verified, attributed to the removal of oxidised groups from the graphene sheet as displayed in the XPS C1s spectra (Figure 4.5).

Upon carbonisation, the reduction in apparent density was slightly higher in *0.5:*CU_rGO_{ag}*(5:50)* samples. This could be attributed to the elimination of larger quantities of additives and oxidised groups attached to the rGO because of their higher GO concentration (0.5 wt.% GO suspension) without entailing significant volumetric shrinkage. The apparent density of scaled-up *0.25:*ICL_GO_{ag}*(5:50)*⊥ and *0.5:*ICL_GO_{ag}*(5:50)*⊥ aerogels of 30 mm diameter (Figure 4.12b) was also verified after carbonisation, yielding 2.1 ± 0.3 and 4.3 ± 0.1 mg cm^{-3} respectively. Despite the increase in dimensions, these values matched those from lab-sized aerogels, with analogous density reductions of 53 – 60% after carbonisation.

The internal structure of *0.25:*CU_rGO_{ag}*(5:50)* scaffolds was examined by FE-SEM (Figure 4.16). The extremely low density 1.4 mg cm^{-3} combined with the small flake size delivered a highly broken structure and poorly interconnected network, in which aligned channels can be guessed although completely disrupted. Despite the partial loss of alignment in the scaffold, the rGO network interconnection was still preserved, which explains the self-supporting capability of aerogels produced from

0.25 wt.% GO suspensions.

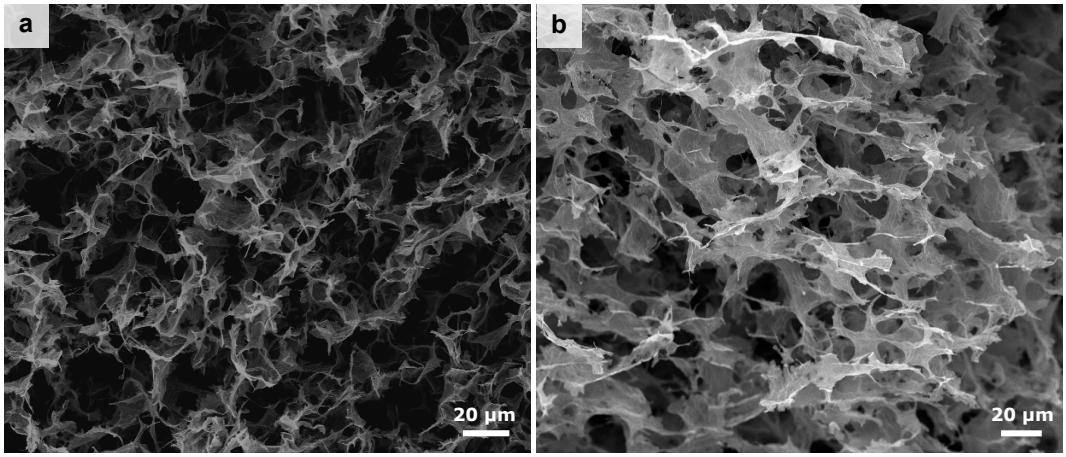

Figure 4.16: *FESEM of 1.4 mg cm^{-3} 0.25:CU_rGO$_{ag}$(5:50) aerogels showing a disrupted freeze-cast structure. a) Cross-sectional plane to the freezing direction. b) Parallel plane to the freezing direction.*

Increasing the GO concentration in suspension from 0.25 to 0.5 wt.% had an acute effect in preserving the structural alignment of the freeze-cast aerogels even after thermal reduction, as revealed by FESEM images of the 3.7 mg cm^{-3} *0.5:CU_-rGO$_{ag}$(5:50)* aerogels (Figure 4.17) highlighting the cross-section of parallel and perpendicular planes to the direction of freezing.

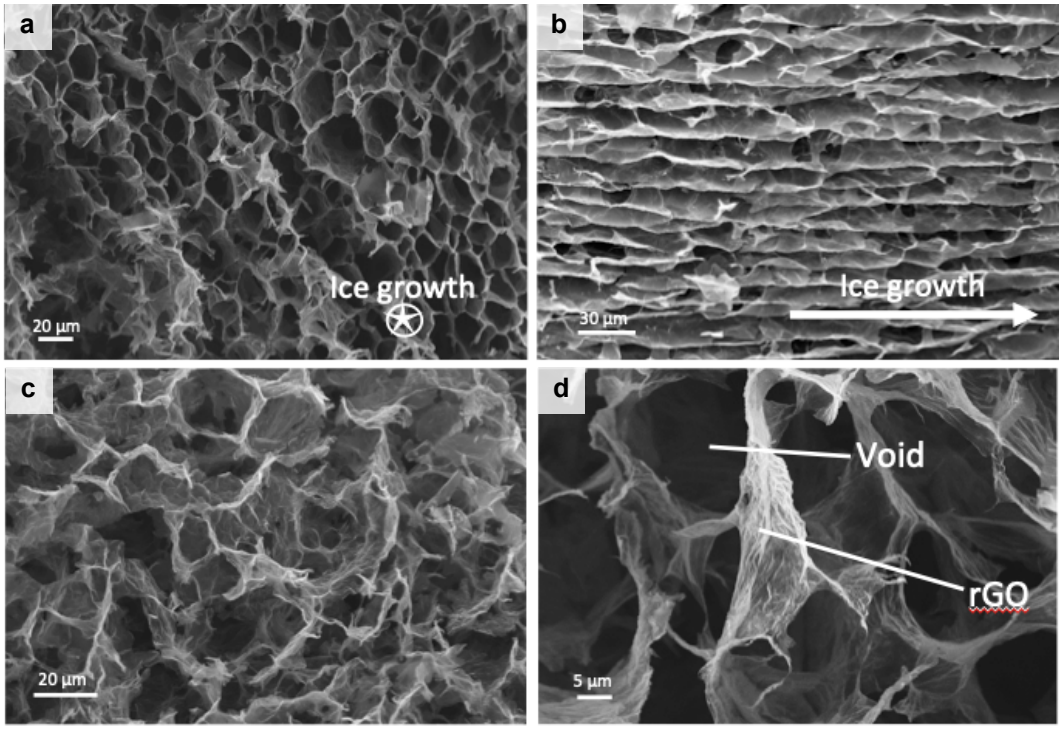

Figure 4.17: *FESEM images of 3.7 mg cm^{-3} 0.5:CU_rGO$_{ag}$(5:50) aerogels. a) Cross-sectional plane to the freezing direction. b) Parallel plane to the freezing direction. c and d) rGO sheets at higher magnification.*

The unidirectional alignment granted by freeze-casting was verified in the parallel cross-section, displaying a channel width of 15 - 20 ± 4 μm). Similarly, the normal cross-section plane shown a quasi-honeycomb structure created by the interlocking of rGO flakes, which is in agreement with previous works in the literature regarding the production of elastomeric graphene networks following a similar freeze-casting approach and conditions [152, 154, 176, 182]. Graphene walls in the structure appeared comprised of stacked layers of rGO sheets, with an approximate thickness smaller than 20 nm based on high-magnification FESEM images obtained at 60 kX. Although this value coincides with previously reported aerogels, higher precision would require the use of complementary techniques such as Transmission Electron Microscopy (TEM).

The direct comparison of perpendicular cross-sections in *0.25:CU_rGO$_{ag}$(5:50)* and *0.5:CU_rGO$_{ag}$(5:50)* at similar magnifications demonstrates the disruption of the obtained internal structure (Figure 4.18) when limiting the GO content in suspension to 0.25 wt.%.

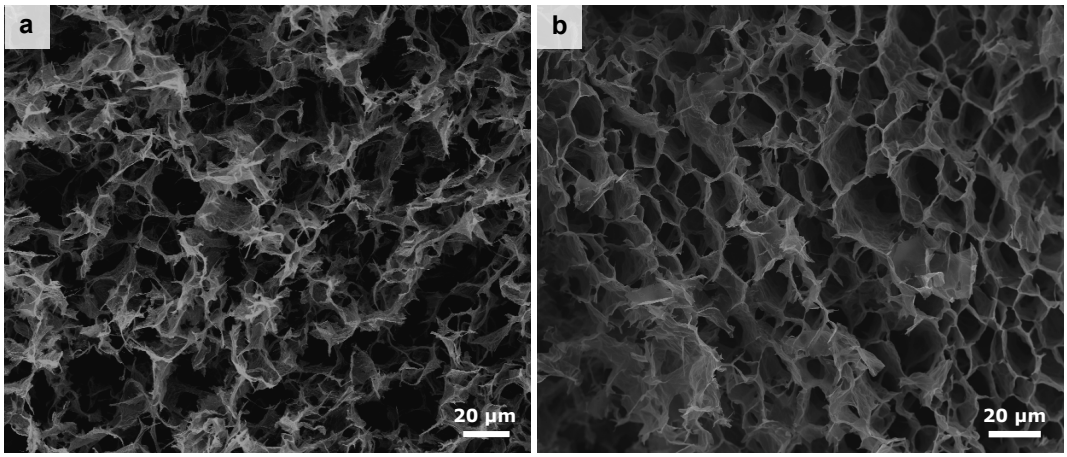

Figure 4.18: *Cross-section comparison of freeze-cast alignment showing the effect of GO concentration in the honeycomb-like structure. a) 0.25:CU_rGO$_{ag}$(5:50). b) 0.5:CU_rGO$_{ag}$(5:50 aerogels).*

Despite achieving lower scaffold densities and potentially reducing the agglomeration in the graphene structural walls, *0.25:CU_rGO$_{ag}$(5:50)* appears excessively damaged to maintain the envisioned structure in the target composite. It is worth noting that 0.25 wt.% GO comprises a particularly diluted GO suspension, with similar works in the field commonly settling with GO suspensions of higher loading (0.5 – 1 wt.%) as a precursor. The reduction in GO content in suspension was proposed to reduce the agglomerates of GO flakes in the scaffold walls, which could be improved by increasing the quality grade of the GO precursor selected.

The apparent density of lab-scale rGO aerogels freeze-cast with 2 – 10 °C min^{-1} freezing rates (*0.5:CU_ rGO_{ag}(2:50)* and *0.5:CU_ rGO_{ag}(10:50)*) was also studied (Figure 4.19), comparing the changes in apparent density to the green aerogels previously displayed on Figure 4.11.

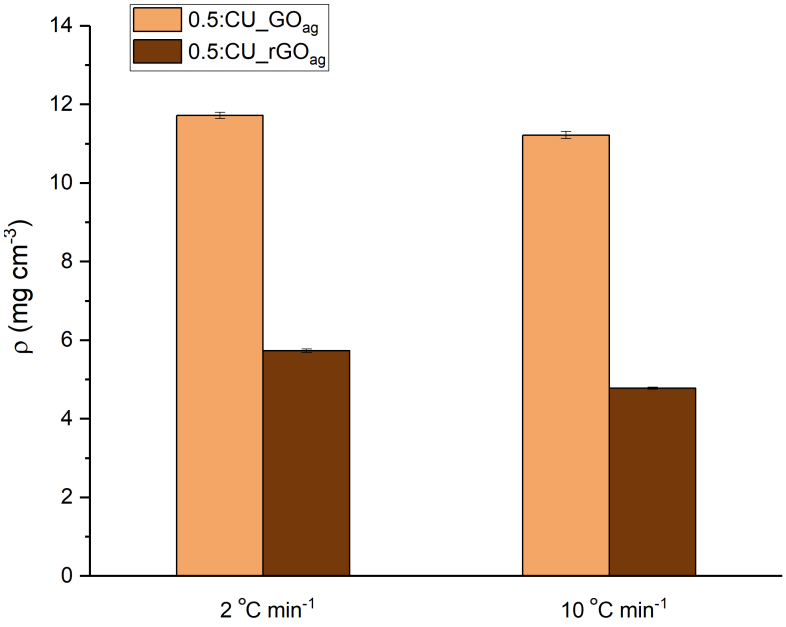

Figure 4.19: *Comparison of apparent densities of lab-scale CU_ GO_{ag} aerogels before and after thermal annealing, as a function of the freezing rate (2 vs 10 °C min^{-1}).*

The apparent density of *0.5:CU_ rGO_{ag}(2:50)* changed from 11.7 ± 0.1 mg cm^{-3} to 5.7 ± 0.1 mg cm^{-3} after carbonisation (a 51% reduction), with *0.5:CU_ rGO_{ag}(10:50)* going from 11.2 ± 0.1 mg cm^{-3} to 4.8 ± 0.1 mg cm^{-3} (a 57 % reduction). Although green bodies from both formulations were almost equal in density, the carbonisation led to higher shrinkage of *0.5:CU_ rGO_{ag}(2:50)* structures. It has been widely reported that lower freezing rates result in an increase of the channel widths from the freeze-cast structures given the increased time for solid particle mobility during the advancing freezing front [14, 85, 86]. Therefore, an inner structure with increased channel width could be subjected to higher shrinkage upon thermal treatment than a finer structure achieved with higher freezing rates.

The microstructure of *0.5:CU_ rGO_{ag}(2:50)* and *0.5:CU_ rGO_{ag}(10:50)* scaffolds was evaluated by FESEM to support this hypothesis and study the experienced change in densities (Figure 4.20). Comparing the perpendicular cross-section to the direction of freezing at similar magnifications shown the difference between each structure. While aerogels obtained at 2 °C min^{-1} displayed broader channels similar to the honeycomb-like structure from 5°C min^{-1} rates, the structural alignment of 10 °C min^{-1} aerogels was lost entirely. As both *0.5:CU_ rGO_{ag}(2:50)* and *0.5:CU_ rGO_{ag}(10:50)* aerogels were annealed under similar conditions, this disruption was not attributed to the carbonisation step. At these reduced aerogel sizes (19 mm

diameter, 15 mm height), the applied temperature gradient during freeze-casting could lead to freezing front velocities exceeding the critical velocity. Above it, the graphene sheets could be trapped in the frozen solvent without producing the desired structuring as covered in Section 1.3.

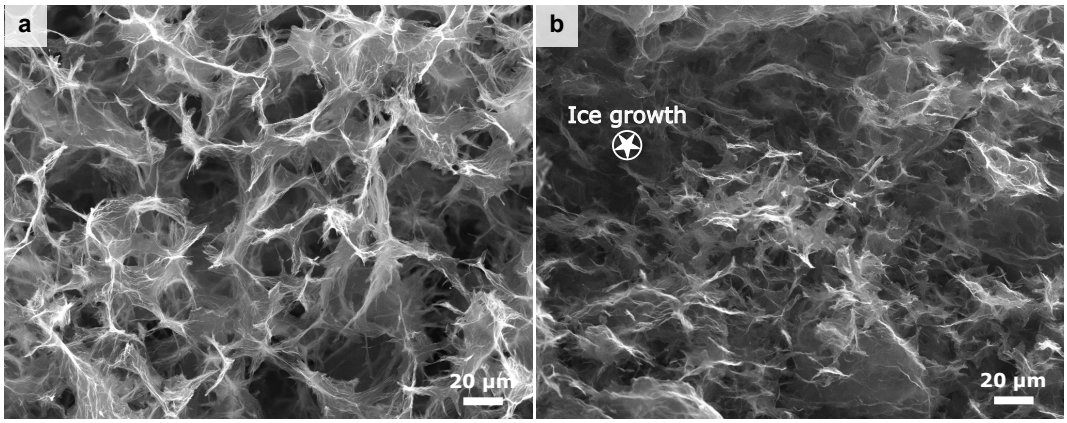

Figure 4.20: *FESEM of cross-sectional freeze-cast structure in a)0.5:CU_-rGO_{ag}(2:50) and b) 0.5:CU_rGO_{ag}(10:50).*

Focusing only on the non-damaged domains, the difference in channel widths obtained for each freezing rate (2, 5 and 10 °C min^{-1}) was highlighted in Figure 4.21. *0.5:CU_rGO_{ag}(2:50)* scaffolds exhibited 33 ± 3 μm wide channels, lowering to 21 ± 4 μm for *0.5:CU_rGO_{ag}(5:50)* and 16 ± 2 μm for *0.5:CU_rGO_{ag}(10:50)*, similarly showing the reduction in ice crystal thickness during freeze-casting because of the increased freezing velocity.

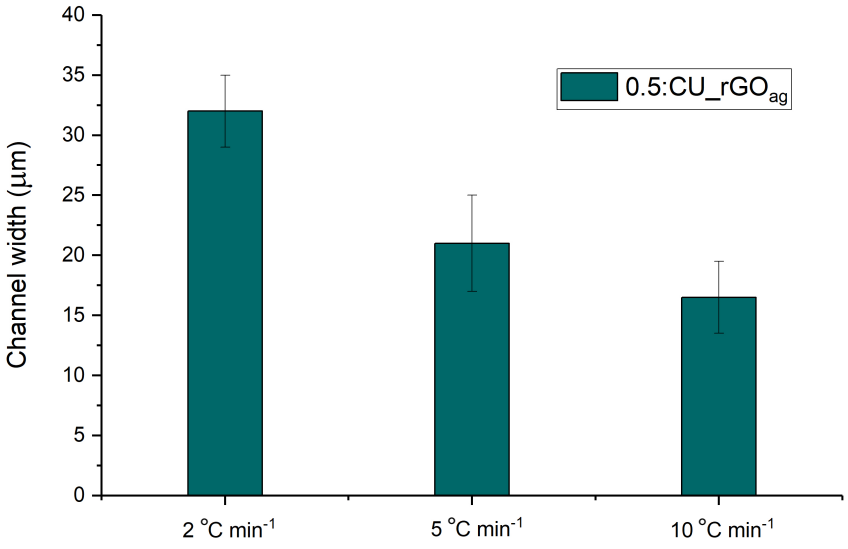

Figure 4.21: *Average channel widths of 0.5:CU_rGO_{ag} aerogels as a function of the freezing rate (2 - 10 °C min^{-1}).*

The removal of PVA and sucrose additives from the GO suspension was additionally tested in aerogels after carbonisation, aiming to simplify the suspension

formulation and reduce flake agglomeration after freeze-casting. Even if all tested freeze-casting conditions (from Table 4.3) led to obtaining lab-sized self-supporting CU_rGO_{ag} aerogels of smaller dimensions, removing additives in suspension negatively affected the consistency of scaled-up aerogels, which collapsed after freeze-drying and subsequent annealing steps. The inclusion of additives proved more relevant in maintaining the coherence of aerogels produced from the improved ICL_GO precursor, as shown after comparison of scaled-up 30 mm $0.5{:}ICL\_GO_{ag}(5{:}0)\perp$ and $0.5{:}ICL\_GO_{ag}(5{:}50)\perp$ samples (Figure 4.22).

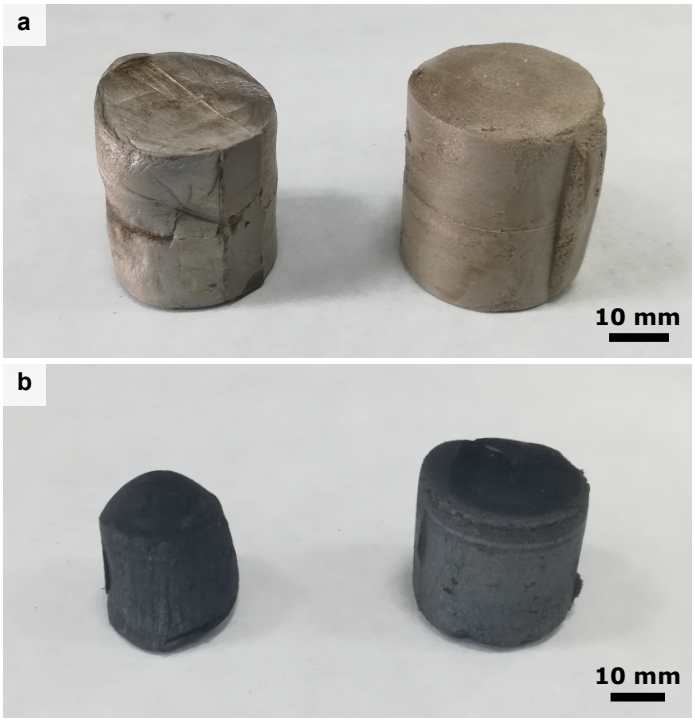

Figure 4.22: *Self-standing 30 mm* $0.5{:}ICL\_GO_{ag}(5{:}0)\perp$ *(left) vs* $0.5{:}ICL\_GO_{ag}(5{:}50)\perp$ *(Right). a) After freeze-drying for 72 hours. b) After carbonisation at 900 °C.*

4.5.2 Selection of freeze-casting conditions

A significant advantage of applying a freeze-casting approach for manufacturing highly porous graphene aerogels resides in its flexibility in achieving self-supporting structures with a wide range of channel morphologies and external shapes. The extended research performed during the 2010s permitted narrowing the starting range of additive selection and ratio, freeze-casting rates and GO concentration in this work, producing self-supporting scaffolds relatively quickly. The results presented in this chapter verified how changes in the freeze-casting conditions are reflected in the aerogels density (1.5 - 9 mg cm^{-3}), microstructure (15 – 35 μm channel widths) and loss of internal alignment, which should be adapted to the constraints of the graphene/ceramic composite processing strategy.

As the envisioned structure in the bioinspired graphene/ceramic composite is directly inspired from the hierarchical structure of nacre (or mother-of-pearl), it is intended to achieve a parallelism between ceramic-graphene phases in the manufactured composite and the inorganic-organic phases of nacre. This could be translated into two constraints: the relative weight ratio between the two constituent phases (consisting of 95 wt.% of $CaCO_3$ vs 5 wt.% of organic material in nacre) and the spacing of roughly 0.5 μm between layers of soft organic matrix arising from ceramic block thickness in nacre's brick and mortar structure [66, 181]. Tuning the weight ratio between hard and soft constituents appears crucial to resemble the structure of nacre. However, adding excessive reinforcing material in the composite can significantly detriment the matrix's properties (in the case of alumina matrix, a reduction in hardness, strength, and wear resistance).

GO's light-weight behaviour and flake aspect ratio permitted obtaining self-supporting rGO aerogels with apparent density values of 1.5 - 4 mg cm^{-3} as seen in Figure 4.15. From these low-density levels, the graphene-based scaffolds were not expected to comprise more than 1 wt.% of the total composite weight, which extensively meets the 5 wt.% threshold of nacre-like materials. Limiting the graphene content is essential to prevent the loss of mechanical properties of the ceramic matrix selected and reduce the presence of graphene agglomerates in the scaffold, which can negatively impact the properties of the final composite.

All configurations for freeze-casting of *CU_GO* suspensions outlined in Table 4.3 proved successful in achieving self-supporting aerogels that withstood the carbonisation step suitable for integration in the main strategy. However, aerogels produced from diluted 0.25 wt.% GO suspensions (*0.25:CU_rGO$_{ag}$*) exhibited a disrupted structure that did not maintain the intended microstructural alignment. An excessively low content of solids in suspension could result in a reduction of freezing velocity of the solidification front during freeze-casting, because of the increase in solvent quantities [101], preventing the obtention of the desired internal structure.

Regarding the selection of freezing rates, increasing the applied freezing rate up to 10 °C min^{-1} was attractive to obtain thinner channels in the scaffold with less agglomeration of rGO sheets forming the structural walls, closer to the natural compounds taken as reference. However, after comparing *0.5:CU_rGO$_{ag}$(5:50)* and *0.5:CU_rGO$_{ag}$(10:50)* (Figure 4.21), the reduction in channel widths obtained was very limited while also experiencing significant structural damage under 10 °C min^{-1} rates. Therefore, the application of freezing rates above 5 °C min^{-1} was eventually discarded. The inclusion of PVA and sucrose additives on a 0.5:0.5 ratio in the GO suspension formulation (as inspired by previous works [152, 177, 183]) was reinforced after testing the carbonisation of scaled-up 30 mm GO aerogels produced with the *ICL_GO* precursor.

Based on these results, the formulation of GO scaffolds selected for the following

stages in the processing strategy was settled on a freezing rate of 5 °C min^{-1} and the inclusion of PVA and sucrose additives *x:GO_{ag}(5:50)*, with x being the GO concentration in the precursor suspension (0.25 - 0.5 wt.%), which was kept for all aerogels produced in the following experiments. Moving forward in the document, the labelling system of the aerogels has been simplified from *x:GO_{ag}(5:50)* to simply *x:GO_{ag}*.

After settling on these conditions, the only differences between as-produced aerogels resided in the GO precursor selected and the GO concentration in suspension (0.25 and 0.5 wt.%). Despite the partial structural disruption experienced in aerogels cast from 0.25 wt.% GO, these were still produced for various tests based on the efficient use of the GO precursor (being in a more diluted state) while maintaining a moderate interconnection of graphene flakes verified by their self-standing behaviour.

4.5.3 Electrical characterisation

Epoxy/rGO composites were produced by infiltration of lab-sized graphene-based aerogels to verify the structural resistance of the rGO aerogels on an infiltration procedure based on vacuum casting as well as evaluating the restoration of electrical capabilities provided by the graphene network embedded in an insulating material (Figure 4.23). Prismatic specimens of various dimensions were cut and polished by following the procedure from Section 3.2.7.

The characterised aerogels were prepared using both GO precursors (*CU_GO* and *ICL_GO*), and the two selected GO concentrations in suspension (0.25 and 0.5 wt.% GO), leaving a total of four aerogel configurations (*0.25:CU_GO_{ag}*, *0.25:ICL_GO_{ag}*, *0.5:CU_GO_{ag}*, *0.5:ICL_GO_{ag}*) infiltrated in the epoxy before and after carbonisation.

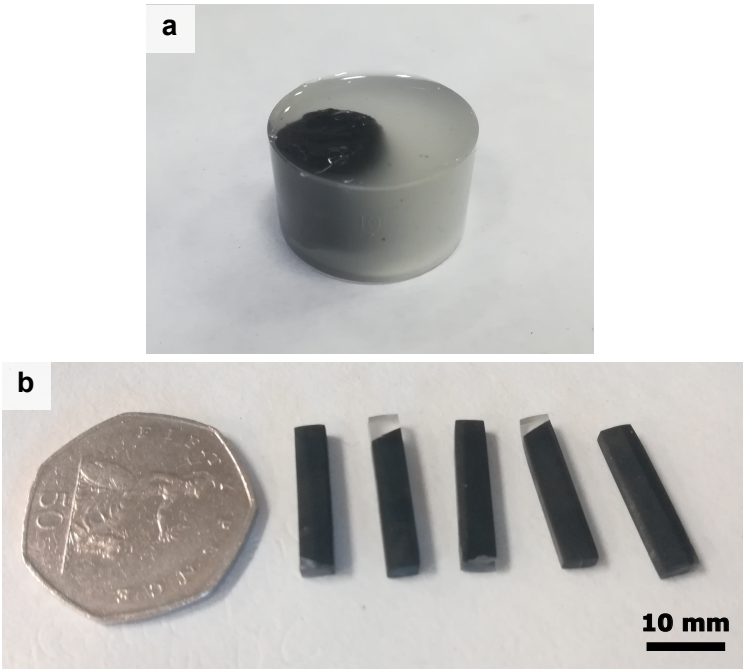

Figure 4.23: *a) Epoxy infusion of 0.5:CU_rGO$_{ag}$ aerogels. b) Prismatic epoxy/0.5:CU_rGO$_{ag}$ specimens (20 × 3 × 4 mm^3).*

Owing to the insulating behaviour of epoxies, any display of electrical conductivity in the material was conferred by the embedded graphitic network. Measurements along the transversal and parallel axes to the freeze-cast freezing direction of rGO scaffolds for each configuration were collected and displayed in Figure 4.24.

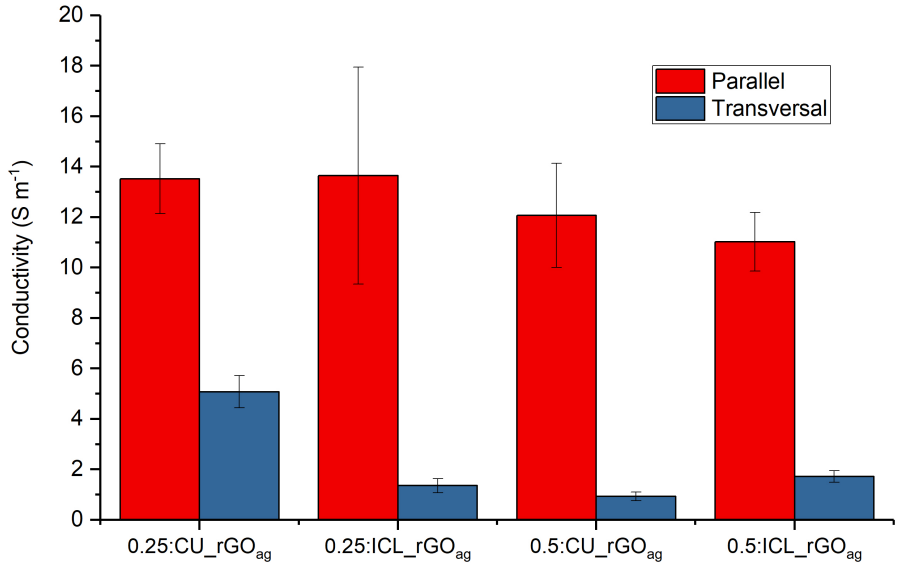

Figure 4.24: *Electrical conductivity of epoxy/rGO composites along the parallel and transversal axes to the freeze-casting direction in the rGO network.*

The directional alignment of embedded rGO scaffolds in the epoxy was confirmed in these tests, with measurements parallel to the alignment direction being one order of magnitude higher than the measures along transversal axes (12 – 14 S m^{-1} vs 0.5 –

5 S m^{-1}, respectively). Aerogels produced from 0.25 and 0.5 wt.% GO suspension led to similar conductivity ranges, retaining some form of directional alignment beyond the structural disruption verified in the former's through FESEM (Figure 4.16).

Despite the differences in lateral size from each GO precursor (shown in Section 4.3.1), changing from CU_rGO_{ag} to ICL_rGO_{ag} did not modify the electrical conductivity. Moreover, the transversal conductivity appeared maximised in the epoxy/*0.25:*CU_rGO_{ag} composite compared to the rest of the samples. This could result from the smaller GO flake size from CU_GO delivering a less anisotropic behaviour during freeze-casting of the scaffold.

Overall, the inclusion of embedded CU_rGO_{ag} and ICL_rGO_{ag} in the epoxy resin matrix granted a moderate increase of electrical conductivity in the composite compared to the epoxy's insulating behaviour. It should be remembered that the 900 °C temperature selected for annealing graphene-based aerogels is a relatively low temperature of graphitisation, which significantly limits the restored electrical conductivity.

Previous work using random mixing procedures of ceramic and graphene reinforcements had reached network percolation at 0.2 – 10 wt.% ratios (Figure 1.22) [23–31], showing an exponential rise in electrical conductivity by additions of sufficient reinforcement to consolidate a continuous network inside the composite. The continuity of the embedded rGO network was ensured in the specimens presented here by the followed freeze-casting processing approach, maintaining the original 15 – 20 μm channel widths as confirmed via FESEM (Figure 4.25). Despite the small contribution of graphene to the epoxy/rGO composite (0.5 - 4 wt.% depending on the selected configuration), a continuous graphene network was maintained.

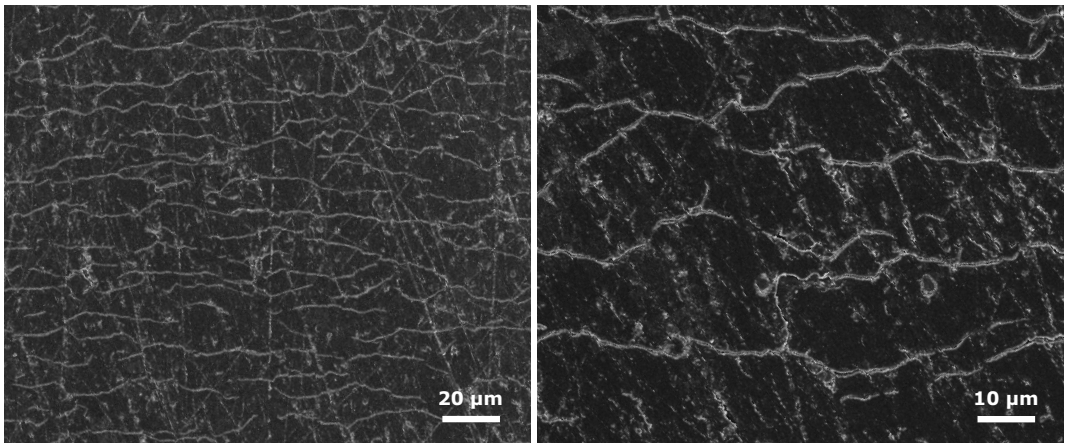

Figure 4.25: *FESEM of epoxy/0.5:*CU_rGO_{ag} *microstructure, showing the maintained alignment of the embedded aerogel.*

In the literature, epoxy/graphene composites of similar characteristics have been reported with a range of electrical conductivity of 0.1 – 120 S m^{-1} along the alignment direction depending on the quality of graphene precursor (FLG vs rGO) and

content in the composite (0.01 - 2 wt.%) [169, 180, 227]. Few works have reported conductivity values above 200 S m^{-1} [176] using GO as a precursor, by reaching remarkably higher reduction temperatures above 1500 °C. The results presented here match this range of electrical conductivities on the lower end of the spectrum, based on the selection of rGO as the graphene phase and the low temperature of carbonisation. Although the followed measurement procedure could not provide high accuracy (as illustrated by the error bars from Figure 4.24), this method has been previously reported for analogous graphene-based composites [182, 213, 214]. An automated procedure of higher measuring accuracy (such as a four-point probe) would be advisable in future testing to account for the lower conductivity values.

As mentioned in Section 1.4.2, one of the main drawbacks of selecting GO as a graphene precursor resides on its poorer restoration of electrical conductivity compared to bottom-up synthesis approaches, limiting its use in electronic devices [130]. Although a different graphene precursor would be prioritised for such applications, the dispersibility and water affinity of GO still justify its selection in the water-based processing strategy from this work, still managing to achieve conductivities of 10 – 15 S m^{-1} suitable for electrical sensing capabilities [176, 182].

4.6 Enhancement of the graphene scaffolds hierarchy by decoration with alumina nanoparticles

The hierarchy of freeze-cast graphene-based aerogels was extended by the decoration of the rGO sheets with as-produced alumina nanoparticles (NPs). The sol-gel production of alumina NPs has been predominantly accomplished by employing precursors such as aluminium isopropoxide [46, 228, 229], aluminium chloride [230–232], also in penta- or hexahydrate form [233, 234], or aluminium nitrate [46, 235].

In this work, aluminium-L-lactate was selected as a promising precursor for alumina NPs due to its environmentally-friendly and non-toxic behaviour along with its possibility of delivering water-based gelation of aluminium hydroxide compatible with GO colloidal suspensions. The processing route employed in this study was inspired by former works of Zhang et al. (2003), (2007) on the production of alumina-based glasses [189, 190] and Tan et al. (2013) [236] on continuous alumina gel fibres, who produced the aluminium lactate in situ by combining aluminium nitrate and lactic acid.

According to the first works on the aluminium lactate-based approach by Zhang et al. (2007) [190], the interaction of the aluminium lactate with the $[H]^+$ from the acidic pH in default water solutions results in a positively charged ion of hexahydrate aluminium. He et al. (2019) [237] expanded the work by studying the lactate-based gel formation process across a range of pH (3 - 11). By increasing the concentration of $[OH]^-$ through ammonia additions in solution, the hydrolysis reactions triggering

the cross-linking of lactate ligands could be altered. While in the acidic medium the attack with $[H]^+$ led to the formation of a six-hydrated aluminium compound $Al(H_2O)_6$, the increase of pH leads to the substitution of lactate with hydroxide groups, obtaining a combination of $Al(lact)(OH)_2$ and $Al(lact)_2(H_2O)(OH)$ species facilitating the network formation upon polycondensation (Section 1.1.2.1). The authors concluded that decomposition of lactate ligands occurred around 250 °C, with crystallization of γ-alumina around 800 – 1000 °C after thermogravimetric analysis through the formation of Al-O-Al bonds.

4.6.1 Synthesis of alumina nanoparticles

Aluminium hydroxide gels were produced by gelation of an aluminium lactate precursor in water and converted to aluminium oxide through thermal treatment. 0.2 M lactate solutions in water exhibited by default an acidic pH typically around 3.2 - 3.4. In this acidic medium, the attack with $[H]^+$ would lead to the formation of a six-hydrated aluminium compound $Al(H_2O)_6$ as described by Zhang (2003) [189]. To facilitate the formation of aluminium hydroxide $Al(OH)_3$ instead, the concentration of $[OH]^-$ in solution was increased by shifting to a basic pH of 10 [237], which resulted in a noticeable change in the colour of the solution from clear to a cloudy white (Figure 4.26a).

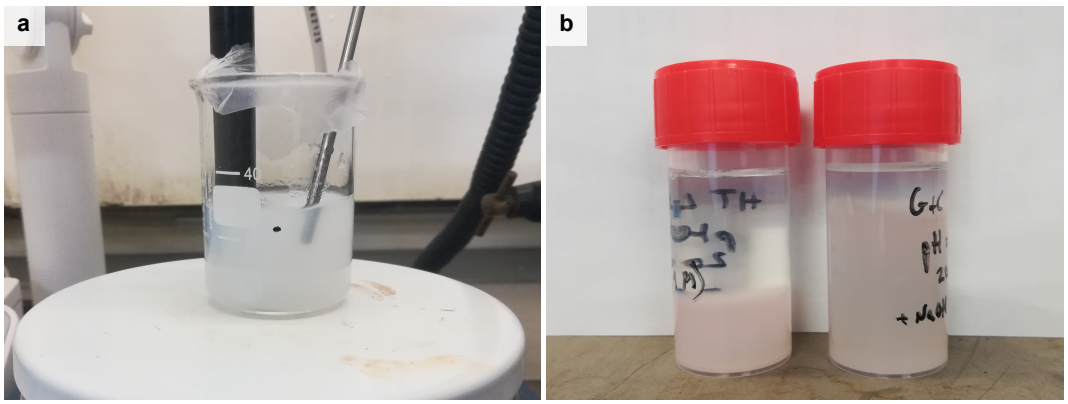

Figure 4.26: *a) Production of aluminium hydroxide gel after NaOH additions and mechanical stirring. b) Aluminium hydroxide gel at two different states of ageing, 1 week (left) vs 1 day (right) showing the evolution of the water supernatant phase.*

After ageing, the mixture appeared divided into two distinct phases: the aluminium hydroxide gel concentrating at the bottom part of the container and a supernatant phase containing the excess NaOH and H_2O in the mixture (Figure 4.26b). The low concentration of NaOH dropwise additions used for tuning the pH of the lactate sol also introduced additional water in the system, which was collected in the supernatant formed after ageing. After retrieving the water supernatant and leaving the samples for further ageing at room temperature, centrifugation of the remaining gel helped separate the extra water and obtain proper gelation of the aluminium

hydroxide network.

Aluminium hydroxide gels were thermally annealed at 900 °C in similarity with the partial reduction applied to graphene-based scaffolds and evaluated through X-ray diffraction to study the crystallographic phases of the material (Figure 4.27). The obtained pattern confirmed a mixture of aluminium oxide phases in a partially amorphous configuration, with the most characteristic 2θ peaks obtained at roughly 38, 44, 54, 72 and 79 °. Besides the amorphous structure, the γ-alumina crystallographic phase was predominantly confirmed after comparison with an XRD pattern reference from the ICDD database (00-029-0063).

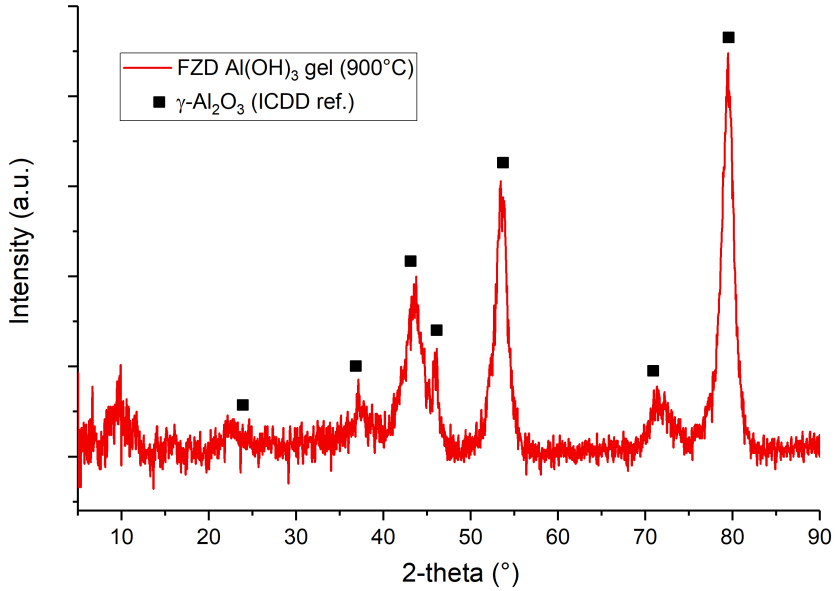

Figure 4.27: *XRD spectrum of freeze-dried aluminium hydroxide gel thermally treated at 900 °C.*

Beyond a stable α crystalline structure in the hexagonal system, alumina can exhibit other seven metastable crystallographic phases, some of which are easily induced via heat treatment through a phase transformation sequence (including temperatures of reference) [232, 238, 239]:

$$Amorphous \rightarrow \gamma(750°C) \rightarrow \delta(900°C) \rightarrow \theta(1200°C) \rightarrow \alpha \tag{4.1}$$

The γ phase is characteristic of lower consolidation temperatures (below 1000 °C) before achieving the thermodynamically stable alpha phase. This is in concordance with He et al. (2019) [237], in which gels of similar nature synthesised at pH 9 and thermally treated above 600 °C displayed a mixture of three AlO_x species: AlO_4, AlO_5 and AlO_6. However, the alumina obtained from this process is expected to reach the α phase once integrated into the composite processing strategy, because of the 1300 – 1500 °C temperatures reached during the sintering stage.

Thermogravimetric analysis of the freeze-dried aluminium hydroxide gel showed a decrease in weight at an approximate 250 °C mark, followed by a sharp secondary drop at 350 °C (Figure 4.28). This decrease was expected based on the decomposition of lactate ligands favouring Al-O-Al bonds in the compound [237], which is later accentuated by the coordination shifts of AlO_x species at progressively higher temperatures. The initial 10% reduction below 150 °C could be attributed to removing the remaining humidity and volatiles in the sample.

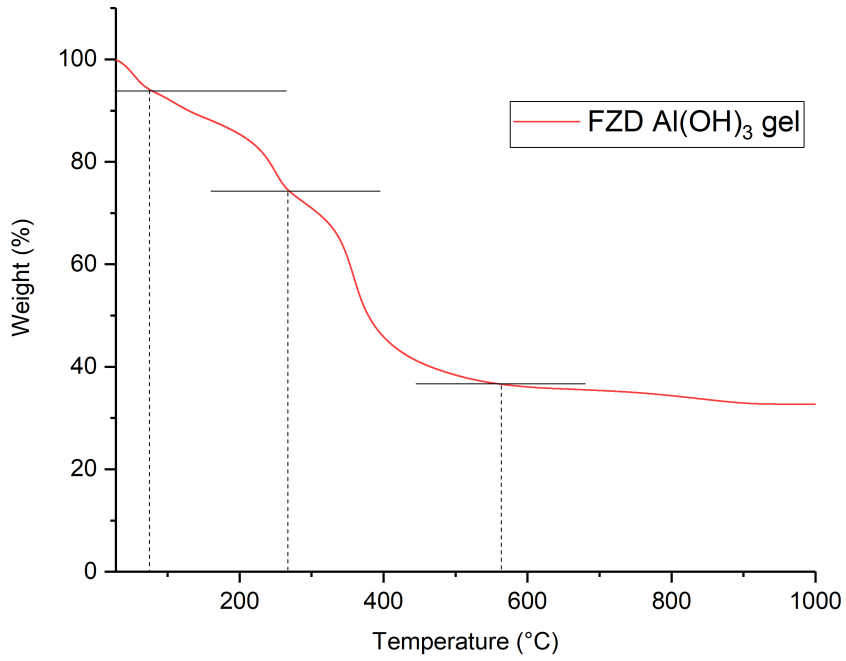

Figure 4.28: *Thermogravimetric study of the selected freeze-dried hydroxide gel. Average of three runs performed under N_2 atmosphere.*

At the 900 °C annealing temperature previously selected as the partial reduction temperature for graphene-based scaffolds, the lactate ligands are assumed to be entirely removed (as confirmed by the XRD spectrum), reaching a stable threshold above the 450 °C mark. The overall 65% decrease in weight confirmed by these TGA measurements was used to derive the calculations regarding the aluminium hydroxide added to the GO precursor to determine the alumina concentrations decorating the surface of the rGO aerogels.

4.6.2 Integration with graphene oxide suspensions

As-produced aluminium hydroxide gels were mixed with GO suspensions to produce *0.5:CU_ GO_{ag}(nN)* scaffolds. The ratio n was defined as the Al_2O_3/C wt./wt. ratio to be obtained in the aerogels after thermal reduction at 900 °C.

$$m_{graphene} = n \times m_{Al_2O_3} \tag{4.2}$$

The mass of graphene and alumina in the final material was related to their selected precursors using the previous sections' characterisation results. A 65% weight reduction from GO to rGO was assumed after partial reduction at 900 °C based on the TGA performed on *0.5:CU_ rGO_{ag}* (Figure 4.13), of which 96 wt.% was attributed to carbon material based on the XPS spectra from freeze-dried GO (*CU_ rGO_{fzd}*) also presented in Table 4.2. From the additional TGA measurements of freeze-dried aluminium hydroxide gel (Figure 4.27), a yield of 35% alumina was obtained at 900 °C, from which the following relationships were derived:

$$\begin{aligned} m_{graphene} &= 0.96 \times 0.35 \times C \times m_{GOsus} \\ m_{Al_2O_3} &= 0.35 \times m_{Al(OH)_3} \end{aligned} \tag{4.3}$$

with C being the wt/wt % of the original GO suspension.

By substitution of each variable the following relationship was identified:

$$0.96 \times 0.35 \times C \times m_{GOsus} = n \times 0.35 \times m_{Al(OH)_3} \tag{4.4}$$

The mass of aluminium hydroxide gel added to the GO suspension directly depended on the chosen Al_2O_3/C ratio n, the mass of GO suspension and its wt.% concentration C. The purity of the aluminium lactate powder used as a precursor was considered, omitting the remaining material from the calculations (95% according to the supplier), as well as the stoichiometric yield from aluminium lactate to aluminium hydroxide in the sol preparation.

The amount of lactate precursor corresponding to the calculated hydroxide gel added to the GO suspension was derived from the following assumptions:

1. 100% conversion of aluminium lactate into aluminium hydroxide in the gel (without intermediate species).
2. No aluminium lactate was lost while retrieving the water supernatant during the gel formation.
3. Homogeneous distribution of hydroxide gel in the container.
4. Water from the aluminium hydroxide gel added to the GO suspension could be negligible and did not modify the concentration of the slurry.

Three different GO/$Al(OH)_3$ suspension mixes were produced by following Equation 4.2, settling the n ratio on 0.01, 0.02 and 0.05, aiming to limit the effect on the graphene structure. To differentiate GO/$Al(OH)_3$ mixes from standard GO slurries, an updated labelling system was applied with an additional tag highlighting the n ratio of the mixture. *0.5:CU_ GO(0.01N)*, *0.5:CU_ GO(0.02N)*, and *0.5:CU_ GO(0.05N)* suspensions were freeze-dried and heated up under air up to 1000 °C to

compare the alumina residue left in the crucibles and verify the increase of hydroxide gel added to the precursor suspension. An oxidising atmosphere was selected to permit the elimination of carbon from the system. The weight of the alumina residue for each sample was contrasted by subtracting the weight of its crucible measured in advance, as shown in Table 4.4.

Table 4.4: *Relative alumina residue for each GO/Al(OH)$_3$ configuration after TGA up to 1000 °C at 5 °C min^{-1}.*

Sample Id	**Sample wt. (mg)**	**Alumina residue (mg)**	**Relative wt. of residue (%)**
0.5:CU_ GO(0.01N)	4.0	0.6	15
0.5:CU_ GO(0.02N)	4.0	0.6	15
0.5:CU_ GO(0.05N)	3.7	1.2	33

The collected data verified an increase of alumina residue between *0.5:CU_ GO(0.01N)* and *0.5:CU_ GO(0.05N)*. However, the expected evolution of alumina weight under an increasing quantity of hydroxide from *0.5:CU_ GO(0.01N)* to *0.5:CU_ GO(0.02N)* was not represented correctly, obtaining seemingly identical residue weights after thermal treatment. Visual inspection verified an increase in alumina residue remaining in the crucibles after calcination, matching the increasing $Al(OH)_3$ content added to each aerogel during freeze-casting (crucibles 3 to 5 from Figure 4.29). The discordance with the registered weights from Table 4.4 was attributed to an insufficient precision in the balance, which could not measure differences under 0.1 mg reliably.

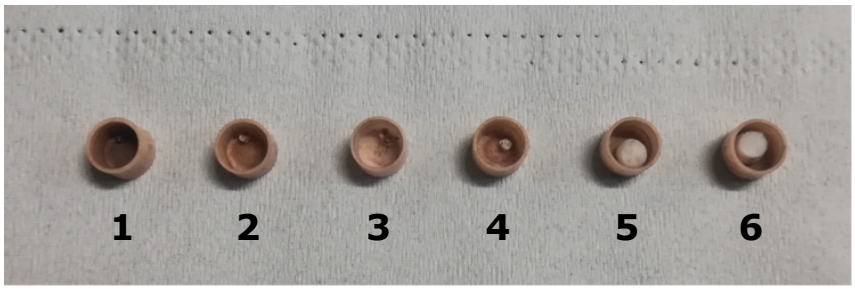

Figure 4.29: *Alumina residue in crucibles after 1000 °C carbonisation of GO/Al(OH)$_3$ aerogels on air. 1) 0.5:CU_ GO. 2,3) 0.5:CU_ GO(0.01N). 4) 0.5:CU_ GO(0.02N). 5,6) 0.5:CU_ GO(0.05N).*

4.6.3 Hierarchical graphene scaffolds decorated with alumina nanoparticles

Cylindrical graphene-based aerogels (19 mm diameter, 13 mm height) were successfully decorated with alumina nanoparticles by adding the aluminium hydroxide gel in the GO slurry formulation, following the freeze casting and carbonisation applied for *0.5:CU_ GO$_{ag}$* scaffolds. Decorated aerogels were easier to cleave and appeared

more brittle than the almost identical non-decorated aerogels that exhibited a more characteristic elastic behaviour (Figure 4.30).

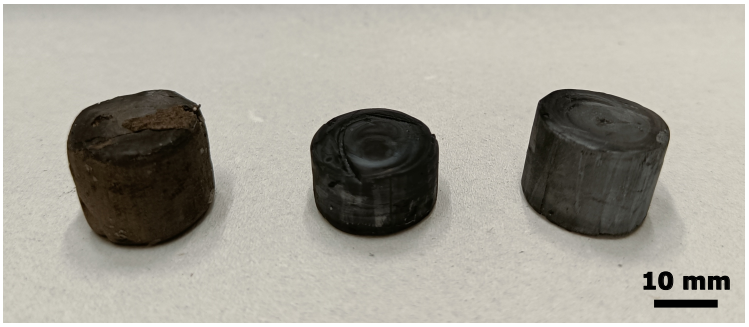

Figure 4.30: *Visual comparison of thermally reduced aerogels. Left: 0.5:CU_ -rGO$_{ag}$. Middle: 0.5:CU_ GO$_{ag}$(0.02N). Right: 0.5:CU_ GO$_{ag}$(0.05N).*

The apparent density of *0.5:CU_ GO$_{ag}$(nN)* at increasing n values before and after carbonisation is displayed in (Figure 4.31). *0.5:CU_ GO$_{ag}$(0.01N)* aerogels delivered apparent densities of 9.2 ± 0.2 mg cm^{-3} in similarity with non-decorated *0.5:CU_ GO$_{ag}$*. After thermal reduction, the densities were lowered to 2.8 ± 0.1 mg cm^{-3}, comprising a 70% reduction. *0.5:CU_ GO$_{ag}$(0.02N)* and *0.5:CU_ GO$_{ag}$(0.05N)* aerogels reached progressively higher densities because of the increase in aluminium hydroxide gel mixed with the GO suspension, (10.0 ± 0.1 and 12.1 ± 0.1 mg cm^{-3} respectively), leading to 3.2 ± 0.1 mg cm^{-3} and 4.2 ± 0.05 mg cm^{-3} after carbonisation. Both configurations resulted in a 68% and a 60% reduction of density, respectively. These values of density reduction contrast the 52% reduction obtained for non-decorated *0.5:CU_ rGO$_{ag}$* aerogels (Section 4.5.1).

Although the self-supporting capabilities of GO aerogels were not affected by the extra weight additions of aluminium hydroxide gel during freeze-casting, the additional density reductions could be explained by the carbonisation process, removing more material from the graphene scaffold because of the transformation of aluminium hydroxide into alumina nanoparticles.

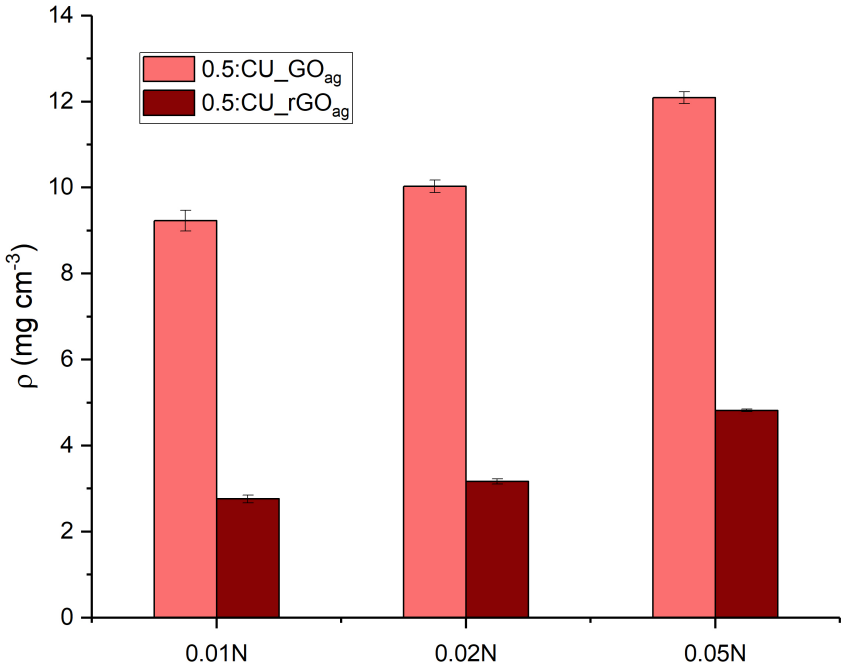

Figure 4.31: *Comparison of apparent densities of 0.5:CU_ GO_{ag}(nN) aerogels before and after thermal annealing as a function of the Al_2O_3/C ratio n of nanoparticles (n = 0.01 - 0.05).*

The extent of reduction in the graphene sheets has an acute effect on the aerogel densities obtained due to the carbonisation step, closely related to the sp^2:sp^3 hybridisation ratio in the materials. XPS characterisation was applied to each of the deposited configurations (*0.5:CU_ rGO_{ag}(0.01N)*, *0.5:CU_ rGO_{ag}(0.02N)* and *0.5:CU_ rGO_{ag}(0.05N)*) to determine the evolution of this sp^2:sp^3 ratio and additionally evaluate the crystallization of alumina structure after carbonisation and quantify its atomic percentage in the scaffolds. After comparing the relative atomic percentage of the main elements present in the reduced scaffolds (Table 4.5), an expected increase of aluminium element was confirmed from 0.9 to 4.3 at.%. in *0.5:CU_ rGO_{ag}(0.01N)* and *0.5:CU_ rGO_{ag}(0.05N)*.

Table 4.5: *Relative at.% of detected elements by the XPS general survey of 0.5:CU_ rGO_{ag} scaffolds. Al_2O_3/C ratio n of nanoparticles increased from 0.01 to 0.05.*

Sample	Relative at. %						
	C	**O**	**Al**	**S**	**Na**	**Si**	**N**
0.5:CU_rGO_{ag}	94.2	3.5	0	0.5	0.2	1.6	0
0.5:CU_rGO_{ag}(0.01N)	94.8	2.9	0.9	1.2	0.2	0	0
0.5:CU_rGO_{ag}(0.02N)	95.3	2.5	1.2	0.4	0	0	0.5
0.5:CU_rGO_{ag}(0.05N)	87.1	7.9	4.3	0.1	0.4	0	0

The change in aluminium content displayed by the XPS analysis remarked the differences in alumina content deposited in *0.5:CU_ rGO_{ag}(0.01N)* and *0.5:CU_ rGO_{ag}(0.02N)* aerogels, which was anticipated from the analysis of apparent density

although not verified by the alumina residue comparison presented in Table 4.4. The oxygen content also appeared remarkably higher in *0.5:CU_ rGO_{ag}(0.05N)*, in contrast with the other two configurations. Despite the apparent oxygen contribution from higher alumina deposition in the structure, it could also represent a lesser removal of oxidised groups attached to the graphene oxide flakes during thermal annealing in these aerogels. Silicon impurities were not detected in any of the examined aerogels. Binding energy peaks for other components such as S, Na, and N were detected and included in the relative atomic disclosure. These components, however, were also expected to appear as a result of the early oxidation stages from GO synthesis based on Hummers method (Section 1.4.2.1) [127].

The XPS C1s spectra from each *0.5:CU_ rGO_{ag}(nN)* formulation after increasing the Al_2O_3/C ratio was compared and displayed in Figure 4.32.

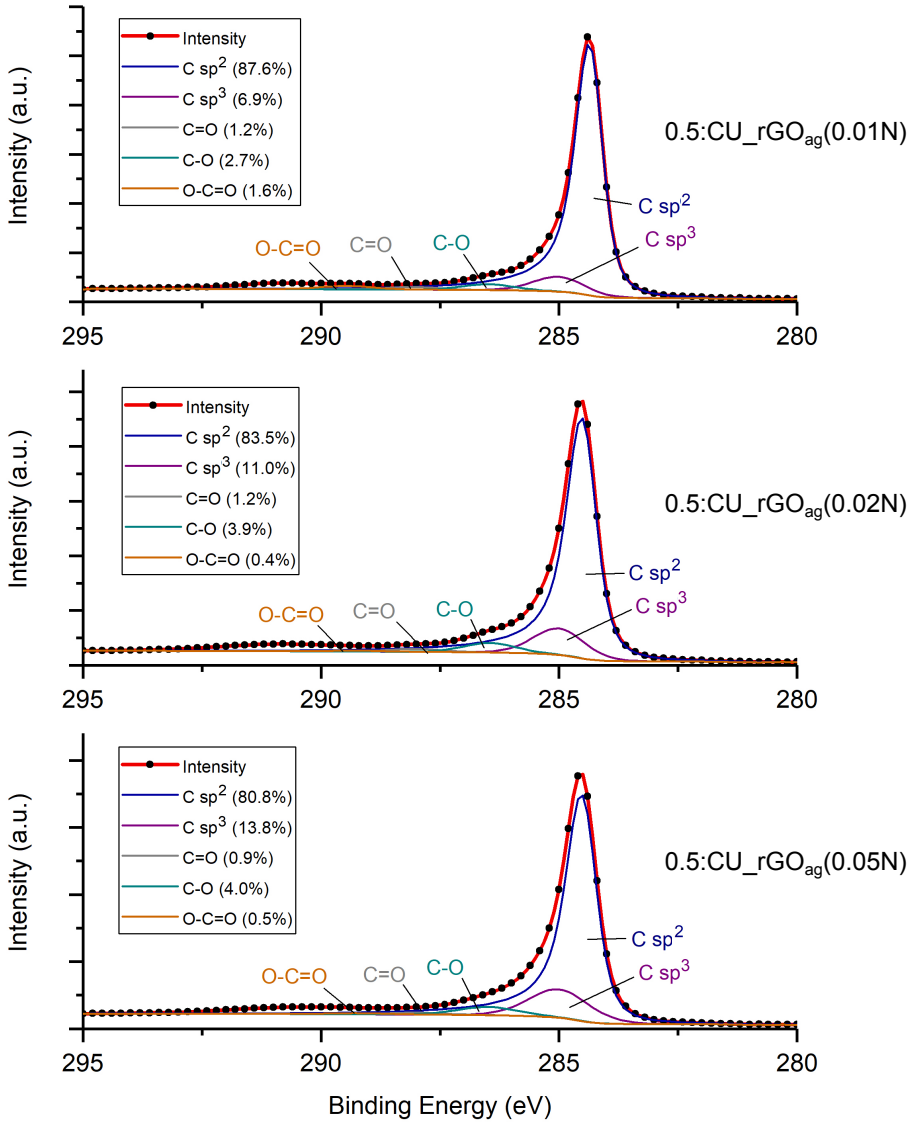

Figure 4.32: *Comparison of XPS C1s spectra for 0.5:CU_ rGO_{ag}(nN) with increasing Al_2O_3/C ratio n (top = 0.01, middle = 0.02, bottom = 0.05).*

As in plain *0.5:CU_rGO$_{ag}$* aerogels, the epoxide, carbonyl and carboxyl groups binding energies were obtained at 286.0, 287.0 eV and 288.6 eV approximately, with minimal contributions as a result of the reduction step at 900 °C. Increasing the Al_2O_3 content in 0.01N, 0.02N, and 0.05N scaffolds resulted in a reduction in the carbon sp^2:sp^3 hybridisation ratio of 12.7, 7.59 and 5.9 respectively. This suggests that higher additions of aluminium hydroxide gel in the GO slurry could inhibit the restoration of the graphitic sp^2 domains in the GO sheet, maintaining a higher percentage of GO's original sp^3 carbon.

The binding energies from O1s spectra were also compared and presented in Figure 4.33. A peak at 531.5 eV increased in percentage with Al_2O_3 content in 0.01N, 0.02N and 0.05N scaffolds, attributed to the increased quantities of aluminium oxide decorating the aerogels despite the minor contribution of oxygen to the general surveys (Table 4.5). This signal masked the carbonyl peak found in non-decorated *CU_rGO$_{ag}$* at similar binding energies (Figure 4.6). The deconvolution between the hydroxyl and the epoxide groups was found at approximately 532.5 and 534 eV.

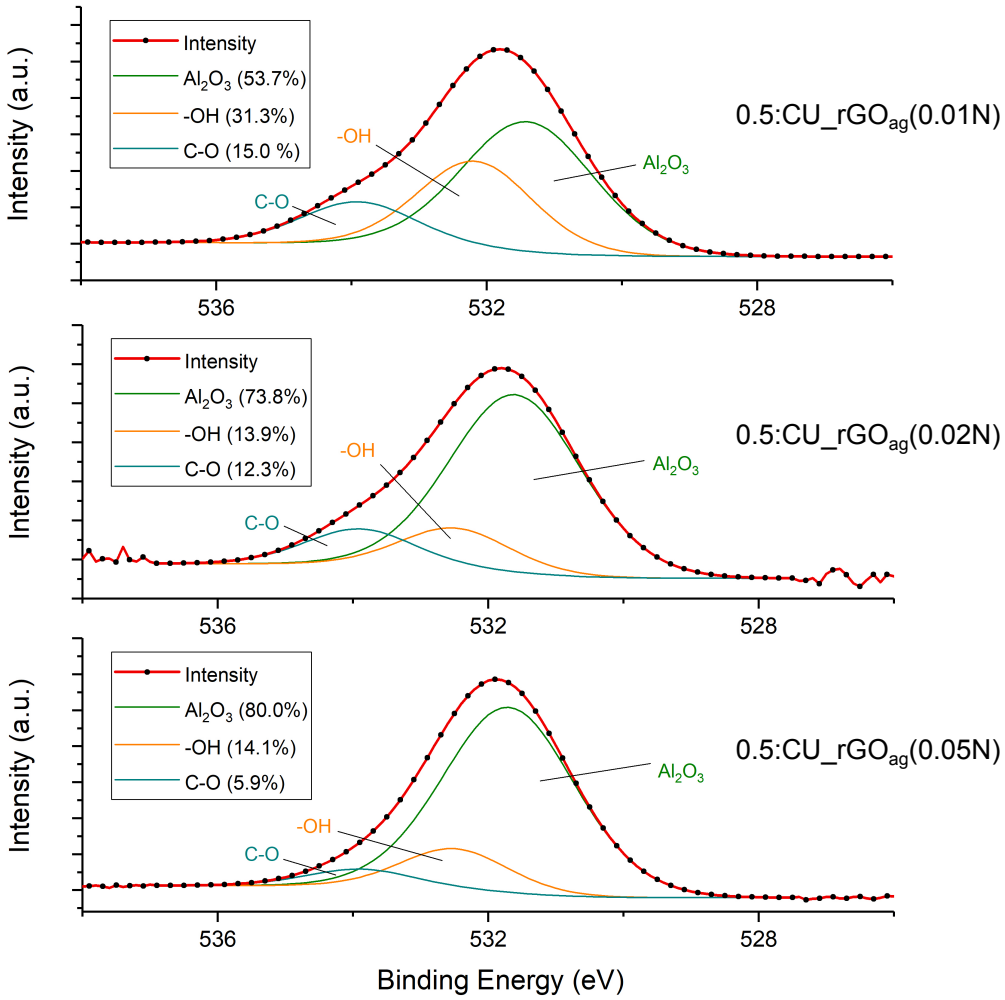

Figure 4.33: *Deconvolution of XPS O1s spectra for 0.5:CU_rGO$_{ag}$(nN) (top = 0.01, middle = 0.02, bottom = 0.05).*

The Al2p spectra were examined to determine the oxidation state of aluminium in the aerogel, with *0.5:CU_ rGO_{ag}(0.05N)* presented as an example in Figure 4.34. The deconvolution of the signal resulted in one single $2p$ peak, yielding two different signals ($2p^{1/2}$ and $2p^{3/2}$) with pre-defined area ratios. This is a characteristic trait for p orbitals called spin-orbit splitting [240], relating to the parallel or anti-parallel coupling between the electron spin and the defining vector of the orbital angular momentum.

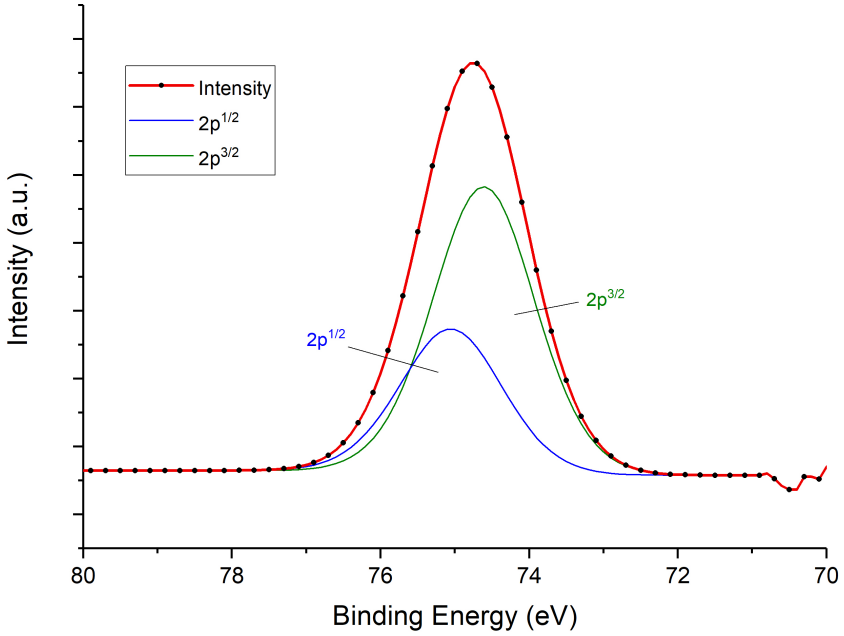

Figure 4.34: *Al2p binding energy for 0.5:CU_ rGO_{ag}(0.05N), deconvoluted in $2p^{1/2}$ and $2p^{3/2}$ peaks.*

The binding energy of the $2p$ peak was obtained at 74.7 eV. This matches the characteristic peak of γ-alumina reported at 74.6 eV [241], which was anticipated by the XRD measurements on aluminium hydroxide gel presented in Figure 4.27. This analysis of the $2p$ spectra verified that the aluminium hydroxide from the precursor was not transformed into the aluminium metal instead of alumina, which was considered based on the inert atmosphere applied during carbonisation of the rGO scaffolds at 900 °C.

The internal structure of all configurations of decorated *0.5:CU_ rGO_{ag}(nN)* was observed under FESEM to confirm the morphology and distribution of the alumina nanoparticles on the graphene network, compared with aerogels processed without alumina decoration. Each configuration's internal structure was highly dependent on the aerogels cutting and deposition direction, with the two representative images for each of the three mixing conditions displayed in Figure 4.35.

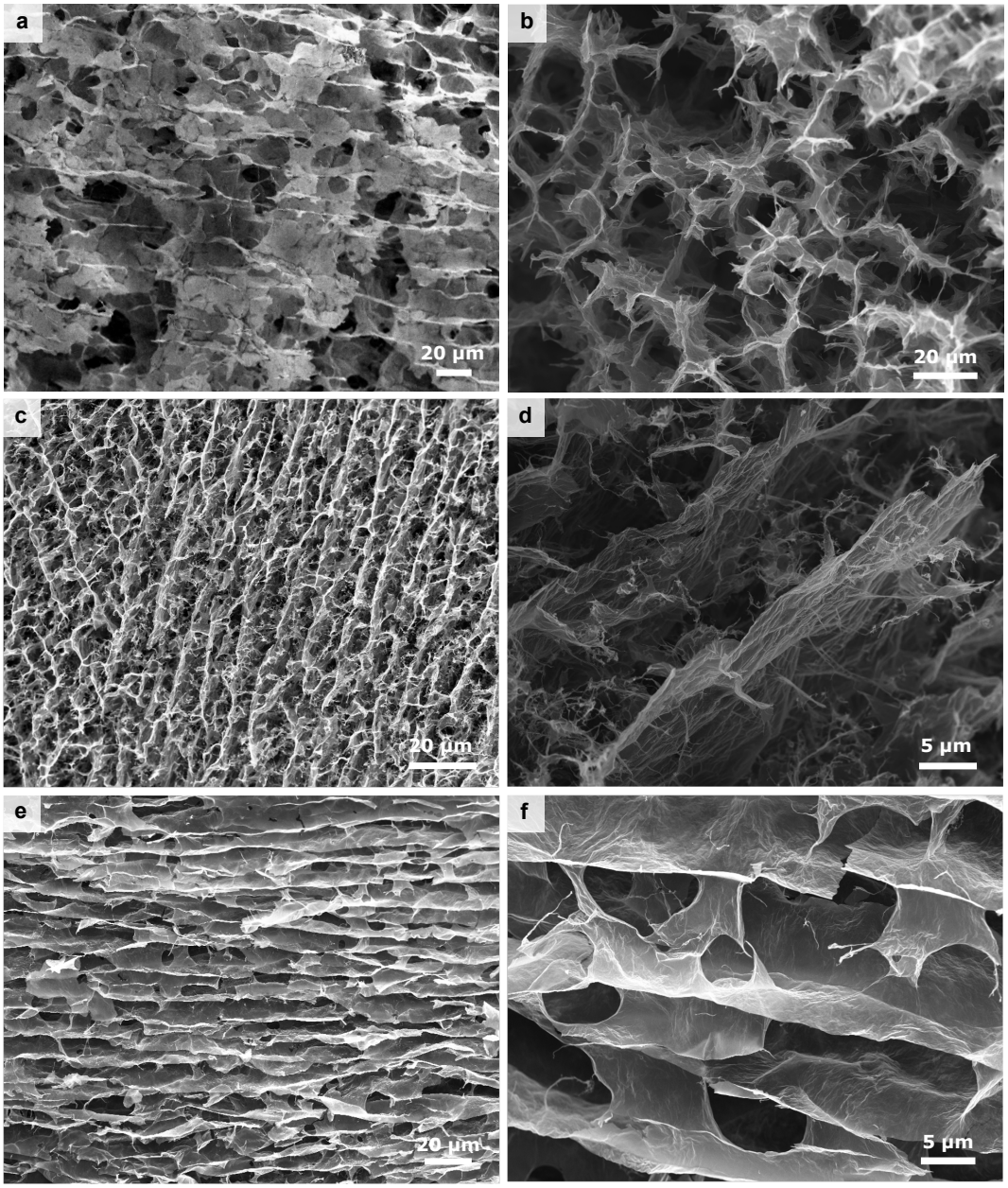

Figure 4.35: *Internal structure of graphene-based aerogels decorated with alumina nanoparticles at low magnification by FESEM. (a, b) 0.5:CU_rGO_{ag}(0.01N) (c, d) 0.5:CU_rGO_{ag}(0.02N) (e, f) 0.5:CU_rGO_{ag}(0.05N)*

All three configurations maintained the expected directional alignment provided by the freeze-casting processing. Despite exhibiting partial damage to the scaffold internal structure, unidirectionally aligned channels of 10 - 25 μm width were preserved for every condition, as expected from the selected 5 °C min^{-1} freezing rate and starting GO concentration in the slurry [152]. In *0.5:CU_rGO_{ag}(0.01N)* aerogels (Figure 4.35a,b), the perpendicular cross-section validated the honeycomb-like structure previously presented for *0.5:CU_rGO_{ag}* without any NP addition. Due to the low level of deposited alumina NPs, the internal structure of these aerogels closely resembled non-decorated aerogels. This contrasted with the structure of *0.5:CU_rGO_{ag}(0.02N)* (Figure 4.35c,d), which appeared significantly affected. Al-

though maintaining an overall freeze-casting alignment (with reduced channel widths of 5 – 15 μm), wrinkled and shredded graphene sheets were prominent. This change in the morphology could result from NaOH additions introduced in the preparation of GO/$Al(OH)_3$ mixes because of the pH tuning of the hydroxide gels, resulting in substantial deterioration of the expected unidirectional structure.

0.5:CU_ rGO_{ag}(0.05N) aerogels (Figure 4.35e,f) mainly shown the preservation of a unidirectional freeze-cast structure, highlighting the compatibility of the alumina NP decoration with the intended hierarchical structuring of the scaffolds. These aerogels could be easily cut parallel to the freeze-casting direction because of the reduced elasticity from containing the highest quantities of alumina in the formulation. Although maintaining the expected channel widths (10 - 20 μm), graphene sheets appeared partially damaged at higher magnifications (Figure 4.35e,f), potentially due to the increased weight of alumina in the suspension.

The alumina NPs decoration was examined more closely by FESEM of higher magnification (Figure 4.36). The deposited particles appeared homogeneously distributed throughout the graphene flakes of *0.5:CU_ rGO_{ag}(nN)* scaffolds upon verifying several locations of the aerogels.

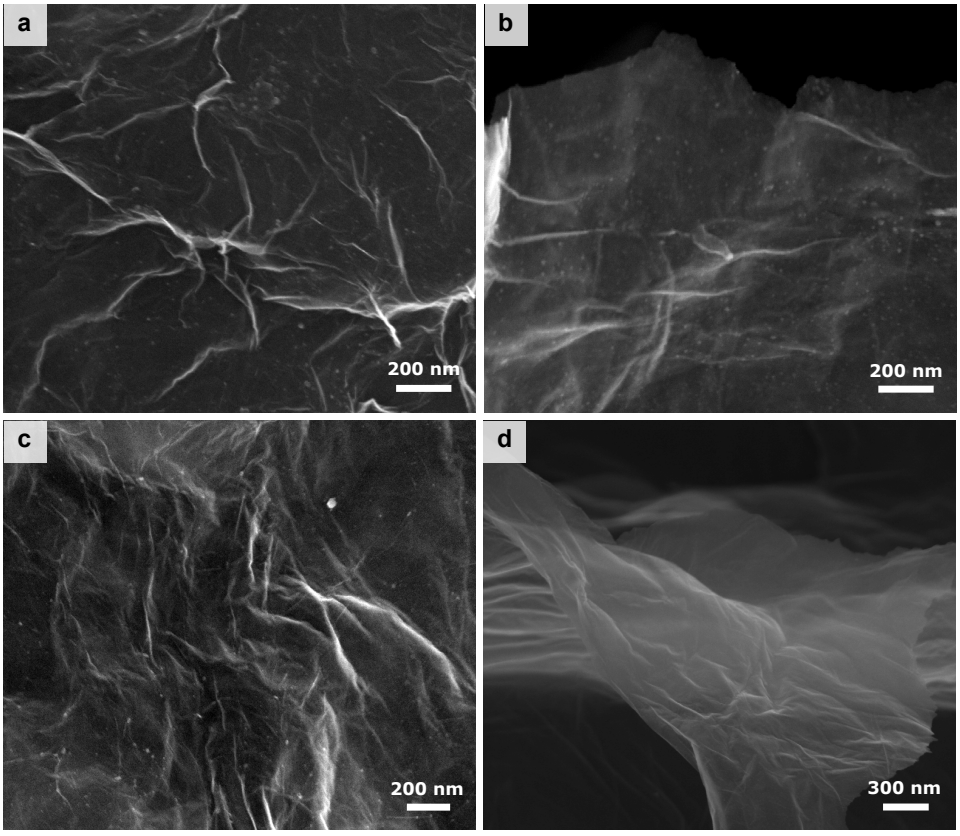

Figure 4.36: *High-magnification FESEM images of as-produced alumina nanoparticles deposited on the rGO flakes in a) 0.5:CU_ rGO_{ag}(0.01N) aerogels, b) 0.5:CU_ rGO_{ag}(0.02N) aerogels and c) 0.5:CU_ rGO_{ag}(0.05N) aerogels. d) High-magnification of rGO sheets from non-decorated 0.5:CU_ rGO_{ag} scaffolds.*

From these FESEM images, the increase of alumina NP content in the scaffolds was not translated into a change in the decoration profile (although the variations in alumina content have already been presented as part of the XPS analysis). For comparison purposes, an rGO flake from a non-decorated *0.5:CU_ rGO_{ag}* scaffold has been included (Figure 4.36d), in which no particles or additional impurities could be identified in the sheet surface at similar magnification range. This confirmed the positive outcome of adding the aluminium hydroxide species to a highly oxidised graphene precursor in combination with speed mixing and selecting an adequate slurry formulation.

The alumina NPs also appeared remarkably smaller than initially anticipated ($<$ 20 nm) based on previous works on the deposition of ceramic nanoparticles via gelation and thermal treatment (around 100 nm from Wang et al. (2016) [108]). The small size of the as-produced particles hindered its thorough examination using FE-SEM, only identified above 40 kX magnification resulting in higher picture blurriness. Additional techniques of higher resolution, such as transmission electron microscope (TEM), would be required to examine the morphology of the as-produced nanoparticles in further detail. As *0.5:CU_ rGO_{ag}(0.05N)* rendered decorated graphene sheets with higher alumina content without inducing structural damage to the scaffolds, this formulation was selected for future steps.

Aiming to put into perspective the enhanced strategy of nanoparticle production developed in this work, analogous decorated rGO aerogels were prepared with commercial water-based nano-alumina suspensions in the 0.5 wt.% *CU_ GO* precursor slurry and following similar processing steps. Although the commercial nanoparticles decorated the graphene scaffolds homogeneously due to the intense speed-mixing applied, FESEM imaging of these newly produced scaffolds (labelled as *CU_ rGO_{ag}(US-N)*) showed how the deposited commercial nanoparticles appeared in the range of 50 - 150 nm size, much larger than previous as-synthesised nanoparticles (Figure 4.37). Commercial alumina particles still exhibited some degree of agglomeration, contrasting with the as-produced alumina nanoparticles from the aluminium hydroxide gel.

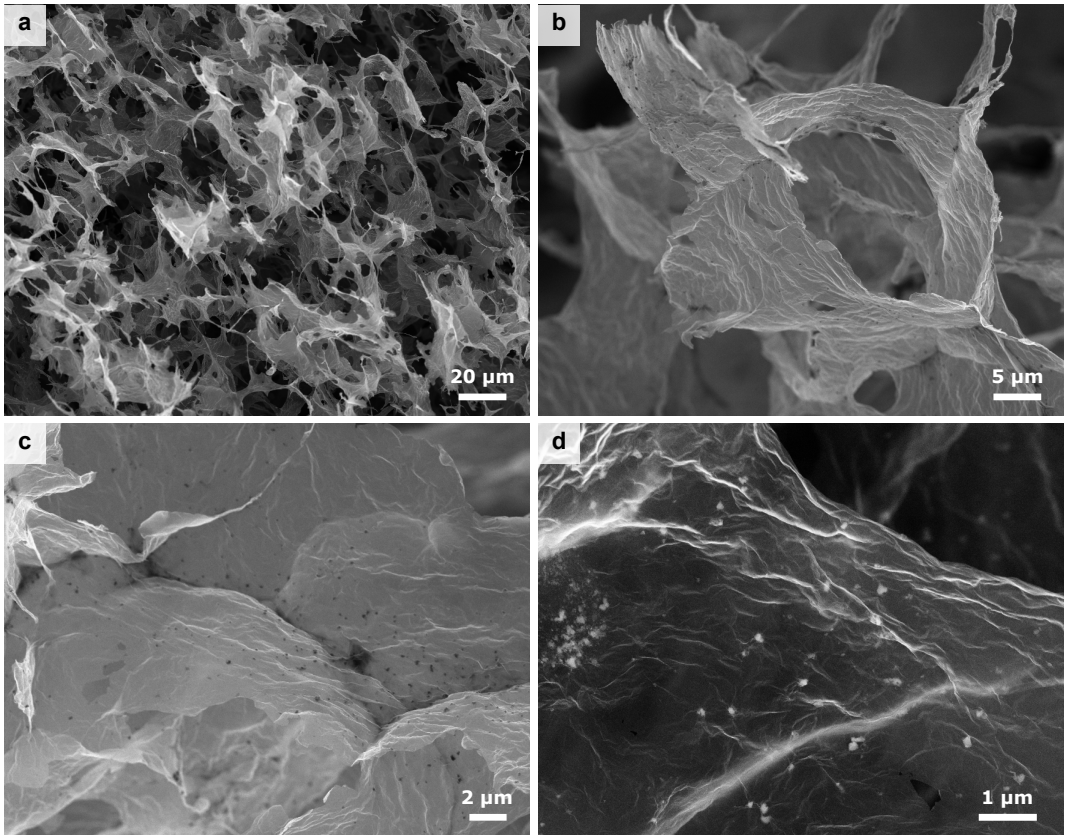

Figure 4.37: *Collection of FESEM images from CU_rGO_{ag}(US-N) scaffolds decorated with 2 wt.% commercial alumina nanoparticles. a) Freeze-cast structuring. b,c,d) Higher magnification images exhibiting the increased size of the decorating particles.*

Although alumina nanoparticles are available commercially in several formats and could be alternatively selected, there are various advantages in producing the particles in-situ using the aluminium lactate precursor route described in this chapter. Beyond the intrinsic benefit of validating a scarcely explored precursor route for novel applications, the particle size obtained from each route is significantly different. Via the aluminium lactate-based synthesis, nanoparticles of substantially reduced particle size could be produced and homogenously distributed across the graphene flakes. It also enables an environmentally-friendly water-based approach without the formation of toxic agents (e.g. chlorine in the case of aluminium chloride-based synthesis [231, 232]).

This processing technique could be extended to the deposition of other ceramic nanoparticles such as titania or silica by integrating analogous lactate-metal compounds in the formulation GO slurries, with additional applications in the field of catalysts and drug-carriers based on the reduced dimensions of the produced NPs beyond the processing of structural composites that is the aim of this work. By providing an extra layer of hierarchy in the composite, a positive effect on the mechanical properties of the envisioned graphene/ceramic material could be expected by providing extrinsic toughening mechanisms [15]. Additionally, the introduction

of bimodal alumina (from mixing the as-produced alumina NPs and water-based alumina slurry) could increase the densification of the composite during sintering, as seen in works of similar nature [184]. To evaluate the effect of the NP-deposition on the material's properties, it is first necessary to achieve consolidation of the bulk composite and subject it to further characterisation and testing.

4.7 Conclusions

Two different graphene precursors: *CU_GO* (commercial supply) and *ICL_GO* (produced from Imperial College London through an improved Hummers method [148]) were used to produce water-based GO suspensions, comparing their GO flake lateral size, and elemental composition. Extended characterisation (XRD, TGA, Raman, XPS and viscosity measurements) was applied to *CU_GO*, selected as the testing precursor throughout this work based on its higher availability.

The conformation of ultralight rGO aerogels up to 30 mm in diameter by freeze-casting and carbonisation to 900 °C was validated in this chapter. A range of 1.5 – 4 mg cm^{-3} rGO aerogels was successfully produced, adjusting the formulation parameters to 0.25 - 0.5 wt.% GO concentration in water, 0.5:0.5 ratio of PVA:sucrose additives to GO solid content and 5 °C min^{-1} freezing rate. The structural alignment of rGO aerogels produced from 0.5 wt.% GO suspensions was maintained, displaying channel widths of 15 – 30 μm, whilst scaffolds made from 0.25 wt.% GO experienced higher structural disruption due to insufficient solid material in suspension.

Scaled-up 30 mm aerogels were successfully freeze-cast using an improved 4-piece mould concept in which the alignment direction of the produced scaffolds was perpendicular to the geometry's axis of revolution. This upgrade permitted the integration of scaled-up aerogels with a later sintering stage without crushing the tailored structure, otherwise caused by the alignment of the freezing and sintering pressure directions. Scaled-up *ICL_GO* aerogels also demonstrated the effect of PVA and sucrose additions in the GO suspension formulation to preserve their integrity and self-standing behaviour. Graphene/epoxy composites were produced by resin infusion of rGO aerogels setling a preliminary infiltration procedure for future graphene/alumina composites and producing specimens for electrical conductivity testing. The specimens displayed an electrical conductivity of 10 – 15 S m^{-1} along the freezing direction, confirming the effective reduction of the rGO aerogels at 900 °C and the preservation of directional alignment in the composite.

An additional level of hierarchy was implemented by deposition of as-synthesised alumina nanoparticles through a promising sol-gel route based on an aluminium lactate precursor. An aluminium hydroxide gel was obtained by gelation of a lactate sol and integrated with GO suspensions at various mixing ratios. rGO aerogels were homogeneously decorated with alumina nanoparticles under selected C/Al_2O_3

wt./wt. ratios verified by XPS (0.01 – 0.05) maintaining the alignment obtained through freeze-cast processing. FESEM characterization confirmed the as-produced nanoparticles (< 20 nm) were smaller in size and better distributed than commercial alternatives under similar conditions, produced at lower cost and through a water-based approach.

Chapter 5

Infiltration of graphene-based scaffolds with alumina/PF127 slurries

5.1 Introduction

The production of hierarchical graphene/ceramic composites using a scaffold and infiltration approach has not been presented in the literature other than by exploiting polymer-derived ceramic matrices [14, 176]. Through this method, a polymeric matrix can infiltrate the graphene aerogel in similarity with epoxy/graphene pairings (readily reported in recent years), later transformed into a ceramic phase by pyrolysis at higher temperature [185]. This promising approach cannot be extended to the infiltration of water-based advanced ceramic slurries due to the hydrophobic (water-repelling) behaviour of graphene aerogels after carbonisation.

This chapter studies the introduction of an amphiphilic additive (a triblock copolymer commercially labelled Pluronic-F127) in the ceramic formulation to overcome the critical challenge of graphene's hydrophobicity (Figure 5.1). Additions of PF127 can modify the alumina surface interaction, inspired by its use as a surfactant in traditional ceramic processing and its recent surge in popularity as a particle carrier upon higher loadings in 3D-printing inks [36, 213, 242].

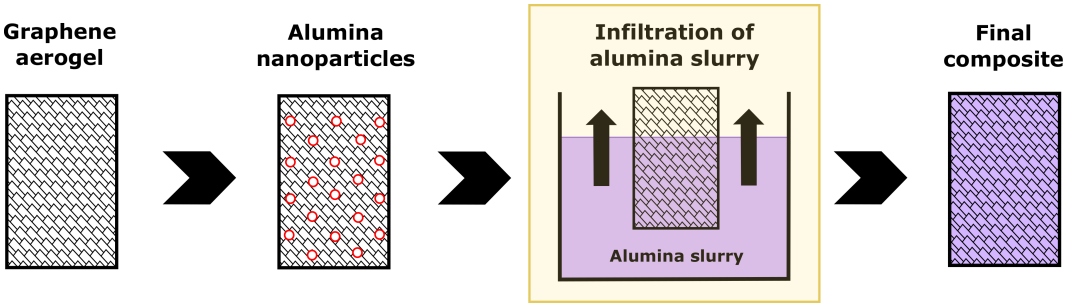

Figure 5.1: *Second stage of the composite processing strategy: Optimising the infiltration of graphene-based scaffolds with water-based alumina slurries.*

After characterisation of the alumina powder selected in this work, water-based Al_2O_3 slurries were produced with varying PF127 content in solution. Wettability measurements between spin-coated graphene-based films and alumina slurries with PF127 in their formulation were performed to evaluate the effect of the copolymer additions. The optimisation of alumina solid loading and PF127/Al_2O_3 ratio in the slurries was studied in more depth by infiltration tests on cylindrical lab-scale sized graphene aerogels and alumina slurries prepared from a range of formulations. The selected conditions were extended to scaled-up graphene aerogels of 30 mm diameter to obtain graphene/alumina green bodies ready for final densification via SPS sintering.

5.2 Background on Pluronic F-127

5.2.1 Structure and properties

Pluronics are commercially labelled triblock copolymers containing polyoxyethylene (hydrophilic external chains) and poloxypropylene (hydrophobic central chain) in the form of $[PEO]_a$-$[PPO]_b$-$[PEO]_a$ (Figure 5.2). The a and b subscripts in the formulation refer to the series of groups concatenated in the chain, which vary depending on the Pluronic type. The notation of the Pluronic starts either with L (liquid), P (paste) or F (flakes), with the first two numbers referring to the molecular weight of the [PPO] unit, and the last number signifies the weight fraction of the [PEO]. Pluronic F127 has been used throughout this work, with a and b comprising 101 and 56 groups, respectively.

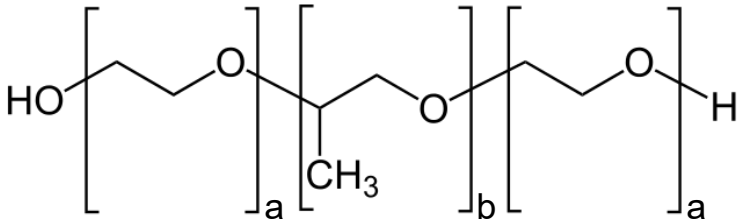

Figure 5.2: *Depiction of triblock copolymer chain in Pluronics ($[PEO]_a$-$[PPO]_b$-$[PEO]_a$).*

Pluronics are known for their thermoresponsive behaviour and amphiphilic properties owing to the mix of hydrophobic and hydrophilic groups in its formulation [35, 243]. These copolymers have been conventionally used as surfactants [244], drug-delivery carriers (0.5 - 2 wt.% of solid material) and for wound or burn healing purposes in the field of pharmaceutics [245]. PF127, in particular, has become a widespread selection because of its good colloidal stability, low toxicity and ability to reverse thermal gelation.

PF127 combines high molecular weight and large size of hydrophobic PPO chains, exhibiting an adaptative rheological behaviour with tendency to self-assemble into micelles upon reaching a critical concentration in suspension. This concentration is addressed in the literature as the critical micelle concentration (CMC), a temperature-dependent property established at 0.45 wt.% at 25 °C in the case of PF127 [246]. Above this concentration threshold, a phenomenon of dehydration occurs in the central PPO blocks, attracting neighbouring PPO blocks that act as the core of newly formed micelles with the PEO external chains creating the micelle's outer surface [243]. Therefore, the ability of the triblock copolymer to self-assemble in micelles is highly dependent on the hydrophobic PPO units, with the hydrophilic ending blocks not having a substantial role in the process beyond increasing the molecular weight of the copolymer [247].

The combination of high molecular weight along with higher concentrations of the copolymer in water can lead to massive cross-linking if activated by sufficient temperature, which removes the hydration layer covering the PF127 molecules [248]. When micellisation achieves a critical volume fraction, a change of viscosity occurs in the solution [247] because of the increase in the freely available dehydrated groups of the copolymer.

Lenaerts et al. (1987) [35] conducted a rheological study of 15 – 30 wt.% PF127 aqueous solutions from 15 to 30 °C, finding an exponential relationship between viscosity and temperature with a slope dependent on the concentration of Pluronic (Figure 5.3). An initial decrease in viscosity of the samples is first shown, which is related to a rise in the activation energy in similarity with other colloidal systems. The second part corresponds to the gelation of the Pluronic system when the concentration is increased, and it is associated with conformational changes in the polymer.

This gelation process is fully reversible after returning to 4 – 5 °C [245].

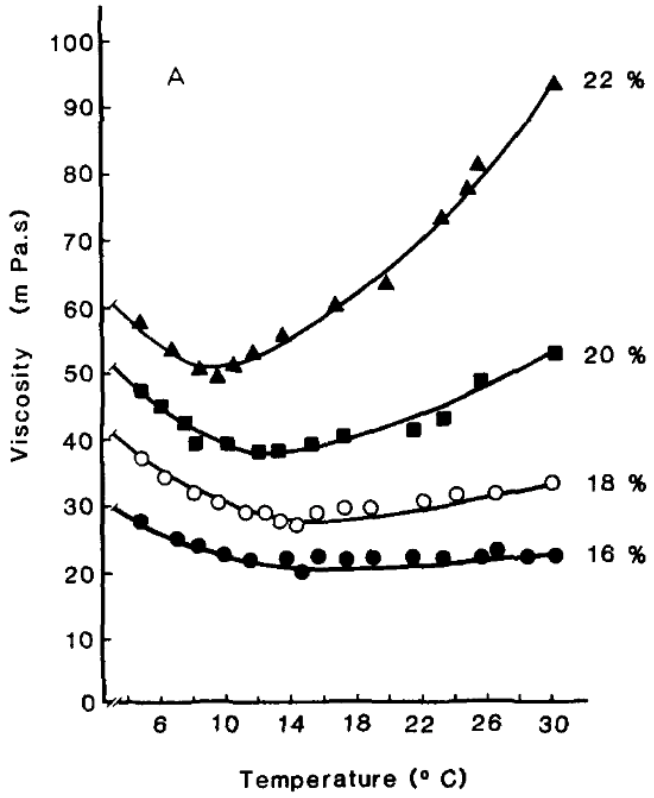

Figure 5.3: *PF127 thermoreversible gelation as a function of temperature and concentration in water. From Lenaerts et al. (1987) [35].*

5.2.2 PF127 resurgence for 3D-printing applications

The thermoresponsive behaviour of triblock copolymers has been known for more than 30 years generally applied as surfactants ($<$ 2 wt.% of solids in suspension). Pluronics have been re-explored during the last decade at higher concentrations (above 15 wt.%) in the robocasting field (robotic-assisted deposition) by exploiting their amphiphilic behaviour and thermoreversible gelation capabilities for manufacturing 3D inks [36, 213, 242, 249].

The seed for this application was proposed by Franco et al. (2010) [242], who prepared water-based calcium phosphate 3D-printing inks using PF127 solutions. The addition of the copolymer permitted obtaining high-loading ceramic inks that displayed a shear-thinning behaviour (decrease of viscosity under shear strain conditions), flowing through the printing nozzle and settling after deposition. Once deposited, the high concentration of Pluronic in the inks (20 – 30 wt.%) at room temperature led to the system gelation, providing self-standing printed lines.

PF127-based robocasting works have been expanded since, with other notable reports improving the working conditions and extending the technique to other ma-

terials. Muller et al. (2015) [249] applied a nano-structuring strategy to PF127-based inks to enhance cell encapsulation capabilities and enable 3D-printing of biologically relevant materials). Feilden et al. (2016) [36] applied PF127 to 3D-printing of 40 vol.% advanced ceramic inks based on Al_2O_3 and SiC and demonstrated the mechanical properties of the sintered printed parts. The authors provided a viability map (Figure 5.4) that narrowed the printing conditions incorporating the most significant limitations. The strength and toughness displayed by 3D-printed alumina parts after sintering (18.6 GPa and 3.31 MPa $m^{1/2}$ respectively) were slightly lower but comparable to commercially available materials.

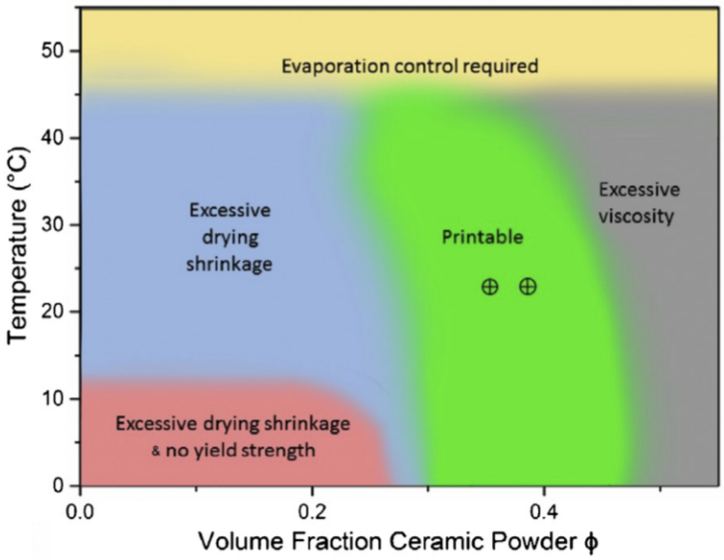

Figure 5.4: *Viability map for SiC and Al_2O_3 ink highlighted in the printable domain. From Feilden et al. (2016) [36].*

Graphene-based inks have also been recently explored by exploiting PF127's thermoresponsive capabilities. Garcia-Rocha et al. (2017) [213] produced electrically conductive reduced graphene oxide (rGO) electrodes for electrochemical energy storage applications by one-step printing of mixed materials using GO/PF127 and copper/PF127 inks. GO inks were prepared using a 25 wt.% PF127 solution, adding the as-prepared GO flakes on a GO/PF127 weight ratio of 1:1. The 3D-printed 0.4 mm filaments exhibited adequate viscoelastic flow at room temperature and maintained their consistency upon freezing, freeze-drying and thermal reduction. Similarly, $3D$-printed GO, and GNP filaments were prepared by Moyano et al. (2019) [250] from inks containing 30 wt.% of PF127 in water (in their work, Poloxamer 407, a different proprietary name), resulting in electrical conductivity of 2470 and 860 S m^{-1} for GNP and GO filaments, respectively.

Even if applied to the field of 3D-printing and robocasting, these last works highlight the possibilities of integrating amphiphilic PF127 with chemically-derived graphene precursors as a promising agent to help translate graphene's $2D$ potential into a $3D$ setting for integration with ceramic-based composites.

5.3 Methodology

5.3.1 Alumina slurry preparation and characterisation

Commercial alumina powder was first characterised via helium pycnometry to determine its density and XRD for its crystallographic phase and degree of crystallinity. The physical state and aggregation of the as-received powder were evaluated by FESEM, also serving as initial estimations of particle size using an average of 50 particles per area of examination. More thorough particle size measurements were obtained by wet laser diffraction of the powder.

Water-based alumina suspensions up to 25 wt.% Al_2O_3 solid loading were prepared by suspending alumina powder in DI H_2O and PF127 mixtures. The obtained PF127/Al_2O_3 wt./wt. ratio in suspension was labelled as $Al_2O_3(r\text{P})$, with r being 0, 0.07 and 0.15. The alumina slurries were prepared by first dissolving the PF127 copolymer in DI H_2O, preparing batches of 1, 5 and 15 wt.% in H_2O. PF127/H_2O mixtures were kept in a fridge at 5 °C for at least 24 hours without stirring to prevent excessive foaming. Once fully homogenised, the calculated quantities of alumina were added to the mixture on a precision scale, speed-mixed for 10 minutes until complete homogenisation. Due to the micellisation of PF127 [243, 247], some degree of foaming was expected to occur during the mixing process, although partially controlled by the application of speed-mixing steps.

A 24 h ball-milling step was applied to the alumina slurries after preparation. Its effect on the deagglomeration of 25 wt.% Al_2O_3(0P) suspensions was evaluated through particle-size analysis and viscosity measurements using a rotational viscometer. Extended viscosity measurements were applied to 12.5 and 25 wt.% Al_2O_3 suspensions with a progressive increase in the PF127/Al_2O_3 ratio (0P, 0.07P and 0.15P), under a rotation speed range of 5 - 250 rpm and an average spindle torque of 50 - 80% at 20 °C.

5.3.2 Wettability tests for graphene/alumina pairs

The wettability of water-based alumina slurries on graphene-based materials such as GO and partially reduced GO was studied by contact angle measurements via the sessile drop technique (Section 3.4.1.7). The contact angle (CA) between droplets from various PF127/Al_2O_3 suspensions and spin-coated graphene-based films (0.37 wt.% GO) before and after thermal reduction at 400 °C (labelled as CU_GO_f and $CU\_r(400)GO_f$) was studied. The structural integrity of the spin-coated films was examined by FESEM, with their degree of thermal reduction evaluated through Raman Spectroscopy and XPS.

The PF127/Al_2O_3 suspensions were similarly prepared with 0.1 - 25 wt.% Al_2O_3

solid loading and a fixed PF127/Al_2O_3 ratio of 0.15P. In these CA measurements, this ratio was set to 0.15 as a starting point for studying the potential effect of the amphiphilic addition. All alumina suspensions were kept at room temperature. Due to the small quantity of PF127 present in every mixture (below 4 wt.% in the most concentrated sample), gelation was not expected [35, 245]. Therefore, maintaining lower working temperatures using an ice bath was not a requirement for this set of experiments. To ensure good dispersion, mechanical stirring up to 300 rpm was applied to the alumina suspensions before deposition on the substrate.

5.3.3 Infiltration testing of alumina slurries on graphene-based aerogels

A range of infiltration tests was designed to study the viability of achieving the target graphene/alumina composite by infiltrating lab-scale graphene scaffolds with water-based PF127/Al_2O_3 suspensions and optimise the PF127/Al_2O_3 wt./wt. ratio. Cylindrical *0.25:CU_rGO$_{ag}$* (13 mm diameter and 19 mm height) were produced following the freeze-casting and carbonisation procedure at 900 °C from Section 4.5. The weight and apparent density of the aerogels were measured before and after the thermal treatment. *0.25:CU_GO$_{ag}$* and *0.25:CU_rGO$_{ag}$* scaffolds were deposited on top of 15 mL PF127/Al_2O_3 suspension batches of 12.5 and 25 wt.% alumina loading contained in a 25 mL glass beaker. Several PF127/Al_2O_3 wt./wt. ratios in suspension were tested from 0 to 1.

The prepared suspensions were homogenised by speed-mixing for 10 min and mechanical stirring at 400 rpm while cooled down to 4 °C under an ice bath. Lower temperatures were preferred to prevent potential gelation of the ceramic mixtures containing higher quantities of PF127 (above 15 wt.% in H_2O) caused by the dehydration of hydrophobic bonding of central [PPO] groups in the copolymer [243].

The infiltration tests were divided into batches of eight runs, using eight aerogels produced in a single freeze-casting session. A series of timestamps were identified and registered to compare the infiltrating performance during each test:

1. Aerogel dropped on top of the slurry, defining t = 0 sec.
2. One-third of the aerogel's volume infiltrated in the slurry.
3. Two-thirds of the aerogel's volume infiltrated in the slurry.
4. Aerogel fully immersed in the ceramic slurry.

The infiltration of two-thirds of aerogel volume was selected as the endpoint to compare different tests (Figure 5.5) to compensate for uncontrolled factors such as tilting, surface flatness and inaccuracies from the camera positioning. A Nikon

D5100 camera was used to record each infiltration test and evaluate the different time stamps for each condition during the initial 10 minutes of infiltration.

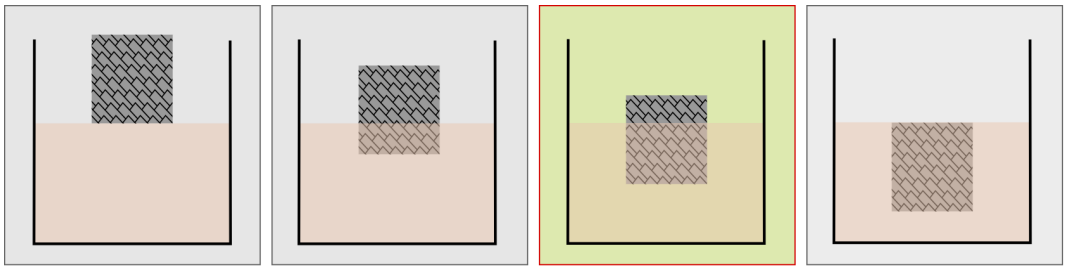

Figure 5.5: *Schematic displaying four key timestamps identified for each infiltration, highlighting the selected endpoint for comparing different tests.*

The infiltration tests were also performed on cylindrical *0.25:CU_rGO$_{ag}$(0.05N)* (13 mm diameter and 19 mm height) decorated with alumina nanoparticles (NPs) from the aluminium hydroxide gel procedure presented in Chapter 4. The scaffolds were similarly deposited on top of 15 mL PF127/Al_2O_3 suspension batches of 12.5 and 25 wt.% Al_2O_3 after equivalent freeze-casting, freeze-drying and carbonisation at 900 °C.

5.3.4 Preparation of graphene/alumina green bodies

Lab-scaled *0.5:CU_rGO$_{ag}$* aerogels (13 mm diameter and 19 mm height) successfully infiltrated with 12.5 and 25 wt.% alumina slurries from the infiltration tests were frozen and freeze-dried for a minimum of 48 h. The selected PF127/Al_2O_3 ratios from the infiltration tests on lab-scaled aerogels were extended to the infiltration of scaled-up cylindrical aerogels (*0.25:CU_rGO$_{ag}$⊥* and *0.5:CU_rGO$_{ag}$⊥*) of 28 mm diameter and 30 mm height.

The PF127/Al_2O_3 slurries were mixed in the required quantities and wet ball-milled for 24 hours. The slurries were additionally speed-mixed for 10 minutes, deposited dropwise on top of the graphene scaffolds to enhance soaking and reduce the effects of viscosity of the alumina slurries in the absence of vacuum. After infiltration, the scaled-up aerogels were frozen and freeze-dried for 72 hours, producing rGO/PF127/Al_2O_3 green bodies ready for consolidation via SPS sintering.

5.4 Processing oxide structural ceramics: Aluminium oxide

5.4.1 Characterisation of alumina powders

The commercial alumina powder used to prepare the ceramic slurries in this work (BA15W) was first characterised through various techniques to determine the powder morphology and crystallographic phase. The real density of the powder as measured via helium pycnometry was found to be 3.96 ± 0.007 g cm^{-3}. This density value sits in the standard range for commercial alumina of 3.95 - 3.99 g cm^{-3} and was used as a reference for density measurements of sintered alumina materials from later stages.

According to the XRD spectrum from Figure 5.6, the as-received alumina powder appeared highly ordered, predominantly in the α-alumina crystallographic phase [251] after comparison with the ICDD reference spectrum [00-00-1243].

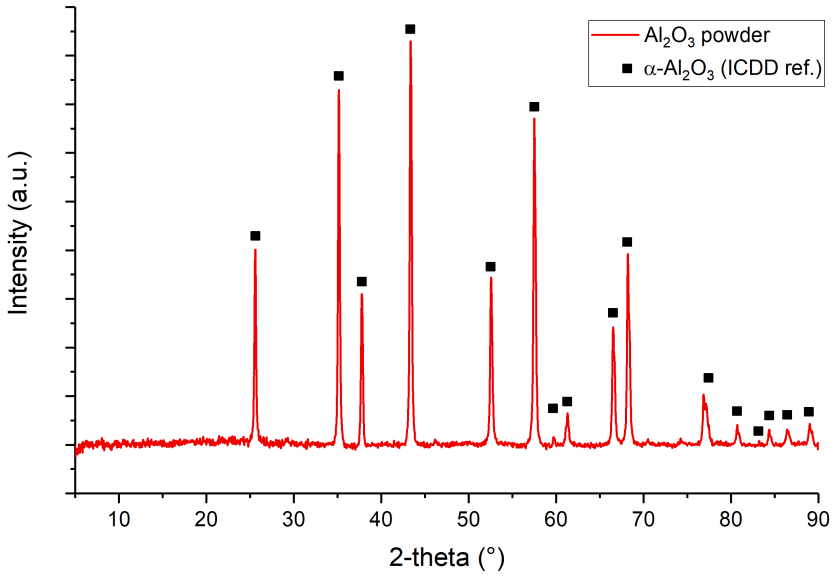

Figure 5.6: *XRD spectrum of alumina powder compared with an ICDD reference spectrum for α-alumina.*

XRD validated the high percentage of crystalline α phase on the alumina powder used throughout the work. Being the most stable alumina phase (as introduced in 4.6.1), no crystallographic changes were expected once included in the general composite processing.

As-received alumina powders were characterised by FESEM to evaluate their physical state and the processing method employed. The powder appeared agglomerated in quasi-spherical beads of 10 – 40 μm (Figure 5.7a). This morphology is characteristic of spray-dried powders, a processing technique in which by the atomisation of a ceramic slurry under a gas/liquid mixing step, agglomerated alumina is

dried in the shape of the original water droplets from the processing stage [1].

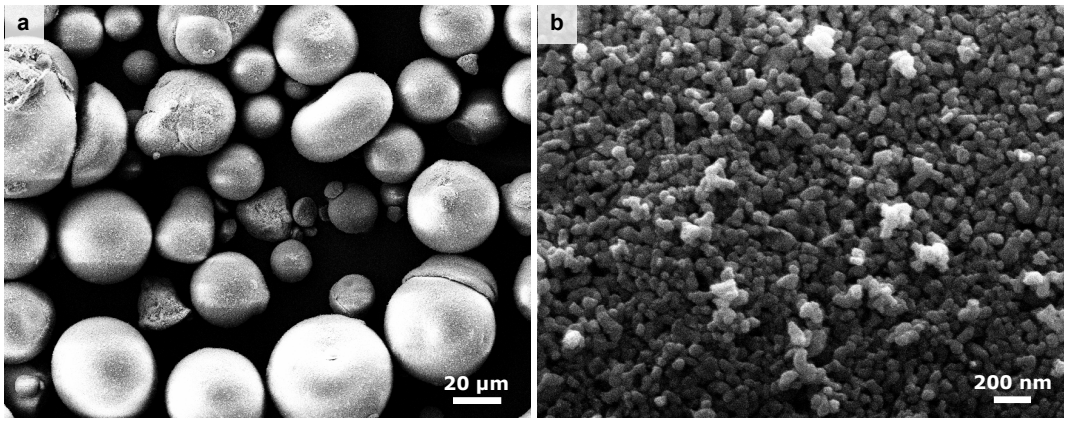

Figure 5.7: *FESEM of as-received alumina powder. a) Spray-dried morphology at low magnification. b) Agglomeration of the alumina nanoparticles (particle size of 100 nm).*

Closer examination of the spray-dried beads revealed the actual size of the alumina particles, sitting in average particle size of 100 ± 12 nm (Figure 5.7b). The selection of alumina powder with dimensions below the micrometric scale was intended to ensure the infiltration of the particles within the interconnected $3D$ graphene-based scaffolds. Alumina particles of bigger diameter than the graphene network's structural channels (5 – 30 μm) would result in the physical blockage of alumina, preventing the strategy's success. Therefore, tuning the formulation of produced water-based alumina slurries was still necessary to deagglomerate the spray-dried powders and get closer to the sub-micrometric level.

The particle size distribution of the as-received Al_2O_3 powder was further studied through wet laser diffraction (Figure 5.8). The degree of stirring and ultrasonication applied was adjusted to ensure the breakage of the spray-dried agglomerates. Both the histogram frequency and the cumulative density have been presented to obtain a visual display of the median diameter of the particles (D_{50}).

Under lower stirring (600 – 800 rpm) and before the application of ultrasonication (Figure 5.8a), a D_{50} of 28.6 μm was obtained (indicated by the 50% cumulative density), verifying the expected median of spray-dried beads as examined by FESEM imaging. Increasing the mechanical stirring above 1200 rpm resulted in a significant breakage of agglomerates (Figure 5.8b), achieving a median particle size of 0.5 μm. The particles still exhibited agglomeration, with diameters five times above the sizes found through high-magnification FESEM. The application of ultrasonication reduced the size of alumina particles significantly, as seen in the distribution from Figure 5.8c. A 20% level of ultrasonication was sufficient to obtain a D_{50} of 63 nm, smaller than diameters observed in FESEM, which indicated the splitting of alumina particles. As ultrasonication increased, the diameters obtained appeared progressively smaller approaching 20 nm, which led to discarding the latest set of

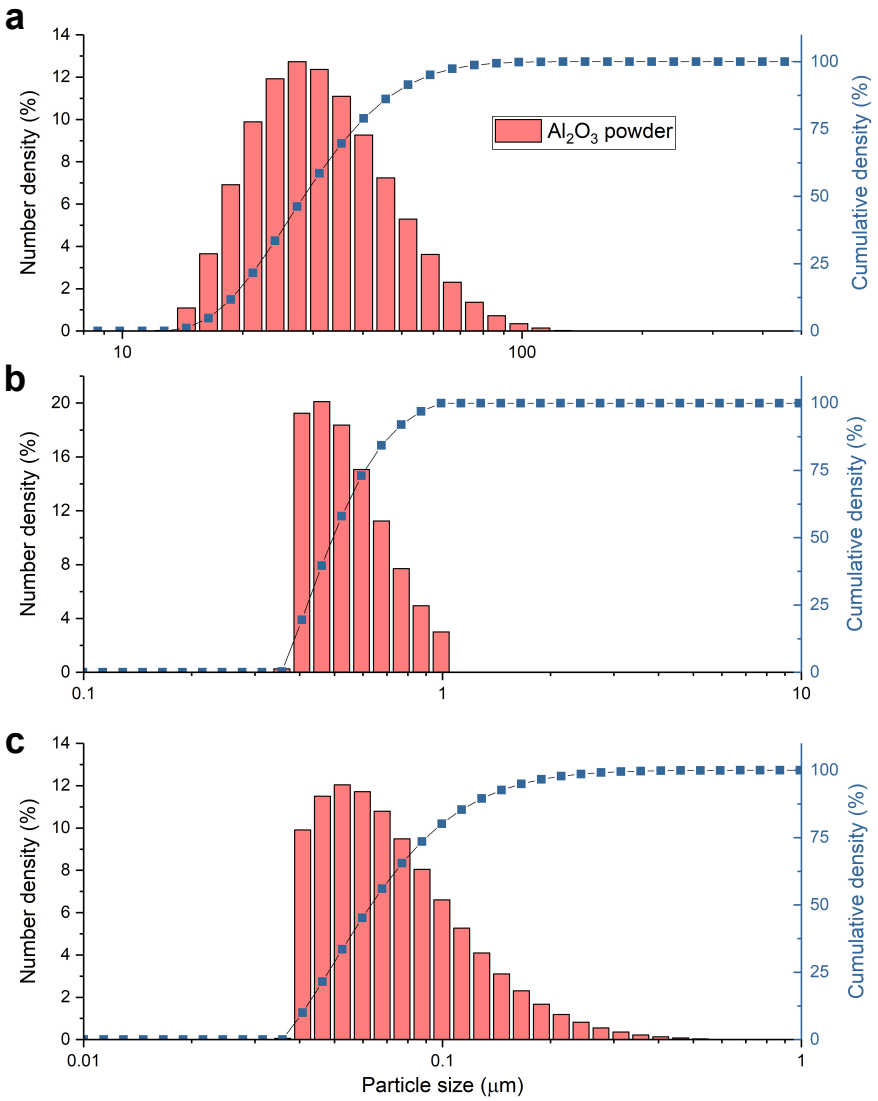

Figure 5.8: *Particle-size distribution of alumina powder, including number and cumulative densities under a) lower stirring rate (600 - 800 rpm) and no ultrasonication, b) higher stirring rate (above 1200 rpm) and no ultrasonication, c) higher stirring rate and 20% ultrasonication.*

values and settling the processing on purely mechanical stirring.

These initial characterisation results confirmed that the formulation of water-based alumina suspensions required careful tuning to deliver disaggregated alumina particles able to infiltrate the internal channels from graphene-based aerogels produced in Chapter 4. Balancing the breakage of agglomerates in the slurry without incurring potential particle disruption from excessive ultrasonication was needed. This was approached by producing water-based slurries of various solid loading, introducing a 24 h ball-milling stage and PF127 additions in suspension.

5.4.2 Formulation of water-based alumina slurries using PF127

Alumina powders were transformed into slurry form using water as the medium, aiming to settle a general cost-effective and environmentally-friendly approach. Water-based alumina slurries of 0.1 - 25 wt.% solid loading were readily produced throughout the work, intended as the selected formulations to infiltrate graphene-based aerogels described in the previous chapter as structural scaffolds. A 24 h wet ball-milling step (detailed in Section 3.2.1.1) was integrated into the processing of the water-based alumina slurries to help with the deagglomeration of as-received spray-dried alumina powder and improve their rheological behaviour [188].

The particle size of the alumina powder in a 25 wt.% slurry before and after ball-milling was evaluated to determine the effect of the milling step in breaking the agglomerates (Figure 5.9).

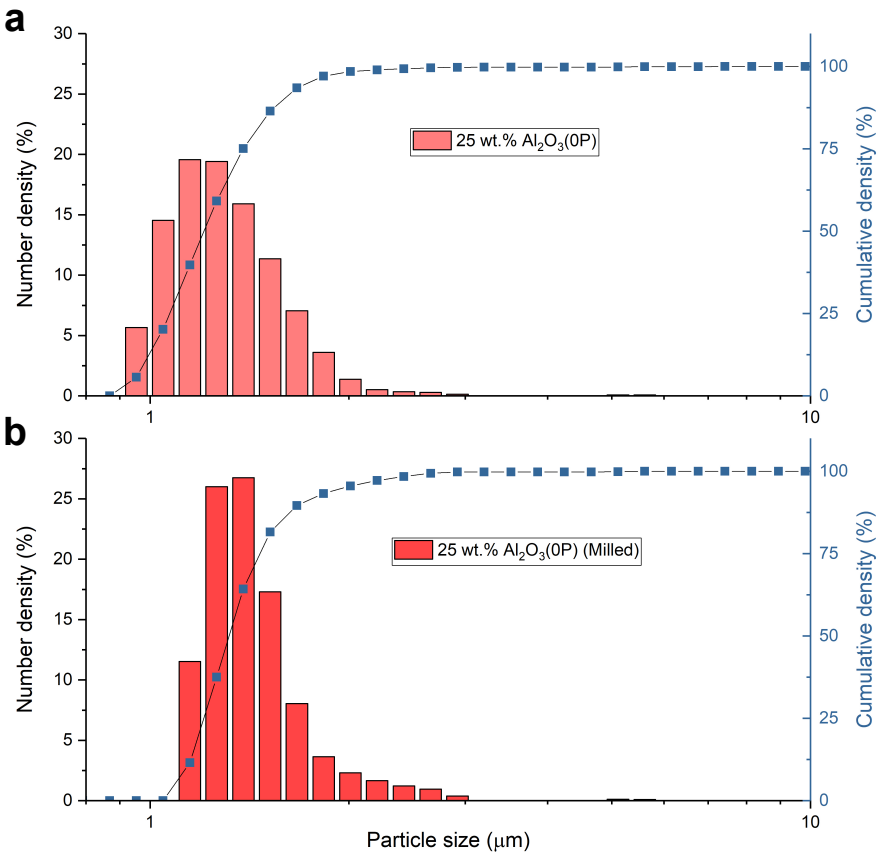

Figure 5.9: *Particle size distribution of 25 wt.% Al_2O_3 slurries: a) without wet ball-milling, b) after 24 h wet ball-milling.*

Laser diffraction measurements did not show any effect of ball-milling in the particle diameters, with similar size distributions registered before and after the milling stage. The D_{50} obtained was roughly equal (1.32 μm before and 1.33 μm after milling) as represented by the cumulative density curves, only differing in the reduced spread of the distribution after milling. These slight variations could be caused by

differences in the alumina sample tested (accounting for the effects of gravity or small inhomogeneities in the slurry), not sufficient to indicate a detrimental effect on the agglomeration after milling.

The 1200 rpm mechanical stirring applied during particle size analysis could cause sufficient deagglomeration (verified in previous particle size distributions of as-received Al_2O_3 powder) to offset any effect of the ball-milling stage. For such reason, the rotational viscosity of 25 wt.% Al_2O_3 slurries before and after applying the 24 h ball-milling step was additionally evaluated (Figure 5.10).

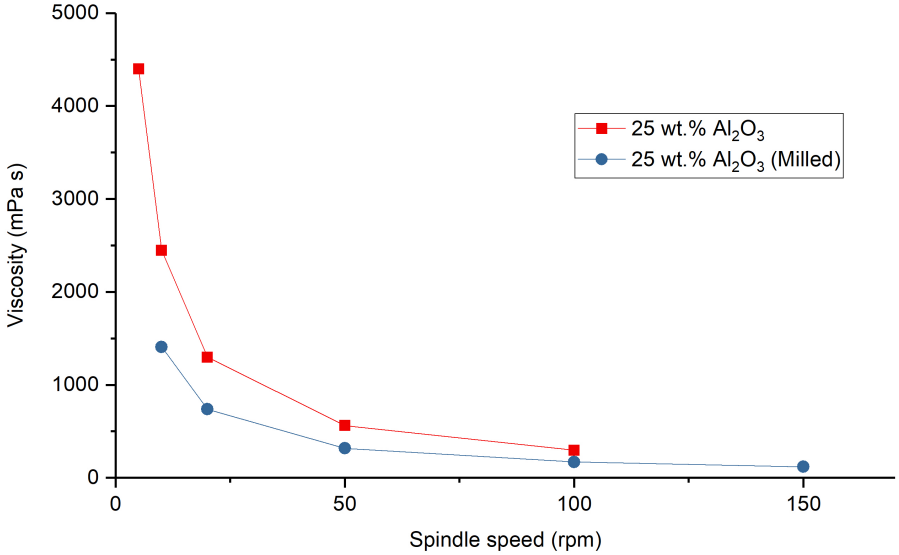

Figure 5.10: *Viscosity profile comparison of 25 wt.% Al_2O_3 suspensions before and after a ball-milling step.*

After the milling step, the viscosity profile of the slurries was lowered without affecting the non-Newtonian trend, validating the enhanced deagglomeration while increasing the stability of the readings. Below 10 rpm, the viscosity of non-milled 25 wt.% Al_2O_3 slurries dropped from 4000 - 4500 to a 1000 - 1500 mPa s range, which could enhance the integration with the graphene phase while maintaining equal solid loadings. From these results, the ball-milling step was considered an improvement for better infiltration of graphene aerogels in the ceramic suspension. Rotational viscometry measurements were additionally settled as a valuable tool to study the influence of later PF127 additions to the slurry formulation.

PF127 was added to the alumina suspensions on various PF127/Al_2O_3 wt./wt. ratios to bridge the interaction with the hydrophobic graphene phase and permit the infiltration of the ceramics. The inclusion of PF127 additions in various quantities (from a surfactant level to a 3D-ink carrier as explained in Section 5.2) resulted in micellisation upon mixing with the water solvent, leading to foaming of the suspensions as seen in Figure 5.11, which was controlled by the application of speed-mixing and wet-ball milling.

Figure 5.11: *25 wt.% Al_2O_3(0.15P) suspension after 24 hours of ball-milling showing the foaming effect of PF127 additions.*

The viscosity of 12.5 and 25 wt.% alumina slurries under increasing amounts of PF127 (0P, 0.07P and 0.15P) was studied by rotational viscometry (Figure 5.12). Two different spindles were used for each graph due to the difference in viscosity range (TL6 on top vs TL5 on bottom), which prevented their direct superposition. All alumina suspensions exhibited a typical non-Newtonian profile, implying a dependency of the fluid's viscosity with the shear rate and a shear-thinning behaviour [252]. The viscosity of 12.5 wt.% slurries remained in the 8 - 65 mPa s range across the 20 - 250 rpm working range with stable values over time. The additions of PF127 appeared to have a mixed effect on the displayed viscosity. 0.07P seemed to increase the overall viscosity, with higher additions (0.15P) lowering the viscosity to an in-between point, still maintaining a similar trend in the same viscosity range. 12.5 wt.% suspensions containing no PF127 were found at the lower torque at the highest spindle speeds, for which only one point could be included in the graph without incurring unstable readings. Achieving more measurements would require the use of specific low-viscosity test kits.

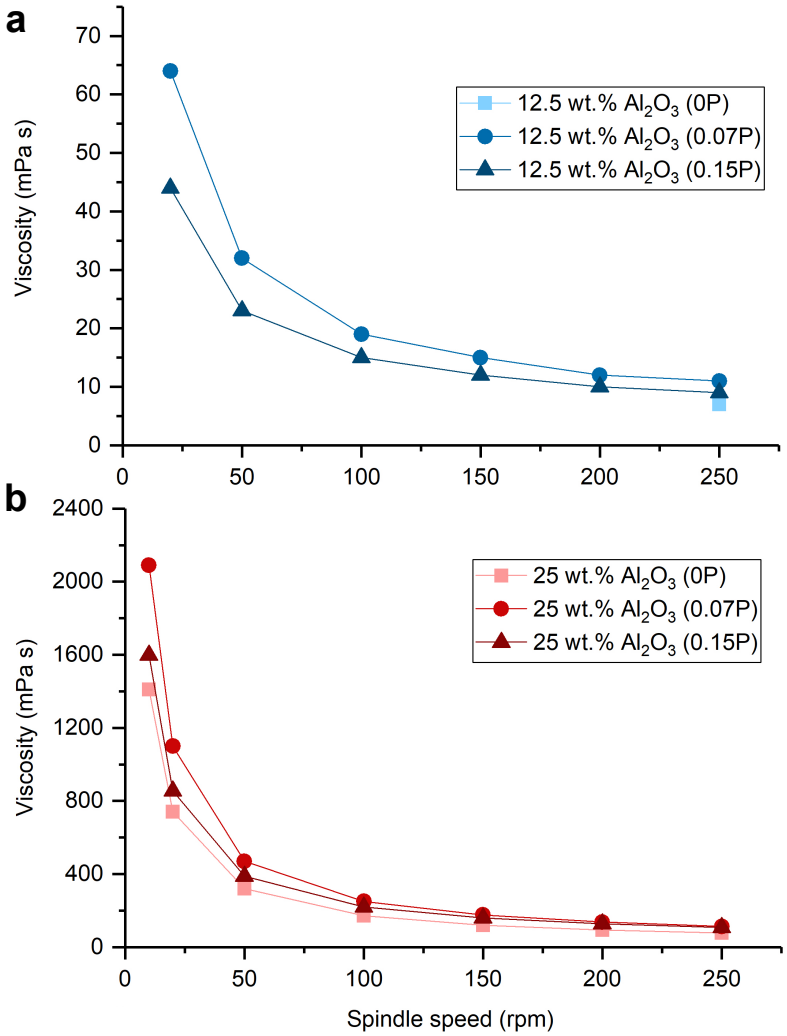

Figure 5.12: *Rotational viscosity measurements of alumina suspensions at increasing PF127/Al_2O_3 ratios (0, 0.07 and 0.15) for (a) 12.5 wt.% and (b) 25 wt.% solid loadings.*

25 wt.% suspensions with equivalent PF127/Al_2O_3 ratios maintained a similar non-Newtonian trend. The increase in solid loading had a remarkable effect displacing the curves on the Y-axis, an effect most noticeable at lower speeds, with a sharper increase in viscosity towards the 1000 - 2000 mPa s range. In similarity with the 12.5 wt.% suspensions, increasing the PF127 content to 0.07P and 0.15P led to a slight increase of viscosity in the slurry, with the former giving the highest values of viscosity.

From these measurements, the change in viscosity between 12.5 and 25 wt.% loading slurries appeared remarkable and was considered during infiltration tests. The effect of modifying the PF127/Al_2O_3 ratio in suspension remained marginal, not affecting the overall trend. A rheometer should be applied in the future to fully expand on the viscosity of these suspensions and their non-Newtonian behaviour.

5.5 Integration of hierarchical graphene scaffolds on alumina matrix by infiltration

Initial tests were performed to measure the wettability of PF127/Al_2O_3 suspensions against graphene-based films deposited on silicon substrates as a first step towards defining the formulation of the ceramic suspensions. These films were produced to simplify the interaction between the alumina phase (in droplet form) and freeze-cast graphene-based aerogels by substituting the latter with a flat surface that could provide more consistent contact angles (CA) between the two materials.

5.5.1 Characterisation of graphene-based films

To preserve their integrity, adequate control of the thermal reduction of spin-coated CU_GO_f films was required. An annealing temperature of 400 °C was selected instead of the 900 °C applied to previous freeze-cast graphene aerogels to ensure a balance between sufficient temperature capable of removing the functional groups attached to GO [138] and excessive temperature that could damage the continuity of the film [139, 153]. To highlight this, partially-reduced films are labelled $CU\_r(400)GO_f$. The $CU\_r(400)GO_f$ films exhibited sufficient thickness showing no trace of the underlying silicon substrate upon FESEM examination. However, at the substrate edges, the advancing front of the film as a result of spin-coating was visible (Figure 5.13).

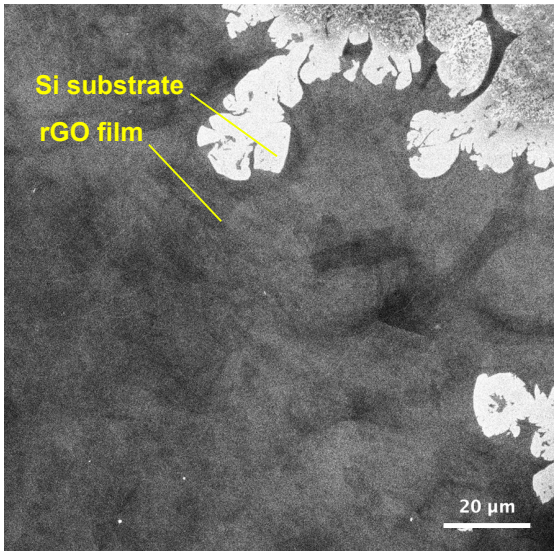

Figure 5.13: *Edge of spin-coated $CU\_r(400)GO_f$ film revealing the silicon substrate underneath.*

The contact angle (CA) tests were directed to the centre of the substrates to prevent any negative effect from the lack of edge covering. The limited thermal reduction of the GO films partially maintained their electrically insulating behaviour,

which hindered obtaining higher resolution images via FESEM.

Different areas of CU_GO_f and $CU\_r(400)GO_f$ films were studied by Raman Spectroscopy (Figure 5.14) to account for localised annealing effects expected from the lower reduction temperature selected, which could selectively alter the GO structure and provide distinct Raman measurements depending on the region of examination. Raman spectra obtained for these measurements using custom equipment appeared of particularly low intensity, with D and G shifts not surpassing the 300 counts, a noticeable difference compared to the commercial unit used for the study of CU_GO_{fzd} in Section 4.3.1.

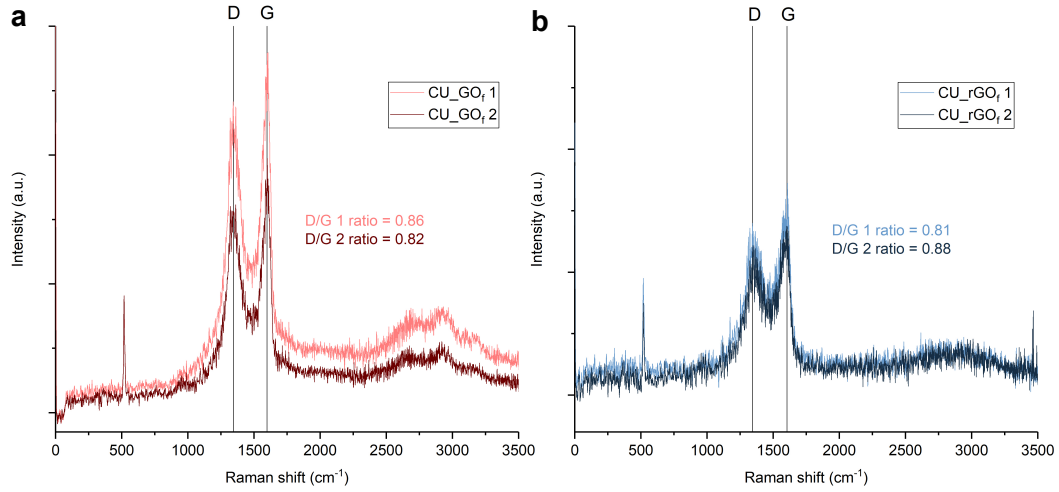

Figure 5.14: *Raman spectra from two different film areas. a) CU_GO_f films. b) $CU\_r(400)GO_f$ films.*

The influence of the silicon substrate in these measurements was noticeable because of the sharp peak present at 520 cm^{-1}, characteristic of a typical silicon wafer. In the case of CU_rGO_f, D and G shifts appeared at 1342 and 1600 cm^{-1} with a D/G ratio of 0.86 in the first location selected and at 1361 and 1600 cm^{-1} with a D/G ratio of 0.82 in the second location, analogous to the Raman on CU_GO_{fzd} with the prominent D band representative of the defective graphene structure in the sheets [149] [140, 156]. $CU\_r(400)GO_f$ measurements displayed a substantial drop in intensity, increasing the background noise and slightly deviating the characteristic shifts. D and G shifts were obtained at 1342 and 1606 cm^{-1} in the first location with a D/G ratio of 0.81 and 1354 and 1600 cm^{-1} with a D/G ratio of 0.88 for the second one. Differences between CU_GO_f and $CU\_r(400)GO_f$ measurements appeared almost negligible, with the D/G ratio displayed by each film being highly dependent on the region of examination. D/G ratio in $CU\_r(400)GO_f$ films was even lower than in previously discussed CU_GO_{fzd} material despite the partial reduction at 400 °C.

In all locations examined before and after annealing, the D/G ratio fluctuated between 0.80 and 0.89. Based on these results, 400 °C seemed an excessively low tem-

perature to identify any substantial changes in graphitic sp^2 domains restoration and GO's defective structure via Raman Spectroscopy. The deviations in the obtained D/G ratios seemed more related to local areas of the GO film selectively annealed to different levels by the incident Raman laser. As a result, the presented evolution of D/G ratios after partial reduction was considered not fully representative of the whole sample to predict a trend in wettability measurements.

CU_ GO$_f$ and *CU_ r(400)GO$_f$* were additionally characterised by XPS to determine if the partial reduction at 400 °C applied to the GO films would be able to trigger a different hydrophobic response during wettability tests. The atomic percentage of elements identified in an XPS general survey is presented in Table 5.1. The silicon substrate underneath the films exhibited a non-negligible contribution slightly accentuated upon thermal annealing due to the elimination of functional groups present in the GO films.

Table 5.1: *Relative at.% of elements from general XPS survey of CU_ GO$_f$ and CU_ r(400)GO$_f$ films.*

Material	**Relative at. %**					
	C	**O**	**S**	**Na**	**Si**	**N**
CU_GO$_f$	64	30.6	0.9	0.2	1.9	2.5
CU_r(400)GO$_f$	79.1	15.9	0	0.5	2.9	1.6

This decrease of functional groups attached to the graphene films is demonstrated by the oxygen atomic contribution in the annealed samples, which is reduced to half despite the low temperature of reduction selected. From an initial C:O ratio of 2.09 (similar to the 2.35 ratio primarily registered for *CU_ GO$_{fzd}$* samples although dependent on the region of examination), a C:O ratio of 4.97 was obtained in the film after annealing. Although comprising an increase above 200%, it highlights the difference between applying 900 °C reduction temperatures, which raised the C:O ratio to 48.8 as seen in Section 4.3.1.

As shown in the XPS of *CU_ GO$_{fzd}$* (Figure 4.2), traces of sulphur and sodium impurities were expected to appear in the material because of the typical mix of sulphuric acid and sodium nitrate used during the Hummers based synthesis of *CU_ GO* suspensions [143]. In this analysis, the nitrogen impurities associated with the sodium nitrate were also present, diminishing after partial reduction of the films. The C1s spectra analysis for *CU_ GO$_f$* and *CU_ r(400)GO$_f$* is presented in Figure 5.15. In contrast with the XPS of *CU_ rGO$_{fzd}$* reduced at 900 °C presented in the previous chapter (Figure 4.5), the graphitic structure of the films was restored to a lesser degree at 400 °C, with carbon evolving from an atomic sp^2:sp^3 hybridisation ratio of 0.27 into 2.35. Moreover, the carbon related to the epoxide and carbonyl groups was substantially lowered upon partial reduction of the films, implying the effective elimination of functional groups decorating the graphene flakes of the film.

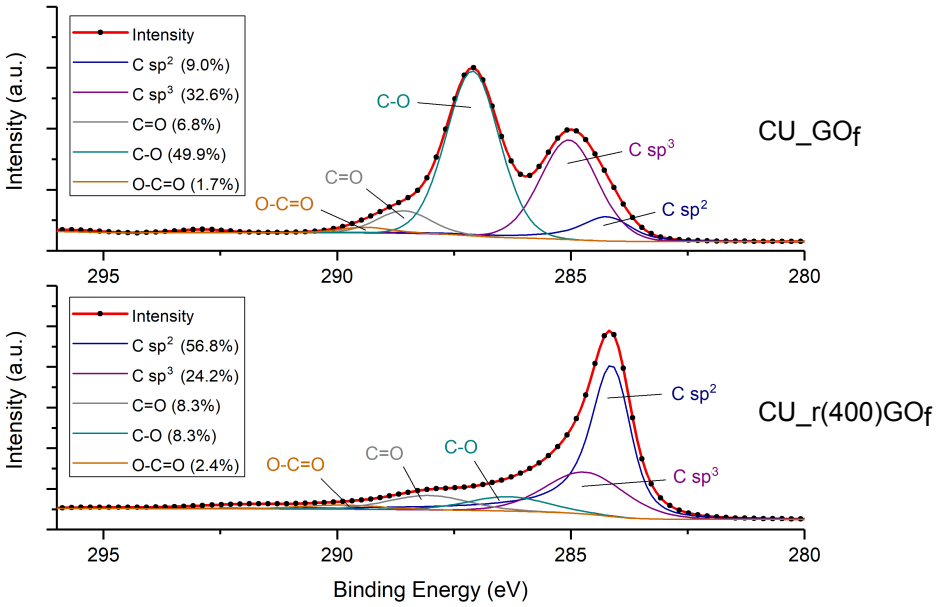

Figure 5.15: *Comparison of C1s XPS spectra of CU_GO_f (top) and $CU\_r(400)GO_f$ (bottom).*

The analysis of the O1s binding energies also reflected the lower degree of graphitic restoration in $CU\_r(400)GO_f$, obtaining a different evolution of the oxidised group signals compared to CU_rGO_{fzd} (Figure 5.16). The overall envelope between the CU_GO_f and $CU\_r(400)GO_f$ was quite similar, with shifts towards higher binding energies not as significant as seen after 900 °C annealing. The relative contribution associated with the carbonyl ($C = O$) group also changed from 21.8 to 37.8%, a lower increase than the 45.1% from CU_rGO_{fzd} at 900 °C.

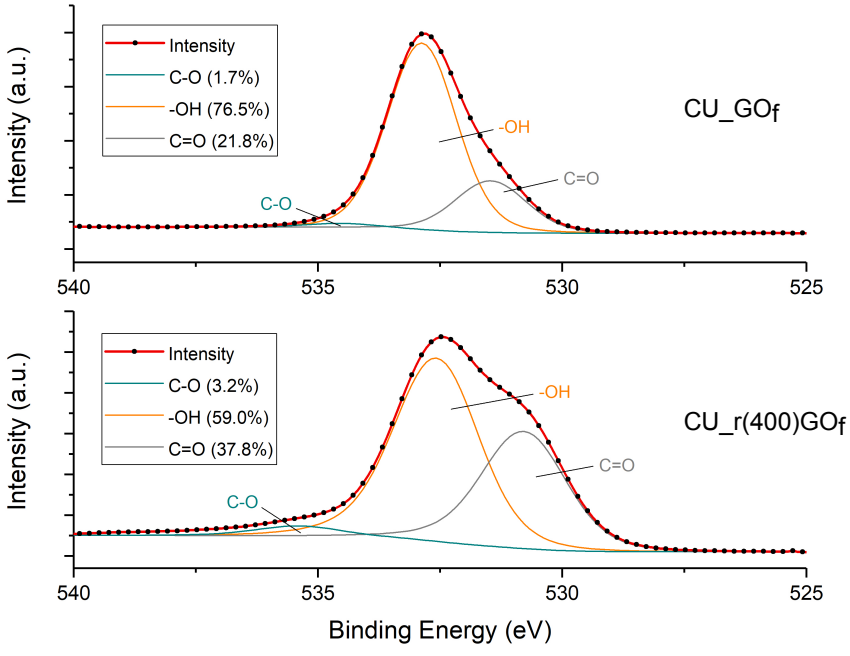

Figure 5.16: *Comparison of O1s XPS spectra of CU_GO_f (top) and $CU\_r(400)GO_f$ (bottom).*

The XPS characterisation of the films verified a noticeable transformation of sp^3 carbon into sp^2 carbon and the substantial elimination of several epoxide and carbonyl groups from the graphene sheets at this temperature of partial reduction. This is in accordance with the thermogravimetric analysis performed on CU_GO_{fzd} (Figure 4.7) that predicted a substantial weight decrease above 250 °C annealing. Therefore, it was concluded that the temperature of annealing selected (400 °C) was sufficient to modify the hydrophobic behaviour of pre- and post-annealed films without causing further damage to the spin-coated films [139], allowing to determine the effect of including PF127 additions in the alumina suspensions during wettability measurements.

5.5.2 Contact angle study between graphene-based films and alumina slurries

PF127 was selected as an intermediate agent in the slurries formulation to modify the hydrophilic alumina surface interaction with the hydrophobic graphene phase. The CA of PF127/Al_2O_3 suspensions dispensed on the spin-coated graphene-based films was evaluated. The slurries formulations used in these wettability measurements have been reported in Table 5.2, tested on two sets of equivalent CU_GO_f and $CU\_r(400)GO_f$ films.

Table 5.2: *Formulation of PF127/Al_2O_3 slurries produced for wettability tests against GO and rGO films.*

Al_2O_3 wt.%	**PF127 wt.%**	**PF127/Al_2O_3 wt./wt. ratio**
0.1	-	-
1	-	-
5	-	-
12.5	-	-
25	-	-
0.1	0.015	0.15
1	0.15	0.15
5	0.75	0.15
12.5	1.875	0.15
25	3.75	0.15

The PF127/Al_2O_3 wt./wt. ratio was fixed at 0.15 in these CA tests (labelled as Al_2O_3(0.15P)), envisioned as a starting point in the context of selecting an optimum formulation for the graphene/ceramic composite. The summary of CAs obtained has been included in Figure 5.17, comparing the performance of alumina suspensions in the absence of PF127 (0P) on CU_GO_f and $CU\_r(400)GO_f$ (Figure 5.17a) and the inclusion of 0.15 PF127 in the alumina droplet against $CU\_r(400)GO_f$ films (Figure 5.17b).

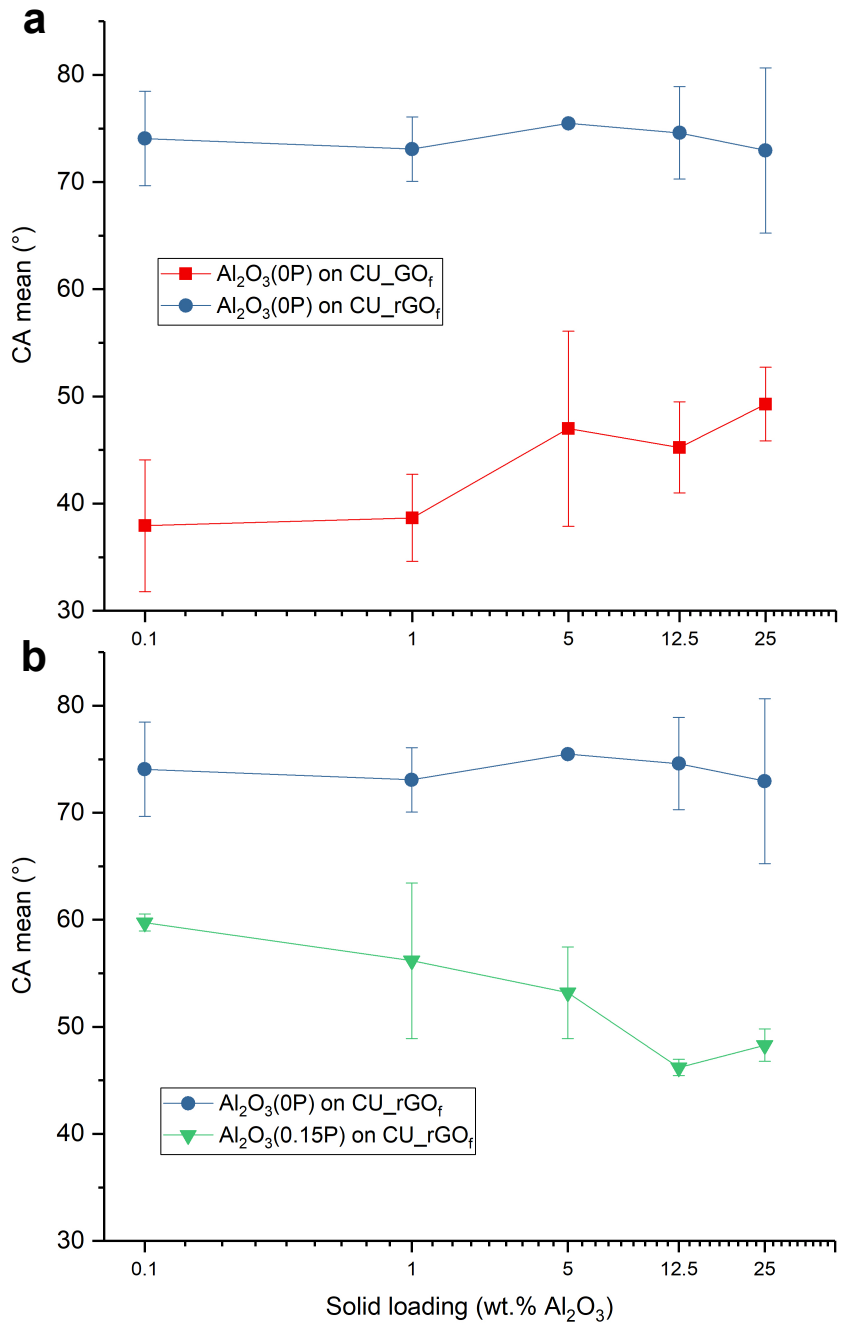

Figure 5.17: *(a) Average contact angle of Al_2O_3(0P) droplets with increasing solid loading (0.1 - 25 wt.%) on CU_ GO_f and CU_ r(400)GO_f. (b) Average contact angle of Al_2O_3(0P) and Al_2O_3(0.15P) droplets against CU_ r(400)GO_f.*

The registered CA averages of Al_2O_3(0P) droplets shifted from a 35 – 50 ° to a 70 – 75 ° range against *CU_ GO_f* and *CU_ r(400)GO_f*, respectively, after increasing the concentration of alumina in suspension (Figure 5.17a). This increase was expected from the depletion of sp^3 carbon and carbon-oxygen links in GO films, along with a higher presence of sp^2 carbon after annealing, which augmented the hydrophobicity of the film. Although far from the super-hydrophobic behaviour reported for graphene nanoplatelets and fully-reduced GO sheets around 120 – 150 ° [253], partial reduction at 400 °C proved sufficient to alter the droplet response, for which a sharper change

would be expected in CU_rGO_{ag} aerogels annealed at 900 °C. As the Al_2O_3 solid loading increased to 12.5 and 25 wt.%, the obtained CAs were progressively higher, indicating the effect of selecting increased solid loading in the slurries.

A significant increase in wettability was obtained after adding PF127 in the alumina suspensions, drawing closer the behaviour of CU_GO_f and $CU\_r(400)GO_f$ (Figure 5.17b). Measured CA averages of Al_2O_3(0.15P) droplets on $CU\_r(400)GO_f$ decreased when increasing the alumina solid content of the suspension. The amphiphilic effect of the copolymer addition was intensified on the 12.5 - 25 wt.% Al_2O_3 solid content range, with barely any difference in the reported CAs for GO films before and after partial reduction. This could be explained by the higher presence of PF127 in the alumina droplet, interacting equally with both the hydrophilic oxidised groups of GO and the hydrophobic regions of sp^2 carbon. It should be considered that this drop in hydrophobicity would also be related to the increase of PF127 content in the slurry, arising from maintaining an equal PF127/Al_2O_3 ratio. The viscosity of the alumina slurries at higher solid loadings (12.5 and 25 wt.%) was also significantly increased as shown in Figure 5.12, which could pin the deposited droplet and limit its spread on the spin-coated film.

Commonly, CAs measured through the sessile drop technique in similar works are provided without an adequate evaluation of equilibrium states, without reporting the settling times [254] or by selecting only 0 – 2 seconds without providing further justification [255]. Longer deposition times may be necessary to obtain a fully-stable contact angle in equilibrium, including an analysis of the advancing and receding contact angles for a complete evaluation [210]. This was illustrated by the dynamic behaviour exhibited by one iteration of 5, 12.5 and 25 wt.% of Al_2O_3(0.15P) droplets against $CU\_r(400)GO_f$ (Figure 5.18), with CAs slightly dependent on the deposition time (10 vs 30 seconds).

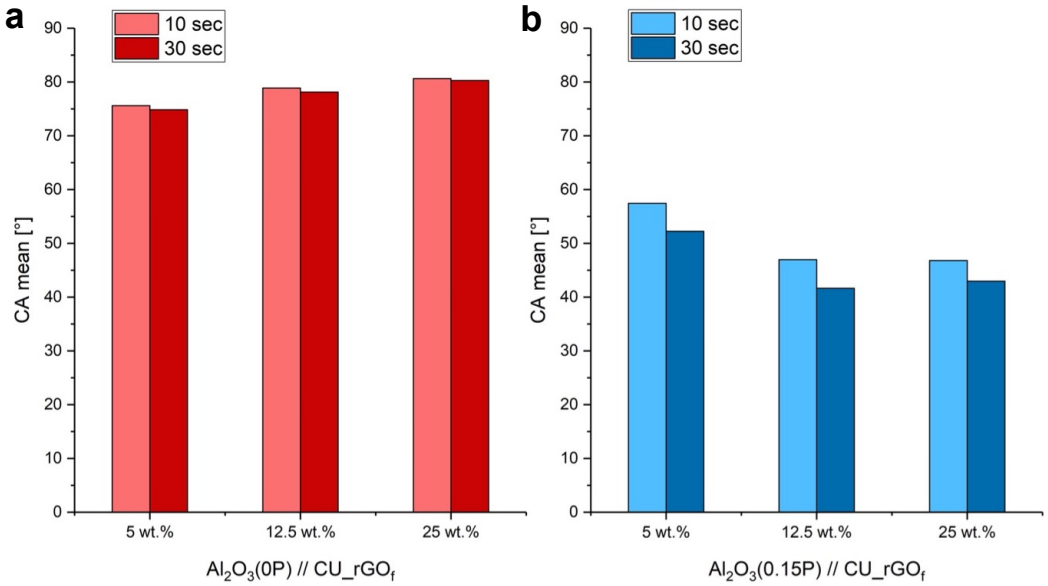

Figure 5.18: *Comparison of the average contact angle registered between 10 and 30 seconds of deposition. a) Al_2O_3(0P) on CU_r(400)GO_f b) Al_2O_3(0.15P) on CU_r(400)GO_f.*

The CA obtained for Al_2O_3(0P) droplets deposited on *CU_r(400)GO_f* was highly stable (Figure 5.18a), decreasing only slightly (1 – 2 °) throughout the first 30 seconds of deposition. PF127 additions favoured a higher film spread, lowering the average CAs 5 – 6 ° when comparing the 10- and 30-seconds mark from droplet deposition (Figure 5.18b). These variations appeared not significant to modify the behaviour against the rGO films. These results showed that the addition of PF127 on the ceramic slurry formulation enhances the wettability of a hydrophobic surface such as the *CU_r(400)GO_f*, with a more comprehensive approach being out of scope for the presented work.

5.5.3 Lab-scale infiltration of alumina into graphene-based aerogels

The wettability studies on *CU_GO_f* films showed the positive effect of PF127 in wetting the hydrophobic surface of graphene-based films with a hydrophilic alumina suspension. These tests were expanded by evaluating the infiltration capabilities of cylindrical laboratory-scale *0.25:CU_GO_{ag}* and *0.25:CU_rGO_{ag}* aerogels (13 mm diameter, 15 mm height, Figure 5.19) after adjusting the PF127 content in the alumina suspension.

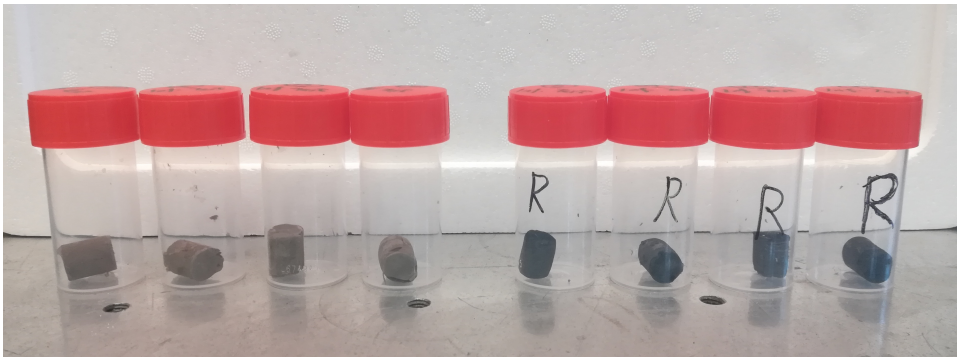

Figure 5.19: *Sample set of 8 analogous lab-sized aerogels (13 mm diameter, 15 mm height) produced for infiltration tests. Left half: 0.25:CU_ GO_{ag}. Right half: 0.25:CU_ rGO_{ag}.*

The infiltration tests were designed to find an optimum formulation of the ceramic slurry regarding the concentration of alumina, PF127 content, and GO reduction degree for graphene-based aerogels. From the Al_2O_3(0.15P) taken as a reference in previous wettability tests, PF127 in suspension was both decreased towards 0 – 1 wt.% behaving like a general surfactant in traditional ceramic processing [1] and increased towards 15 – 25 wt.% inspired by its use as an amphiphilic carrier in novel ceramic inks for 3D-printing [36, 213]. The infiltration tests covered the following variables:

1. Reduced vs non-reduced GO aerogels.
2. 12.5 and 25 wt.% alumina solid loadings.
3. PF127/Al_2O_3 wt./wt. ratio.

Combining these different parameters led to 8 testing conditions displayed in Figure 5.20 (tested on *0.25:CU_* GO_{ag} and *0.25:CU_* rGO_{ag} aerogels) with the two axes highlighting the increase of total PF127 wt.% in the mixture and the alumina solid loading in suspension, respectively. The PF127/Al_2O_3 wt./wt. ratio for every condition was included inside each cell.

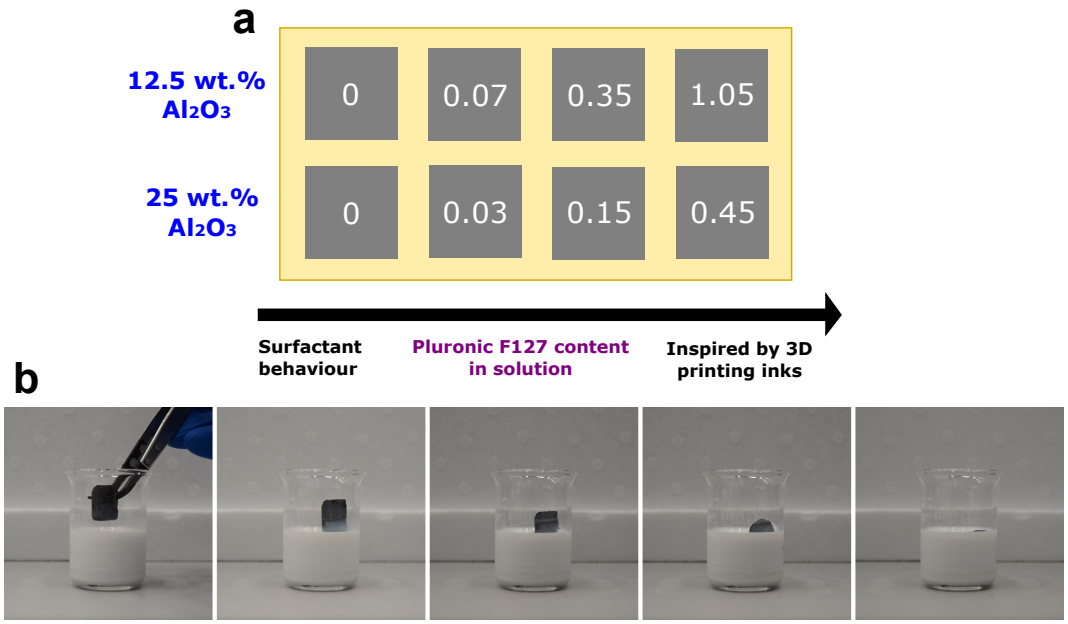

Figure 5.20: *a) Configurations selected for the initial infiltration tests. Organised by wt.% of PF127 in solution, alumina solid loading, reduction state of the GO foams and PF127/Al_2O_3 ratio. b) Display of stages from foam deposition in suspension to complete infiltration. In the example, an rGO aerogel deposited in a 0.15 PF127/Al_2O_3 suspension fully infiltrating after 70 seconds.*

After one iteration, the infiltration endpoint (2/3 of volume) achieved for every aerogel was compared with the PF127/Al_2O_3 ratio in suspension (Figure 5.21). In 12.5 and 25 wt.% Al_2O_3(0P) suspensions, the change in hydrophobic behaviour from aerogels before and after carbonisation was verified, as anticipated by previous CA wettability tests. *0.25:CU_GO_{ag}* infiltrated in the alumina slurry successfully in less than 20 seconds, whereas *0.25:CU_rGO_{ag}* was ultimately repelled for an indefinite amount of time.

Upon adding PF127 and increasing the PF127/Al_2O_3 ratio in suspension, the infiltration time of *0.25:CU_rGO_{ag}* was progressively reduced, validating the expected effect of PF127 additions. The infiltration time for *0.25:CU_GO_{ag}* also increased slightly under higher PF127/Al_2O_3 ratios, matching infiltration times for reduced GO foams. A possible explanation could lie in the higher number of functional groups present in *CU_GO* before carbonisation, delivering an amphiphilic interaction that could interact with hydrophobic [PPO] and hydrophilic [PEO] groups from PF127 in suspension.

Increasing the alumina solid loading in suspension from 12.5 to 25 wt.% appeared to influence infiltration times beyond selecting a PF127/Al_2O_3 ratio, with *0.25:CU_rGO_{ag}* infiltrating at slightly faster rates due to the higher contents of PF127. However, this increase in alumina solid loading also accompanied an increase in the viscosity of the suspensions (shown in Figure 5.12) that could hinder the infiltration of the aerogel at lower PF127/Al_2O_3 ratios from the higher slurry

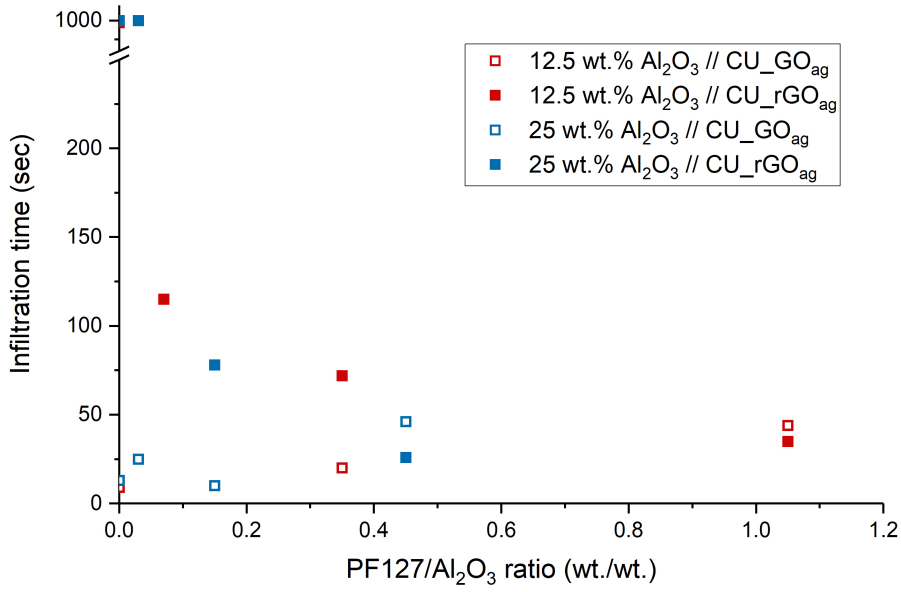

Figure 5.21: *First iteration of infiltration conditions based on PF127/Al_2O_3 ratio in the alumina slurry.*

thickness.

A second repetition of the conditions from Figure 5.20 was performed and compared with previous results. Although maintaining the overall behaviour when increasing PF127/Al_2O_3 ratio in suspension, infiltration times were comparatively longer, obtaining a significant translation along the time axis. The experienced variability was attributed to several factors. An excessive settling time of PF127/Al_2O_3 suspensions could result in a thin layer of supernatant water in the slurry, neglecting the contact of the foam with PF127/Al_2O_3 and preventing further infiltration (Figure 5.22). To minimise this effect, speed-mixing was applied immediately before deposition of the aerogel, replacing the magnetic stirring step.

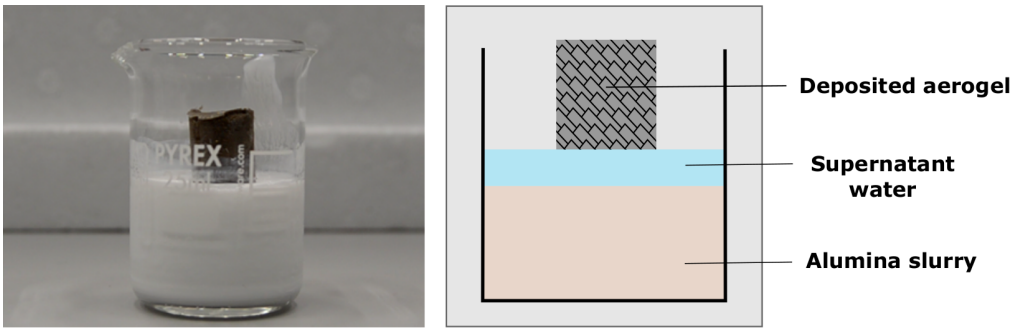

Figure 5.22: *Infiltration test showing a 0.25:CU_GO_{ag} aerogel deposited on a 25 wt.% Al_2O_3(0.03P) suspension. The attached schematic shows the water supernatant hypothesis.*

A secondary factor could include the extreme lightweightness of tested *0.25:CU_GO_{ag}* and *0.25:CU_rGO_{ag}*, which were subjected to tilting and drifting once deposited in the beaker in combination with the high viscosity of 25 wt.% alumina sus-

pensions (Section 5.4.2). Obtaining an array of aerogels with equivalent behaviour is highly difficult for two main reasons: GO synthesised through Hummers based methods is subjected to localised structural changes due to the heavy oxidation of exfoliated graphene sheets [127], in combination with the intrinsic variability of the freeze-casting process. As the 900 °C thermal reduction applied to GO scaffolds removed the great majority of attached oxidised groups (verified by TGA and XPS measurements in Section 4.3.1), focusing on *0.25:CU_rGO$_{ag}$* guaranteed a consistent hydrophobic response to highlight the influence of PF127 from previous wettability tests.

An updated experiment setup was designed based on the results of previous iterations, leading to higher efficiency and reliability of aerogel infiltration. The improved setup was exclusively focused on 12.5 wt.% alumina slurries, which reduced their viscosity significantly. Although higher solid loadings would be required in the composite processing route, this limitation allowed repeatability with lab-scale aerogels directly deposited on top of the alumina slurry. The conditions of the updated infiltration tests have been displayed in the schematic from Figure 5.23:

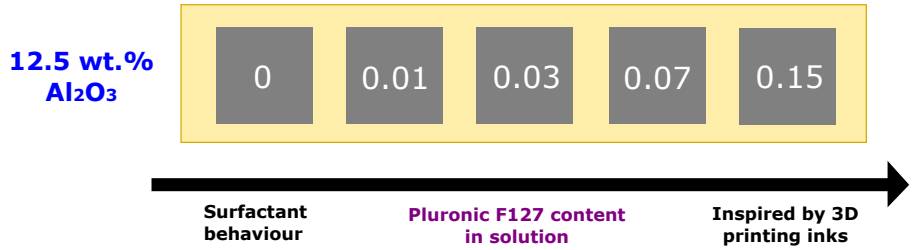

Figure 5.23: *Updated conditions for improved infiltration tests. Limited to 0.25:CU_rGO$_{ag}$, 12.5 wt.% alumina loading and PF127/Al_2O_3 of 0 - 0.15P.*

As the PF127/Al_2O_3 ratios were limited to much lower quantities ($<$ 0.15P), gelation of PF127 was not expected, allowing to remove the temperature control of 4 °C. These improvements permitted the succession of quicker tests and prevented the formation of a water supernatant layer in the beaker, obtaining better repeatability and consistent times for each timestamp. New infiltration times up to the selected endpoint (2/3 of aerogel volume) for three equivalent *0.25:CU_rGO$_{ag}$* scaffolds were averaged and arranged in Figure 5.24.

These registered times were in concordance with the expected behaviour from CA measurements when increasing the amount of PF127 in suspension, substantially reducing the standard deviation from previous infiltration results. In 12.5 wt.% Al_2O_3(0P) suspensions infiltration never occurred as expected from the hydrophobic behaviour of the reduced scaffold. This was only slightly improved in 12.5 wt.% Al_2O_3(0.01P), with PF127 additions in the range of surfactant wt.% from ceramic processing, although not sufficient to accomplish the infiltration of the aerogels.

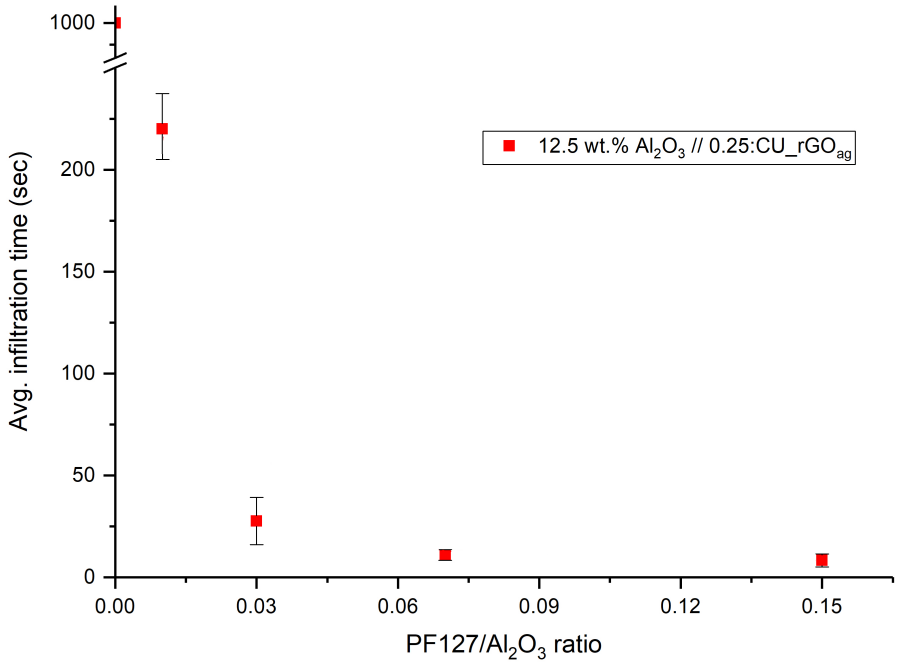

Figure 5.24: *Infiltration times registered for 0.25:CU_rGO_{ag} scaffolds in 12.5 wt.% alumina slurries with increasing PF127/Al_2O_3 content. Averaged on three measurements.*

Using 12.5 wt.% Al_2O_3(0.03P), infiltration of rGO aerogels was significantly enhanced, changing the trend entirely and obtaining progressively reduced times (around 30 seconds). These conditions already verified a drastic change in the hydrophobic response of *CU_rGO_{ag}* after PF127 additions in suspension. However, at these low quantities of PF127 complete infiltration was never reached, as freezing and freeze-drying of the mixture revealed the slurry did not fully infiltrate the scaffold. As efficient infiltration was provided for 0.07 and 0.15 PF127/Al_2O_3 ratios, these conditions were selected for the general processing route.

5.5.3.1 Infiltration tests on lab-scaled aerogels with alumina NP-decoration

The infiltration capabilities of lab-sized aerogels with the extended hierarchy provided by alumina nanoparticles decoration (from Section 4.6.3) was also tested. An equivalent array of thermally-reduced aerogels (13 mm diameter and 19 mm height) was infiltrated, substituting *0.25:CU_rGO_{ag}* for *0.25:CU_rGO_{ag}(0.05N)* samples while following the infiltration conditions presented in Figure 5.23. The obtained infiltration times for the decorated graphene aerogels was compared to non-decorated ones and displayed in Figure 5.25.

The infiltration profile obtained for decorated *0.25:CU_rGO_{ag}(0.05N)* showed a similar trend to plain *0.25:CU_rGO_{ag}* aerogels. However, infiltration was found slower for every tested PF127/Al_2O_3 ratio in the decorated samples, inhibiting the infiltration at 0.01P ratios completely. These results suggested that the introduction

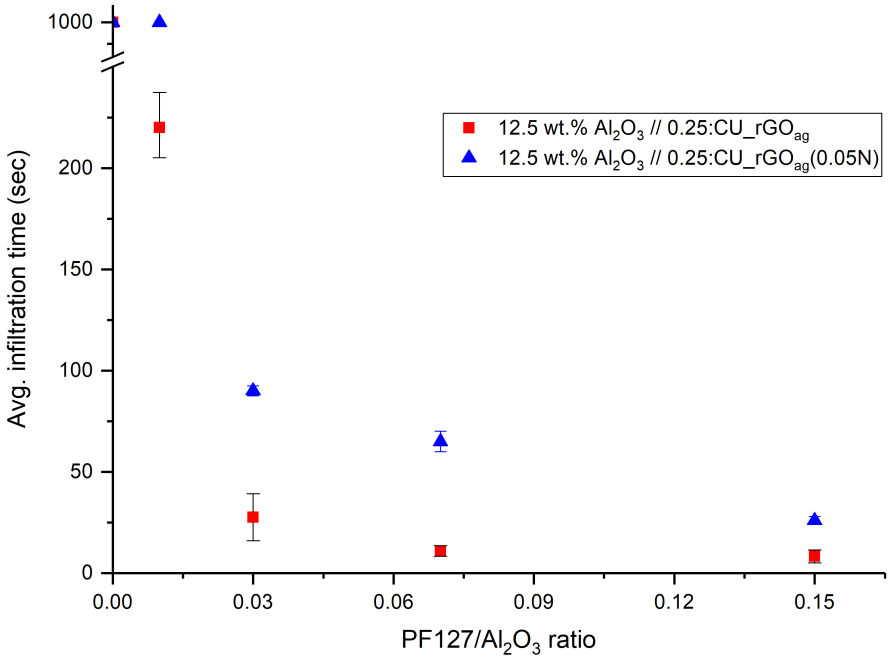

Figure 5.25: *Infiltration of 0.25:CU_rGO_{ag}(0.05N) aerogels in 12.5 wt.% alumina slurries with increasing PF127/Al_2O_3 content, compared to previous non-decorated 0.25:CU_rGO_{ag}. Averaged on three measurements.*

of aluminium hydroxide gel (alumina NPs precursors) in the GO suspension formulation hindered the interaction of the hydrophilic alumina surface with the hydrophobic graphene phase despite PF127 additions.

The introduction of basic aluminium hydroxide gels (pH 10) in the GO suspension could affect the hydrophobicity of the aerogels produced, even though traces of NaOH in the graphene aerogels were not significant after carbonisation (verified by the XPS surveys on decorated *0.25:CU_rGO_{ag}(0.05N)* aerogels). This could be avoided by improving the production of NP-decorated graphene aerogels by freeze-drying the NP precursor (aluminium hydroxide gels) before integrating with GO suspensions. As the infiltration of decorated graphene aerogels with enhanced hierarchy appeared slightly more challenging, the scalability of the graphene/alumina processing strategy was focused on non-decorated aerogels exclusively.

5.5.4 Scaled-up graphene/alumina green bodies

Conditions selected from infiltration tests on lab-scale aerogels (0.07P and 0.15P ratios) were applied to infiltrate scaled-up *0.25:ICL_$rGO_{ag}\perp$* and *0.5:ICL_$rGO_{ag}\perp$* (28 mm diameter and 30 mm height). Green bodies were produced integrating both the improved *ICL_GO* precursor and the 4-piece freeze-casting mould with the perpendicular axis of revolution from Figure 3.3b. Even if Al_2O_3(0.07P) slurries appeared sufficient to enable the infiltration from the results in Figure 5.24, 0.15P ratios were also tested, as the scaffold infiltration could be hindered by the increase

in viscosity from selecting alumina solid loadings of 25 wt.% Al_2O_3 (demonstrated in Figure 5.12) and the scaled-up aerogel dimensions.

Constraints derived from selecting the SPS equipment for final consolidation stages were applied to adjust the alumina slurry loading. Higher quantities of PF127 copolymer in the pre-sintered composite could comprise an increase in volatiles inside the SPS graphitic dies, released during the following sintering stage. At the range of solid loadings in this work (12.5 - 25 wt.% Al_2O_3), the quantity of PF127 should be limited to avoid obtaining a binary PF127/Al_2O_3 composite, in which the latter could not be negligible. A compromise was needed between restricting the amount of PF127 in the Al_2O_3 slurries and losing its beneficial effects towards overcoming the hydrophobic behaviour of graphene scaffolds.

Another constraint related to the minimum quantity of solid material required to produce a dense composite that could be manufactured into specimens for mechanical testing. Enough alumina weight was needed in the SPS dies so that the physical dimensions of sintered ceramic/graphene discs could meet the dimensional requirements from ASTM standards (Figure 5.26).

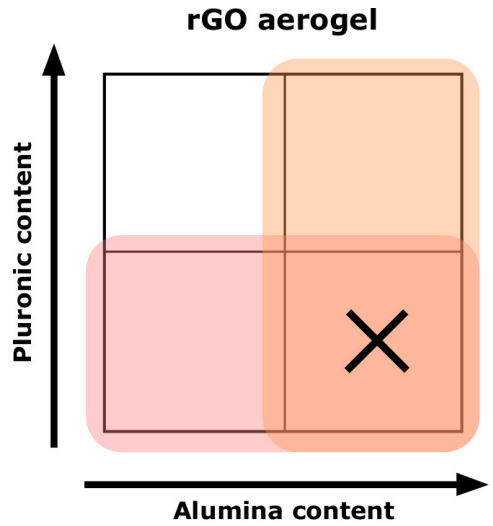

Figure 5.26: *Preferred region of operation: high alumina loading and low quantity of PF127 in suspension*

The ultra-low weight of the supporting rGO scaffolds (40 – 85 mg after thermal annealing at 900 °C) was considered negligible and expected to account for < 1 wt.% of the total composite weight after embedding in the alumina matrix [183]. From the guidelines provided by *C1161-18* (flexural strength of advanced ceramics) and *C1421-18* (determination of fracture toughness of advanced ceramics at ambient temperature) [256, 257], a disc thickness of 3 mm was set as the objective, including potential grinding and polishing steps.

Based on the 3.96 g cm^{-3} Al_2O_3 powder density as measured by helium pycnometry, 4 g of material were needed in the SPS dies to produce 20 mm sintered discs with

a minimum height of 3.5 mm. $4 \times 2.25 = 9$ g of solid alumina were required to obtain 30 mm discs matching the exact thickness requirement, adjusted after calculating the volume difference from both setups:

$$\frac{V_{30mm}}{V_{20mm}} = \frac{\pi 15^2 H}{\pi 10^2 H} = 2.25 \tag{5.1}$$

In the case of selecting diluted 12.5 wt.% Al_2O_3 slurries, 72 g would be necessary to meet the 9 g of alumina solid weight. The volume corresponding to this weight was estimated by a simple rule of mixtures excluding the contribution of varying PF127, obtaining 65.28 cm^3.

$$V_{total} = m_{Al_2O_3} \times \rho_{Al_2O_3} + m_{H_2O} \times \rho_{H_2O} \tag{5.2}$$

This volume was required to infiltrate the scaled-up ICL_GO_{ag} aerogels fully. However, 30 mm ICL_GO_{ag} aerogels only occupied an average volume of 24.03 cm^3 based on the dimensions of the 4-piece freeze-casting mould, not enough to support the amount of 12.5 wt.% Al_2O_3 slurry needed to produce specimens of sufficient thickness. Applying the same calculations to 25 wt.% Al_2O_3 slurries, the slurry weight required to guarantee the 9 g of alumina solid material in the 30 mm SPS dies was reduced to 36 g. This weight corresponded to a slurry volume of 29.28 cm^3, which validated the almost complete filling of the 24.03 cm^3 volume available in the scaled-up ICL_GO_{ag} aerogels.

From these calculations, the infiltration scalability was solely focused on 25 wt.% Al_2O_3 slurries, with the PF127/Al_2O_3 ratios of 0.07P and 0.15P derived from tests on lab-scale aerogels. The increase in viscosity of the 25 wt.% Al_2O_3 slurries proved excessive to allow the infiltration by aerogel deposition in suspension in the absence of vacuum, as performed with earlier tests on lab-scale rGO aerogels. However, the vacuum-driven infusion processing applied for epoxy/rGO composites in the previous chapter (Section 4.5.3) could not be used due to the foaming effect occurring with PF127 in higher quantities arising from its micellisation capabilities (Figure 5.11) [247].

The PF127/Al_2O_3 slurries were deposited dropwise onto the scaled-up rGO aerogels until complete infiltration (reversing the aerogel deposition protocol employed for infiltration tests with lab-scale samples). After infiltration and freezing, the scaled-up ICL_GO_{ag} scaffolds appeared homogeneously covered by the slurry for both 0.07 and 0.15 PF127/Al_2O_3 ratios (Figure 5.27). Removing the ice by freeze-drying revealed the rGO scaffolds underneath, validating the infiltration conditions and delivering scaled-up rGO/PF127/Al_2O_3 green bodies ready for final consolidation through SPS.

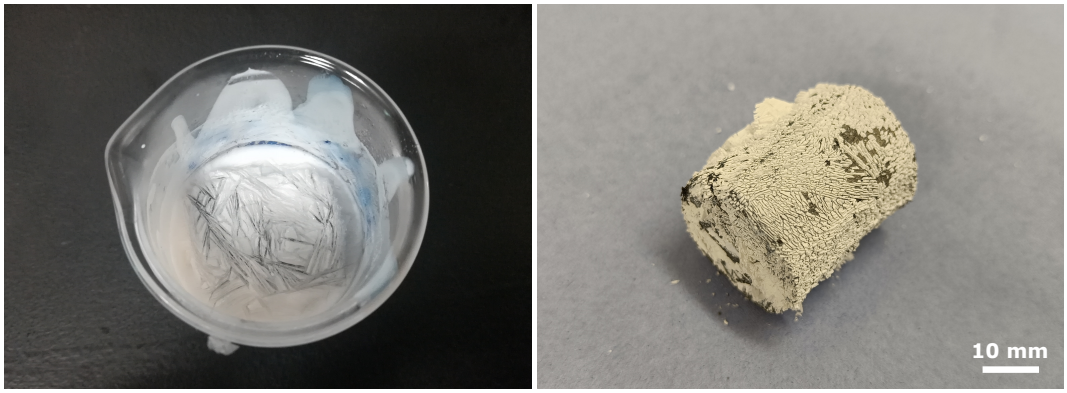

Figure 5.27: *Infiltration and freeze-drying of scaled-up 0.5:ICL_ $rGO_{ag}\perp$ aerogels.*

5.6 Conclusions

The spray-dried commercial alumina powder used in this work was first characterised through XRD, FESEM and particle size measurements. Water-based alumina slurries of 12.5 and 25 wt.% solid loading were produced, evaluating the change in viscosity and the introduction of the amphiphilic copolymer Pluronic F127 (PF127) in suspension at various quantities. PF127 was included in the water-based alumina slurries to control the surface response of the ceramic particles and permit the infiltration in hydrophobic graphene-based structures. Its effect was first validated by wettability measurements between alumina slurries containing 0.15 PF127/Al_2O_3 wt./wt. ratio and rGO spin-coated films, obtaining reduced contact angles with increased PF127 content in suspension. The films were partially reduced at 400 °C, which preserved the film continuity and validated a significant elimination of oxidised groups in the GO sheets as confirmed by Raman and XPS characterisation.

The optimum PF127/Al_2O_3 ratio in suspension was adjusted to 0.07 - 0.15 via custom infiltration tests, performed by deposition of lab-scale rGO aerogels (13 mm diameter, 19 mm height) on 12.5 wt.% alumina slurries. These infiltration tests were aimed to reduce the PF127 quantities in suspension to a minimum without neglecting the improvements in wettability with the graphene structures. Expanding the tests to lab-scale rGO aerogels decorated with as-produced alumina nanoparticles under similar conditions confirmed the infiltration capabilities were negatively affected. From these results, the scalability of the processing route was focused on non-decorated aerogels. Scaled-up graphene/alumina green bodies were obtained by infiltration of *ICL_ GO* aerogels (30 mm diameter) with the PF127/Al_2O_3 formulation from previous tests, followed by freeze-drying.

The critical challenge of enabling the infiltration of a hydrophobic scaffold with water-based alumina slurries was overcome, which comprises the main breakthrough of this work.

Chapter 6

Composite consolidation via Spark Plasma Sintering

6.1 Introduction

Sintering is a crucial stage in processing ceramic-based materials to densify green bodies, providing structural cohesion and mechanical strength. Spark Plasma Sintering (SPS) has stood out as a standard in non-conventional sintering combining direct electrical current and uniaxial pressure, applied in graphene/ceramic pairs due to its high reliability and reduced sintering times compared to conventional techniques [6]. Successful sintering of ceramic-based composites requires extensive optimisation of the parameters involved, such as the temperature of consolidation, the duration of isothermal dwelling, applied heating/cooling rates or uniaxial pressure. All these parameters affect the mechanical and thermal stress exerted on the ceramic bodies, which can be subjected to failure due to their reduced fracture resistance and plasticity compared to metals.

This chapter presents the third stage in producing the novel graphene/ceramic composite, targeting the consolidation of graphene/alumina green bodies by optimising the sintering procedure (Figure 6.1). Taking inspiration from previous works on SPS sintering of alumina and randomly oriented graphene/ceramic composites in the literature [86, 157, 158, 171], starting sintering conditions were defined. These include maximum temperatures of 1350 – 1500 °C, 50 MPa or pressure, heating and cooling rates up to 100 °C min^{-1} and isothermal dwell times as low as 1 minute.

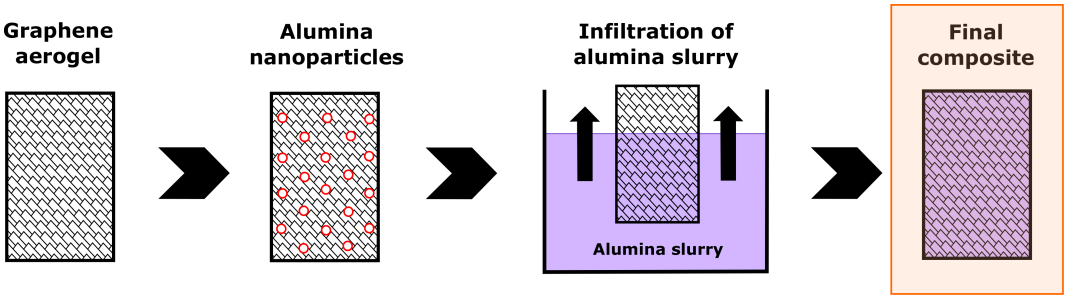

Figure 6.1: *Third stage of the composite processing strategy: Achieving a consolidated graphene/ceramic composite using SPS.*

Single-phase alumina samples were first produced to optimise the sintering cycles and compensate for the challenges arising during ceramic-based materials' sintering. The degree of densification and grain microstructure in the discs were evaluated, adjusting the parameters to deliver densified discs without failure. The selected conditions were extended to lab-sized rGO aerogels infiltrated with water-based PF127/Al_2O_3 slurries and freeze-dried presented in the previous chapter. The scalability of the processing route was also approached by sintering scaled-up green bodies of 30 mm in diameter. In both cases, the fracture surface of the SPSed composites was studied to determine the preservation of the embedded rGO network and the microstructure of the alumina matrices, evaluating the challenges for future works in this field.

6.2 Methodology

6.2.1 Production of SPS discs

Dense 20 mm alumina discs (2 – 4 mm in height) were first produced by SPS sintering of 3 – 4 g of BA-15W powder as a preliminary optimisation for sintering cycles of graphene/alumina mixtures. As a standard procedure, a maximum temperature of 1350 - 1500 °C was achieved by applying a pulsating current sequence of 10-5-12-2 (ON time - OFF time - number of pulses - extra pause) combined with a maximum uniaxial pressure of 50 MPa.

Various sintering conditions were tested by modifying the heating and cooling rates to 50 - 100 °C min^{-1} and applying extended dwelling times (1 – 10 min) (Figure 6.2). Throughout the optimisation section, the sintering conditions have been labelled as *Al_2O_3(a:b:c:d)* with a referring to the maximum isothermal temperature (in °C), b the dwelling time (in min), c the heating rate applied (°C min^{-1}) and d the controlled cooling rate (°C min^{-1}). The exerted pressure of 50 MPa was maintained throughout all the cycles tested.

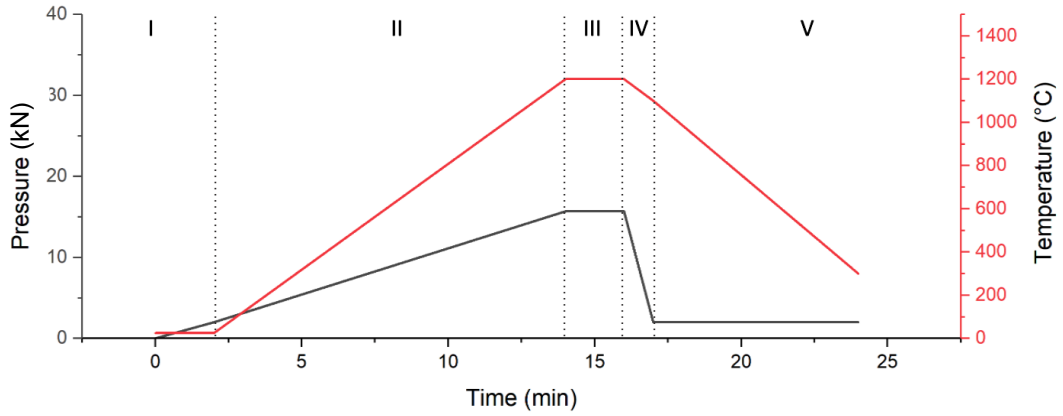

Figure 6.2: *Temperature (red line) and pressure (black line) profiles applied by the SPS unit during sintering. Sintering stages comprise I: Cold pressing, II: Current-assisted heating, III: Isothermal dwell, IV: Pressure release and V: Controlled cooling step.*

The microstructure and density of produced alumina discs were evaluated through Field-Emission Scanning Electron Microscopy (FESEM). Before characterisation, the graphite foil attached to the surface of the discs was removed with a scalpel knife, cleaning the sample with isopropanol. The porosity of alumina discs sintered through various parameters was evaluated by Archimedes density on an average of three specimens (Equations 3.8 and 3.9 from Section 3.3.7) and compared to the density of raw alumina powder obtained by helium pycnometry.

6.2.2 SPS of graphene/alumina green bodies

Lab-scale $0.5{:}CU\_rGO_{ag}$ scaffolds (13 mm diameter, 19 mm height) infiltrated with 12.5 and 25 wt.% PF127/Al_2O_3 mixtures and freeze-dried for 72 hours were placed on 20 mm SPS graphitic dies (Figure 3.9) and protected with graphite foil. The freezing direction in the rGO scaffolds was kept perpendicular to the SPS uniaxial pressing direction. Additional BA15W alumina powder was added to ensure an approximate weight of 4 g inside the graphitic dies, providing samples of sufficient thickness. The assembled dies were cold-pressed up to 2 kN before fitting in the SPS chamber to improve packing and compaction.

Sintered graphene/alumina composites (labelled $25{:}Al_2O_3/0.5{:}CU\_rGO_{ag}$) were embedded in epoxy resin and polished for characterisation following the protocol outlined in Sections 3.2.5 and 3.2.7. The specimens were evaluated through optical microscopy and X-ray diffraction to study their microstructure and crystallography, respectively. The fracture surface of the obtained graphene/alumina composites was additionally characterised by FESEM, evaluating the preservation of the embedded graphene-based scaffolds measuring the channel widths between the rGO walls using *ImageJ*. Scaled-up $25{:}Al_2O_3/0.5{:}ICL\_rGO_{ag}$ (30 mm diameter) were freeze-dried for 72 hours and placed on 30 mm SPS dies (Figure 6.3), densified via SPS using

the previous optimisation of the sintering cycles. The microstructure was similarly examined via FESEM.

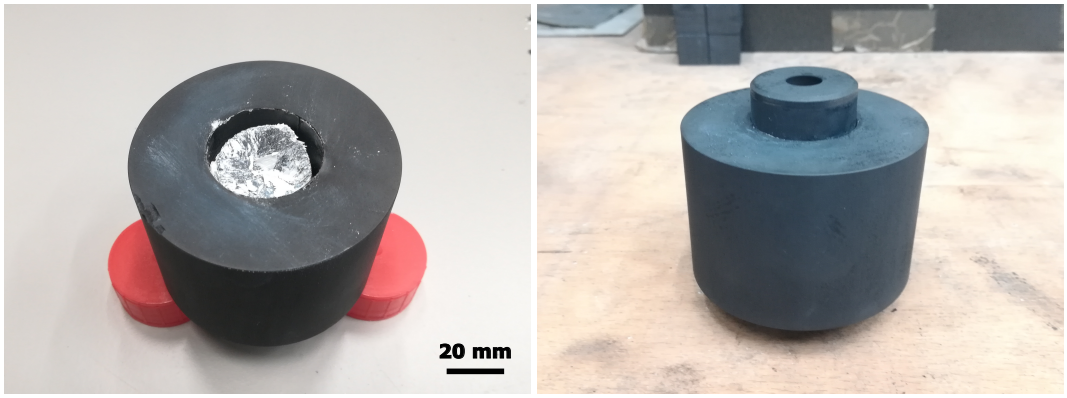

Figure 6.3: *Preparation of graphitic die assembly for scaled-up 5:Al_2O_3/0.5:ICL_-rGO_{ag} samples.*

6.3 Sintering of alumina discs by SPS

SPS was selected as the consolidation technique in this study to achieve improved densification of the materials, which permitted fast sintering times and high heating rates (50 – 100 °C min^{-1}) to limit grain growth. The complexity of the equipment required a greater understanding of sintering ceramic-based materials and the performance of several optimisation runs, permitting great flexibility of sintering parameters in terms of pressure, current-assisted heating and cooling.

SPS cycles were optimised for bulk alumina powder before defining a sintering program suitable for graphene/alumina discs. The ceramic phase in the composite appeared more challenging to sinter [41] without including an internal graphene network providing higher flexibility and resistance to the exerted thermal and mechanical stress. Many sintering parameters could be tested with the bulk powder efficiently. This permitted avoiding the extensive composite processing required, extrapolating the defined sintering cycles to the graphene/ceramic composite green bodies.

6.3.1 Optimisation of SPS sintering cycle

Various sintering parameters were tested to achieve densification in the alumina, limit the porosity and produce unbroken sample discs (Table 6.1). A 100 °C heating pre-treatment of the alumina powder in the graphite die before insertion in the SPS chamber was also tested to eliminate potential humidity traces in the sample. However, it did not result in any noticeable effect on the integrity of consolidated discs.

Table 6.1: *Summary of sintering parameters tested for 20 mm Al_2O_3 discs.*

Heat rate (C min-1)	**Cool rate (C min-1)**	**Max. P (MPa)**	**Max. T (C)**	**Dwell (min)**	**Pressure release**
100	-	50	1250	1	-
100	-	50	1250	1	Y
100	-	50	1350	1	-
100	-	50	1350	1	Y
100	-	50	1500	1	-
100	-	50	1500	1	Y
100	100	50	1350	1	Y
100	100	50	1350	3	Y
100	100	50	1350	5	Y
100	50	50	1350	5	Y
100	50	50	1350	10	Y
50	50	50	1350	5	Y
50	50	50	1350	10	Y

20 mm alumina discs sintered upon 1 min dwelling times displayed a central splitting crack after consolidation. A quick pressure release step was included after the isothermal dwell to lower the mechanical stress exerted on the samples during the cooling stage. As one main weakness of ceramic materials lies in their poor resistance to thermal shock, natural cooling was also discarded, favouring smoother controlled cooling rates of 50 – 100 °C min^{-1}.

A comparison of two of the obtained sintering cycles for *Al_2O_3(1350:5:50:50)* and *Al_2O_3(1350:10:100:50)* is displayed in Figure 6.4, highlighting the temperatures and pressure achieved as well as both the hydraulic piston's displacement and speed. The most significant features were present in every test. A sudden rise in the piston displacement (pink curve) with a spike in the piston speed (blue curve) up to 2 mm min^{-1} were registered at the very beginning of the cycle. This was a consistent behaviour for every sample, belonging to the quick compaction of the ceramic powder during the initial pressing stage up to 10 kN. As the temperature increased, a progressive rise in the piston displacement (almost 4 mm) was found starting circa 900 °C extended up to 1350 °C, showing a much more smoothed piston speed curve. This secondary compaction is related to the actual sintering process of the alumina grains and the reduction of the system's total energy arising from both a reduction in the interfacial energy and the surface area between particles (Section 1.1.2.2) [4].

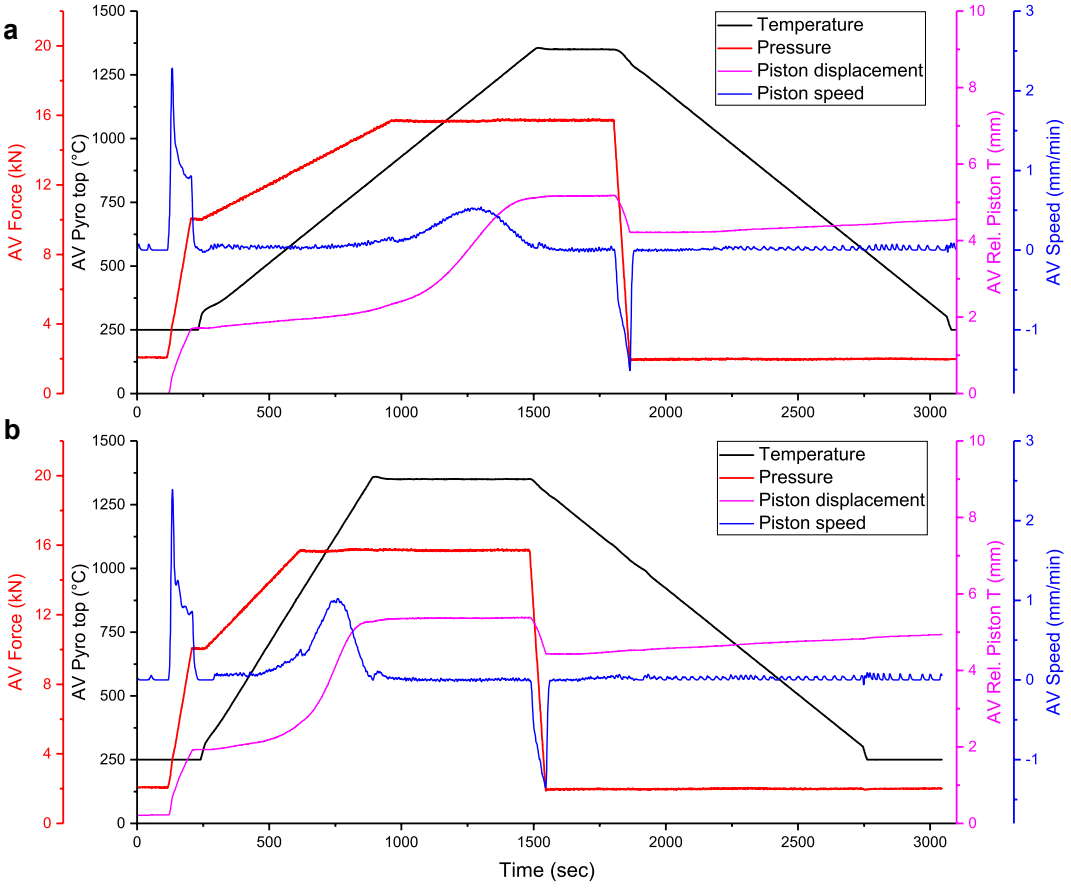

Figure 6.4: *Examples of SPS graphs for 20 mm alumina discs showing sintering parameters: Temperature registered by the top pyrometer (black), exerted uniaxial compression (red), piston displacement (pink) and piston speed (blue). a) Al_2O_3(1350:5:50:50). b) Al_2O_3(1350:10:100:50).*

After the isothermal stage, a sudden drop of force (blue curve) back to the contact 2 kN was applied from the pressure release stage, included to ease the mechanical stress exerted to the ceramic disc during cooling (around 1500 seconds in Figure 6.4b). This pressure drop was translated into a subtle sample expansion, exerting an outwards piston displacement of 1 mm. The sintered alumina disc shrank slightly during cooling, shown by the progressive 0.5 mm piston displacement until reaching room temperature. The fluctuations in piston speed (blue curve) obtained during the cooling stage were attributed to artefacts in its calculation as the first derivative of the piston displacement registered by the equipment. These sintering cycles also confirmed that the length of the dwelling stage did not influence the densification process itself, ending by the start of the isothermal stage (circa 1000 sec in Figure 6.4b) as demonstrated by the absence of piston displacement. Beyond this point, maintaining higher temperatures could affect the sample's microstructure and result in the formation of pores and defects detrimental to the material's performance.

Extending the isothermal stage proved essential in producing non-damaged 20 mm alumina discs with 100 °C min^{-1} heating and cooling rates for both maximum temperatures of 1350 and 1500 °C. Increased dwelling times (3 – 10 min) maintaining

equal heating and cooling rates were applied to reduce the thermal gradient between the core and periphery of the sintered discs before rapid cooling and help prevent cracking. As displayed in Figure 6.5, adjusting this parameter led to a higher percentage of unbroken discs, resulting in a more reliable production of alumina discs without failure.

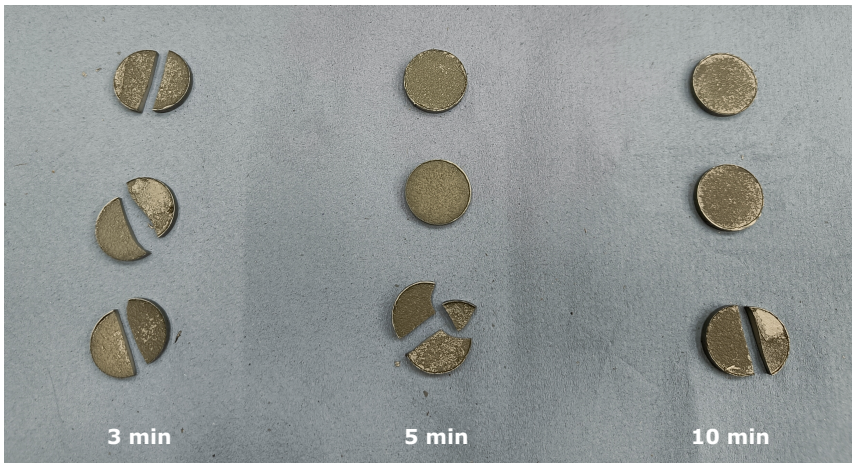

Figure 6.5: *20 mm discs consolidated by SPS of Al_2O_3(1350:100:50:X) with increasing dwelling times. From left to right: 3, 5 and 10 min.*

The selection of slower cooling rates of 50 °C min^{-1} did not result in more consistency in achieving unbroken alumina discs, for which 100 °C min^{-1} were preferred to accelerate the production. The careful application of pressure and temperature was needed to avoid crack formation via the combination of mechanical and thermal stresses. This is a critical issue for ceramic-based materials exhibiting barely any plasticity compared to metals, thus resulting in more difficult manufacture and conformation [1, 38]. The insulating behaviour of alumina additionally provided poorer heat distribution in the sample at higher temperatures, as the electrical current is forced to circulate through the outer graphitic dies, exclusively hindering the SPS heating mechanism by the Joule effect (Equation 1.5) [51, 53]. Although 1 min dwelling times for have been previously reported in the literature [258], the alumina in this work appeared highly sensitive to the thermal gradients between the core and periphery of the discs.

6.3.2 Characterisation of 20 mm alumina discs

One of the main advantages of selecting an SPS sintering procedure relies on the possibility of achieving an adequate degree of densification in the material. 20 mm alumina discs were compared through Archimedes density measurements after SPS, presented for each test condition in Table 6.2. The effect of changing the isothermal temperature (1350 – 1500 °C) and dwelling times (3 – 10 min) was evaluated by comparing the porosity (ϵ) obtained for the sintered alumina discs using the pycnometry results of BA15 powder (3.96 g cm^{-3}) previously presented in Section 5.4.1.

Table 6.2: *Archimedes density and porosity values obtained for 20 mm SPS alumina discs.*

Sample IDs	**Heat rate (°C min^{-1})**	**Max. T (°C)**	**Dwell (min)**	**Density (g cm^{-3})**	**Porosity (%)**
Al_2O_3(1350:3:100:50)	100	1350	3	3.87	2.24
Al_2O_3(1350:5:100:50)	100	1350	5	3.94	0.55
Al_2O_3(1350:10:100:50)	100	1350	10	3.90	1.43
Al_2O_3(1500:5:100:50)	100	1500	5	3.89	1.70
Al_2O_3(1350:10:50:50)	50	1350	5	3.95	0.28

All tested cycles resulted in consistent high densification (97.8 - 99.7%) for the provided conditions. The shortest dwelling times led to obtaining the highest porosity value, although the individual effects from further dwelling extension or the effect of temperature could not be properly evaluated. The highest densification was achieved for *Al_2O_3(1350:10:50:50)* samples by providing longer times at maximum temperature combined with a slower heating ramp. However, this resulted in slower processing times (with an increased operational cost) without significantly improving densification. Increasing the maximum sintering temperature from 1350 to 1500 °C did not increase the real density of the SPS discs, with the influence of dwelling time and heating rates appearing more significant after comparison of *Al_2O_3(1350:5:100:50)* and *Al_2O_3(1500:5:100:50)* from Table 6.2.

Differences in the microstructure of the produced alumina discs obtained after densification at these two temperatures (1350 vs 1500 °C) were evaluated by studying the fracture surface via FESEM (Figure 6.6), maintaining the rest of the sintering parameters. The average grain size obtained for 1350 °C was 0.7 ± 0.15 μm compared to 1.2 ± 0.3 μm for 1500 °C, which showed slight grain growth associated with higher sintering temperatures. The fracture mechanisms also appeared significantly different, with sintered samples at 1350 °C displaying predominantly intergranular fracture with well-defined grain boundaries. In contrast, at 1500 °C the grain boundaries were less obvious, indicating a higher degree of sintering with instances of transgranular fracture. Grain coarsening was also identified in some areas from the merging of neighbouring grain boundaries, which could affect the material's mechanical strength.

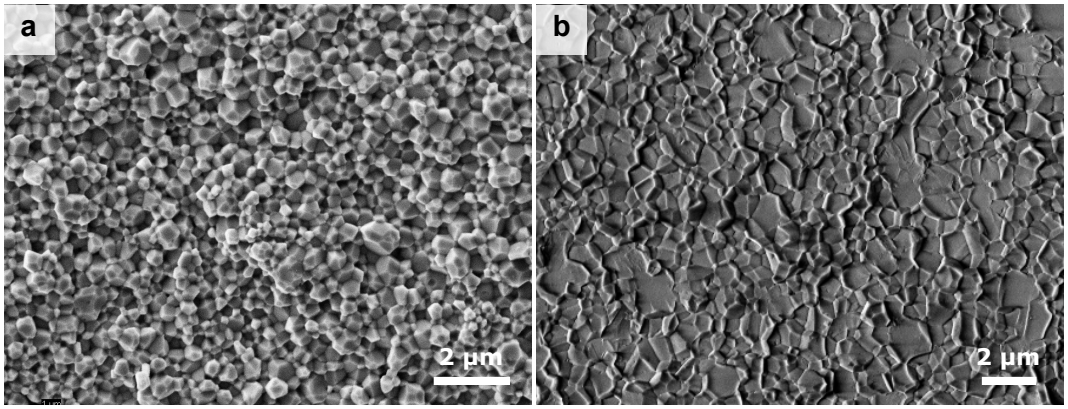

Figure 6.6: *FESEM of fracture surface of 20 mm discs. a) Al_2O_3(1350:5:100:50) sintered at 1350 °C b) Al_2O_3(1500:5:100:50) sintered at 1500 °C.*

The combination of pressure, temperature and heating rates affected the resulting grain size of the densified alumina from the competing processes of densification and grain coarsening during the final stages of sintering [4]. Higher temperatures can maximise densification while triggering the formation of temperature-induced pores that can provide potential locations for crack initiation. Excessive grain growth is also detrimental to the mechanical strength and hardness of the ceramic matrices [259, 260].

From these results, sintering parameters were settled on dwelling times above 5 minutes, heating rates of 100 °C min^{-1} and cooling rates of 100 °C min^{-1}. The grain microstructure was preserved by combining high heating rates and uniaxial pressure enabled by SPS while achieving limited porosity. The sintering temperature could be limited at 1350 °C without negatively affecting the densification of the alumina matrix and still producing unbroken specimens. However, as a preliminary cycle optimisation towards graphene/alumina composites, the sintering isothermal temperature affects both the alumina matrix microstructure and the embedded rGO scaffold phase. Higher temperatures of sintering permit an extended restoration of the sp^2 graphitic domains from the rGO structure, leading to higher electrical conductivity in the network that can be key for sensing and monitoring applications. Therefore, 1500 °C were preferred expecting to obtain a higher degree of graphitisation in the graphene-based scaffold.

6.4 Consolidation of hierarchical graphene/alumina composites

6.4.1 Lab-scale graphene/alumina composites

Lab-scale *25:Al_2O_3/0.5:CU_rGO_{ag}* green bodies (13 mm diameter, 19 mm height) were sintered at a standard heating rate of 100 °C min^{-1}, 1500 °C temperature and 5 min dwelling times according to the optimisation of the sintering cycles performed in the previous section. From applying a partial thermal reduction of the aerogels at 900 °C before the integration with the alumina phase via infiltration, most oxidised groups attached to the former GO structure in the network were priorly removed from the material (as confirmed by XPS measurements of *CU_rGO_{fzd}* from Figure 4.5).

An example of the applied sintering cycle for *25:Al_2O_3/0.5:CU_rGO_{ag}* is included in Figure 6.7. Similar to the graphs for plain alumina powder, a quick rise of piston displacement (pink curve) with its corresponding speed derivative (blue curve) was registered during the initial cold-pressing up to 10 kN. However, in these graphs, a secondary jump in piston displacement of 1.5 mm was also recorded at the end of the pressing stage, coinciding with a sudden spike in piston speed and a pressure fluctuation (red curve). This spike was attributed to the breakage of the embedded rGO aerogel, maximising packing and accommodating the uniaxial stress. The sintering of the alumina phase similarly occurred near the isothermal stage (at 1000 sec), verified by the smoother rise in piston displacement.

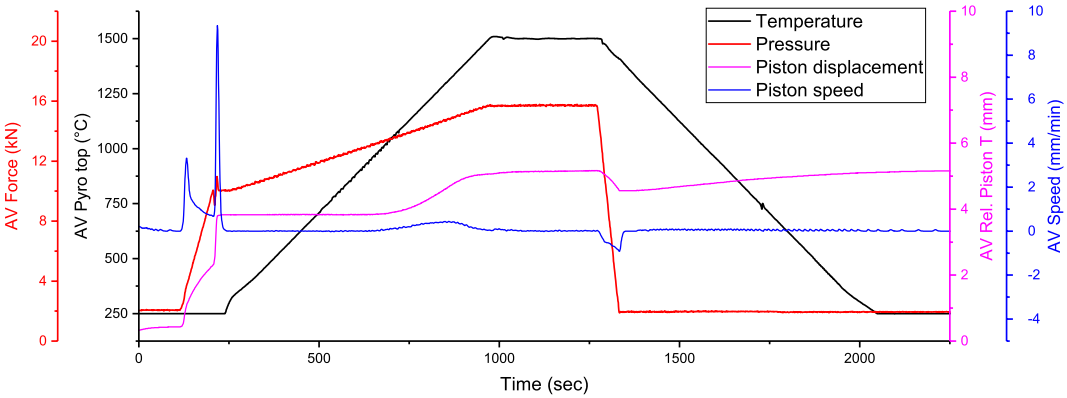

Figure 6.7: *SPS sintering graph for 20 mm 25:Al_2O_3/0.5:CU_rGO_{ag} discs. Sintering parameters: Top pyrometer temperature (black), uniaxial compression (red), piston displacement (pink) and piston speed (blue).*

After the isothermal dwell, the response matched plain alumina discs (Figure 6.4), with a minor expansion of the piston of 0.5 mm after the pressure release and progressive sample contraction during cooling until room temperature. In this particular graph, a slight temperature fluctuation was also registered during the cooling stage at around 1750 sec. It was attributed to disturbances in the applied

pulsating current, which did not affect the displacement of the sample.

As discussed, higher sintering temperatures could induce bigger thermal shock in pure ceramic discs during consolidation. However, it was expected that the embedded graphitic scaffold would provide sufficient electrical conductivity to permit the flow of electrical current through the sample during SPS sintering in contrast with pure ceramic samples, lowering the thermal gradient between the core and the periphery of the discs. The graphitic second phase could also influence the grain growth of alumina at higher temperatures of sintering.

25:Al_2O_3/0.5:CU_ rGO_{ag} samples sintered at 1500 °C were examined by XRD after embedding in epoxy resin and polishing (Figure 6.8). The crystallinity of the alumina matrix was preserved, showing the stability of the α-alumina phase after comparison with the ICDD reference from Section 5.4.1.

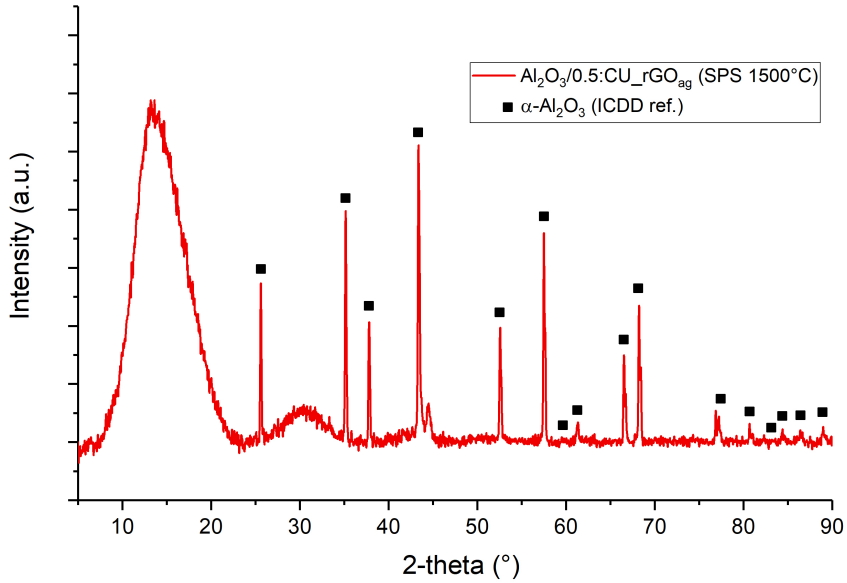

Figure 6.8: *XRD spectrum of 25:Al_2O_3/0.5:CU_ rGO_{ag} embedded in epoxy, including an ICDD reference of α-alumina.*

While the XRD spectrum of *CU_ rGO_{fzd}* delivered a broad peak at around 20 – 25 ° (Section 4.3.1), the embedded rGO scaffold in the composite did not produce any signal at 2θ values around 25 °. The increase in reduction temperature provided by the SPS sintering (from 900 to 1500 °C) was expected to sharpen the rGO shift and bring it closer to graphite's characteristic [002] diffraction peak at 26.5 °, given the higher restoration of sp^2 domains and the further reduction in the graphene sheets interplanar spacing without oxidising groups. However, as XRD is a surface-sensitive technique, the incident X-rays could not be diffracted by the ultra-light rGO scaffolds composing a marginal weight contribution to the overall composite. The broader peaks of higher intensity around 13 and 30 ° were attributed to the organic chains present in the resin used to embed the *25:Al_2O_3/0.5:CU_ rGO_{ag}* samples.

The polished $25{:}Al_2O_3/0.5{:}CU\_rGO_{ag}$ composites were examined by optical microscopy to identify the embedded rGO network in the alumina matrices (Figure 6.9). The light polarisation applied in these images permitted identifying the ceramic matrix and the infiltrated scaffold separately, with the latter exhibiting a darker shade and a seemingly intricate structure. However, the directional alignment and microstructure of the graphene phase could not be confirmed, requiring higher quality imaging.

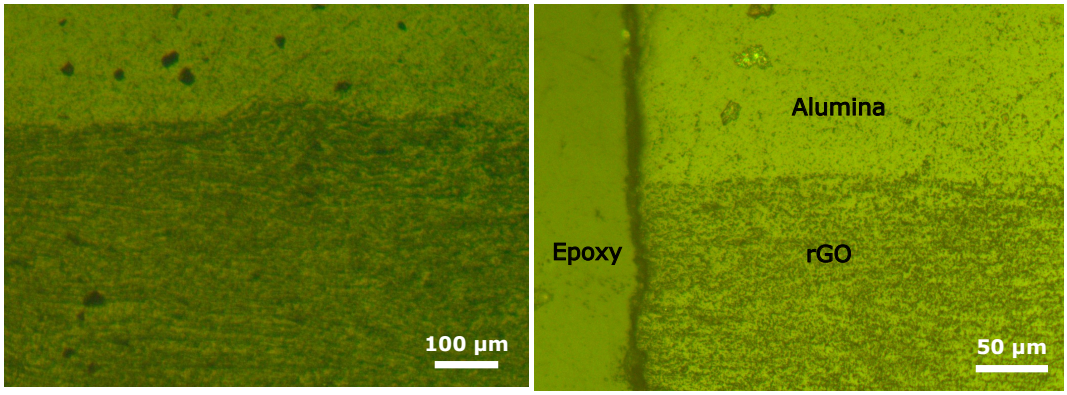

Figure 6.9: *Optical microscopy of lab-scale $25{:}Al_2O_3/0.5{:}CU\_rGO_{ag}$ composites.*

FESEM characterisation of the fracture surface of 20 mm $25{:}Al_2O_3/0.5{:}CU\_rGO_{ag}$ discs after sintering at 1500 °C permitted obtaining more information about the composite (Figure 6.10). The unidirectional alignment of the embedded graphene scaffolds was maintained in the alumina matrix after the 1500 °C sintering temperature, exhibiting the former freeze-cast structure of the GO aerogels. After exploring several fracture sections in the composite, the scaffold channel spacing ranged from 5 – 15 μm depending on the examination area. It is possible that the cylindrical shape of the lab-sized CU_rGO_{ag} aerogels led to stress concentrations under SPS pressing, with localised areas of the composite subjected to more significant compression selectively reducing the channel width. Another explanation could lie in a non-homogeneous infiltration of alumina material during previous steps, which would explain the gaps in the ceramic matrix found upon sintering (Figure 6.10b).

Pull-out of rGO flakes was found along the fracture surface (Figure 6.10d), matching other works in the field [86, 187, 261], which could constitute extrinsic toughening mechanisms for deflecting crack propagation and increase the fracture toughness of the composite material. Agglomeration of the rGO sheets was found after examining the fracture surface of the composite. Limiting the GO content (below the 0.5 wt.% GO concentration selected for the aerogel production) could help reduce agglomeration while maintaining the unidirectional alignment provided by freeze-casting [152]. However, the relatively low GO flake lateral size of 9 μm found for CU_GO suspensions (Figure 4.2) prevented lowering the GO concentration in suspension below 0.5 wt.% without a significant loss of alignment in the scaffolds during the freeze-casting stage.

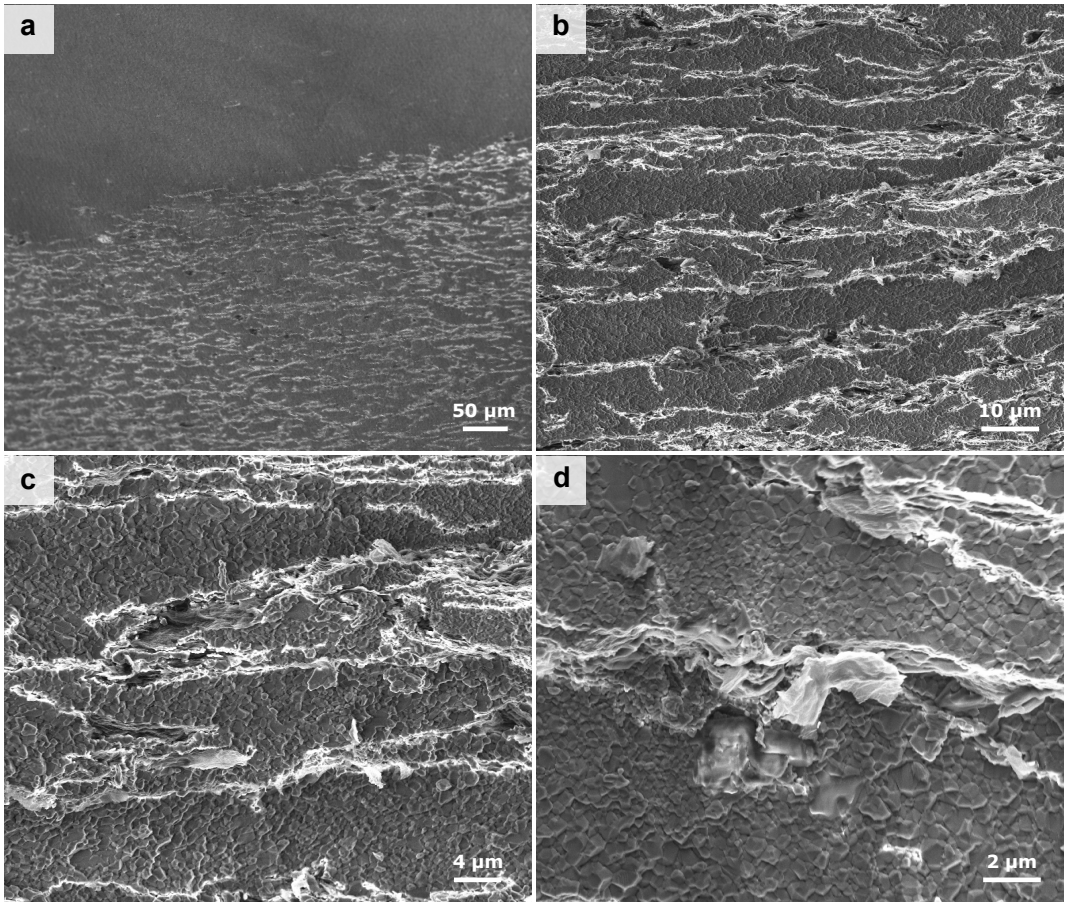

Figure 6.10: *FESEM characterisation showing the fracture surface of 25:Al_2O_3/0.5:CU_rGO_{ag} composites, sintered by SPS at 1500 °C. (a, b) Preservation of alignment of the graphene scaffolds (5 - 15 µm channel widths) embedded in the alumina matrix. (c, d) Higher-magnification image on graphene flake pull-out at the fracture surface.*

The alumina matrix was found fully sintered with a mean grain size of 0.97 ± 0.2 μm (Figure 6.11). These values are lower than those obtained for bulk alumina powder sintered at 1500 °C without embedded graphene from Figure 6.6, which could be associated with a grain boundary pinning effect limiting the grain growth in the alumina matrix. The successful preservation of freeze-cast structural alignment of rGO scaffolds embedded in the alumina matrix (after infiltration of water-based slurries) constitutes a breakthrough in the production of hierarchical graphene/alumina composites, which has not yet been reported to the best of the author's knowledge. This work poses an extension of previous works on polymer-derived ceramics (PDCs) [176], maintaining a similar range of rGO channel widths in the obtained composite and confirming the infiltration capabilities after introducing PF127 in the alumina slurries and exploiting its amphiphilic behaviour [187].

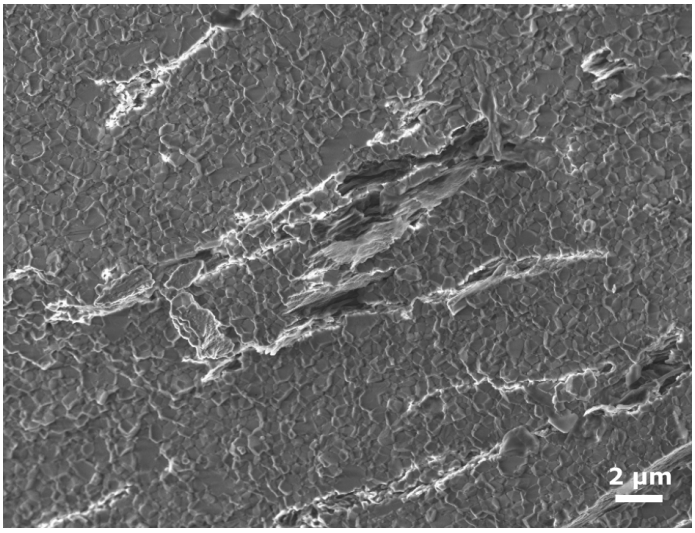

Figure 6.11: *Embedded rGO network of graphene/alumina discs showing sintered alumina grains (0.97 µm grain size). Slight hindering of alumina grain growth can be appreciated on grains neighbouring the rGO channels.*

6.4.2 Towards scaled-up graphene/alumina composites

Scaled-up PF127/Al_2O_3/rGO green bodies were densified at 1500 °C following the same sintering parameters previously applied to lab-scale specimens, extended to *0.5:ICL_* $rGO_{ag}\perp$ infiltrated aerogels. After sintering, the 30 mm discs obtained did not achieve a minimum 4 mm thickness that would allow evaluating the mechanical properties of the composite Figure 6.12.

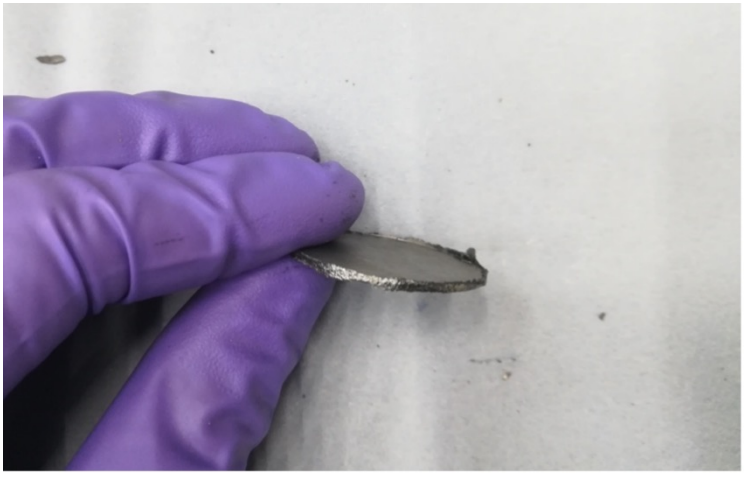

Figure 6.12: *30 mm discs after SPS of scaled-up 25:*Al_2O_3*/0.5:ICL_* $rGO_{ag}\perp$ *green bodies.*

The fracture surface of scaled-up *25:*Al_2O_3*/0.5:ICL_* $rGO_{ag}\perp$ composites after sintering at 1500 °C was examined by FESEM (Figure 6.13) to get a better understanding of the microstructure. In some locations, the 25 wt.% Al_2O_3 slurry had successfully infiltrated the rGO channels and transformed into a densified alumina

matrix (Figure 6.13a). However, FESEM characterisation shows that the infiltration was not fully complete, with several internal channels not wet by the alumina slurry before freeze-drying the green body. The upper part of Figure 6.13b exhibited some degree of the expected alignment of rGO channels mirroring the structure from lab-scale specimens (Figure 6.10), maintaining channel widths of 5 μm after compression in the SPS dies. However, this was only partially achieved in rGO channels, also experiencing significant agglomeration of the flakes leading to the structure collapse, as shown in the bottom part of the same picture. The inefficient infiltration of the scaled-up aerogels also resulted in a significant imbalance between the graphene and alumina phases (Figure 6.13c,d), with broader sections of exclusively sintered alumina contrasting with the compressed rGO walls from the original aerogel structure. This explained the lack of thickness obtained in the 30 mm sintered discs.

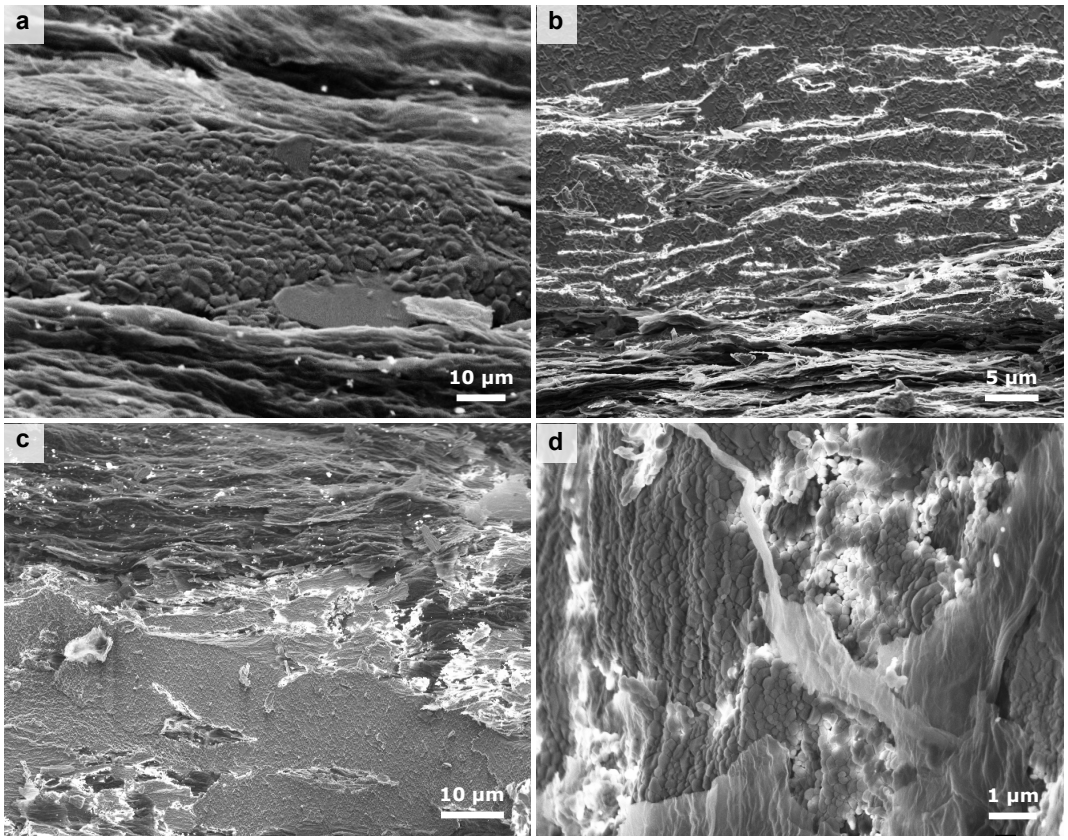

Figure 6.13: *FESEM images showing the fracture surface of scaled-up 25:Al_2O_3/0.5:CU_$rGO_{ag}\perp$ composites, sintered by SPS at 1500 °C. a) Sintered alumina matrix within rGO channels. b) Expected rGO alignment after successful infiltration of alumina (top section) vs collapsed aerogel structure (bottom section). (c,d) Extra images with imbalanced graphene and alumina phases indicating the inefficient infiltration.*

From these results, it was derived that the scalability of the infiltration processing route could not be resolved by simply extending the same conditions applied for lab-scale aerogels, still requiring further optimisation of the processing route. Although infiltration appeared successful upon PF127 additions in the ceramic slurry (Figure

5.27 after freeze-drying), not enough alumina solid was deposited inside the channels. This could result from the higher surface tension of the infiltrating ceramic slurry in the scaled-up scenario, preventing the ascension through the rGO channels by capillarity.

This concern was not present in the epoxy-infusion of rGO aerogels (from Section 4.5.3) as vacuum could be applied as the driving force to enhance infiltration of the polymer and fill the internal cavities of the scaffold completely. In the case of PF127/Al_2O_3 mixtures, the foaming effect caused by micellisation of PF127 in water prevented the application of vacuum [243]. Manual infiltration was sufficient to ensure the soaking of the channels in lab-scale aerogels of smaller dimensions, but proved much more challenging in the scaled-up scenario.

Various strategies could be tested to overcome the lack of vacuum in the infiltration and achieve similar results. The scaled-up aerogel could be segmented into several parts, with each section infiltrated separately and later re-stacked in the SPS graphitic dies for combined sintering. Another approach could consist of successive infiltration runs. Higher alumina solid weight could be ensured inside the graphene channels by repeated cycles of infiltration and freeze-drying, preventing structural collapse during SPS sintering.

Based on the successful infiltration of lab-scale aerogels of reduced dimensions (13 mm diameter, 19 mm height), another limitation could rely on the produced scaled-up structures during freeze-casting. Despite producing 30 mm *0.5:ICL_-GO_{ag}⊥* aerogels, implementing the improved mould setup with a perpendicular axis of revolution (Figure 3.3b) could have resulted in poorer heat transmission, because of the reduced contact area with the copper plate connecting to the cold source in the freeze-casting setup. Compared to standard cylindrical mould shapes, the rotated shape can result in a branching structure as shown by a sample alumina scaffold freeze-cast on the same mould, limiting the advancing freezing front and increased casting times (Figure 6.14).

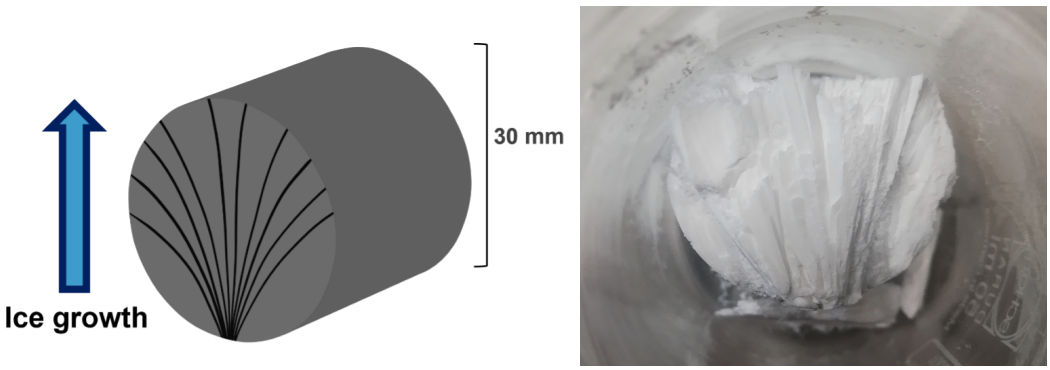

Figure 6.14: *Channel alignment deviation in the 4-piece freeze-casting mould for scaled-up conditions, including the cross-section of a test freeze-cast alumina sample.*

Substituting the lower half of the improved freeze-casting mould with copper

material could represent an additional improvement for future works on this theme (Figure 6.15). This modification could enhance heat distribution in the lower section of the mould, providing parallel freezing channels that can improve the alignment and enhance the infiltration of the ceramic slurries after carbonisation. However, this modification could entail other difficulties regarding mould manufacture and harder assembly from switching from a 4-piece to an 8-piece setup.

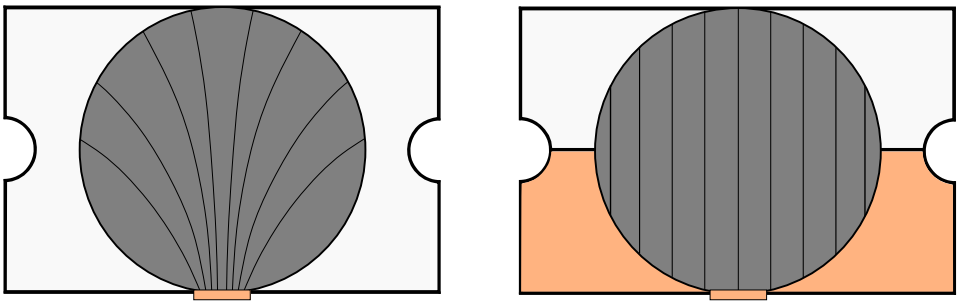

Figure 6.15: *Expected alignment improvement in freeze-casting using the proposed mould concept (8-piece upgrade with a copper bottom section).*

Achieving scalability is essential to enable the production of specimens for electrical testing and evaluating the mechanical properties via strength and R-curve measurements. Overcoming this threshold can lead to the production of electroconductive, tougher ceramic-based materials that meet the challenge of applying new concepts for extended assembly in ceramic processing outlined in this decade [40]. This strategy also permits to translate properties the properties of graphene-like precursors into $3D$ settings for engineering applications at an assumable cost and through an environmentally-friendly processing route, helping settle the presence of graphene outside the laboratory scale and into the industry.

6.5 Conclusions

SPS was selected as the consolidation technique in this project, allowing rapid sintering times (below 45 minutes) and limiting any effect on the material's microstructure [51]. The working parameters (heating and cooling rates, maximum temperature, dwelling times and pressure cycle) were adjusted using the alumina powder from the water-based alumina slurries as a baseline. A pressure release stage was included at the end of the isothermal dwell to soften the applied stress to the sintered discs.

20 mm alumina discs were produced, exhibiting porosity values of 0.3 – 2.3% across all tested parameters. FESEM characterisation confirmed a higher degree of sintering at 1500 °C than 1350 °C, with the fracture surface exhibiting a combination of transgranular and intergranular fracture. The integrity of 20 mm alumina discs was also preserved after increasing dwelling times above 5 minutes, attributed to a lower thermal gradient between the core and periphery of the produced discs. These

sintering conditions were extended to graphene/alumina pairs.

The densification of lab-scale graphene/alumina green bodies (from infiltrated rGO aerogels of 13 mm diameter, 19 mm height and 4 mg cm^{-3} in density) was settled on maximum temperatures of 1500 °C and 100 °C min^{-1} heating/cooling rates. The rGO scaffold's alignment from the freeze-casting processing route was preserved after infiltration and embedding in the alumina matrix as verified by FE-SEM. Through this processing route, it was possible to limit the amount of graphene material inside the ceramic-based composite (1 wt.%) while maintaining a directional graphene interconnected network of 5 – 15 μm channel widths, with high prospects for obtaining superior mechanical capabilities and added functionalities derived from its restoration of electrical conductivity.

The scalability of the processing route was only partially accomplished, delivering 30 mm graphene/alumina discs of insufficient thickness for mechanical and electrical evaluation. FESEM characterisation confirmed the internal wetting of scaled-up rGO aerogels with the PF127/Al_2O_3 slurries was insufficient. Complementary strategies such as applying successive cycles of infiltration and freeze-drying or improving the stage of scaled-up aerogel production could be tested in the future to overcome this issue.

Chapter 7

General conclusions and future research

7.1 Conclusions

This work has contributed to previous knowledge of graphene-based aerogels produced by freeze-casting water-based GO suspensions, approaching the limitations of the process with a range of conditions (GO concentration, freezing rates and inclusion of PVA/sucrose additives). Ultralight reduced GO aerogels of 1.5 - 4 mg cm^{-3} in apparent density were successfully obtained after freeze-drying and carbonisation, preserving directional alignment and channel widths of 15 – 30 μm.

Two GO precursors from different sources (commercial vs as-synthesised at Imperial College London) were extensively characterised, studying the effect of carbonisation on the graphene sheets chemistry and verifying the partial restoration of graphitic domains with an increase in electrical conductivity up to 10 - 15 S m^{-1}. Novel ideas were also integrated in the production of freeze-cast aerogels. Cylindrical custom-made moulds with a perpendicular axis of revolution were tested, achieving 30 mm diameter aerogels with self-supporting capabilities and permitting integration with SPS sintering. An extended hierarchical level was also studied by alumina NP-decoration ($<$ 10 nm) based on gelation of a scarcely researched alumina precursor (aluminium-L-lactate) maintaining a water-based approach of low toxicity.

The main breakthrough of infiltrating water-based advanced ceramic slurries into hydrophobic graphene-based scaffolds using a triblock copolymer agent in solution (PF127) was validated, adjusting the PF127/Al_2O_3 wt./wt. ratio to 0.07 - 0.15 through wettability and infiltration tests. These conditions were successfully applied to lab-scale cylindrical rGO aerogels (13 mm diameter, 19 mm height) of 3 mg cm^{-3} improving their wettability with hydrophilic alumina slurries (12.5 and 25 wt.% solid loading). The graphene/ceramic green bodies were densified via SPS sintering

maintaining the original freeze-cast aligned structure in the rGO scaffolds, displaying channel widths of 5 – 15 μm and graphene pull-out on the fracture surface. These experiments confirmed the potential of the proposed strategy for achieving hierarchical advanced ceramic composites containing a graphene interconnected network high prospects for obtaining superior mechanical capabilities and added functionalities.

The scalability of the approach was not yet resolved as confirmed by the inefficient wetting of scaled-up 30 mm rGO aerogels, which prevented the mechanical and electrical evaluation of the composites following consolidation. The direct translation of the infiltration conditions from the lab-scale scenario did not succeed, requiring more extensive adjustment of the parameters involved in the future.

7.2 Future Research

The infiltration and consolidation of scaled-up rGO aerogels could not be fully achieved due to time constraints and the effect of the COVID-19 pandemic on the expected experimental workflow. Although validated for lab-scale specimens, upscaling the processing route is essential to validate the effect of the hierarchical structure on the mechanical performance of the composite (via bending and R-curve testing) and evaluate the restoration of electrical conductivity.

Several areas require extended research to accomplish the scalability milestone. The effect of selecting a GO precursor of higher quality (ICL_GO) could be studied in more depth, exploiting the self-assembly behaviour of GO liquid crystal phases more efficiently at the selected values of GO concentration and flake lateral sizes. Alternative freeze-casting mould concepts could be explored to ensure the intended stacking and alignment of rGO sheets in scaled-up samples, maintaining a perpendicular axis of revolution to the SPS uniaxial pressure direction. Optimising the mesostructure of scaled-up aerogels can improve the capillarity with the ceramic slurries, reducing agglomeration of graphene sheets, which could be verified by complementary imaging methods like CT scanning. Studying the heat distribution profile and the advancing freezing front inside the moulds during freeze-casting would also result in better understanding of the produced aligned structure. This could be achieved by applying Finite Element Analysis (FEA) simulations to determine the heat profile in the suspension or recording the advancing freezing front in-situ using X-ray tomography.

Enhancing the graphene aerogel soaking with the PF127/Al_2O_3 slurry is also necessary to increase the amount of alumina solid in the mixture and prevent the structural collapse of scaled-up specimens. This could be achieved by successive infiltration and freeze-drying runs, aiming to obtain sufficient solid ceramic weight and provide sufficient thickness for mechanical and electrical characterisation of the specimens. Additional characterisation (such as hardness and density measurements)

could be performed on densified alumina and graphene/alumina SPS discs for a more systematic evaluation of the sintering conditions and its effect on the composite microstructure.

Resolving the processing scalability would permit comparing NP-decorated aerogels with the extended hierarchy and standard rGO aerogels. The NP-decoration was successfully achieved at different concentration levels with a noticeable effect on the infiltration times with PF127/Al_2O_3 slurries. However, any tangible effect on the structural and mechanical properties in scaled-up composites still needs evaluation in the future. The water-based aluminium lactate synthesis route to decorate the rGO scaffolds could also prove valuable beyond the graphene/ceramic structural materials proposed here, extrapolated to other ceramics nanoparticles such as titania or silica. Embedding NP-decorated scaffolds in polymer-based matrices constitutes another side path of great potential, which could confirm any increase in strength or extrinsic toughening mechanisms through R-curve measurements provided by the NP-decoration strategy without requiring water-based ceramic slurries. The graphene-based scaffold would provide electrical conductivity similar to the hybrid composite validated in this work, sufficient for sensing and monitoring capabilities.

The general processing strategy suggested has also given room for complementary approaches without the use of PF127 in the ceramic formulation. For example, inverting the graphene and alumina phases appears a promising route, first consolidating an alumina scaffold through freeze-casting and freeze-drying of water-based slurries, later infiltrated with GO suspensions. This opposite approach could ensure sufficient alumina weight in the composite for SPS sintering (One of the main constraints from this work), producing aerogels of sufficient solid loading while allowing the hydrophilic interaction with water-based GO suspensions before reduction.

Bibliography

[1] R. Moreno. Colloidal methods. In N. P. Bansal and A. R. Boccaccini, editors, *Ceramics and Composites Processing Methods*, chapter 4, pages 145–181. John Wiley Sons, Ltd, 2012.

[2] B. G. Rao, D. Mukherjee, and B. M. Reddy. Chapter 1 - novel approaches for preparation of nanoparticles. In Denisa Ficai and Alexandru Mihai Grumezescu, editors, *Nanostructures for Novel Therapy*, pages 1–36. Elsevier, 2017.

[3] S. L. Kang. 4 - initial stage sintering. In S. L. Kang, editor, *Sintering*, pages 39–55. Butterworth-Heinemann, Oxford, 2005.

[4] S. L. Kang. 1 - sintering processes. In S. L. Kang, editor, *Sintering*, pages 3–8. Butterworth-Heinemann, Oxford, 2005.

[5] M. Biesuz and V. M. Sglavo. Flash sintering of ceramics. *Journal of the European Ceramic Society*, 39(2):115–143, 2019.

[6] O. Guillon, J. Gonzalez-Julian, B. Dargatz, T. Kessel, G. Schierning, J. Räthel, and M. Herrmann. Field-assisted sintering technology/spark plasma sintering: Mechanisms, materials, and technology developments. *Advanced Engineering Materials*, 16(7):830–849, 2014.

[7] H. J. Ensikat, P. Ditsche-Kuru, C. Neinhuis, and W. Barthlott. Superhydrophobicity in perfection: the outstanding properties of the lotus leaf. *Beilstein Journal of Nanotechnology*, 2:152–161, 2011.

[8] J. Aizenberg, J. C. Weaver, M. S. Thanawala, V. C. Sundar, D. E. Morse, and P. Fratzl. Materials science: Skeleton of euplectella sp.: Structural hierarchy from the nanoscale to the macroscale. *Science*, 309(5732):275–278, 2005.

[9] M. A. Meyers, P. Chen, A. Y. Lin, and Y. Seki. Biological materials: Structure and mechanical properties. *Progress in Materials Science*, 53(1):1–206, 2008.

[10] R. O. Ritchie. Mechanisms of fatigue-crack propagation in ductile and brittle solids. *International Journal of Fracture*, 100:55–83, 1999.

[11] U.G.K. Wegst, H. Bai, E. Saiz, A.P. Tomsia, and R.O. Ritchie. Bioinspired structural materials. *Nature Materials*, 14(1):23–36, 2015.

[12] F. Barthelat and H. D. Espinosa. An experimental investigation of deformation and fracture of nacre-mother of pearl. *Experimental Mechanics*, 47(3):311–324, 2007.

[13] S. Deville. Ice-templating, freeze casting: Beyond materials processing. *Journal of Materials Research*, 28(17):2202–2219, 2013.

[14] G. Shao, D. A. H. Hanaor, X Shen, and A. Gurlo. Freeze casting: From low-dimensional building blocks to aligned porous structures—a review of novel materials, methods, and applications. *Advanced Materials*, 32(17):1907176, 2020.

[15] F. Bouville, E. Maire, S. Meille, B. Van De Moortèle, A. J. Stevenson, and S. Deville. Strong, tough and stiff bioinspired ceramics from brittle constituents. *Nature Materials*, 13(5):508–514, 2014.

[16] A.K. Geim and K.S. Novoselov. The rise of graphene. *Nature Materials*, 6(3):183–191, 2007.

[17] E. W. Hill, A. Vijayaragahvan, and K. Novoselov. Graphene sensors. *IEEE Sensors Journal*, 11(12):3161–3170, 2011.

[18] P. Miranzo, M. Belmonte, and M. I. Osendi. From bulk to cellular structures: A review on ceramic/graphene filler composites. *Journal of the European Ceramic Society*, 37(12):3649–3672, 2017.

[19] M. Yi and Z. Shen. A review on mechanical exfoliation for the scalable production of graphene. *Journal of Materials Chemistry A*, 3(22):11700–11715, 2015.

[20] M. Nasrollahzadeh, F. Babaei, P. Fakhri, and B. Jaleh. Synthesis, characterization, structural, optical properties and catalytic activity of reduced graphene oxide/copper nanocomposites. *RSC Advances*, 5:10782–10789, 2015.

[21] D. Li, M. B. Müller, S. Gilje, R. B. Kaner, and G. G. Wallace. Processable aqueous dispersions of graphene nanosheets. *Nature Nanotechnology*, 3(2):101–105, 2008.

[22] W. Gao, L. B. Alemany, L. Ci, and P. M. Ajayan. New insights into the structure and reduction of graphite oxide. *Nature Chemistry*, 1(5):403–408, 2009.

[23] A. Centeno, V. G. Rocha, B. Alonso, A. Fernández, C. F. Gutierrez-Gonzalez, R. Torrecillas, and A. Zurutuza. Graphene for tough and electroconductive alumina ceramics. *Journal of the European Ceramic Society*, 33(15-16):3201–3210, 2013.

[24] Y. Fan, W. Jiang, and A. Kawasaki. Highly conductive few-layer graphene/Al_2O_3 nanocomposites with tunable charge carrier type. *Advanced Functional Materials*, 22(18):3882–3889, 2012.

[25] J. H. Shin and S. H. Hong. Fabrication and properties of reduced graphene oxide reinforced yttria-stabilized zirconia composite ceramics. *Journal of the European Ceramic Society*, 34(5):1297–1302, 2014.

[26] C. Ramírez, S. M. Vega-Diaz, A. Morelos-Gómez, F. M. Figueiredo, M. Terrones, M. I. Osendi, M. Belmonte, and P. Miranzo. Synthesis of conducting graphene/Si_3N_4 composites by spark plasma sintering. *Carbon*, 57:425–432, 2013.

[27] C. Ramirez, F. M. Figueiredo, P. Miranzo, P. Poza, and M. Isabel Osendi. Graphene nanoplatelet/silicon nitride composites with high electrical conductivity. *Carbon*, 50(10):3607–3615, 2012.

[28] I. N. G. Simsek, A. Nistal, E. García, D. Pérez-Coll, P. Miranzo, and M. I. Osendi. The effect of graphene nanoplatelets on the thermal and electrical properties of aluminum nitride ceramics. *Journal of the European Ceramic Society*, 37(12):3721–3729, 2017.

[29] C. Yun, Y. Feng, T. Qiu, J. Yang, X. Li, and L. Yu. Mechanical, electrical, and thermal properties of graphene nanosheet/aluminum nitride composites. *Ceramics International*, 41(7):8643–8649, 2015.

[30] B. Román-Manso, F. M. Figueiredo, B. Achiaga, R. Barea, D. Pérez-Coll, A. Morelos-Gómez, M. Terrones, M. I. Osendi, M. Belmonte, and P. Miranzo. Electrically functional 3D-architectured graphene/SiC composites. *Carbon*, 100:318–328, 2016.

[31] Y. Tan, H. Zhang, and S. Peng. Electrically conductive graphene nanoplatelet/boron carbide composites with high hardness and toughness. *Scripta Materialia*, 114:98–102, 2016.

[32] B.D. Cullity. *Elements of X-ray Diffraction*. Addison-Wesley series in metallurgy and materials. Addison-Wesley Publishing Company, 1978.

[33] A. C. Ferrari and J. Robertson. Interpretation of raman spectra of disordered and amorphous carbon. *Physical Review B*, 61:14095–14107, 2000.

[34] W. Zhou, R. Apkarian, Z. L. Wang, and D. Joy. Fundamentals of scanning electron microscopy (sem). In W. Zhou and Z. L. Wang, editors, *Scanning Microscopy for Nanotechnology: Techniques and Applications*, pages 1–40. Springer New York, New York, NY, 2007.

[35] V. Lenaerts, C. Triqueneaux, M. Quartern, F. Rieg-Falson, and P. Couvreur. Temperature-dependent rheological behavior of pluronic F-127 aqueous solutions. *International Journal of Pharmaceutics*, 39(1):121–127, 1987.

[36] E. Feilden, E. G. Blanca, F. Giuliani, E. Saiz, and L. Vandeperre. Robocasting of structural ceramic parts with hydrogel inks. *Journal of the European Ceramic Society*, 36(10):2525–2533, 2016.

[37] P. Boch and J. Baumard. Ceramic compounds: Ceramic materials. In *Ceramic Materials*, chapter 1, pages 1–28. John Wiley Sons, Ltd, 2007.

[38] R. Riedel, E. Ionescu, and I. Chen. Modern trends in advanced ceramics. In *Ceramics Science and Technology*, chapter 1, pages 1–38. John Wiley Sons, Ltd, 2008.

[39] I. Ahmad, B. Yazdani, and Y. Zhu. Recent advances on carbon nanotubes and graphene reinforced ceramics nanocomposites. *Nanomaterials*, 5(1):90–114, 2015.

[40] K. T. Faber, T. Asefa, M. Backhaus-Ricoult, R. Brow, J. Y. Chan, S. Dillon, W. G. Fahrenholtz, M. W. Finnis, J. E. Garay, R. E. García, Y. Gogotsi, S. M. Haile, J. Halloran, J. Hu, L. Huang, S. D. Jacobsen, E. Lara-Curzio, J. LeBeau, W. E. Lee, C. G. Levi, I. Levin, J. A. Lewis, D. M. Lipkin, K. Lu, J. Luo, J. Maria, L. W. Martin, S. Martin, G. Messing, A. Navrotsky, N. P. Padture, C. Randall, G. S. Rohrer, A. Rosenflanz, T. A. Schaedler, D. G. Schlom, A. Sehirlioglu, A. J. Stevenson, T. Tani, V. Tikare, S. Trolier-McKinstry, H. Wang, and B. Yildiz. The role of ceramic and glass science research in meeting societal challenges: Report from an nsf-sponsored workshop. *Journal of the American Ceramic Society*, 100(5):1777–1803, 2017.

[41] B. Basu and K. Balani. *Sintering of Ceramics*. John Wiley Sons, Ltd, 2011.

[42] J. A. Lewis. Colloidal processing of ceramics. *Journal of the American Ceramic Society*, 83(10):2341–2359, 2004.

[43] E. H. Lan and B. Dunn. Processing and applications of sol–gel glass. In *Ceramics and Composites Processing Methods*, chapter 5, pages 183–197. John Wiley Sons, Ltd, 2012.

[44] C. J. Papini, W. K. Yoshito, D. Gouvêa, and R. M. Leal Neto. Particle size distribution analysis of an alumina powder: Influence of some dispersants, ph and supersonic vibration. In *Materials Science Forum*, volume 498-499, pages 73–78. 2005.

[45] L. L. Hench and J. K. West. The sol-gel process. *Chemical Reviews*, 90(1):33–72, 1990.

[46] A. R. Keshavarz, M. Rezaei, and F. Yaripour. Preparation of nanocrystalline γ-Al_2O_3 catalyst using different procedures for methanol dehydration to dimethyl ether. *Journal of Natural Gas Chemistry*, 20(3):334–338, 2011.

[47] M.N. Rahaman. *Ceramic Processing and Sintering*. Manufacturing, Engineering and Materials Processing. M. Dekker, 1995.

[48] Z. A. Munir, D. V. Quach, and M. Ohyanagi. Electric current activation of sintering: A review of the pulsed electric current sintering process. *Journal of the American Ceramic Society*, 94(1):1–19, 2011.

[49] K. I. Rybakov, E. A. Olevsky, and E. V. Krikun. Microwave sintering: Fundamentals and modeling. *Journal of the American Ceramic Society*, 96(4):1003–1020, 2013.

[50] M. Yu, S. Grasso, R. Mckinnon, T. Saunders, and M. J. Reece. Review of flash sintering: materials, mechanisms and modelling. *Advances in Applied Ceramics*, 116(1):24–60, 2017.

[51] T. Hungría, J. Galy, and A. Castro. Spark plasma sintering as a useful technique to the nanostructuration of piezo-ferroelectric materials. *Advanced Engineering Materials*, 11(8):615–631, 2009.

[52] I. Kiyoshi. Apparatus for electrically sintering discrete bodies, U.S. Patent 3,250,892, issued May 1966.

[53] M. Suárez, A. Fernández, J.L. Menéndez, R. Torrecillas, H. U. Kessel, J. Hennicke, R. Kirchner, and T. Kessel. Challenges and opportunities for spark plasma sintering: A key technology for a new generation of materials. In Burcu Ertuğ, editor, *Sintering Applications*, chapter 13. IntechOpen, Rijeka, 2013.

[54] S. Eqtesadi, A. Motealleh, F. H. Perera, P. Miranda, A. Pajares, R. Wendelbo, F. Guiberteau, and A. L. Ortiz. Fabricating geometrically-complex B_4C ceramic components by robocasting and pressureless spark plasma sintering. *Scripta Materialia*, 145:14–18, 2018.

[55] C. Manière, E. Torresani, and E. A. Olevsky. Simultaneous spark plasma sintering of multiple complex shapes. *Materials*, 12(4), 2019.

[56] A. V. Srinivasan. *Smart structures : analysis and design*. Cambridge : Cambridge University Press, Cambridge, 2001.

[57] V. I. Vullev. From biomimesis to bioinspiration: What's the benefit for solar energy conversion applications? *The Journal of Physical Chemistry Letters*, 2(5):503–508, 2011.

[58] N. A. Yaraghi and D. Kisailus. Biomimetic structural materials: Inspiration from design and assembly. *Annual Review of Physical Chemistry*, 69(1):23–57, 2018.

[59] H. Dodiuk, P. F. Rios, A. Dotan, and S. Kenig. Hydrophobic and self-cleaning coatings. *Polymers for Advanced Technologies*, 18(9):746–750, 2007.

[60] H. Gao, X. Wang, H. Yao, S. Gorb, and E. Arzt. Mechanics of hierarchical adhesion structures of geckos. *Mechanics of Materials*, 37(2):275–285, 2005.

[61] P. Fratzl and R. Weinkamer. Nature's hierarchical materials. *Progress in Materials Science*, 52(8):1263–1334, 2007.

[62] R. O. Ritchie. The conflicts between strength and toughness. *Nature Materials*, 10(11):817, 2011.

[63] M. E. Launey, E. Munch, D. H. Alsem, H. B. Barth, E. Saiz, A. P. Tomsia, and R. O. Ritchie. Designing highly toughened hybrid composites through nature-inspired hierarchical complexity. *Acta Materialia*, 57(10):2919–2932, 2009.

[64] M. Mirkhalaf, A. K. Dastjerdi, and F. Barthelat. Overcoming the brittleness of glass through bio-inspiration and micro-architecture. *Nature Communications*, 5:3166, 2014.

[65] Y. Zhang and X. Li. Bioinspired, graphene/Al_2O_3 doubly reinforced aluminum composites with high strength and toughness. *Nano Letters*, 17(11):6907–6915, 2017.

[66] E. Munch, M. E. Launey, D. H. Alsem, E. Saiz, A. P. Tomsia, R. O. Ritchie, and R. O. Alsem. Tough, bio-inspired hybrid materials. *Science*, 322(5907):1516–1520, 2008.

[67] F. Barthelat and R. Rabiei. Toughness amplification in natural composites. *Journal of the Mechanics and Physics of Solids*, 59(4):829–840, 2011.

[68] Q. Cheng, C. Huang, and A. P. Tomsia. Freeze casting for assembling bioinspired structural materials. *Advanced Materials*, 29(45), 2017.

[69] K. Evers, S. Falco, N. Grobert, and R. I. Todd. Nacre-like alumina with unique high strain rate capabilities. *Journal of the European Ceramic Society*, 40(2):417–426, 2020.

[70] F. Song, A. K. Soh, and Y. L. Bai. Structural and mechanical properties of the organic matrix layers of nacre. *Biomaterials*, 24(20):3623–3631, 2003.

[71] L. Mao, H. Gao, H. Yao, L. Liu, H. Cölfen, G. Liu, S. Chen, S. Li, Y. Yan, Y. Liu, and S. Yu. Synthetic nacre by predesigned matrix-directed mineralization. *Science*, 354(6308):107–110, 2016.

[72] M. E. Launey and R. O. Ritchie. On the fracture toughness of advanced materials. *Advanced Materials*, 21(20):2103–2110, 2009.

[73] K. Markandan, J. K. Chin, and M. T. T. Tan. Recent progress in graphene based ceramic composites: A review. *Journal of Materials Research*, 32(1):84–106, 2017.

[74] S. Deville, E. Saiz, R. K. Nalla, and A. P. Tomsia. Freezing as a path to build complex composites. *Science*, 311(5760):515–518, 2006.

[75] S. Deville. Freeze-casting of porous ceramics: A review of current achievements and issues. *Advanced Engineering Materials*, 10(3):155–169, 2008.

[76] W. A. Maxwell, R. S. Gurnick, and A. C. Francisco. Preliminary investigation of the 'freeze-casting' method for forming refractory powders, UNT digital library report, March 1954.

[77] S. W. Sofie and F. Dogan. Freeze casting of aqueous alumina slurries with glycerol. *Journal of the American Ceramic Society*, 84(7):1459–1464, 2001.

[78] T. Fukasawa, M. Ando, T. Ohji, and S. Kanzaki. Synthesis of porous ceramics with complex pore structure by freeze-dry processing. *Journal of the American Ceramic Society*, 84(1):230–232, 2001.

[79] S. R. Mukai, H. Nishihara, and H. Tamon. Formation of monolithic silica gel microhoneycombs (smhs) using pseudosteady state growth of microstructural ice crystals. *Chemical Communications*, 10(7):874–875, 2004.

[80] H. Nishihara, S.R. Mukai, D. Yamashita, and H. Tamon. Ordered macroporous silica by ice templating. *Chemistry of Materials*, 17(3):683–689, 2005.

[81] H. Zhang, I. Hussain, M. Brust, M.F. Butler, S.P. Rannard, and A.I. Cooper. Aligned two- and three-dimensional structures by directional freezing of polymers and nanoparticles. *Nature Materials*, 4(10):787–793, 2005.

[82] A. Lasalle, C. Guizard, E. Maire, J. Adrien, and S. Deville. Particle redistribution and structural defect development during ice templating. *Acta Materialia*, 60(11):4594–4603, 2012.

[83] S. Deville, E. Saiz, and A. P. Tomsia. Ice-templated porous alumina structures. *Acta Materialia*, 55(6):1965–1974, 2007.

[84] L. Qian and H. Zhang. Controlled freezing and freeze drying: a versatile route for porous and micro-/nano-structured materials. *Journal of Chemical Technology & Biotechnology*, 86(2):172–184, 2011.

[85] H. Zhang and A. I. Cooper. Aligned porous structures by directional freezing. *Advanced Materials*, 19(11):1529–1533, 2007.

[86] G. Liu and T. W. Button. The effect of particle size in freeze casting of porous alumina-zirconia composite. *Ceramics International*, 39(7):8507–8512, 2013.

[87] K. L. Scotti and D. C. Dunand. Freeze casting – a review of processing, microstructure and properties via the open data repository, freezecasting.net. *Progress in Materials Science*, 94:243–305, 2018.

[88] T. Waschkies, R. Oberacker, and M.J. Hoffmann. Investigation of structure formation during freeze-casting from very slow to very fast solidification velocities. *Acta Materialia*, 59(13):5135–5145, 2011.

[89] H. Zhang, J. Y. Lee, A. Ahmed, I. Hussain, and A. I. Cooper. Freeze-align and heat-fuse: Microwires and networks from nanoparticle suspensions. *Angewandte Chemie - International Edition*, 47(24):4573–4576, 2008.

[90] E. Munch, E. Saiz, A. P. Tomsia, and S. Deville. Architectural control of freeze-cast ceramics through additives and templating. *Journal of the American Ceramic Society*, 92(7):1534–1539, 2009.

[91] Y. Zhang, L. Hu, J. Han, and Z. Jiang. Freeze casting of aqueous alumina slurries with glycerol for porous ceramics. *Ceramics International*, 36(2):617–621, 2010.

[92] Y. Tang, Q. Miao, S. Qiu, K. Zhao, and L. Hu. Novel freeze-casting fabrication of aligned lamellar porous alumina with a centrosymmetric structure. *Journal of the European Ceramic Society*, 34(15):4077–4082, 2014.

[93] K. Lebreton, J. M. Rodríguez-Parra, R. Moreno, and M. I. Nieto. Effect of additives on porosity of alumina materials obtained by freeze casting. *Advances in Applied Ceramics*, 114(5):296–302, 2015.

[94] C. Peko, B. Groth, and I. Nettleship. The effect of polyvinyl alcohol on the microstructure and permeability of freeze-cast alumina. *Journal of the American Ceramic Society*, 93(1):115–120, 2010.

[95] X. Zeng, L. Ye, S. Yu, R. Sun, J. Xu, and C. Wong. Facile preparation of superelastic and ultralow dielectric boron nitride nanosheet aerogels via freeze-casting process. *Chemistry of Materials*, 27(17):5849–5855, 2015.

[96] A. Knöller, T. Runčevski, R.E. Dinnebier, J. Bill, and Z. Burghard. Cuttlebone-like V_2O_5 nanofibre scaffolds - advances in structuring cellular solids. *Scientific Reports*, 7, 2017.

[97] Y. Si, X. Wang, L. Dou, J. Yu, and B. Ding. Ultralight and fire-resistant ceramic nanofibrous aerogels with temperature-invariant superelasticity. *Science Advances*, 4(4):eaas8925, 2018.

[98] Y. Yao, X. Zhu, X. Zeng, R. Sun, J. Xu, and C. Wong. Vertically aligned and interconnected SiC nanowire networks leading to significantly enhanced thermal conductivity of polymer composites. *ACS Applied Materials & Interfaces*, 10(11):9669–9678, 2018.

[99] H. Bai, F. Walsh, B. Gludovatz, B. Delattre, C. Huang, Y. Chen, A. P. Tomsia, and R. O. Ritchie. Bioinspired hydroxyapatite/poly(methyl methacrylate) composite with a nacre-mimetic architecture by a bidirectional freezing method. *Advanced Materials*, 28(1):50–56, 2016.

[100] A. Wat, J.I. Lee, C.W. Ryu, B. Gludovatz, J. Kim, A.P. Tomsia, T. Ishikawa, J. Schmitz, A. Meyer, M. Alfreider, D. Kiener, E.S. Park, and R.O. Ritchie. Bioinspired nacre-like alumina with a bulk-metallic glass-forming alloy as a compliant phase. *Nature Communications*, 10(1), 2019.

[101] A. Preiss, B. Su, S. Collins, and D. Simpson. Tailored graded pore structure in zirconia toughened alumina ceramics using double-side cooling freeze casting. *Journal of the European Ceramic Society*, 32(8):1575–1583, 2012.

[102] Y. Tang, S. Qiu, Q. Miao, and C. Wu. Fabrication of lamellar porous alumina with axisymmetric structure by directional solidification with applied electric and magnetic fields. *Journal of The European Ceramic Society*, 36:1233–1240, 2016.

[103] Y.F. Tang, K. Zhao, J.Q. Wei, and Y.S. Qin. Fabrication of aligned lamellar porous alumina using directional solidification of aqueous slurries with an applied electrostatic field. *Journal of the European Ceramic Society*, 30(9):1963–1965, 2010.

[104] M. M. Porter, M. Yeh, J. Strawson, T. Goehring, S. Lujan, P. Siripasopsotorn, M. A. Meyers, and J. McKittrick. Magnetic freeze casting inspired by nature. *Materials Science and Engineering: A*, 556:741–750, 2012.

[105] I. Nelson, T. A. Ogden, S. Al Khateeb, J. Graser, T. D. Sparks, J. J. Abbott, and S. E. Naleway. Freeze-casting of surface-magnetized iron(ii,iii) oxide particles in a uniform static magnetic field generated by a helmholtz coil. *Advanced Engineering Materials*, 21(3):1801092, 2019.

[106] P. I.B.G.B. Pelissari, F. Bouville, V. C. Pandolfelli, D. Carnelli, F. Giuliani, A. P. Luz, E. Saiz, and A. R. Studart. Nacre-like ceramic refractories for high temperature applications. *Journal of the European Ceramic Society*, 38(4):2186–2193, 2018.

[107] R. Henry, H. Saad, S. Dankic-Cottrino, S. Deville, and S. Meille. Nacre-like alumina composites reinforced by zirconia particles. *Journal of the European Ceramic Society*, 2021.

[108] X. Wang, M. Lu, L. Qiu, H. Huang, D. Li, H. Wang, and Y. Cheng. Graphene/titanium carbide composites prepared by sol–gel infiltration and spark plasma sintering. *Ceramics International*, 42(1, Part A):122–131, 2016.

[109] K. S. Novoselov, A. K. Geim, S. V. Morozov, D. Jiang, Y. Zhang, S. V. Dubonos, I. V. Grigorieva, and A. A. Firsov. Electric field in atomically thin carbon films. *Science*, 306(5696):666–669, 2004.

[110] S. Stankovich, D. A. Dikin, G. H. Dommett, K. M. Kohlhaas, E. J. Zimney, E. A. Stach, R. D. Piner, S. T. Nguyen, and R. S. Ruoff. Graphene-based composite materials. *Nature*, 442(7100):282–6, 2006.

[111] P. R. Wallace. The band theory of graphite. *Physical Reviews*, 71:622–634, 1947.

[112] H. Zhou and S. Kitagawa. Metal–organic frameworks (mofs). *Chemical Society Reviews*, 43:5415–5418, 2014.

[113] S. Cahangirov, M. Topsakal, E. Aktürk, H. Şahin, and S. Ciraci. Two- and one-dimensional honeycomb structures of silicon and germanium. *Phys. Rev. Lett.*, 102:236804, 2009.

[114] F. Schäffel. Chapter 2 - the atomic structure of graphene and its few-layer counterparts. In J. H. Warner, F. Schäffel, A. Bachmatiuk, and M. H. Rümmeli, editors, *Graphene. Fundamentals and emergent applications*, pages 5–59. Elsevier, 2013.

[115] C. Lee, X. Wei, J. W. Kysar, and J. Hone. Measurement of the elastic properties and intrinsic strength of monolayer graphene. *Science*, 321(5887):385–388, 2008.

[116] S. Park and R. S. Ruoff. Chemical methods for the production of graphenes. *Nature Nanotechnology*, 4(4):217–24, 2009.

[117] J. H. Warner, F. Schäffel, A. Bachmatiuk, and M. H. Rümmeli. Chapter 3 - properties of graphene. In J. H. Warner, F. Schäffel, A. Bachmatiuk, and M. H. Rümmeli, editors, *Graphene. Fundamentals and emergent applications*, pages 61–127. Elsevier, 2013.

[118] A. Shekhawat and R. O. Ritchie. Toughness and strength of nanocrystalline graphene. *Nature Communications*, 7:10546, 2016.

[119] A. Zandiatashbar, G.-H. Lee, S.J. An, S. Lee, N. Mathew, M. Terrones, T. Hayashi, C.R. Picu, J. Hone, and N. Koratkar. Effect of defects on the intrinsic strength and stiffness of graphene. *Nature Communications*, 5, 2014.

[120] M. D. Stoller, S. Park, Y. Zhu, J. An, and R. S. Ruoff. Graphene-based ultracapacitors. *Nano Letters*, 8(10):3498–3502, 2008.

[121] K.S. Novoselov, A.K. Geim, S.V. Morozov, D. Jiang, M.I. Katsnelson, I.V. Grigorieva, S.V. Dubonos, and A.A. Firsov. Two-dimensional gas of massless dirac fermions in graphene. *Nature*, 438(7065):197–200, 2005.

[122] Y. Zhang, Y.-W. Tan, H.L. Stormer, and P. Kim. Experimental observation of the quantum hall effect and berry's phase in graphene. *Nature*, 438(7065):201–204, 2005.

[123] Y. Zhu, S. Murali, W. Cai, X. Li, J. W. Suk, J. R. Potts, and R. S. Ruoff. Graphene and graphene oxide: Synthesis, properties, and applications. *Advanced Materials*, 22(35):3906–3924, 2010.

[124] P. Iqbal, J. A. Preece, and P. M. Mendes. Nanotechnology: The "top-down" and "bottom-up" approaches. In *Supramolecular Chemistry*. John Wiley Sons, Ltd, 2012.

[125] A. Reina, X. Jia, J. Ho, D. Nezich, H. Son, V. Bulovic, M. S. Dresselhaus, and J. Kong. Large area, few-layer graphene films on arbitrary substrates by chemical vapor deposition. *Nano Letters*, 9(1):30–35, 2009.

[126] W. A. de Heer, C. Berger, X. Wu, P. N. First, E. H. Conrad, X. Li, T. Li, M. Sprinkle, J. Hass, M. L. Sadowski, M. Potemski, and G. Martinez. Epitaxial graphene. *Solid State Communications*, 143(1):92–100, 2007.

[127] S. Stankovich, D. A. Dikin, R. D. Piner, K. A. Kohlhaas, A. Kleinhammes, Y. Jia, Y. Wu, S. T. Nguyen, and R. S. Ruoff. Synthesis of graphene-based nanosheets via chemical reduction of exfoliated graphite oxide. *Carbon*, 45(7):1558–1565, 2007.

[128] U. Khan, A. O'Neill, M. Lotya, S. De, and J. N. Coleman. High-concentration solvent exfoliation of graphene. *Small*, 6(7):864–871, 2010.

[129] D.V. Kosynkin, A.L. Higginbotham, A. Sinitskii, J.R. Lomeda, A. Dimiev, B.K. Price, and J.M. Tour. Longitudinal unzipping of carbon nanotubes to form graphene nanoribbons. *Nature*, 458(7240):872–876, 2009.

[130] D. W. Johnson, B. P. Dobson, and K. S. Coleman. A manufacturing perspective on graphene dispersions. *Current Opinion in Colloid Interface Science*, 20(5):367–382, 2015.

[131] B. C. Brodie. On the Atomic Weight of Graphite. *Philosophical Transactions of the Royal Society of London Series I*, 149:249–259, 1859.

[132] R. J. J. Riobóo, E. Climent-Pascual, X. Díez-Betriu, F. Jiménez-Villacorta, C. Prieto, and A. de Andrés. Elastic constants of graphene oxide few-layer films: correlations with interlayer stacking and bonding. *Journal of Materials Chemistry C*, 3:4868–4875, 2015.

[133] J. W. Suk, R. D. Piner, J. An, and R. S. Ruoff. Mechanical properties of monolayer graphene oxide. *ACS Nano*, 4(11):6557–6564, 2010.

[134] H. Bai, C. Li, and G. Shi. Functional composite materials based on chemically converted graphene. *Advanced Materials*, 23(9):1089–1115, 2011.

[135] V. V. Neklyudov, N. R. Khafizov, I. A. Sedov, and A. M. Dimiev. New insights into the solubility of graphene oxide in water and alcohols. *Physical Chemistry Chemical Physics*, 19(26):17000–17008, 2017.

[136] S. Al-Zangana, M. Iliut, M. Turner, A. Vijayaraghavan, and I. Dierking. Confinement effects on lyotropic nematic liquid crystal phases of graphene oxide dispersions. *2D matter*, 4(4):041004, 2017.

[137] A. P. Draude and I. Dierking. Lyotropic liquid crystals from colloidal suspensions of graphene oxide. *Crystals*, 9(9), 2019.

[138] F. Kim, L. J. Cote, and J. Huang. Graphene oxide: Surface activity and two-dimensional assembly. *Advanced Materials*, 22(17):1954–1958, 2010.

[139] D. R. Dreyer, P. Park, C. W. Bielawski, and R. S. Ruoff. The chemistry of graphene oxide. *Chemical Society Reviews*, 39:228–240, 2010.

[140] S. Pei and H. Cheng. The reduction of graphene oxide. *Carbon*, 50(9):3210–3228, 2012.

[141] F. Perrozzi, S. Prezioso, M. Donarelli, F. Bisti, P. De Marco, S. Santucci, M. Nardone, E. Treossi, V. Palermo, and L. Ottaviano. Use of optical contrast to estimate the degree of reduction of graphene oxide. *The Journal of Physical Chemistry C*, 117(1):620–625, 2013.

[142] H. A. Becerril, J. Mao, Z. Liu, R. M. Stoltenberg, Z. Bao, and Y. Chen. Evaluation of solution-processed reduced graphene oxide films as transparent conductors. *ACS Nano*, 2(3):463–470, 2008.

[143] W. S. Hummers Jr and R. E. Offeman. Preparation of graphitic oxide. *Journal of the American Chemical Society*, 80(6):1339, 1958.

[144] R. Ikram, B. M. Jan, and W. Ahmad. An overview of industrial scalable production of graphene oxide and analytical approaches for synthesis and characterization. *Journal of Materials Research and Technology*, 9(5):11587–11610, 2020.

[145] L. Staudenmaier. Verfahren zur darstellung der graphitsäure. *Berichte der deutschen chemischen Gesellschaft*, 31(2), 1898.

[146] J. Chen, B. Yao, C. Li, and G. Shi. An improved hummers method for eco-friendly synthesis of graphene oxide. *Carbon*, 64:225–229, 2013.

[147] M. Hirata, T. Gotou, S. Horiuchi, M. Fujiwara, and M. Ohba. Thin-film particles of graphite oxide 1: High-yield synthesis and flexibility of the particles. *Carbon*, 42(14):2929–2937, 2004.

[148] D. C. Marcano, D. V. Kosynkin, J. M. Berlin, A. Sinitskii, Z. Sun, A. Slesarev, L. B. Alemany, W. Lu, and J. M. Tour. Improved synthesis of graphene oxide. *ACS Nano*, 4(8):4806–4814, 2010.

[149] D. Yang, A. Velamakanni, G. Bozoklu, S. Park, M. Stoller, R. D. Piner, S. Stankovich, I. Jung, D. A. Field, C. A. Ventrice, and R. S. Ruoff. Chemical analysis of graphene oxide films after heat and chemical treatments by x-ray photoelectron and micro-raman spectroscopy. *Carbon*, 47(1):145–152, 2009.

[150] S. Eigler, C. Dotzer, and A. Hirsch. Visualization of defect densities in reduced graphene oxide. *Carbon*, 50(10):3666–3673, 2012.

[151] G. Wang, J. Yang, J. Park, X. Gou, B. Wang, H. Liu, and J. Yao. Facile synthesis and characterization of graphene nanosheets. *The Journal of Physical Chemistry C*, 112(22):8192–8195, 2008.

[152] N. Ni, S. Barg, E. Garcia-Tunon, F. M. Perez, M. Miranda, C. Lu, C. Mattevi, and E. Saiz. Understanding mechanical response of elastomeric graphene networks. *Scientific Reports*, 5, 2015.

[153] S. H. Huh. Thermal reduction of graphene oxide. In *Physics and Applications of Graphene-Experiments*. InTech, 2011.

[154] L. Qiu, J. Z. Liu, S. L. Chang, Y. Wu, and D. Li. Biomimetic superelastic graphene-based cellular monoliths. *Nature Communications*, 3:1241, 2012.

[155] C. Gómez-Navarro, J. C. Meyer, R. S. Sundaram, A. Chuvilin, S. Kurasch, M. Burghard, K. Kern, and U. Kaiser. Atomic structure of reduced graphene oxide. *Nano Letters*, 10(4):1144–1148, 2010.

[156] H. Porwal, S. Grasso, and M. J. Reece. Review of graphene–ceramic matrix composites. *Advances in Applied Ceramics*, 112(8):443–454, 2014.

[157] T. He, J. Li, L. Wang, J. Zhu, and W. Jiang. Preparation and consolidation of alumina/graphene composite powders. *Materials Transactions*, 50(4):749–751, 2009.

[158] K. Wang, Y. Wang, Z. Fan, J. Yan, and T. Wei. Preparation of graphene nanosheet/alumina composites by spark plasma sintering. *Materials Research Bulletin*, 46(2):315–318, 2011.

[159] J. Liu, H. Yan, M. J. Reece, and K. Jiang. Toughening of zirconia/alumina composites by the addition of graphene platelets. *Journal of the European Ceramic Society*, 32(16):4185–4193, 2012.

[160] H. Porwal, P. Tatarko, S. Grasso, J. Khaliq, I. Dlouhý, and M. J. Reece. Graphene reinforced alumina nano-composites. *Carbon*, 64:359–369, 2013.

[161] B. Lee, M. Y. Koo, S. H. Jin, K. T. Kim, and S. H. Hong. Simultaneous strengthening and toughening of reduced graphene oxide/alumina composites fabricated by molecular-level mixing process. *Carbon*, 78:212–219, 2014.

[162] L. S. Walker, V. R. Marotto, M. A. Rafiee, N. Koratkar, and E. L. Corral. Toughening in graphene ceramic composites. *ACS Nano*, 5(4):3182–3190, 2011.

[163] C. F. Gutierrez-Gonzalez, A. Smirnov, A. Centeno, A. Fernández, B. Alonso, V. G. Rocha, R. Torrecillas, A. Zurutuza, and J. F. Bartolome. Wear behavior of graphene/alumina composite. *Ceramics International*, 41(6):7434–7438, 2015.

[164] C. Sun, Y. Huang, Q. Shen, W. Wang, W. Pan, P. Zong, L. Yang, Y. Xing, and C. Wan. Embedding two-dimensional graphene array in ceramic matrix. *Science Advances*, 6(39):eabb1338, 2020.

[165] M. Belmonte, C. Ramírez, J. González-Julián, J. Schneider, P. Miranzo, and M. I. Osendi. The beneficial effect of graphene nanofillers on the tribological performance of ceramics. *Carbon*, 61:431–435, 2013.

[166] J. Llorente, B. Román-Manso, P. Miranzo, and M. Belmonte. Tribological performance under dry sliding conditions of graphene/silicon carbide composites. *Journal of the European Ceramic Society*, 36(3):429–435, 2016.

[167] I. Hussainova, M. Drozdova, D. Pérez-Coll, F. Rubio-Marcos, I. Jasiuk, J. A. N. T. Soares, and M. A. Rodríguez. Electroconductive composite of zirconia and hybrid graphene/alumina nanofibers. *Journal of the European Ceramic Society*, 37(12):3713–3719, 2017.

[168] V. T. Rathod, J. S. Kumar, and A. Jain. Polymer and ceramic nanocomposites for aerospace applications. *Applied Nanoscience*, 7(8):519–548, 2017.

[169] J. Liang, Y. Wang, Y. Huang, Y. Ma, Z. Liu, J. Cai, C. Zhang, H. Gao, and Y. Chen. Electromagnetic interference shielding of graphene/epoxy composites. *Carbon*, 47(3):922–925, 2009.

[170] P. Ajayan and J. Tour. Nanotube composites. *Nature*, 447:1066–1068, 2007.

[171] Y. Fan, L. Wang, J. Li, J. Li, S. Sun, F. Chen, L. Chen, and W. Jiang. Preparation and electrical properties of graphene nanosheet/Al_2O_3 composites. *Carbon*, 48(6):1743–1749, 2010.

[172] A. Gómez-Gómez, C. Ramírez, J. Llorente, A. Garcia, P. Moreno, H. Reveron, J. Chevalier, M.I. Osendi, M. Belmonte, and P. Miranzo. Improved crack resistance and thermal conductivity of cubic zirconia containing graphene nanoplatelets. *Journal of the European Ceramic Society*, 40(4):1557–1565, 2020.

[173] A. Rincón, R. Moreno, A. S. A. Chinelatto, C. F. Gutierrez, M. D. Salvador, and A. Borrell. Effect of graphene and cnfs addition on the mechanical and electrical properties of dense alumina-toughened zirconia composites. *Ceramics International*, 42(1, Part B):1105–1113, 2016.

[174] M. Belmonte, A. Nistal, P. Boutbien, B. Román-Manso, M. I. Osendi, and P. Miranzo. Toughened and strengthened silicon carbide ceramics by adding graphene-based fillers. *Scripta Materialia*, 113:127–130, 2016.

[175] H. Seiner, C. Ramirez, M. Koller, P. Sedlák, M. Landa, P. Miranzo, M. Belmonte, and M. I. Osendi. Elastic properties of silicon nitride ceramics reinforced with graphene nanofillers. *Materials Design*, 87:675–680, 2015.

[176] O. T. Picot, V. G. Rocha, C. Ferraro, N. Ni, E. D'Elia, S. Meille, J. Chevalier, T. Saunders, T. Peijs, M. J. Reece, and E. Saiz. Using graphene networks to build bioinspired self-monitoring ceramics. *Nature Communications*, 8, 2017.

[177] S. Barg, F. M. Perez, N. Ni, P. Do Vale Pereira, R. C. Maher, E. Garcia-Tuñon, S. Eslava, S. Agnoli, C. Mattevi, and E. Saiz. Mesoscale assembly of chemically modified graphene into complex cellular networks. *Nature Communications*, 5, 2014.

[178] Y. Xu, K. Sheng, C. Li, and G. Shi. Self-assembled graphene hydrogel via a one-step hydrothermal process. *ACS Nano*, 4(7):4324–4330, 2010.

[179] G. Lian, C. C. Tuan, L. Li, S. Jiao, Q. Wang, K. S. Moon, D. Cui, and C. P. Wong. Vertically aligned and interconnected graphene networks for high thermal conductivity of epoxy composites with ultralow loading. *Chemistry of Materials*, 28(17):6096–6104, 2016.

[180] J. Kim, N. M. Han, J. Kim, J. Lee, J. K. Kim, and S. Jeon. Highly conductive and fracture-resistant epoxy composite based on non-oxidized graphene flake aerogel. *ACS Applied Materials and Interfaces*, 10(43):37507–37516, 2018.

[181] J. Peng, C. Huang, C. Cao, E. Saiz, Y. Du, S. Dou, A. P. Tomsia, H. D. Wagner, L. Jiang, and Q. Cheng. Inverse nacre-like epoxy-graphene layered nanocomposites with integration of high toughness and self-monitoring. *Matter*, 2(1):220–232, 2020.

[182] E. D' Elia, S. Barg, N. Ni, V. G. Rocha, and E. Saiz. Self-healing graphene-based composites with sensing capabilities. *Advanced Materials*, 27(32):4788–4794, 2015.

[183] E. D'Elia, H.S. Ahmed, E. Feilden, and E. Saiz. Electrically-responsive graphene-based shape-memory composites. *Applied Materials Today*, 15:185–191, 2019.

[184] L. Wang, J. Bi, W. Wang, Y. Chen, R. Liu, and X. Sun. Microstructure and mechanical properties of nacre-like alumina toughened by graphene oxide. *Ceramics International*, 45(7, Part A):8081–8086, 2019.

[185] P. Colombo, G. Mera, R. Riedel, and G. D. Sorarù. Polymer-derived ceramics: 40 years of research and innovation in advanced ceramics. *Journal of the American Ceramic Society*, 93(7):1805–1837, 2010.

[186] F. Ji, Y. Li, J. Feng, D. Su, Y. Wen, Y. Feng, and F. Hou. Electrochemical performance of graphene nanosheets and ceramic composites as anodes for lithium batteries. *Journal of Materials Chemistry*, 19:9063–9067, 2009.

[187] X. Fan, N. Ni, X. Wang, W. Hao, F. Guo, and X. Zhao. Mechanically isotropic alumina prepared by spark plasma sintering: The role of pyrolytic carbon and

multilayer graphene. *Journal of the European Ceramic Society*, 41(7):4242–4251, 2021.

[188] C. F. Burmeister and A. Kwade. Process engineering with planetary ball mills. *Chemical Society Reviews*, 42:7660–7667, 2013.

[189] L. Zhang, J. C. C. Chan, H. Eckert, G. Helsch, L. P. Hoyer, and G. H. Frischat. Novel sol−gel synthesis of sodium aluminophosphate glass based on aluminum lactate. *Chemistry of Materials*, 15(14):2702–2710, 2003.

[190] L. Zhang, C. C. de Araujo, and H. Eckert. Aluminum lactate - an attractive precursor for sol-gel synthesis of alumina-based glasses. *Journal of Non-Crystalline Solids*, 353(13-15 SPEC. ISS.):1255–1260, 2007.

[191] C. Walter, S. Barg, N. Ni, R. C. Maher, E. Garc´ıa-Tuñón, M. M. Z. Ismail, F. Babot, and E. Saiz. A novel approach for the fabrication of carbon nanofibre/ceramic porous structures. *Journal of the European Ceramic Society*, 33(13):2365 – 2374, 2013.

[192] S. Kashyap, S. Mishra, and S. K. Behera. Aqueous colloidal stability of graphene oxide and chemically converted graphene. *Journal of Nanoparticles*, 2014:1–6, 2014.

[193] G. A. Parks and P. L. De Bruyn. The zero point of charge of oxides. *Journal of Physical Chemistry*, 66(6):967–973, 1962.

[194] T. Hiemstra and W.H. Van Riemsdijk. A surface structural approach to ion adsorption: The charge distribution (cd) model. *Journal of Colloid and Interface Science*, 179(2):488–508, 1996.

[195] S. Loganathan, V. Ravi babu, R. Mishra, G. Pugazhenthi, and S. Thomas. *Thermogravimetry Analysis for Characterization of Nanomaterials*. 2017.

[196] R. Jones, D. Hooper, L. Zhang, D. Wolverson, and V. Valev. Raman techniques: Fundamentals and frontiers. *Nanoscale Research Letters*, 14, 12 2019.

[197] A. C. Ferrari, J. C. Scardaci, V. Casiraghi, C. Piscanec, M. Meyer, F. Roth, S. Lazzeri, D. Mauri, K. S. Jiang, S. Novoselov, and A. K. Geim. Raman spectrum of graphene and graphene layers. *Physical Review Letters*, 97(18), 2006.

[198] A. C. Ferrari. Raman spectroscopy of graphene and graphite: Disorder, electron-phonon coupling, doping and nonadiabatic effects. *Solid State Communications*, 143(1-2):47–57, 2007.

[199] A. C. Ferrari and D. M. Basko. Raman spectroscopy as a versatile tool for studying the properties of graphene. *Nature Nanotechnology*, 8(4):235–246, 2013.

[200] F. Tuinstra and J. L. Koenig. Raman spectrum of graphite. *Journal of Chemical Physics*, 53(3):1126–1130, 1970.

[201] S. Hofmann. Introduction and outline. In *Auger- and X-Ray Photoelectron Spectroscopy in Materials Science: A User-Oriented Guide*, pages 1–10. Springer Berlin Heidelberg, Berlin, Heidelberg, 2013.

[202] N. Díez, A. Śliwak, S. Gryglewicz, B. Grzyb, and G. Gryglewicz. Enhanced reduction of graphene oxide by high-pressure hydrothermal treatment. *RSC Advances*, 5:81831–81837, 2015.

[203] J. I. Goldstein, D. E. Newbury, J. R. Michael, N. W. M. Ritchie, J. H. J. Scott, and D. C. Joy. Electron beam—specimen interactions: Interaction volume. In *Scanning Electron Microscopy and X-Ray Microanalysis*, pages 1–14. Springer New York, New York, NY, 2018.

[204] A. M. Sereno, M. A. Silva, and L. Mayor. Determination of particle density and porosity in foods and porous materials with high moisture content. *International Journal of Food Properties*, 10(3):455–469, 2007.

[205] A.B. Spierings, M. Schneider, and R. Eggenberger. Comparison of density measurement techniques for additive manufactured metallic parts. *Rapid Prototyping Journal*, 17(5):380–386, 2011.

[206] A. Sarkar and A. Kietzig. General equation of wettability: A tool to calculate the contact angle for a rough surface. *Chemical Physics Letters*, 574:106 – 111, 2013.

[207] G. R. Lester. Contact angles of liquids at deformable solid surfaces. *Journal of Colloid Science*, 16(4):315 – 326, 1961.

[208] Y. Yuan and T. R. Lee. Contact angle and wetting properties. In Gianangelo Bracco and Bodil Holst, editors, *Surface Science Techniques*, pages 3–34. Springer Berlin Heidelberg, Berlin, Heidelberg, 2013.

[209] A. Krishnan, Y. H. Liu, P. Cha, R. Woodward, D. Allara, and E. A. Vogler. An evaluation of methods for contact angle measurement. *Colloids and Surfaces B: Biointerfaces*, 43(2):95–98, 2005.

[210] J. Drelich. Guidelines to measurements of reproducible contact angles using a sessile-drop technique. *Surface Innovations*, 1(4):248–254, 2013.

[211] P. Solís-Fernández, J. I. Paredes, S. Villar-Rodil, L. Guardia, M. J. Fernández-Merino, G. Dobrik, L. P. Biró, A. Martínez-Alonso, and J. M. D. Tascón. Global and local oxidation behavior of reduced graphene oxide. *The Journal of Physical Chemistry C*, 115(16):7956–7966, 2011.

[212] N. Fairley, V. Fernandez, M. Richard-Plouet, C. Guillot-Deudon, J. Walton, E. Smith, D. Flahaut, M. Greiner, M. Biesinger, S. Tougaard, D. Morgan, and J. Baltrusaitis. Systematic and collaborative approach to problem solving using x-ray photoelectron spectroscopy. *Applied Surface Science Advances*, 5:100112, 2021.

[213] V. G. Rocha, E. García-Tuñón, C. Botas, F. Markoulidis, E. Feilden, E. D'Elia, N. Ni, M. Shaffer, and E. Saiz. Multimaterial 3D printing of graphene-based electrodes for electrochemical energy storage using thermoresponsive inks. *ACS Applied Materials & Interfaces*, 9(42):37136–37145, 2017.

[214] E. García-Tuñon, S. Barg, J. Franco, R. Bell, S. Eslava, E. D'Elia, R. C. Maher, F. Guitian, and E. Saiz. Printing in three dimensions with graphene. *Advanced Materials*, 27(10):1688–1693, 2015.

[215] Q. Zhang, F. Zhang, S. P. Medarametla, H. Li, C. Zhou, and D. Lin. 3D printing of graphene aerogels. *Small*, 12(13):1702–1708, 2016.

[216] J. Li, H. Meng, S. Xie, B. Zhang, J. Li, L. Li, H. Ma, J. Zhang, and M. Yu. Ultra-light, compressible and fire-resistant graphene aerogel as a highly efficient and recyclable absorbent for organic liquids. *Journal of Materials Chemistry A*, 2(9):2934–2941, 2014.

[217] S. P. Sasikala, J. Lim, I. H. Kim, H. J. Jung, T. Yun, T. H. Han, and S. O. Kim. Graphene oxide liquid crystals: a frontier 2D soft material for graphene-based functional materials. *Chemical Society Reviews.*, 47:6013–6045, 2018.

[218] Z.H. Ni, H.M. Wang, J. Kasim, H.M. Fan, T. Yu, Y.H. Wu, Y.P. Feng, and Z.X. Shen. Graphene thickness determination using reflection and contrast spectroscopy. *Nano Letters*, 7(9):2758–2763, 2007.

[219] I. Jung, M. Pelton, R. Piner, D.A. Dikin, S. Stankovich, S. Watcharotone, M. Hausner, and R.S. Ruoff. Simple approach for high-contrast optical imaging and characterization of graphene-based sheets. *Nano Letters*, 7(12):3569–3575, 2007.

[220] G.B. Olowojoba, S. Kopsidas, S. Eslava, E.S. Gutierrez, A.J. Kinloch, C. Mattevi, V.G. Rocha, and A.C. Taylor. A facile way to produce epoxy nanocomposites having excellent thermal conductivity with low contents of reduced graphene oxide. *Journal of Materials Science*, 52(12):7323–7344, 2017.

[221] Q. Mei, B. Liu, G. Han, R. Liu, M. Han, and Z. Zhang. Graphene oxide: From tunable structures to diverse luminescence behaviors. *Advanced Science*, 6(14):1900855, 2019.

[222] R. Jalili, D. Esrafilzadeh, S.H. Aboutalebi, Y.M. Sabri, A.E. Kandjani, S.K. Bhargava, E. Della Gaspera, T.R. Gengenbach, A. Walker, Y. Chao, C. Wang,

H. Alimadadi, D.R.G. Mitchell, D.L. Officer, D.R. MacFarlane, and G.G. Wallace. Silicon as a ubiquitous contaminant in graphene derivatives with significant impact on device performance. *Nature Communications*, 9(1), 2018.

[223] Y.C.G. Kwan, G.M. Ng, and C.H.A. Huan. Identification of functional groups and determination of carboxyl formation temperature in graphene oxide using the xps o 1s spectrum. *Thin Solid Films*, 590:40–48, 2015.

[224] P. Kumar, S. Yu, F. Shahzad, S. M. Hong, Y. Kim, and C. M. Koo. Ultrahigh electrically and thermally conductive self-aligned graphene/polymer composites using large-area reduced graphene oxides. *Carbon*, 101:120–128, 2016.

[225] I.K. Moon, J. Lee, R.S. Ruoff, and H. Lee. Reduced graphene oxide by chemical graphitization. *Nature Communications*, 1(6), 2010.

[226] C. Shen, E. Barrios, and L. Zhai. Bulk polymer-derived ceramic composites of graphene oxide. *ACS Omega*, 3(4):4006–4016, 2018.

[227] N. Yousefi, X. Lin, Q. Zheng, X. Shen, J. R. Pothnis, J. Jia, E. Zussman, and J. Kim. Simultaneous in situ reduction, self-alignment and covalent bonding in graphene oxide/epoxy composites. *Carbon*, 59:406–417, 2013.

[228] J. Chandradass and M. Balasubramanian. Sol-gel based extrusion of alumina-zirconia fibres. *Materials Science and Engineering A*, 408(1-2):165–168, 2005.

[229] Y. K. Park, E. H. Tadd, M. Zubris, and R. Tannenbaum. Size-controlled synthesis of alumina nanoparticles from aluminum alkoxides. *Materials Research Bulletin*, 40(9):1506–1512, 2005.

[230] M. S. Ghamsari, Z. A. S. Mahzar, S. Radiman, A. M. A. Hamid, and S. R. Khalilabad. Facile route for preparation of highly crystalline γ-Al_2O_3 nanopowder. *Materials Letters*, 72:32–35, 2012.

[231] H. K. Park, K. Y. Park, and K. Y. Jung. Alumina-precursor nanoparticles prepared by partial hydrolysis of $AlCl_3$ vapor in tubular flow reactor: Effect of hydrolysis conditions on particle size distribution. *Industrial & Engineering Chemistry Research*, 53(25):10372–10379, 2014.

[232] A. I. Osman, J. K. Abu-Dahrieh, D. W. Rooney, S. A. Halawy, M. A. Mohamed, and A. Abdelkader. Effect of precursor on the performance of alumina for the dehydration of methanol to dimethyl ether. *Applied Catalysis B: Environmental*, 127:307–315, 2012.

[233] M. Shojaie-Bahaabad and E. Taheri-Nassaj. Economical synthesis of nano alumina powder using an aqueous sol-gel method. *Materials Letters*, 62(19):3364–3366, 2008.

[234] P. K. Sharma, M. H. Jilavi, D. Burgard, R. Nass, and H. Schmidt. Hydrothermal synthesis of nanosize α-Al_2O_3 from seeded aluminum hydroxide. *Journal of the American Ceramic Society*, 81(10):2732–2734, 1998.

[235] M. Suarez, V. Rocha, A. Fernandez, J. L. Menendez, and R. Torrecillas. Synthesis and processing of spinel powders for transparent ceramics. *Ceramics International*, 40(3):4065–4069, 2014.

[236] H. Tan, X. Ma, and M. Fu. Preparation of continuous alumina gel fibres by aqueous sol-gel process. *Bulletin of Materials Science*, 36(1):153–156, 2013.

[237] J. He, D. Avnir, and L. Zhang. Sol-gel derived alumina glass: Mechanistic study of its structural evolution. *Acta Materialia*, 174:418–426, 2019.

[238] Y. Wang, C. Suryanarayana, and L. An. Phase transformation in nanometer-sized γ-alumina by mechanical milling. *Journal of the American Ceramic Society*, 88(3):780–783, 2005.

[239] R. Venkatesh and S. R. Ramanan. Influence of processing variables on the microstructure of sol-gel spun alumina fibres. *Materials Letters*, 55(3):189–195, 2002.

[240] J.F. Moulder and J. Chastain. *Handbook of X-ray Photoelectron Spectroscopy: A Reference Book of Standard Spectra for Identification and Interpretation of XPS Data*. Physical Electronics Division, Perkin-Elmer Corporation, 1992.

[241] B. R. Strohmeier. Gamma-alumina (γ-Al_2O_3) by xps. *Surface Science Spectra*, 3(2):135–140, 1994.

[242] J. Franco, P. Hunger, M.E. Launey, A.P. Tomsia, and E. Saiz. Direct write assembly of calcium phosphate scaffolds using a water-based hydrogel. *Acta Biomaterialia*, 6(1):218–228, 2010.

[243] A. Šturcová, P. Schmidt, and J. Dybal. Role of hydration and water coordination in micellization of pluronic block copolymers. *Journal of Colloid and Interface Science*, 352(2):415–423, 2010.

[244] J. Orth, W. H. Meyer, C. Bellmann, and G. Wegner. Stabilization of aqueous α-Al_2O_3 suspensions with block copolymers. *Acta Polymerica*, 48(11):490–501, 1997.

[245] J. Escobar-Chávez, M. López-Cervantes, A. Naïk, Y. Kalia, D. Quintanar, and A. Ganem. Applications of thermo-reversible pluronic F-127 gels in pharmaceutical formulations. *Journal of pharmacy pharmaceutical sciences : a publication of the Canadian Society for Pharmaceutical Sciences, Société canadienne des sciences pharmaceutiques*, 9:339–58, 02 2006.

[246] L.M.U. Dutra, M.E.N.P. Ribeiro, I.M. Cavalcante, D.H.A. De Brito, L. De Moraes Semião, R.F. Da Silva, P.B.A. Fechine, S.G. Yeates, and N.M.P.S. Ricardo. Binary mixture micellar systems of F127 and P123 for griseofulvin solubilisation. *Polimeros*, 25(5):433–439, 2015.

[247] P. Alexandridis, J. F. Holzwarth, and T. A. Hatton. Micellization of poly(ethylene oxide)-poly(propylene oxide)-poly(ethylene oxide) triblock copolymers in aqueous solutions: Thermodynamics of copolymer association. *Macromolecules*, 27(9):2414–2425, 1994.

[248] M. Jalaal, G. Cottrell, N. Balmforth, and B. Stoeber. On the rheology of pluronic F127 aqueous solutions. *Journal of Rheology*, 61:139–146, 01 2017.

[249] M. Müller, J. Becher, M. Schnabelrauch, and M. Zenobi-Wong. Nanostructured pluronic hydrogels as bioinks for 3D bioprinting. *Biofabrication*, 7(3):035006, 2015.

[250] J.J. Moyano, A. Gómez-Gómez, D. Pérez-Coll, M. Belmonte, P. Miranzo, and M.I. Osendi. Filament printing of graphene-based inks into self-supported 3d architectures. *Carbon*, 151:94–102, 2019.

[251] F. Murjalili, H. Mohamad, and L. Chuah. Preparation of nano-scale α-Al_2O_3 powder by the sol-gel method. *Ceramics - Silikaty*, 55(4):378–383, 2011.

[252] M. Majić Renjo, M. Lalić, L. Ćurković, and G. Matijašić. Rheological properties of aqueous alumina suspensions. *Materialwissenschaft und Werkstofftechnik*, 43(11):979–983, 2012.

[253] X. Zhang, S. Wan, J. Pu, L. Wang, and X. Liu. Highly hydrophobic and adhesive performance of graphene films. *Journal of Materials Chemistry*, 21(33):12251, 2011.

[254] M. Wu, J. Chen, Y. Wen, H. Chen, Y. Li, C. Li, and G. Shi. Chemical approach to ultrastiff, strong, and environmentally stable graphene films. *ACS Applied Materials & Interfaces*, 10(6):5812–5818, 2018.

[255] Y. Chen, S. Yang, D. Fan, G. Li, and S. Wang. Dual-enhanced hydrophobic and mechanical properties of long-range 3D anisotropic binary-composite nanocellulose foams via bidirectional gradient freezing. *ACS Sustainable Chemistry & Engineering*, 7(15):12878–12886, 2019.

[256] ASTM C1161-18. Standard test method for flexural strength of advanced ceramics at ambient temperature. Standard, ASTM International, West Conshohocken, PA, 2018.

[257] ASTM C1421-18. Standard test methods for determination of fracture toughness of advanced ceramics at ambient temperature. Standard, ASTM International, West Conshohocken, PA, 2018.

[258] Z. Shen, M. Johnsson, Z. Zhao, and M. Nygren. Spark plasma sintering of alumina. *Journal of the American Ceramic Society*, 85(8):1921–1927, 2002.

[259] O. Tokariev, L. Schnetter, T. Beck, and J. Malzbender. Grain size effect on the mechanical properties of transparent spinel ceramics. *Journal of the European Ceramic Society*, 33:749–757, 04 2013.

[260] K. Kambale, A. Mahajan, and S. P. Butee. Effect of grain size on the properties of ceramics. *Metal Powder Report*, 74, 04 2019.

[261] C. Ramirez and M. I. Osendi. Toughening in ceramics containing graphene fillers. *Ceramics International*, 40(7 PART B):11187–11192, 2014.